Tailor-made blanks for the aircraft industry

Tailor-made blanks for the aircraft industry

Proefschrift

ter verkrijging van de graad van doctor
aan de Technische Universiteit Delft,
op gezag van de Rector Magnificus prof. ir. K.C.A.M. Luyben,
voorzitter van het College voor Promoties,
in het openbaar te verdedigen op dinsdag 12 januari 2010 om 10:00 uur

door

Amir Abbas Zad Poor
Master of Science in Biomedical Engineering
Amir Kabir University of Technology, Tehran, Iran
geboren te Ghom, Iran

Dit proefschrift is goedgekeurd door de promotor:
Prof.dr.ir. R. Benedictus

Samenstelling promotiecommissie:

Rector Magnificus,	voorzitter
Prof.dr.ir. R. Benedictus,	Technische Universiteit Delft, promotor
Prof.dr. Z. Gürdal ,	Technische Universiteit Delft
Prof.dr. I.M. Richardson,	Technische Universiteit Delft
Prof.dr.ir. J. Huétink ,	Universiteit Twente
Prof. dr.-ing. A. E. Tekkaya,	Technische Universität Dortmund
Ir. J. Sinke,	Technische Universiteit Delft
Dr. ir. H. Vegter,	Corus Group

Ir. J. Sinke heeft als begeleider in belangrijke mate aan de totstandkoming van het proefschrift bijgedragen.

This research was carried out under project number MC1.05224 in the framework of the Strategic Research Programme of the Materials Innovation Institute M2i (www.m2i.nl), the former Netherlands Institute for Metals Research.

ISBN 978-90-77172-51-3

Keywords: Tailor-made blanks, aircraft industry, forming, and formability.

Printed in The Netherlands

To

My father who taught me how to think

My mother who taught me how to live

and my Fatemeh who taught me how to love

Table of Contents

PART I: INTRODUCTION AND BACKGROUND

1. Introduction **1**

1.1. Problem definition 2

1.2. Outline of the thesis 3

1.3. References 4

2. Literature review **5**

2.1. Mechanical properties of TWBs 7

2.2. Formability 10

2.3. Failure and fatigue analysis 17

2.4. FEM modeling of TWBs 20

2.5. Conclusions 23

2.6. References 24

PART II: MECHANICAL BEHAVIOR AND MICROSTRUCTURE

3. Machined tailor-made blanks **31**

3.1. Experimental study 32

3.2. Experimental results 35

3.3. Numerical study 38

3.4. Simulations results 40

3.5. Discussions 42

3.6. Conclusions 46

3.7. References 47

3.8. Appendix A- nomenclature 48

4. Adhesively bonded tailor-made blanks **51**
4.1. Experimental methods 53
4.2. Experimental results 55
4.3. Numerical methods 56
4.4. Numerical results and discussions 61
4.5. Conclusions 74
4.6. References 75
4.7. Appendix A- nomenclature 76

5. Dissimilar-alloy adhesively bonded TMBs **79**
5.1. Experimental methods 80
5.2. Experimental results 81
5.3. Numerical methods 83
5.4. Numerical results 87
5.5. Discussions 90
5.6. Conclusions 93
5.7. References 93

6. Friction stir welded blanks I **95**
6.1. Welding procedure 97
6.2. Microstructural features 98
6.3. Mechanical properties 103
6.4. Conclusions 108
6.5. References 109

7. Friction stir welded blanks II **113**
7.1. Materials and methods 114
7.2. Results and discussion 115
7.3. Conclusions 134
7.4. References 135

PART III: FORMING AND FORMABILITY

8. Comparison of formability prediction theories 139

8.1. Experimental data 141

8.2. Phenomenological models 143

8.3. Porous metal plasticity theory 147

8.4. Marciniak-Kuczynski theory 156

8.5. Combined porous metal plasticity and Marciniak-Kuczynski model 159

8.6. Comparative discussion on the results 163

8.7. Conclusions 165

8.8. References 166

8.9. Appendix A 169

8.10. Appendix B- Nomenclature 172

8.11. Appendix C 175

9. Effects of thickness on formability 179

9.1. Methodology 180

9.2. Experimental results 182

9.3. Discussions 182

9.4. Conclusions 189

9.5. References 189

10. FEM modeling and failure prediction of FSW blanks 191

10.1. Limiting dome height test 192

10.2. S-rail problem 194

10.3. Friction stir welded blanks 195

10.4. Failure prediction 198

10.5. Simulation results 200

10.6. Discussions 202

10.7. Conclusions 208

10.8. References 209

11. Bendability of machined TMBs **211**
11.1. Experiments 212
11.2. Experimental results 213
11.3. Numerical methods 214
11.4. Numerical results 217
11.5. Discussions 220
11.6. Conclusions 222
11.7. References 222

PART IV: CONCLUSIONS

12. Conclusions **225**
12.1. Recommendations for future research 226

Summary **227**
Samenvatting **229**
Curriculum Vitae **231**
List of publications **232**
Acknowledgements **235**

1. Introduction

Tailor welded blanks (TWBs) as a variant of Tailor made blanks (TMBs) are used in the automotive industry for almost two decades. On the other hand, applications of the tailor-made blanks technology in the aircraft industry are almost non-existent. Therefore, the aircraft industry can potentially benefit from the tailor-made blanks technology as developed in the automotive industry. The technological barriers that prevent the aircraft industry from the use of the tailor-made blanks technologies are mostly related to the production series, the specific alloys, and joining methods used in this industry. Furthermore, limited knowledge of the forming behavior of tailor-made blanks is available. The main aim of this study is to make the ground for application of the tailor-made technology in the aircraft industry.

The main idea of the tailor-made blank concept is that the blanks used for production of the structural parts of ground and air vehicles may have different thicknesses, or be composed of more than one material, or even have different types of coating. Tailor-made blanks are therefore sheet metal assemblies that include areas with different thicknesses, materials, coatings, etc. The sheets which constitute the tailor-made blank are welded or adhesively bonded. Alternatively, a monolithic sheet can be machined to create the required thickness variations. The joining, welding, or machining process is followed by a forming process which brings the tailor-made blank to its functional shape as a structural part.

The possibility of having a heterogeneous distribution of material and/or geometrical properties within the same structural part facilitates the optimal distribution of material within the part and may result in (significant) weight and cost savings. For example, a part with non-uniform loading conditions can be made of one blank with two sections with two different thicknesses (or materials) such that the thicker (stronger) sheet is used at the load-intensive areas and the thinner (weaker) material at the less-loaded places. The weight saving achieved by applying the tailor-made blank concept in the automotive industry is between 6 and 11% (estimated) [1]. Optimal material distribution in the aircraft structural parts is even more important because not only it results in a decrease of the weight of the structural part itself, but also results in smaller wings, smaller engines being required, etc., ultimately resulting in a significant total weight being saved (snowball effect). Moreover, the TMB technology removes the need for the excessive machining of aluminum parts and minimizes the material waste and energy consumption of the machining process. Tailor-made blanks have been being used in the automotive industry since 1990s. The application of the tailor-made blanks technology has become so widespread that today many cars include one or more tailor-made parts and a number of dedicated

companies specialize in tailor-made production of certain parts of car bodies. For the TWBs, the laser beam welding is by far the most widely used joining method in the automotive industry.
High-strength aluminum alloys, used in production of structural parts in the aircraft industry, are not weldable and are sensitive to high welding temperatures. These high temperatures affect the heat-treatments of precipitation-hardened aluminum alloys and disrupt their carefully built microstructures. In addition, welding adversely affects the formability of those alloys. The other point is the difficulty of welding dissimilar alloys which limits the flexibility of the TWB applications. Therefore, new techniques are needed for production of TMBs in the aircraft industry.

1.1. Problem definition

As already discussed, TMBs can offer many advantages to the aircraft industry. However, the specific types of TMBs that can be used in the aircraft industry are different from the ones that are being used elsewhere. Therefore, the already available know-how about TMBs is not directly applicable to the aircraft industry. The main goal of this study is to generate (a part of) the knowledge that is required for the application of the TMB technology in the aircraft industry. The most important questions to be addressed are:

1. What are the phenomena and/or obstacles that may be encountered in production of TMBs in the aircraft industry?
2. What are the effects of design variables such as thickness ratio, material combinations, and loading direction on the forming behavior of TMBs?
3. How can the forming behavior of TMBs be modeled and/or predicted?
4. What are the limits in working with TMBs?

Three production technologies have been chosen for the study: machining, adhesive bonding, and friction stir welding. The selection of the production technologies has been motivated by the specific requirements of the aircraft industry.
Machined TMBs are sheet metals that are machined prior to the forming. In contrast to other types of TMBs, in which also the material and coating can be different, only thickness variations are possible in machined TMBs.
Aircraft manufacturers are using adhesive bonding as an efficient joining method for a long time. Among the advantages of adhesive bonding for the aircraft industry are elimination of stress concentrations which are present in other joining methods (such as riveting), high joint efficiency, and the possibility of joining dissimilar materials. In contrast to welding, the adhesive bonding processes used in the aircraft industry do not include high temperatures and the mechanical properties of the alloys are not affected by the bonding process. Furthermore, dissimilar alloys can be easily bonded together which offers additional flexibility to a designer of TMB parts, while attempting to achieve an optimal material distribution.
Friction stir welding was invented at The Welding Institute (TWI) in the early 1990s [2]. As a solid state joining process, FSW is capable of producing high-quality

defect-free welds even in difficult-to-weld 2000 and 7000 series aluminum alloys [3]. Welds produced by FSW have a higher strength and formability [3] due to lower welding temperatures compared to fusion welding processes [2]. The welding temperatures of friction stir welding are moderate [2] and the effects of welding on the mechanical properties of the precipitation-hardened aluminum alloys as used in the aircraft industry are minimal. Furthermore, weld defects tend to be less in friction stir welding compared to fusion welding processes. As an indication, fusion welding averages one defect in each 8.4 m, whereas there are some reports of 2.5 km continuous friction stir welding without any defect [4].
The materials selected for the study are two high strength aluminum alloys from 2000 and 7000 series which are commonly used in the aircraft structures, namely 2024-T3 and 7075-T6.
The first aim of the study is to understand and characterize the mechanical behavior of TMBs to answer the four questions mentioned at the beginning of this section. The effects of different design parameters such as thickness ratio, material combination and the transition from one material or thickness on the mechanical behavior of TMBs need to be understood. In the case of friction stir welded TMBs, the microstructural features of the welds need to be studied as well, because the thermomechanical evolutions taken place during the welding process drastically influences the mechanical properties of the resulting TMBs. Some FEM models will be developed and will be validated using experimental results.
The second aim of the study is to study the forming behavior of TMBs. Since two different materials and/or thicknesses are present in one single sheet assembly, the forming behavior of the TMB is different from the base materials and needs to be determined. The forming limits of TMBs will be determined experimentally and theoretical models will be developed for prediction of those limits. The theoretically determined forming limits will be compared with the experimentally-obtained forming limits to validate the theoretical approaches.

1.2. Outline of the thesis

This thesis is divided into four main parts: introduction, mechanical behavior and microstructure, forming and formability, and conclusions.
In the first part, the main idea of the tailor-made blanks technology is presented and the background literature is reviewed. Since tailor-made blanks has not been used in the aircraft industry before, the second chapter of the first part which reviews the background literature is limited to tailor-welded blanks (TWB) technology and its applications in the automotive industry.
The second part studies the mechanical behavior and microstructure of the different types of tailor-made blanks. The part has five chapters, each focusing on one type of tailored blanks. The chapter on machined tailor-made blanks presents a combined experimental and numerical study of tensile testing of some specially-designed specimens. The two chapters dealing with adhesively bonded tailor-made blanks define tensile test specimens and study the mechanical behavior of the blanks during tensile testing using FEM models. The results of the FEM models are compared with the experimental results. The fourth and fifth chapters study the mechanical behavior

and microstructure of friction stir welded blanks. The global mechanical properties, local mechanical properties, hardness patterns, fracture mechanisms, microstructure and chemical composition of the welds are studied when sheets with dissimilar alloys and/or thicknesses are welded together.

The third part is concerned about the formability and forming behavior of tailored blanks and is divided into four chapters. The subject of the first chapter of this part is the formability prediction of high strength aluminum alloys. The chapter compares four different approaches for formability prediction of aluminum alloys. The aim of this chapter is to answer the question how one can predict the forming limits of monolithic sheets of high strength aluminum alloys. The study covered in the second chapter aims at the isolated effects of sheet thickness on formability. This is relevant for the formability analysis of the different thicknesses in one TMB. The third chapter of this part is about FEM modeling and failure prediction of friction stir welded blanks. This chapter sheds light on whether or not it is feasible and/or relevant to implement the mechanical properties of the different weld zones such as weld nugget and heat-affected zones in the FEM models of friction stir welded blanks. The effects of implementing the mechanical properties of the weld zones on the predicted failure limits are also studied. The fourth chapter of the third part is focused on the bending limits of machined tailor-made blanks.

The final part consists of one single chapter that summarizes the undertaken research and highlights the main findings of the thesis. Some design guidelines are also suggested and a few areas for future research are recommended.

1.3. References

[1] Shami SN, Good MC. Tailor Welded Blank Technology. Sixth International Conference on Manufacturing Engineering. Barton, ACT: Institution of Engineers, Australia, 1995.

[2] Mishra RS, Ma ZY. Friction stir welding and processing. Mater. Sci. Eng. R 2005;50:1.

[3] Su JQ, Nelson TW, Mishra R, Mahoney M. Microstructural investigation of friction stir welded 7050-T651 aluminium. Acta Mater. 2003;51:713.

[4] Hansen M. A cooler weld. Mech. Eng. 2003;125:D10.

Modified from: Zadpoor, A. A., Sinke, J., Benedictus, R., 2007, "Mechanics of Tailor-Welded Blanks: An Overview", Key Engineering Materials, vol. 344, pp. 373-382.

2. Literature review

Tailor Welded Blanks (TWBs) is a concept developed by the forming community. In this concept, the sheets are welded prior to the forming operation using high-tech welding techniques. As a result of the tailoring, optimal distribution of thickness, strength, etc is possible. Tailor welded blanks offer several advantages to engineers like reduced production cost, reduced weight, and improved structural performance. Due to these advantages, tailor-welded blanks are of particular interest to the automotive and aircraft industries. Today, a number of parts of automobiles are being manufactured by using TWB technology. This technology dates back to the 1980s, and numerous studies are conducted since to explore different aspects of it. Although TWB technology can be reviewed from several viewpoints, this chapter deals only with the *mechanics* of tailor-welded blanks. The chapter is divided into four sections. The first section is devoted to the mechanical properties of the blanks. Tensile properties and hardness of TWBs are covered in this section. The second section deals with the formability of TWBs. The formability tests, effects of different parameters on the formability of TWBs, material flow phenomena, control of material flow, stress and strain distributions, and springback behavior are covered. The third section is focused on the failure and fracture of TWBs. Failure modes, failure criteria, and fatigue behavior of TWBs are the principal topics of this section. FEM modeling is the topic of the final section. FEM modeling of the weld line and the heat-affected zone, material models used in modeling of TWBs, and issues related to modeling of forming parameters are discussed in this section. The chapter ends with a brief outline/overview on research gaps within the area of tailor-welded blanks, and tries to give a picture of possible future research trends.

The demand for lightweight vehicles is rapidly growing due to economic and environmental reasons. Car manufacturers try to produce cars with lower fuel consumption and emissions, partly enforced by legislation. By reducing the weight of the vehicles, the fuel consumption and emissions are considerably reduced as well. Besides the savings caused by the lower fuel consumption, there is another encouraging factor for lighter vehicles, namely reduced environmental impact. Environmental regulations are becoming stricter and that is why new technologies, despite their relatively high cost, are becoming more and more feasible. Weight and fuel consumption reductions are not only important in the automotive industry but also in the aircraft industry where the fuel consumption and environmental issues are even more important. Moreover, sizes of the engines, wings and tail planes, and other related systems decrease when the overall weight of the aircraft decreases. Therefore, it is a prime objective to try to reduce the structural weight of the aircraft. Tailoring of blanks is a promising weight and cost reduction technology for both automotive and aerospace sectors. However, though TWBs is a rather well known concept in the automotive industry, it is not used yet in the aircraft industry.

In this literature review, a comprehensive overview of the tailor-welded blanks is given with emphasis on the *mechanics* of tailor-made blanks. Other related issues such as joining methods are discussed briefly when appropriate.

The tailor-welded blank concept is a rather new concept in metal forming. In manufacturing of TWBs, a structural part or product is made by joining several metal sheets of possibly different thicknesses, materials, and/or surface coatings. Key is that the joining (welding) is performed prior to the forming. The possibility of creating blanks of different thicknesses, strengths, and/or other material properties enables the designer to optimize the structural performance of the part. Optimal performance of the part means lighter structures, higher strengths, and joining before forming results in lower production costs.

Quoting from pioneers, Rooks gives a historical overview of the TWBs technology [1]. As in Rooks article, the first true TWB was produced around 1985. In that year, Thyssen, a German conglomerate engineering company, in cooperation with Rofin-Sinar, a laser welding company, developed a laser welding system for production of the underbody of the Audi 100. Before that time (in 1982), there was merely an experimental use of laser welded blanks at the Rover Swindon processing facility to produce a part required for the Montego car. The technology of TWBs developed almost simultaneously in Europe, Japan, and United States. As Kusuda *et al* discuss, Toyota has used tailor-welded blanks since 1985 [2].

Only aluminum and steel alloys are used in the vast majority of the previous studies of TWBs. Besides steel alloys, which are common in automotive industry, there is a tendency to apply lightweight aluminum alloys in cars. This is because of lower density of aluminum alloys comparing with steel alloys. Among the aluminum alloys, the 5000 and 6000 series are the most frequently used alloys in the studies, because of their applicability in the automotive industry.

Several types of welding methods can be used for the manufacture of TWBs. Among welding methods, Laser Beam Welding (LBW) and mash seam welding have received most attention. Due to a report, either CO_2 or Nd:YAG laser welding is used in approximately 99% of all TWB application [3]. However, other types of welding such as friction stir welding, electron-beam welding, and induction welding can also be used for TWBs [4]. Laser beam welding is the dominant joining method for steel alloys, and friction stir welding is often used for aluminum alloys.

The joining method is very important in production of TWBs. According to Masakazu Tsuji of the Hanwa Company, Honda had produced a precursor of the tailor welded blank back in 1967 [1]. The product had five separate pieces, which were welded together by using tungsten inert gas welding. However, there was such a bad thermal distortion in the product that it made the exercise unsuccessful. Due to unfit welding techniques, the birth of the TWB technology was delayed until the emergence of laser beam welding.

Starting in the 80s, the TWBs technology has received much attention and the literature related to the subject has grown very quickly. Indeed, it is not possible to cover the whole subject in one single chapter. Therefore, this chapter is a survey of the literature related to the *mechanics* of tailor-welded blanks. For a survey of tailor-

welded blanks in general see reference [5], which is written from technological viewpoint. More recent welding techniques, such as friction stir welding, are not covered sufficiently in this survey; for a more up-to-date review of friction stir welding and processing see reference [6]. One may consult other publications on TWB by the Auto-Steel Partnership such as “tailor welded blank acceptance guidelines” [7], “tailor welded blank design and manufacturing manual” [8], and an article on “intangible benefits of tailor welded blank applications” [9]. The technology of aluminum tailor-welded blanks is more recent and most survey articles do not cover this technology satisfactorily. For an overview of “issues and problems in laser welding of automotive aluminum alloys”, see reference [10]. An overview of “research and progress in laser welding of wrought aluminum alloys” can be found in references [11, 12]. In that two-part survey, Cao *et al* give a comprehensive overview of processes, parameters, and metallurgical issues of laser welding of aluminum alloys.
The current chapter is divided into four main sections. The first section is devoted to the mechanical properties of tailor-welded blanks. The second section deals with the formability aspect of TWBs. The third one is concentrated on failure and fatigue analysis of TWBs. The fourth section reviews literature related to the FEM modeling of TWBs. Finally, a last section makes the concluding remarks and highlights research gaps and potential future research trends in this field.

2.1. Mechanical properties of TWBs

Tensile testing. The fact that there might be different materials and thicknesses in one single blank results in potentially non-uniform distribution of strains and stresses in the TWB. Therefore, the uniform strain assumption that is the basis of many conventional strain measurement techniques, such as extensometers, is not valid anymore and one may need to use tailor-made tensile tests specimens or resort to more elaborate measurement techniques.
One important factor in the testing of TWB is the size of the specimens. The size of the specimens depends on what needs to be tested: the joint or the weld. If the joint is tested, the specimen should include both the weld and the base metals. In this case, the size of the specimen can be as large as the size of the standard ASTM E8 specimens. If the weld is being tested, only the material of the weld should be present in the gauge length. Wild *et al* showed that only sub-sized specimens (smaller than ASTM E8 specimens) can give reliable tensile properties [13]. They argued that this is because the relative contribution of the weld to the tensile deformation diminishes as the size of the specimen increases. Indeed, the standard specimens overestimate the ductility of the weld metal [14, 15]. When the relative size of the weld in the gauge length increases, the stress-strain curve of the specimen approaches the stress-strain curve of the weld metal [13]. Therefore, many researchers have chosen to use small [13, 16] or miniature test specimens [17]. The miniature test specimens are small enough to ensure that only the material of the weld is present in the gauge area. It is shown that reliable weld properties can be obtained by using this method [17].

Nevertheless, there are some difficulties associated with the miniature test specimens. For example, manufacturing of the miniature test specimens is not easy.
Due to these problems, some efforts are made to use other methods for the measurement of the tensile properties of the material of the weld. The rule of mixtures (ROM) is one of the methods. This method can be applied only for longitudinal (standard) test specimens. The method assumes that the longitudinal strains are uniform across the welded specimen and that the tensile load is divided between base metal 1, base metal 2, and the material of the weld as follows:

$$P = \sigma_1 A_1 + \sigma_2 A_2 + \bar{\sigma}_w A_w \quad (1)$$

If the strength and strain-hardening coefficients of the base metals are known, the average stress in the material of the weld, $\bar{\sigma}_w$, can be calculated as:

$$\bar{\sigma}_w = \frac{P - K_1 \varepsilon^{n_1} A_1 - K_2 \varepsilon^{n_2} A_2}{A_w} \quad (2)$$

where ε is the uniform longitudinal strain. The rule of mixtures was used by some researchers for the determination of the stress-strain curve of tailor-welded blanks [13, 16, 18]. The most important difficulty associated with the ROM method is the determination of the cross section of the weld. Micro-hardness measurements can be applied to determine this size. A more complete version of ROM which works both for longitudinal and transverse specimens is presented by Liu and Chao [19].
A recent trend for the measurement of the local mechanical properties of TWB is to use non-contact optical methods such as Digital Image Correlation (DIC) technique. DIC uses digital imaging to trace back a pre-applied random ink pattern on the surface of the specimen. After the test, a computer program compares the successive digital images that are taken during the test and correlates the ink patterns of the images. Subsequently, the local strains can be determined using the calculated displacements of the ink pattern. DIC has been used by many researchers, see e.g. [20-24].

Tensile properties. The global mechanical properties of TWB are normally determined by using tensile test specimens that contain the different zones of the weld; the specimens may or may not contain base metal. This category of tests gives information concerning the TWB as a whole and is extensively used for study of the strength and ductility of tailor-welded blanks. Whether the strength of the material is affected by welding is highly dependent on the materials and welding parameters. It is shown that post-weld strengths of some steels, e.g. SPCC (a cold rolled formable low carbon steel), remain at the same level as the base metal regardless of the welding method [25-27]. The same holds for O-tempered aluminum alloys [14, 28, 29]. However, precipitation-hardened aluminum alloys change in properties during welding, and tend to have a lower strength compared to the base metals [29-31] because of the dissolution and coarsening of precipitates. Wherever local re-melting takes places, like in the case of laser welding, or if the material undergoes dynamic re-crystallization, such as the case of FSW, the grain size in the weld zone may be different from that of the base metal. The disparity between grain sizes results in different yield stresses and, thus, reduced strength (Hall-Petch relationship) [31].

However, some experimental studies found that despite large disparity between grain sizes in the weld and the base metal zones, there is no considerable change in tensile strength [31]. Yield strength and tensile strength of TWB are shown to be dependent on the orientation of the weld line. Seo *et al* reported that the yield and tensile strengths of longitudinally welded tensile specimens (laser welded SPC1 sheets, steel standard JIS-G-3141) are 12% better than transversely welded specimens [32].
Experimental results show that ductility of tailor-welded blanks decreases after welding. This decrease is highly dependent on, for example, the welding method [29], weld line orientation [28], the size of the weld area in the cross section of the specimens [14], and the thickness ratio [31]. Miles *et al* showed that FSW TWB have better ductility compared with gas tungsten arc welded TWB [28]. Davies *et al* argued that an increase in the porosity of weld metal and in the size of the weld area in the cross section of the specimen would decrease the ductility [14]. Cheng *et al* showed that transversely welded 5754-O TWB are more ductile than longitudinally welded ones [28]. Smaller thickness ratios will also result in improved ductility [27, 31].

Hardness. The hardness test is often used as an indirect mechanical testing technique. Generally speaking, harder materials are stronger, i.e. have higher yield strengths, are more brittle and deform less until failure [33]. Several studies have shown that the hardness of the area near the weld seam of TWB is significantly changed due to welding [13, 26, 27, 31, 32, 34-36]. However, the changes in hardness and its distribution vary with different welding methods [36], base metals [34], and thickness ratios [27].
As for steels, studies show that the hardness increases in the weld seam in most cases [13, 26, 27, 32, 34, 36]. However, the level of the increase depends on the welding method and metal properties. In laser welding, hardness increases ranging from 50% [27] to 250% [32] are reported. The increase of hardness can also be dependent, for example, on the amount of carbon content [34]. Nevertheless, a level of 120% increase is typical for most applications [26]. Similar increases in hardness are reported for other welding methods. For example, it is shown that the hardness of the weld zone increases by about 50% for mesh and upset welding [26, 34]. The area of hardness increase can have a width from tenths of a millimeter to a few millimeters depending on the material and welding method [34]. Also the type of heat input is important in this regard; because a more concentrated heat input, like laser welding, results in narrower regions of increased hardness compared to other less concentrated methods, like MIG welding [36].
Aluminum alloys can be categorized as being either heat-treatable (precipitation-hardened) or non-heat-treatable (solid solution hardened) [6]. Among the standard series of aluminum alloys, the 2000, 6000, and 7000 series are (generally) heat-treatable, whereas the 1000, 3000, 4000, and 5000 series are (generally) non-heat-treatable. The effects of welding on the hardness of heat-treatable and non-heat treatable alloys tend to be different. Heat-treatable alloys normally undergo significant precipitate dissolution and coarsening due to high welding temperatures. That results in significant strength reductions after laser [30, 31] or GTAW [29] welding, and, thus, considerably lower hardness levels in the weld and heat-affected

zones. Some non-heat-treatable alloys such as 5182-O may develop a slightly higher hardness in the weld zone after FSW due to grain refinement and residual work hardening [29]. It is also well established that, for (5000 series) aluminum alloys, a higher hardness and tensile strength are associated with higher magnesium content [10]. Loss of ductility and tensile strength in laser-welded aluminums may originate from depletion of the magnesium content during welding [35, 37-39]. In general, vaporization of various volatile alloying elements such as zinc, lithium, and magnesium takes place during the laser welding of aluminum alloys because these elements have much higher equilibrium pressure than aluminum [10]. Since these volatile elements can form precipitates, their volatilization may contribute to the degradation of the mechanical properties and softening of the weld metal [10].

2.2. Formability

Formability testing methods. It is well known that the formability of tailor-welded blanks is affected by welding. Therefore, experimental tests are needed for the formability analysis of tailor-welded blanks. The experimental test methods are discussed in this section.

Formability tests are divided in two main categories: intrinsic tests and simulative tests. The intrinsic tests measure material properties. Results of the intrinsic tests are independent from the specimen dimensions, machine parameters, thickness, surface characteristics, and lubricants. Examples of intrinsic tests are the tensile test, bulge test, hardness test, plane strain tensile test, and the Marciniak biaxial stretch test. The major shortcoming of the intrinsic tests is that they do not account for the effects of processing variables such as die and punch geometry, lubrication, punch speed, etc. Simulative tests provide information that are dependent on the process variables such as friction condition and geometry. Hence, the results are related to a particular type of forming process and geometry. Examples of simulative tests are the Olsen test, Erichsen test, Limiting Dome Height (LDH) test, hole expansion test, Yoshida test, bend test, limiting draw ratio test, drawbead test, Swift cup test, Englehardt test, stretch bend test, Fukui test, and the plane-strain stretching test [40].

Although the process variables are neglected in the intrinsic tests, they yet can provide useful information regarding the formability of sheet metals. A high strain-hardening coefficient is an indicator of a larger uniform strain of the material before instability bifurcation. Lower yield strength results in improved shape fixing in “lightly-formed parts”, and reduces springback. A high value of strain-rate dependency index delays the onset of localized necking and, thus, improves material formability. Finally, materials with higher values of anisotropy index resist thinning and, thus, provide better drawing properties [41]. The materials with higher anisotropy values are also more susceptible to earing in deep drawing processes.

Among simulative tests, two tests are more frequently used for assessing the formability of tailor-welded blanks, namely the Swift cup and the limiting dome height (LDH) tests. A comparatively new formability testing method called Ohio State University (OSU) method is occasionally used for formability testing of tailor-welded blanks, e.g. see reference [4, 29, 42]. A brief description of these three tests is given here.

The Swift cup test examines the drawability of sheet metals. Series of blanks of increasing diameter are used in this test. A blank-holder holds the sheet metal, and a small flat-bottomed parallel-sided cup is drawn from the blanks. The test index, called limiting draw ratio (LDR), is determined by using the maximum blank size which can be drawn without flange and without failure [41]. The index is calculated as follows:

LDR= maximum blank diameter/cup diameter

The standardized punch radius is 6.35 mm. Some special surface conditions are required for the specimen and die interfaces. The test is well suited to simulate deep drawing processes. It is not suitable for stamping processes that also involve stretching operations [41].

Limiting dome height test is maybe the most well known formability test in the automotive industry. This test employs a 101.6 mm hemispherical punch with a set of dies that prevent draw-in and assure a pure stretch condition. The blank is stretched to failure and the limiting dome height is recorded at peak load [29]. The operator may mark the blank with a grid of small circles prior to stretching or can use digital cameras to capture the deformations during the test. In case of a circle grid, the circles are usually 2 to 5 mm in diameter and are applied by photochemical etching or electrochemical etching. Strain analysis is performed using the deformed grid. The fracture strain is measured from the circle closest to the failure location. However, the circle itself may not have fractured. Indeed, the formability of sheet metal is usually minimal at the plane strain condition. Therefore, it is desirable to find the blank width that fails in the plane strain condition. Since the formability of sheet metal is minimal at the plane strain condition, the blank width that gives the plane strain condition is regarded as the critical blank width. The dome height corresponding to the critical blank width is called the limiting dome height. Mostly in industry, a fixed blank width of 133 mm is used for finding the LDH, instead of determining the critical blank width experimentally [41].

Ohio State University test is almost similar to the LDH test. The basic principles are the same except for the punch geometry and the fact that the determination of the critical width is no longer necessary. A new flat-elliptical geometry is used in this test. This geometry produces more stable plane strain conditions. This is primarily because of the two-dimensional nature of the punch geometry. Five 124 mm $\times$ 178 mm sheet blanks are used in the test without the need to determine the critical width [29]. The number of samples is much smaller when comparing with the LDH test in which 25 samples are tested to determine the critical width and 18 samples are tested at the critical width [41]. The OSU test is called a stretch-bend test by some authors because it combines stretching and bending [4, 13]. This combination makes the test more suitable for the aircraft industry, because many forming operations in the aircraft industry is done by rubber forming. Bending is the most important deformation mode in the rubber forming process. Stretching also occurs in the rubber forming process as well as in the other forming processes in the aircraft industry. For a detailed discussion of OSU test, see reference [43].

Based on the formability tests, forming limit diagrams can be developed. FLDs depict the forming limits of a sheet metal as a curve in the plane of principal in-plane strains. The least formability usually occurs in the plane strain condition

$(\varepsilon_2 = 0)$. Therefore, in most cases it is a conservative approach to evaluate the formability of sheet metal in the plane strain condition like in the LDH and the OSU test. Forming limit diagrams play an important role in the evaluation and manipulation of deformation processes. Stuart Keeler developed the concept of forming limit diagrams during his PhD study (1957-1961) at the Massachusetts Institute of Technology [44]. In a volume edited by Wagoner, Chan, and Keeler, various experimental and computational methods for the development of forming limit diagrams were reviewed in 1989 [44]. Although there have been further important studies which are not reviewed in that volume, the volume still serves as an invaluable resource in the area of forming limit analysis. A brief discussion of the computational methods for calculation of forming limit diagrams is given later in this chapter.

Concerning tailor-welded blanks, two approaches can be used for the development of the forming limit diagrams. The first approach combines properties of the base metals and the weld material and provides only a forming limit curve representing the whole blank. The second approach provides different forming limit curves for the base metals and the weld material. Most investigators have used the first approach. Ghoo *et al* proposed the second approach to improve the accuracy of forming limits diagrams [45]. In this approach, three different forming limit curves are plotted. Two of the curves represent the forming limits of the base metals and another represents the forming limits of the weld metal. Since there can be a considerable difference between the forming limits of the base metals and the weld material, the forming limit diagrams obtained by the second approach are generally more accurate.

Formability of TWBs. Simulative formability tests, like the limiting dome height or bulge height, have been widely used for the formability analysis of tailor-welded blanks. These tests show that the stress concentrations caused by the inhomogeneous strength distribution across the weld [10, 46] or by an imperfect fusion zone geometry decrease the formability for all alloys. Similar results are available for friction stir welding [10, 47]. Results of formability tests are commonly presented forming limit diagrams, minimum major strain values and failure mode [27].

The formability of tailor-welded blanks is influenced by the microstructure of the weld and the heat-affected zone in particular. Generally, aluminum alloys become more brittle when the grain size increases, because intergranular fracture occurs more easily. However, this is not the case for aluminum-magnesium alloys, in which increase of the grain size results in larger elongations under uniaxial tensile loading [47, 48]. Sato *et al* showed that there is an optimal grain size for which the formability is optimal [47]. Nagasaka *et al* reported that deep drawability of high-strength steel TWBs deteriorates with increasing the carbon equivalence [49].

The thickness ratio also affects the formability of tailor welded blanks. The formability of TWBs (FLD level and minimum major strain in FLD) decreases generally with an increase in the thickness ratio [25, 27, 37, 42]. TWBs with thickness ratios close to unity show a minimum major strain closer to those of the base metals [27, 32].

Both welding method and welding parameters can influence the formability. Miles *et al* showed that friction stir welded TWBs are better formable than gas tungsten arc welded ones [29]. Imperfections at the weld region decrease the ductility of TWBs [14]. For aluminum alloys, a higher tensile strength is associated with a higher amount of magnesium in the weld region. Cheng *et al* found that a higher percentage of magnesium is lost when a lower welding speed or a higher laser power is used [35].

The formability is also dependent on the loading conditions such as the orientation of loading with respect to the weld line. Cheng *et al* observed that minimum major strain of TWBs with longitudinal welds is almost the same as the base metal. However, the minimum major strain was reduced from 0.24 to 0.19 for TWBs with transverse welds [28]. Reis *et al* found that friction stir welded aluminum TWBs have lower forming limits in comparison with the base metals when biaxial strain condition are reached. Although the formability of the TWBs was similar to the base metals in the plain-strain conditions, it rapidly decreased as biaxial strain conditions were approached and straining occurred across the weld line [29]. The above results are consistent with the results of Friedman and Kridli [31]. According to their findings, the formability decreases as the weld orientation becomes perpendicular to the stretching direction. However, they realized that 80% of the base metal formability could be retained with stretching direction oriented 45^o to the weld line.

According to Chan *et al*, geometrical parameters of TWBs like dimensions and radii of cutoffs affect the formability and may cause different major and minor strain values of FLDs [27].

Besides experimental investigations, it is possible to use finite element methods for the formability analysis of tailor-welded blanks. Vijay and Narasimhan used FEM modeling for simulation of tensile and LDH tests [50]. The simulated LDH tests show that as thickness ratio increases, the load-bearing capacity and pole height decreases. Furthermore, it was seen that the formability indicators become almost constant for high thickness ratios. Other important findings were that: 1. the pole height and maximum load are minimal when the weld line is exactly at center 2. The failure location is shifted from punch nose for thickness ratio of 1 to the proximity of the weld line for a critical thickness ratio.

Material flow. Dissimilar properties of the two pieces in a tailor-made blank will cause forming problems such as decreased formability and/or metal flow. The first problem was addressed in the previous section. This section is devoted to the second problem.

Tearing and wrinkling are two primary failure modes in the forming of (tailor-welded) blanks in deep drawing applications. Different pieces of sheet metal, used in a typical tailor-welded blank, have different strengths and they will deform differently. If the material on the punch side is stretched perpendicular to the weld line, the deformation of the weaker material is larger than of the stronger material, and it may cause tearing. Reversely, compressive stresses in the sidewall and the flange area may lead to wrinkling in some forming applications. Inability of the weaker material in withstanding the high compressive stress and the reduced buckling strength in case of thinner sheets result in movement of the weld line towards the thinner material and buckling of the thinner material in the sidewall or the flange area [51].

Associated with the two above-mentioned failure modes, three consequences of the metal flow are more likely to occur in forming of tailor-welded blanks [52]. First, the weld line may move toward thicker material; because the thinner, weaker material undergoes more deformation than the thicker, stronger one during the deformation process. This weld line movement can finally result in tearing failure of the thinner material. Second, the unsupported or unconstrained thin material may wrinkle. The unconstrained condition occurs as result of the initial clearance between the step in the blank-holder plate and the weld line. The clearance is necessary to accommodate the thickness step between the thicker and the thinner material. Finally, the over-constrained condition of the material occurs in some deep drawing processes, and results in a weld line movement toward the thinner material and may finally cause tearing failure [52].

The initial location of the weld line plays an important role in the weld line movement. Studies show that the larger the distance of the weld line from the centerline, the larger the weld line movement [53, 54]. In fact, the maximum drawing depth and maximum drawing force increase as the distance between the centerline and initial weld line decreases [54]. The blank shape influences the weld line movement as well. Choi *et al* showed that the measured value of the weld line movement and the values of the thickness strain in the diagonal direction are larger for circular shape compared to square blanks [53]. Lee *et al* found that there is a correlation between the weld line movement and springback [55]. They showed that minimizing the weld line movement is an effective way to reduce springback as well as to improve the formability. According to Meinders *et al* [56], the weld line movement is considerably dependent on the strain distribution specifically when the material is being stretched perpendicular to the weld line. They argued that placing the weld in a region with low strains perpendicular to the weld line results in minimization of the weld line movement [56].

Although most studies use numerical simulation techniques for prediction of the weld line movement, few analytical models are available for formability analysis of tailor-welded blanks. Kinsey and Cao developed a 2D sectional model for the calculation of the weld line movement and forming height when a uniform binder force is being applied [52]. Results of the model were in good agreement with numerical simulations. He *et al* have also developed an analytical 2D model for control of the weld line movement [57].

Control of material flow. As discussed in the previous section, material flow adversely affects the formability of tailor-welded blanks. Some researchers have tried to find strategies to control the material flow during forming of TWBs. Placement of drawbeads can help in controlling the material flow because they add local constraints to the TWB. Heo *et al* showed that the presence of the drawbeads decrease weld line movement [54, 58]. They showed that the size and height of the drawbeads are also important. Normally, the weld line movement decreases as the size and height of the drawbeads increase. However, thickness strains in the diagonal direction increase. A study of the influence of drawbead is therefore necessary prior to its installation [58].

Control of blank holding force (BHF) is another important strategy to control the weld line movement and to obtain a uniform distribution of the deformation. The main idea is to control the weld line movement by adjusting the BHF. In this strategy, the distribution of the blank holding force is no longer uniform along the periphery of the blank. Ahmetoglu *et al* developed a BHF control mechanism for control of weld line movement in laser welded tailored blanks [59]. They replaced the cushion of the press by a nitrogen cylinder system consisting of six nitrogen cylinders. The system was a multipoint pressure control system capable of adjusting the BHF at the edge of the sheet. They applied a BHF in the thinner section about ten times larger than in the thicker section in order to control the position of the weld line. Since they did not describe the basis for the selection of the BHF ratio, it seems to be on a trial and error basis. By using a 2D analytical model, He *et al* adjusted the BHF to minimize the weld line movement [57]. In contrast to the previous study, they estimated the BHFs with the use of an analytical model. The method was successful in controlling the weld line movement. The results showed that the strategy could reduce the strain level in the thinner material because the thicker material draws in and limits the stretching of the thin part [57]. Siegert and Knabe designed a die with segmented blank-holders in order to increase the drawing in the forming area from the side of the tailor-welded blank with the stronger material [60]. Kinsey *et al* proposed a methodology for reduction and quantification of the wrinkling in tailor welded blank forming [51]. The most important contribution of the work was to present a method for determination of the blank-holder force ratio. Although He *et al* had previously suggested an analytical model for determination of blank-holder force ratio, the model was limited to tearing failure [57].

Some other researchers have worked on modification of the forming die. Cao and Kinsey patented a method for reduction of the weld line movement [61]. They used a segmented die with local adaptive controllers. In this case, the hydraulic cylinders act as adaptive controllers, and add another boundary condition (constraint) to the situation. A rubber edge, or pad, on the hydraulic cylinders prevents the clamping mechanism from deforming the sheet metal. Extensive studies of the method show that the clamping mechanism can reduce the weld line movement by 44% and reduce the relative strain value, transverse to the weld line in the thinner material by over 40% [62-64]. Hetu and Siegert used a segmented blank holder and a 10-point cushion system for transferring the press force onto the blank [16]. Thakkar and Date proposed two innovative methods for control of the weld line movement [65]. These methods are the so-called “back propagation” and “minimum thickness strain contour” methods. The methods tend to be less developed and experimental evidence is not provided yet.

Springback. The formed parts return partially to their original shapes after release of the applied forces. The so-called springback behavior is a common problem of sheet metal forming processes and makes it difficult to get the required part with adequate accuracy. In order to get a part which meets the design tolerances, it is necessary to predict and compensate for the springback. The accurate prediction of the springback behavior of metals is a challenging problem. Even more challenging is accurate prediction of the springback for tailor-welded blanks. In the case of tailor-welded blanks, there are two halves involved with different thicknesses and/or materials properties. Furthermore, the properties of the heat-affected zones and/or weld nuggets are different from the base metals. Therefore, it will be quite difficult to make an accurate model of the springback behavior of TWBs. In any event, prediction and compensation of the elastic recovery is necessary for first-time-right production of tailor-welded parts.

Accounting for specific material properties of the heat-affected zone in FEM simulation of the forming processes can be computationally expensive [4]. Moreover, implementing the heat-affected zone in a FEM model may have a little effect on the springback behavior of steel tailor-welded blanks [4].

There are not sufficient papers dealing with springback behavior of tailor-welded blanks. Some researchers have shown that FEM simulations can give relatively accurate predictions of springback in at least some classes of TWBs [4, 66]. The research has been mostly concentrated on steel alloys, but a limited study of aluminum alloys are also available [67]. Comparison of the numerical results with experiments shows that the numerical solutions are sufficiently accurate for real applications. Comparison between solid 3D elements and shell 3D elements has shown that CPU time for solid elements can be 15 times larger than for shell elements [4]. Moreover, the results of shell elements are fairly accurate. Zhao *et al* suggested that the heat-affected zone in TWB increases the springback slightly in a three-point bending test. Generally, one can say that an increase in thickness of monolithic metal causes a decrease in the springback. In the case of steel TWBs, simulations showed that the amount of springback increases as the sheet thickness decreases or the radius of the punch profile increases [66]. Nevertheless, Zhou showed that larger springback tends to occur at the thicker side of steel TWBs [67]. Min and Kang [34] showed that springback is a little larger for flash welded blanks compared to the parent steel materials. However, Reis *et al* found that the presence of the weld line does not have a considerable effect on springback behavior of steel TWBs [68].

Chang *et al* investigated the effect of the weld bead location on the springback behavior. According to their findings, springback behavior of longitudinally welded strips is similar to non-welded strips [66] and springback of longitudinally welded strips decreased by about 44% at the thinner side. The springback was similar to non-welded strips at the thicker side of the centrally welded strips. However, FEM simulations could not predict reduction of springback of the thinner side of centrally welded strips, probably because the simulations neglected the change of the material properties of the HAZ. One may therefore conclude that the heat-affected zone may play an important role in the springback behavior of TWBs.

Stress and strain distribution. The sudden change from properties (and/or thickness) of one blank half to the weld line and from the weld line to the second blank half can cause localized effects that influence the stress and strain distribution within the part. The local effects may result in, for example, higher stress concentration factors. Moreover, properties of the base metals are considerably affected by the welding process. For example, the heat-affected zone has its own material properties that may be completely different from those of the base metals. It is generally better to have the weld line design located in the low strain regions so the blank can deform more before failure. A priori knowledge of stress and strain distributions within the TWB is important for all of the above-mentioned purposes.

Strain analysis can be performed either numerically or experimentally. It is not easy to measure strains within a part while it is being formed. Strain gauges and optical methods (DIC, photo-elasticity, and thermo-elasticity) are often not applicable, and the grid analysis seems to be the only method for the measurement of the strains of a formed part. Numerical methods can give *full-field* stress and strain distribution during the whole forming period and that is why the FEM models are more widely used for analysis of stress and strain distributions.

Chan *et al* used a FEM model for stress analysis of a laser-welded steel blank [42]. They observed stress concentrations in the weld region. The concentrations become more pronounced as the thickness ratio increases. This observation explains why the level of experimental FLDs decreases as the thickness ratio increases. They concluded that the failure is mainly caused by the thickness difference between the materials. Chien *et al* calculated a strain concentration ratio of 1.5 for the weld's notches [69]. The value was, however, lower than the stress concentration ratio (at failure) measured during the experiments. Kampus and Balic reported stress concentrations in the weld during deep drawing of GTAW tailor-welded blanks [36]. Buste *et al* studied strain distributions in laser and Non-Vacuum Electron Beam (NVEB) welding by using a numerical model as well as experiments [70]. There was a discrepancy between the results of the FEM model and those of the experiments. The model predicted a localized strain distribution adjacent to the weld for all gauge combinations. In the experiments, for some gauge combinations, localization occurred in the thinner sheet several millimeters away from the weld line. Clapham *et al* measured residual stresses in a tailor-welded blank by using a neutron diffraction method [71]. The results of the study indicated that residual stress distributions in the weld region of TWBs can be complex; but the magnitudes of stresses tend to be small comparing to conventionally welded thicker materials. Furthermore, they showed that the residual stress remains the same or diminishes as the TWB deforms.

2.3. Failure and fatigue analysis

Failure modes. Associated with different loading conditions, different failure modes may occur in tailor-welded blanks. As Meinders and co-authors discuss [56], two types of failure can occur during forming of tailor-welded blanks. The first is that a failure initiates in the weld and propagates to other sections. This failure mode is typical when straining parallel to the weld line. Due to the lower ductility of the weld metal compared to the parent material, the weld fails. The second type of failure is that the thinner (weaker) base metal fails. This occurs when the straining is perpendicular to the weld line. Owing to a higher flow stress of the weld material, the strain is localized in the weaker thinner parent material resulting in failure of the thinner base metal. The argument is consistent with the findings of other researchers, e.g. see [28, 37, 64]. However, it holds only for laser-welded blanks. Buste *et al* reported that for longitudinally welded NVEB specimens, failure begins in the weld and propagates to the base metals [37]. However, it is not the case for transversely welded specimens. In fact, the failure location is dependent on the thickness ratio for transversely loaded NVEB TWBs. They observed that the samples with a high thickness ratio failed in the parent material while samples with a low thickness ratio exhibited failure of the weld [37, 70]. Regarding FSW and GTAW, Miles *et al* found that transversely welded samples made of annealed aluminum alloys (5182 and 5754) failed in the base metal for both welding techniques [29]. Sato *et al* reported that longitudinally welded FSW aluminum alloy (5052-O) samples failed in the base metal [47]. In contrast to the annealed aluminum alloys, heat-treated alloys partially loose their superior properties after exposing to the relatively high temperatures of the welding. This phenomenon can cause some variations in the failure modes of such alloys. Miles *et al* observed that in the transverse loading of FSW and GTAW samples made of 6022-T4, failure occurs in the heat-affected zone and the weld metal, respectively [29]. Furthermore, the fracture location is dependent on other parameters such as the existence of superficial defects [37].

Failure criteria. Determination of forming limits is necessary for simulation of the forming of tailor-welded blanks. Two approaches can be used for implementation of failure in FEM models. The first approach is based on experimental forming limit diagrams. In this approach, experimental FLDs are implemented in the FEM package. Once the calculated strains exceed the forming limit indicated by the FLD, the TWB is considered to have failed. This experimental failure based method is used, for example, in references [42, 72]. The second approach is to use a theoretical failure criterion. Theoretically predicted FLDs offer a high degree of versatility because they are not limited to a specific material combination nor are they developed for specific thickness ratio(s). The remainder of this section is devoted to the theoretical failure criteria applied to TWBs..

Plastic deformation in sheet metal consists of two phases: uniform deformation and non-uniform deformation. Non-uniform deformation, consists of three phases: diffuse necking, localized necking, and final rupture [73]. Diffuse necking is the in-plane necking phenomenon that happens, for example, in a sheet metal strip under uniaxial tension at the maximum load. The diffuse necking is followed by rupture [74]. Originally proposed by Swift (1952) [75], diffuse necking is also known as general bifurcation [76]. The other instable condition, local necking, is also a material bifurcation phenomenon. The second instability condition was proposed by Hill (1952) [77]. Localized necking is accompanied with severe local thinning and leads to immediate breakage [74]. Chronologically speaking, the first theory for theoretical computation of FLDs was based on the Hill's criterion. Depending on the strain ratio β, one of two above-mentioned instability conditions is applicable, i.e. local necking condition for $\beta < 0$ and diffuse necking condition for $\beta > 0$. The local necking condition proposed by Hill applies only to proportional loading with $\beta < 0$ [73, 74]. However, it has been observed that thin sheets subjected to

positive bi-axial tension loads can fail through the local necking mechanism [73, 78-80].
In 1967, Marcianik and Kuczynski proposed a new instability condition based on the initial imperfection approach [81]. They assumed that an initial inhomogeneity of the material would eventually lead to rupture. Davies *et al* [17] and Chien *et al* [69] used this method for the prediction of failure in tailor-welded blanks. Nevertheless, the so-called M-K method is mainly used for $\beta > 0$ and is not that straightforward for determination of a FLD when $\beta < 0$ [74]. Moreover, an arbitrary imperfection parameter f is used in the M-K analysis. The factor is not necessarily clearly and appropriately evaluated [74]. In addition, the M-K method seems to be over-sensitive to the imperfection parameter f [73, 76, 80]. A method for the determination of the material imperfection size is to fit the results of the failure/localization analysis to those of the uniaxial tensile tests [69]. The material imperfection parameter can be then used for the prediction of failure strains under biaxial straining conditions. Davies *et al* used a similar tensile instability method, namely the Hart and Ghosh method [82, 83], for quantitative description of the degradation of the material ductility in the weld [14]. Like the M-K theory, this method is based on assuming and quantifying an initial imperfection level in the gauge area of the tensile specimens.
In 1985, Gotoh proposed a new class of plastic constitutive equations with vertex effect [84]. In two papers following that paper, he used the equations to study the material bifurcation problems and develop forming limit diagrams of sheet metals under proportional [74] and non-proportional loading [85]. Iwata *et al* used Gotoh's model for evaluation of failure initiation in the forming of steel tailor welded blanks [86]. Onset of localized necking was considered as the limiting failure. The Gotoh's J_2-corner method [85] was deployed for prediction of localized necking.
Chan *et al* used an anisotropic damage model and damage criterion for analysis of local necking in tailor-welded blanks [87]. The damage model is mainly based on the work of Chow and his co-workers [73, 88-92]. Mainly presented in references [73, 91], the method considers all three phases of non-uniform deformation in a unified approach. The method was originally developed for proportional loading [73], and was improved to include effects of non-proportional loading [91]. The improved model can account for strain-path dependency of the forming limit diagram.
In this section, we only reviewed formability prediction methods previously applied to tailor-welded blanks. There are, however, many other theoretical methods for this purpose. For a comprehensive review of the other methods, see references [73, 91].

Fatigue. Failure of tailor-welded blanks under cyclic loading may be a problem for automotive structural components [93]. However, there are only a limited number of studies concerning the fatigue behavior of tailor-welded blanks. Ono *et al* showed that the fatigue endurance limits of laser welded and mash seam welded TWBs are lower than those of the parent material [94]. Onoro and Ranninger studied the fatigue behavior of same-gauge laser welded blanks and concluded that the cracks start in the fusion zone, near the borderline between the fusion zone and the heat-affected zone [95]. Anand *et al* found that fatigue fracture always occurs in the thinner material [93]. In contrast to this, Ono *et al* found that fatigue fracture occurs in the base metals only for medium cycle fatigue (number of cycles to failure< 5e5 cycles). They found that fatigue fracture happens near the weld line in the long life fatigue exceeding 1e6 cycles [94]. Both papers confirm that fatigue strength diminishes when thickness ratio increases. Besides that, the fracture location is closer to the weld line in case of higher thickness ratios. This is due to higher stress concentration caused by the difference in thickness [93]. Furthermore, it was revealed that the fatigue strength of mash seam welded TWBs is lower than that of the laser-welded TWBs. An explanation might be that the stress concentrations in the overlap zone of the mash seam welds is greater than in the step zone of the laser welds [94]. Lazzarian *et al* compared fatigue strength of bare and hot dip galvanized TWBs and concluded that the fatigue strengths are similar [96]. On the contrary, Anand *et al* showed that the fatigue strength of the bare TWB is about 1.4 times higher than that of the galvanized TWB [93]. Although there have been some efforts towards identifying the fatigue behavior of laser-welded joints (e.g. [97-99]), there is a serious lack of benchmark information regarding fatigue behavior of different configurations of tailor-welded blanks.

2.4. FEM modeling of TWBs

Modeling of the weld area. One of the important challenges of the FEM modeling of tailor-welded blanks is the modeling of the weld area. Two approaches are common in this regard. The first approach is to model the weld area accurately. In this approach, the geometry and properties of the weld and the heat-affected zone are taken into account. Several researchers have adopted this approach in their studies [4, 16, 36, 66, 68, 69, 72, 86, 100-102]. The second approach excludes weld properties and/or geometries from the FEM model. This approach is also extensively used in the literature [4, 36, 56, 59, 70, 103, 104]. Many other papers, in which the procedure of numerical modeling is not sufficiently described, apparently have used the second approach. While it is desirable to make the numerical model as accurate as possible, the reasons for disregarding the weld line and the heat-affected zone is either added computational cost or lack of experimental data for mechanical behavior of the weld metal. The lack of material parameters would be no longer a problem as a growing number of studies are dealing with measurement of the weld properties and new measurement techniques such as DIC are emerging. Therefore, the main debate would be the suitability of implementing the weld properties in the model.

When the geometry and/or material properties of the weld area are excluded from the model, some kind of modeling technique is required to make the connection between the two different parts of the TWB. One may choose to use rigid links (spot welds) for the connection [70, 103]. As far as steel TWBs are considered, it seems reasonable to use this method. Because, due to the high strength of the weld metal in steel TWBs, the failure is more likely to happen in the base metals. The modeling method is particularly efficient while dealing with laser-welded blanks, because the weld area in laser welding is very narrow (about 1-2mm). However, the model may not be efficient for other welding methods such as GTAW, which create a relatively wide weld. The method is also not justified when aluminum TWBs are being modeled. It is because the weld area in the aluminum TWBs is sometimes weaker than the base metal, and the failure is more likely to happen in the weld area. Therefore, a good description of the metal behavior near the weld line is necessary for aluminum TWBs.

Several techniques are used to model the weld area in tailor-welded blanks. One method is to use beam elements for representing the weld [86, 105]. But beam elements limit the geometry that can be represented and the mesh refinement in the weld zone [72]. The second method uses shell elements to model both the weld zone and base metal [4, 101]. Nevertheless, shell elements are not able to describe the geometry of tailor-welded blanks exactly. The third method is to model the weld zone by solid elements. Concerning this method, two strategies can be used. The first strategy uses solid elements for both the base metal and the weld zone [4, 101]. There is a high computational cost associated with this method; since several through-thickness solid elements are required for a good representation of the bending behavior in the forming simulation of the base metal [72]. The second strategy is to use solid elements for the weld zone and shell elements for the base metals [72]. The solid elements are constrained to move with the parent materials. It means that movement of the dependent nodes is interpolated from the movement of a set of independent nodes on the base metal mesh. This strategy does not need a fine solid mesh for the base metal and can significantly reduce the associated computational load. In most of studies the geometry of the weld line is only roughly approximated, accurate representation of the weld geometry is rarely found [69]. In that study, the geometry of the weld included two shallow notches. It was shown that the notches caused stress concentration and, ultimately, failure of the TWB.

As previously stated, there is a debate on the value of the implementation of the weld area in the FEM model. Saunders reported that additional costs associated with the implementation of the weld area are not justified [106, 107]. Zhao *et al* compared three models: one not implementing the weld area and two including the weld area [4]. They found that the solid model with the HAZ and the shell model with the HAZ increase the reaction forces by 25% and 7%, respectively. However, implementation of the HAZ had little effect on the springback. The CPU time was increased from 0.615 hour for the simplest model to 16.26 hour for the 3D solid element model. Kampus and Balic used two different models: one without the weld area and one accounting for the hardening caused by the MIG welding [36]. They found that while the differences between the forming forces are minimal, the second model could give a better approximation of the actual shape of the deformed part. Raymond *et al* concluded that though there are a number of differences between models with the weld area and models without the weld area [72], the differences are subtle. Roque *et al* examined four different models: combinations of shell or solid elements on one hand, and with or without HAZ on the other hand [101]. They showed that only the solid element with the HAZ could provide validated thickness distributions. Buste *et al* used rigid links for making connections between adjacent nodes of thick and thin sheets, and found that the model is lacking accuracy in predicting the strain distribution near the weld line [70]. In summary: whether the weld area should be implemented in the model is highly dependent on the problem specifications. As a rule, the errors caused by excluding the weld area from the model are minimal when the weld line is located in the low strain regions and the FEM model is used for steel TWBs.

Material models. Different strain hardening models can be used for FEM modeling of metal forming processes. However, Hollomon's power law is the simplest and by far the most widely used model. Hollomon's law can be expressed as:

$$\sigma = K{\varepsilon_p}^n \tag{4}$$

The Hollomon's law gives a rather good approximation of the actual stress-strain curve. A modification of the model is Ludwik's law, which can be expressed as :

$$\sigma = \sigma_y + K{\varepsilon_p}^n \tag{5}$$

Ludwik's law includes the yield stress. Both equations have been extensively used in modeling of the metal forming processes including modeling of tailor-welded blanks. Both the base and the weld metal can be approximated by those laws. Similar strain hardening laws are also used by some researchers. Chen *et al* used the Voce law for the description of the strain hardening of both weld and base metals [69]. The Voce law is an exponential law and is expressed as

$$\overline{\sigma} = A - B\exp(-C\overline{\varepsilon}_p) \tag{6}$$

Strain rate dependency of steel and aluminum are generally omitted in FEM analysis of TWBs.

Classic yield criteria are normally used for modeling of TWBs. The classic yield criteria can be categorized as either isotropic or anisotropic. Von Mises and Tresca yield criteria are the most commonly used isotropic yield criteria. Among anisotropic yield criteria, Hill's quadratic anisotropic yield criterion is the most common one; see e.g. [69, 103]. The criterion accounts for normal plastic anisotropy. Iwata *et al* used Gotoh's biquadrate yield function [86]. Gotoh's yield function accounts for planar anisotropy of the material. Kinsey and coworkers used Barlat's yield function for representing the anisotropic behavior of the sheet metal under a plane stress condition [51, 62, 108]. Hosford's yield criterion was used by Davies *et al* [17]. However, modeling the anisotropy is difficult because the anisotropy parameters of the weld area are rather difficult to measure and are not available in the open literature for most materials.

Modeling of forming processes. Commercial FEM packages are widely used for modeling of TWB forming. The punch is normally taken as a rigid body and Coulomb's friction model is adopted. In most forming processes like stamping or bending, it is sufficient to adopt the constant friction coefficient for contact between the base metal and the tool. Tolazzi and Merklein showed that considering friction coefficients of the weld seam could considerably improve the accuracy of the FEM model [109]. As discussed in the section "Material Flow", some special considerations are necessary for the adjustment of the blank holding force to improve the formability of tailor-welded blanks. Besides those considerations, there is no basic difference between the blank holding force of TWBs and those of the base metals.

2.5. Conclusions

The mechanical behavior and modeling of TWBs were reviewed in this chapter. As the formability of tailor-welded blanks is reduced due to welding, the major topic of the paper was the formability of tailor-welded blanks. The formability of tailor-welded blanks is dependent on the orientation of the principal strains with respect to the transition zone (including the weld and heat-affected zones). The size and properties of the transition zone vary with the welding method. However, regardless of the welding method, the presence of the weld metal causes local stress and strain distribution patterns at the transition zone. The thickness difference makes the localization effect more severe. Therefore, high stress concentration factors are reported in the transition zone. For steel alloys, the weld strength is higher or, at least, equal to the base metal strength. This is not the case for aluminum alloys, which is due to welding that removes the original micro structure. Two types of difficulties are associated with the formability analysis of TWBs. On one hand, the inhomogeneous mechanical properties can influence the forming behavior of TWBs. For example, the springback behavior of TWBs is different from their parent materials. On the other hand, some new issues such as weld line movement arise. This chapter covered both types of complexity, and tried to give a picture of current research trends in this field. Although there have been an ever growing number of researches in the field of tailor-welded blanks, many topics of the technology are addressed scarcely.

For the future applications, tailor-made blanks made by newer joining technologies such as friction stir welding are of particular importance. Friction stir welded blanks bring several advantages to fabrication of tailored blanks. First, less intensive welding inspection is necessary for FSW blanks. Second, joining of different materials is easier by FSW. Third, the welding temperature is much lower compared to fusion welding techniques. Moderate welding temperatures reduce the disruption of the heat treatment of aluminum alloys. Although there has been some researches on FSW TWBs (see e.g. [29, 47]), more researches are needed in this area. The forming behavior of TWBs is also understood less. Of particular interest is the springback behavior of TWBs. Corrosion behavior of different combinations of tailor-welded blanks also needs further investigation. Although there is a consensus that TWBs offer good features from economical and environmental issues, detailed analyses of economical and environmental impacts of TWBs are rare (see e.g. [110]). Forming of TWBs by nontraditional forming techniques such as hydroforming is not studied satisfactorily yet. FEM modeling of TWBs is not well established and needs more consideration. Particularly, the effect of the design parameters of TWBs on FEM modeling and the methods of modeling of the weld area are very important. Furthermore, nearly all the previous studies have targeted automotive applications. Given that tailor-made blanks are of potentially similar importance to the aircraft industry, a future research area is the aircraft applications.

2.6. References

[1] B. Rooks, "Tailor-welded blanks bring multiple benefits to car design," *Assembly Automation,* vol. 21, pp. 323-328, 2001.

[2] H. Kusuda, T. Takasago, and F. Natsumi, "Formability of tailored blanks," *Journal of Materials Processing Technology,* vol. 71, pp. 134-140, Nov 1 1997.

[3] A. Montgomery, P. Wild, and L. Clapham, "Defect characterisation using magnetic flux leakage inspection of tailor-welded blanks," *Insight,* vol. 46, pp. 260-264, May 2004.

[4] K. M. Zhao, B. K. Chun, and J. K. Lee, "Finite element analysis of tailor-welded blanks," *Finite Elements in Analysis and Design,* vol. 37, pp. 117-130, 2001.

[5] T. W. B. P. Team, "Tailor welded blank applications and manufacturing - a state of the art survey," Auto-Steel Partnership 2001.

[6] R. S. Mishra and Z. Y. Ma, "Friction stir welding and processing," *Materials Science and Engineering R-Reports,* vol. 50, pp. 1-78, Aug 31 2005.

[7] T. W. B. P. Team, "Tailor welded blank acceptance guidelines," Auto-Steel Partnership 1995.

[8] T. W. B. P. Team, "Tailor welded blank design and manufacturing manual," Auto-Steel Partnership 1995.

[9] T. W. B. P. Team, "The identification and analysis of intangible benefits of tailor welded blank applications," Auto-Steel Partnership 1999.

[10] H. Zhao, D. R. White, and T. DebRoy, "Current issues and problems in laser welding of automotive aluminium alloys," *International Materials Reviews,* vol. 44, pp. 238-266, 1999.

[11] X. Cao, W. Wallace, C. Poon, and J. P. Immarigeon, "Research and progress in laser welding of wrought aluminum alloys. I. Laser welding processes," *Materials and Manufacturing Processes,* vol. 18, pp. 1-22, Jan 2003.

[12] X. Cao, W. Wallace, J. P. Immarigeon, and C. Poon, "Research and progress in laser welding of wrought aluminum alloys. II. Metallurgical microstructures, defects, and mechanical properties," *Materials and Manufacturing Processes,* vol. 18, pp. 23-49, Jan 2003.

[13] P. M. Wild, K. Abdullah, J. J. Jeswiet, and A. Ghasempoor, "Tensile testing for weld deformation properties in similar gage tailor welded blanks using the rule of mixtures," *Journal of Materials Processing Technology,* vol. 112, pp. 91-97, 2001.

[14] R. W. Davies, M. T. Smith, M. A. Khaleel, S. G. Pitman, and H. E. Oliver, "Weld metal ductility in aluminum tailor welded blanks," *Metallurgical and Materials Transactions A,* vol. 31A, pp. 2755-2763, 2000.

[15] R. W. Davies, H. E. Oliver, M. T. Smith, and G. J. Grant, "Characterizing Al tailor-welded blanks for automotive applications," *JOM,* vol. 51, pp. 46-50, 1999.

[16] L. Hetu and K. Siegert, "Hydromechanical deep drawing of tailor welded blanks," *Steel Research International,* vol. 76, pp. 857-865, Dec 2005.

[17] R. W. Davies, G. J. Grant, M. A. Khaleel, M. T. Smith, and H. E. Oliver, "Forming-limit diagrams of aluminum tailor-welded blank weld material," *Metallurgical and Materials Transactions A,* vol. 32A, pp. 275-283, 2001.

[18] B. Y. Ghoo, Y. T. Keum, and Y. S. Kim, "Evaluation of the mechanical properties of welded metal in tailored steel sheet welded by CO2 laser," *Journal of Materials Processing Technology,* vol. 113, pp. 692-698, Jun 15 2001.

[19] S. Liu and Y. J. Chao, "Determination of global mechanical response of friction stir welded plates using local constitutive properties," *Modelling and Simulation in Materials Science and Engineering,* vol. 13, pp. 1-15, 2005.

[20] O. Hatamleh, "Effects of peening on mechanical properties in friction stir welded 2195 aluminum alloy joints," *Materials Science and Engineering A,* vol. 492, pp. 168-176, 2008.

[21] C. Genevois, A. Deschamps, A. Denquin, and B. Doisneau-cottignies, "Quantitative investigation of precipitation and mechanical behaviour for AA2024 friction stir welds," *Acta Materialia,* vol. 53, pp. 2447-2458, 2005.

[22] C. Genevois, A. Deschamps, and P. Vacher, "Comparative study on local and global mechanical properties of 2024 T351, 2024 T6 and 5251 O friction stir welds," *Materials Science and Engineering A,* vol. 415, pp. 162-170, 2006.

[23] W. D. Lockwood and A. P. Reynolds, "Simulation of the global response of a friction stir weld using local constitutive behavior," *Materials Science and Engineering A,* vol. 339, pp. 35-42, 2003.

[24] M. A. Sutton, B. Yang, A. P. Reynolds, and J. Yan, "Banded microstructure in 2024-T351 and 2524-T351 aluminum friction stir welds: Part II. Mechanical characterization," *Materials Science and Engineering A,* vol. 364, pp. 66-74, 2004.

[25] S. M. Chan, L. C. Chan, and T. C. Lee, "Tailor-welded blanks of different thickness ratios effects on forming limit diagrams," *Journal of Materials Processing Technology,* vol. 132, pp. 95-101, 2003.

[26] S. S. Kang, K. B. Min, and K. S. Kim, "A study on resistance welding in steel sheets using a tailor-welded blank. I. Evaluation of upset weldability and formability," *Journal of Materials Processing Technology,* vol. 101, pp. 186-192, 2000.

[27] L. C. Chan, S. M. Chan, C. H. Cheng, and T. C. Lee, "Formability and weld zone analysis of tailor-welded blanks for various thickness ratios," *Journal of Engineering Materials and Technology-Transactions of the ASME,* vol. 127, pp. 179-185, Apr 2005.

[28] C. H. Cheng, L. C. Chan, C. L. Chow, and T. C. Lee, "Experimental investigation on the weldability and forming behavior of aluminum alloy tailor-welded blanks," *Journal of Laser Applications,* vol. 17, pp. 81-88, May 2005.

[29] M. P. Miles, B. J. Decker, and T. W. Nelson, "Formability and strength of friction-stir-welded aluminum sheets," *Metallurgical and Materials Transactions A,* vol. 35A, pp. 3461-3468, Nov 2004.

[30] N. Q. Wu, C. Xia, M. Li, N. Perrusquia, and S. X. Mao, "Interfacial structure and micro and nano-mechanical behavior of laser-welded 6061 aluminum alloy blank," *Journal of Engineering Materials and Technology -Transactions of the ASME,* vol. 126, pp. 8-13, 2004.

[31] P. A. Friedman and G. T. Kridli, "Microstructural and mechanical investigation of aluminum tailor-welded blanks," *Journal of Materials Engineering and Performance,* vol. 9, pp. 541-551, 2000.

[32] D. Seo, H. Kim, Y. Heo, N. Kim, and H. Y. Kim, "Forming and drawing characteristics of tailor welded sheets in a circular drawbead," *Journal of Materials Processing Technology,* vol. 105, pp. 294-301, 2000.

[33] R. Gedney, "Sheet metal formability," *Advanced Materials & Processes,* vol. 160, pp. 33-36, Aug 2002.

[34] K. B. Min and S. S. Kang, "A study on resistance welding in steel sheets for tailor welded blank. Evaluation of flash weldability and formability. II," *Journal of Materials Processing Technology,* vol. 103, pp. 218-224, 2000.

[35] C. H. Cheng, L. C. Chan, C. Y. Tang, and C. L. Chow, "Determination of true stress-strain curve for the weidment of aluminum laser-welded blanks," *Journal of Laser Applications,* vol. 17, pp. 159-170, 2005.

[36] Z. Kampus and J. Balic, "Deep drawing of tailored blanks without a blankholder," *Journal of Materials Processing Technology,* vol. 133, pp. 128-133, Feb 1 2003.

[37] H. R. Shakeri, A. Buste, M. J. Worswick, J. A. Clarke, F. Feng, M. Jain, and M. Finn, "Study of damage initiation and fracture in aluminum tailor welded blanks made via different welding techniques," *Journal of Light Metals,* vol. 2, pp. 95-110, 2002.

[38] S. Venkat, C. E. Albright, S. Ramasamy, and J. P. Hurley, "CO2 laser beam welding of aluminum 5754-O and 6111-T4 alloys," *Welding Journal,* vol. 76, pp. S275-S282, Jul 1997.

[39] M. Pastor, H. Zhao, R. P. Martukanitz, and T. Debroy, "Porosity, underfill and magnesium loss during continuous wave Nd : YAG laser welding of thin plates of aluminum alloys 5182 and 5754," *Welding Journal,* vol. 78, pp. 207s-216s, Jun 1999.

[40] Y. Kim and K. Park, "A plane-strain punch stretching test for evaluating stamping formability of steel sheets," *Metallurgical and Materials Transactions A,* vol. 25, pp. 2199-2205, Oct 1994.

[41] K. Narasimhan, M. P. Miles, and R. H. Wagoner, "A better sheet-formability test," *Journal of Materials Processing Technology,* vol. 50, pp. 385-394, Mar 1995.

[42] L. C. Chan, C. H. Cheng, S. M. Chan, T. C. Lee, and C. L. Chow, "Formability analysis of tailor-welded blanks of different thickness ratios," *Journal of Manufacturing Science and Engineering-Transactions of the ASME,* vol. 127, pp. 743-751, Nov 2005.

[43] R. H. Wagoner, W. Wang, and S. Sriram, "Development of Osu Formability Test and Osu Friction Test," *Journal of Materials Processing Technology,* vol. 45, pp. 13-18, Sep 1994.

[44] R. H. Wagoner, K. S. Chan, and S. P. Keeler, "Forming limit diagrams: concepts, methods, and applications," Warrendale: TMS, 1989.

[45] B. Y. Ghoo, S. W. Park, and Y. T. Keum, "New forming limit diagram of laser tailored blank," *Journal of Strain Analysis for Engineering Design,* vol. 36, pp. 143-152, Mar 2001.

[46] R. P. Martukanitz and D. J. Smith, "Laser beam welding of aluminum alloys," in *Sixth International Conference on Aluminum Weldments; Cleveland, Ohio; USA; 3-5 Apr. 1995*, 1995.

[47] Y. S. Sato, Y. Sugiura, Y. Shoji, S. H. C. Park, H. Kokawa, and K. Ikeda, "Post-weld formability of friction stir welded Al alloy 5052," *Materials Science and Engineering A,* vol. 369, pp. 138-143, 2004.

[48] M. Yanagawa, "Influence of grain size and magnesium content on the ductility of Al-Mg alloys at low temperatures," *Journal of Japan Institute of Light Metals,* vol. 44, pp. 492-497, 1994.

[49] A. Nagasaka, K. I. Sugimoto, M. Kobayashi, K. Makii, and S. Ikeda, "Press formability YAG laser welded TRIP/DP tailored blanks," *Journal De Physique IV,* vol. 115, pp. 251-258, Jun 2004.

[50] V. V. Bhaskar and K. Narasimhan, "Formability studies on transverse tailor welded blanks," in *NUMISHEET 2005: 6th International Conference and Workshop on Numerical Simulation of 3D Sheet Metal Forming Processes*, Detroit, MI; USA, 2005.

[51] B. Kinsey, N. Krishnan, and J. Cao, "A methodology to reduce and quantify wrinkling in Tailor Welded Blank forming," *International Journal of Materials and Product Technology,* vol. 21, pp. 154-168, 2004.

[52] B. L. Kinsey and J. Cao, "An analytical model for tailor welded blank forming," *Journal of Manufacturing Science and Engineering-Transactions of the ASME,* vol. 125, pp. 344-351, May 2003.

[53] D. Seo, Y. Choi, Y. Heo, and H. Y. Kim, "Investigations of weld-line movements for the deep drawing process of tailor welded blanks," *Journal of Materials Processing Technology,* vol. 108, pp. 1-7, 2000.

[54] Y. Heo, Y. Choi, H. Y. Kim, and D. Seo, "Characteristics of weld line movements for the deep drawing with drawbeads of tailor-welded blanks," *Journal of Materials Processing Technology,* vol. 111, pp. 164-169, 2001.

[55] J. K. Lee, B. K. Chun, and H. Y. Kim, "Numerical investigation of tailor welded blank forming and springback," in *NUMIFORM 2001: 7th International Conference on Numerical Methods in Industrial Forming Processes* Toyohashi, Japan, 2001, pp. 729-734.

[56] T. Meinders, A. van den Berg, and J. Huetink, "Deep drawing simulations of Tailored Blanks and experimental verification," *Journal of Materials Processing Technology,* vol. 103, pp. 65-73, Jun 1 2000.

[57] S. J. He, X. Wu, and S. J. Hu, "Formability enhancement for tailor-welded blanks using blank holding force control," *Journal of Manufacturing Science and Engineering-Transactions of the ASME,* vol. 125, pp. 461-467, Aug 2003.

[58] Y. M. Heo, S. H. Wang, H. Y. Kim, and D. G. Seo, "The effect of the drawbead dimensions on the weld-line movements in the deep drawing of tailor-welded blanks," *Journal of Materials Processing Technology,* vol. 113, pp. 686-691, 2001.

[59] M. A. Ahmetoglu, D. Brouwers, L. Shulkin, L. Taupin, G. L. Kinzel, and T. Altan, "Deep drawing of round cups from tailor-welded blanks," *Journal of Materials Processing Technology* vol. 53, pp. 684-694, 1995.

[60] K. Siegert and E. Knabe, "Fundamental research and draw die concepts for deep drawing of tailored blanks," *SAE Transactions: Journal of Materials & Manufacturing,* vol. 104, pp. 866-876, 1995.

[61] B. L. Kinsey and J. Cao, "Adaptive method and apparatus for forming tailor welded blanks." vol. 5941110, U. Patent, Ed. USA: Northern University, 1999.

[62] B. Kinsey, Z. Liu, and J. Cao, "New apparatus and method for forming tailor welded blanks," *SAE Transactions: Journal of Materials & Manufacturing,* vol. 108, pp. 653-660, 1999.

[63] B. Kinsey, N. Song, and J. Cao, "Analysis of clamping mechanism for tailor welded blank forming," *SAE Transactions: Journal of Materials & Manufacturing,* vol. 108, pp. 1062-1068, 1999.

[64] B. Kinsey, V. Viswanathan, and J. Cao, "Forming of aluminum tailor welded blanks," *Society of Automotive Engineers, SAE Transactions: Journal of Materials & Manufacturing,* vol. 110, pp. 673-679, 2001.

[65] M. Thakkar and P. P. Date, "Simulation based control of weld line movement in tailor welded blanks," in *NUMISHEET 2005: 6th International Conference and Workshop on Numerical Simulation of 3D Sheet Metal Forming Processes,* Detroit, MI; USA, 2005.

[66] S. H. Chang, J. M. Shin, Y. M. Heo, and D. G. Seo, "Springback characteristics of the tailor-welded strips in U-bending," *Journal of Materials Processing Technology,* vol. 130, pp. 14-19, 2002.

[67] X. Zhou, "Numerical prediction of springback in U-channel forming of aluminum tailor welded blanks," in *Department of Mechanical and Aerospace Engineering.* vol. MSc Ottawa: Carleton University, 1999.

[68] A. Reis, P. Teixeira, J. F. Duarte, A. Santo, A. B. da Rocha, and A. A. Fernandes, "Tailored welded blanks - an experimental and numerical study in sheet metal forming on the effect of welding," *Computers & Structures,* vol. 82, pp. 1435-1442, Jul 2004.

[69] W. Y. Chien, J. Pan, and P. A. Friedman, "Failure prediction of aluminum laser-welded blanks," *International Journal of Damage Mechanics,* vol. 12, pp. 193-223, Jul 2003.

[70] A. Buste, X. Lalbin, M. J. Worswick, J. A. Clarke, B. Altshuller, M. Finn, and M. Jain, "Prediction of strain distribution in aluminum tailor welded blanks for different welding techniques," *Canadian Metallurgical Quarterly,* vol. 39, pp. 493-501, 2000.

[71] L. Clapham, K. Abdullah, J. J. Jeswiet, P. M. Wild, and R. Rogge, "Neutron diffraction residual stress mapping in same gauge and differential gauge tailor-welded blanks," *Journal of Materials Processing Technology,* vol. 148, pp. 177-185, 2004.

[72] S. D. Raymond, P. M. Wild, and C. J. Bayley, "On modeling of the weld line in finite element analyses of tailor-welded blank forming operations," *Journal of Materials Processing Technology,* vol. 147, pp. 28-37, 2004.

[73] C. L. Chow, L. G. Yu, and M. Y. Demeri, "A unified damage approach for predicting forming limit diagrams," *Journal of Engineering Materials and Technology-Transactions of the ASME,* vol. 119, pp. 346-353, Oct 1997.

[74] M. Gotoh, "A class of plastic constitutive equation with vertex effect .3. applications to calculation of FLD of metal sheets," *International Journal of Solids and Structures,* vol. 21, pp. 1131-1145, 1985.

[75] H. W. Swift, "Plastic Instability under Plane Stress," *Journal of the Mechanics and Physics of Solids,* vol. 1, pp. 1-18, 1952.

[76] C. L. Chow, M. Jie, and X. Wu, "Localized necking criterion for strain-softening materials," *Journal of Engineering Materials and Technology-Transactions of the ASME,* vol. 127, pp. 273-278, Jul 2005.

[77] R. Hill, "On discontinuous plastic states, with special reference to localized necking in thin sheets," *Journal of the Mechanics and Physics of Solids,* vol. 1, pp. 19-30, 1952.

[78] A. K. Ghosh and S. S. Hecker, "Stretching limits in sheet metals - in-plane versus out-of-plane deformation," *Metallurgical Transactions,* vol. 5, pp. 2161-2164, 1974.

[79] A. K. Ghosh and S. S. Hecker, "Failure in thin sheets stretched over rigid punches," *Metallurgical Transactions,* vol. A6, pp. 1065-1074, 1975.

[80] M. J. Painter and R. Pearce, "Instability and fracture in sheet-metal," *Journal of Physics D-Applied Physics,* vol. 7, pp. 992-&, 1974.

[81] Z. Marciniak and K. Kuczynski, "Limit strains in the process of stretch-forming sheet metal," *International Journal of Mechanical Sciences*, vol. 9, pp. 609-620, 1967.

[82] E. W. Hart, "Theory of tensile test," *Acta Metallurgica,* vol. 15, pp. 351-&, 1967.

[83] A. K. Ghosh, "Tensile instability and necking in materials with strain-hardening and strain-rate hardening," *Acta Metallurgica,* vol. 25, pp. 1413-1424, 1977.

[84] M. Gotoh, "A class of plastic constitutive-equations with vertex effect .1. general-theory," *International Journal of Solids and Structures,* vol. 21, pp. 1101-1116, 1985.

[85] M. Gotoh, "A class of plastic constitutive-equations with vertex effect .4. applications to prediction of forming limit strains of metal sheets under nonproportional loadings," *International Journal of Solids and Structures,* vol. 21, pp. 1149-1163, 1985.

[86] N. Iwata, M. Matsui, N. Nakagawa, and S. Ikura, "Improvements in finite-element simulation for stamping and application to the forming of laser-welded blanks," *Journal of Materials Processing Technology,* vol. 50, pp. 335-347, Mar 1995.

[87] L. C. Chan, C. H. Cheng, M. Jie, and C. L. Chow, "Damage-based formability analysis for TWBs," *International Journal of Damage Mechanics,* vol. 14, pp. 83-96, 2005.
[88] C. L. Chow and J. Wang, "An anisotropic theory of continuum damage mechanics for ductile fracture," *Engineering Fracture Mechanics,* vol. 27, pp. 547-558, 1987.
[89] C. L. Chow and Y. Wei, "A damage mechanics model of fatigue crack initiation in notched plates," *Theoretical and Applied Fracture Mechanics,* vol. 16, pp. 123-133, 1991.
[90] C. L. Chow and Y. Wei, "A model of continuum damage mechanics for fatigue failure," *International Journal of Fracture,* vol. 50, pp. 301-316, Aug 15 1991.
[91] C. L. Chow, L. G. Yu, W. H. Tai, and M. Y. Demeri, "Prediction of forming limit diagrams for AL6111-T4 under non-proportional loading," *International Journal of Mechanical Sciences,* vol. 43, pp. 471-486, Feb 2001.
[92] C. L. Chow, X. J. Yang, and E. Chu, "Effect of principal damage plane rotation on anisotropic damage plastic model," *International Journal of Damage Mechanics,* vol. 10, pp. 43-55, Jan 2001.
[93] D. Anand, D. L. Chen, S. D. Bhole, P. Andreychuk, and G. Boudreau, "Fatigue behavior of tailor (laser)-welded blanks for automotive applications," *Materials Science and Engineering A,* vol. 420, pp. 199-207, Mar 25 2006.
[94] M. Ono, A. Yoshitake, and M. Omura, "Laser weldability of high-strength steel sheets in fabrication of tailor welded blanks," *Welding International,* vol. 18, pp. 777-784, 2004.
[95] J. Onoro and C. Ranninger, "Fatigue behaviour of laser welds of high-strength low-alloy steels," *Journal of Materials Processing Technology,* vol. 68, pp. 68-70, Jun 15 1997.
[96] P. Lazzarin, E. Rabino, and D. Zondonella Necca, "Fatigue behaviour of laser and resistance seam welds in the automotive industry. (MITS WP 1697)," *Welding International,* vol. 9, pp. 165-172, 1995.
[97] M. Eibl, C. M. Sonsino, H. Kaufmann, and G. Zhang, "Fatigue assessment of laser welded thin sheet aluminium," *International Journal of Fatigue,* vol. 25, pp. 719-731, Aug 2003.
[98] C. M. Sonsino, M. Kueppers, M. Eibl, and G. Zhang, "Fatigue strength of laser beam welded thin steel structures under multiaxial loading," *International Journal of Fatigue,* vol. 28, pp. 657-662, May-Jun 2006.
[99] K. Y. Rhee, D. S. Kwak, and T. Y. Oh, "Fatigue behavior characterization of laser-welded cold rolled sheet metal (SPCEN)," *Journal of Materials Science,* vol. 37, pp. 1019-1025, Mar 1 2002.
[100] M. Jain, "A simple test to asse the formability of tailor-welded blanks," *International Journal of Forming Processes,* vol. 3, pp. 185-212, 2000.
[101] A. P. Roque, R. M. N. Jorge, M. P. L. Parente, R. A. F. Valente, and A. A. Fernandes, "Numerical study of hydroforming with tailor-welded tubular blanks," in *NUMISHEET 2005: 6th International Conference and Workshop on Numerical Simulation of 3D Sheet Metal Forming Processes*, Detroit, MI; USA, 2005.
[102] A. P. Roque, R. M. N. Jorge, M. P. L. Parente, R. A. F. Valente, and A. A. Fernandes, "Influence of the heat affected zone on hydroforming with tailor-welded tubular blanks," in *VIII International Conference on Computational Plasticity,* Barcelona, 2005.
[103] H. M. Jiang, S. H. Li, H. Wu, and X. P. Chen, "Numerical simulation and experimental verification in the use of tailor-welded blanks in the multi-stage stamping process," *Journal of Materials Processing Technology,* vol. 151, pp. 316-320, 2004.

[104] A. Buste, X. Lalbin, M. J. Worswick, J. A. Clarke, B. Altshuller, M. J. Finn, and M. Jain, "Prediction of strain distribution in aluminum tailor welded blanks for different welding techniques," in *International Symposium on Light Metals as held at the 38th Annual Conference of Metallurgists of CIM; Quebec City, Quebec; Canada; 22-26 Aug. 1999*, 1999.

[105] N. Nakagawa, S. Ikura, F. Natsumi, and N. Iwata, "Finite element simulation of stamping a laser-welded blank," in *Sheet Metal and Stamping Symposium*, Detroit, Michigan; USA, 1993.

[106] F. I. Saunders and R. H. Wagoner, "Forming of tailor-welded blanks," *Metallurgical and Materials Transactions A*, vol. 27A, pp. 2605-2616, 1996.

[107] F. I. Saunders, "Forming of tailor-welded blanks," in *Department of Mechanical Engineering*. vol. PhD: Ohio State University, 1994.

[108] J. Cao, B. Kinsey, and Z. Liu, "A novel forming technology for tailor-welded blanks," *Journal of Materials Processing Technology* vol. 99, pp. 145-153, 2000.

[109] M. Tolazzi and M. Merklein, "Precise material properties as a prerequisite for FE-analysis of the hydroforming of tailored welded blanks," *Steel Research International*, vol. 76, pp. 915-919, Dec 2005.

[110] J. M. Trogolo and J. R. Dieffenbach, "Evaluation of tailor welded blanks through technical cost modeling," *SAE Transactions: Journal of Materials & Manufacturing*, vol. 107, pp. 268-272, 1998.

Modified from: Zadpoor, A. A., Sinke, J., Benedictus, R., 2008,"Experimental and numerical study of machined aluminum tailor-made blanks", Journal of Materials Processing Technology, vol. 200, pp. 289-300.

3. Machined tailor-made blanks

In this chapter, the mechanical behavior of machined aluminum tailor-made blanks and the effects of the thickness difference are studied both from experimental and numerical viewpoints. Tensile test specimens with different thickness ratios are machined from Clad and Bare aluminum 2024-T3 monolithic sheets and used for the experimental study. Two different machining processes, i.e. milling and grinding, are applied to prepare the samples. Also a numerical study is conducted to understand the effects of the thickness difference on the mechanical behavior of machined tailor-made blanks. The numerical study is carried out by FEM simulations using ABAQUS. The stress concentrations, the bending caused by the thickness difference and the effects of the thickness ratio on the stress and strain fields are studied numerically. It is shown that both the machining process and thickness difference have significant impact on the forming behavior and failure mechanism of the specimens. It is concluded that stress concentration and strain localization are two competing failure mechanisms in the tensile testing of machined tailor-made blanks.

Despite the popularity of TWBs, other types of tailor-made blanks have not received much attention. Adhesively-bonded and machined TMBs are more appropriate for the aircraft industry compared to the other types of TMBs, because high-strength aluminum alloys, specifically 2000 and 7000 series, often used in the aircraft industry, have poor weldability and are very sensitive to high welding temperatures. The sensitiveness is caused by removing the careful created microstructure and results in significantly reduced mechanical properties. Therefore, fusion welding techniques are not good candidates to make TMBs for the aircraft industry. In an earlier pilot study, the feasibility of machining and adhesive-bonding methods for production of TMBs in the aircraft industry was investigated [1], and it was concluded that both methods are promising. Apart from this study, there have been limited previous studies of tailor-made blanks for aircraft applications, see e.g. references [2, 3].

This chapter focuses on machined tailor-made blanks. Machined TMBs are sheet metals that are machined prior to forming. In contrast to other types of TMBs, in which also the material, and coating can be different, only thickness variations are possible in machined TMBs. In this context, machined TMB is the simplest type of TMBs. Since the thickness difference may also occur in other types of TMBs, study of machined TMBs is useful for all types of TMBs. In addition, in FEM models of machined TMBs, the effects of the thickness difference are isolated from other effects such as the welding effects. Figure 3.1 depicts some machined blanks, that have been deformed into experimental parts of the above-mentioned pilot study [1]. The pilot study showed the potential of the concept and the need for further research in order to exploit the concept. In that subsequent research an important topic should be the forming behavior near the transition line from the larger thickness to the smaller one.

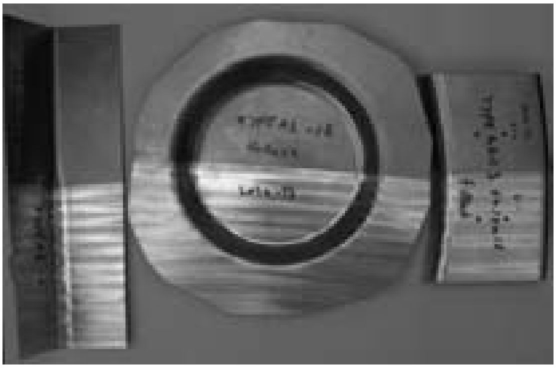

Figure 3.1. Some samples of machined aluminum tailor-made blanks used in the pilot study [1].

Table 3.1. Chemical composition of AA2024-T3 alloy used in the experiments (values are given in percent weight).

Si (%wt)	Fe (%wt)	Cu (%wt)	Mn (%wt)	Mg (%wt)	Ti (%wt)	Al (%wt)
0.051	0.101	4.616	0.623t	1.540	0.0253	remainder

This chapter studies the mechanical behavior of machined TMBs from both experimental and numerical viewpoints. The experimental study deals with the independent effects of the machining process and the effects of the thickness difference on the mechanical behavior of TMBs. With regard to the specimens: Aluminum 2024-T3 is used for all experiments. Further, two different manufacturing methods, i.e. grinding and milling, are used for preparation of the tensile test specimens. A circular (2 mm in diameter) grid pattern is applied on the surface of the specimens, which can be used for local strain measurements. The experimental tests are simulated by using FEM. The stress concentrations near the transition zone and the mechanical behavior of the specimens during the tensile test are analyzed numerically.

3.1. Experimental study

The tensile test specimens were made from Aluminum 2024-T3, a base line alloy in the aircraft industry. Chemical composition of the alloy was determined and is given in Table 3.1. Dimensions of the specimens are based on the ASTM E8 standard. The only difference with the standard is the increased clamping length. Figure 3.2a shows the dimensions of the specimens. Since there is a thickness difference in the gauge length of some specimens, the clamping length is increased so we have the same clamping thickness at both sides of the specimens (see Figure 3.2). The transition line is defined as the boundary line between thick (larger-thickness) and thin (smaller-thickness) sections of the specimens. Specimens in which the transition line is parallel to the loading direction are called *longitudinal* (long.) specimens - see Figure 3.2b. In this figure the machined surfaces are hatched. Specimens in which the transition line is perpendicular to the loading direction are called *transverse* (trans.) specimens (see Figure 2c). There were also some common tensile test specimens that are called *regular* (reg.) specimens, in which no thickness difference was present. The sheet's rolling direction was parallel to the loading direction all specimens.

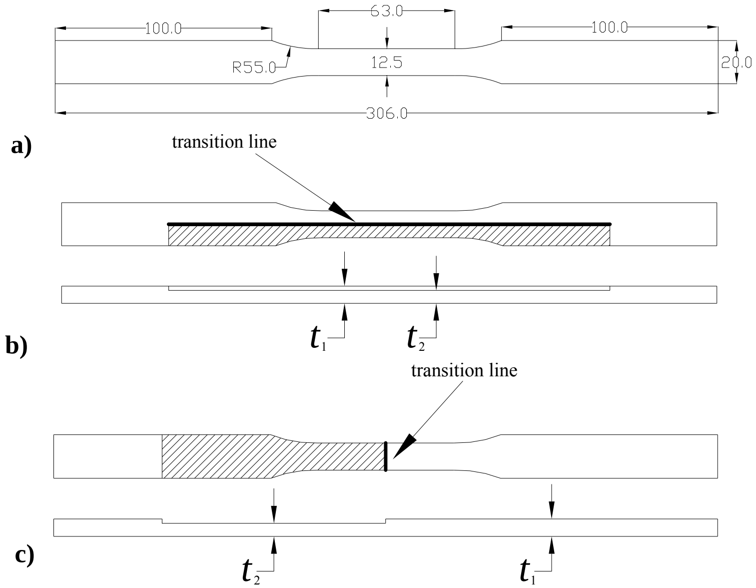

Figure 3.2. Dimensions of the tensile test specimens used in the experimental study (a) and schematic drawings of longitudinal (b) and transverse (c) TMB specimens.

Two different machining operations were used to decrease the thickness of the sheets: milling and grinding. Routing is the edge milling process creating the dog-bone shape of the specimens. Milling is a general machining process that was applied to most specimens to reduce the thickness locally. However, milling gives a relatively rough surface which may influence the mechanical behavior of the specimens. Therefore, grinding was also used to investigate whether the surface roughness influences the mechanical behavior. In principle, grinding of aluminum alloys is a very specialized and expensive process. This is because aluminum is a soft material and clogs normal grinding wheels. The roughness parameters for both milling and grinding processes were measured by a surface analyzer and are listed in Table 3.2. One may notice that the ground surface is smoother than the milled surface. Besides that, the scatter of the roughness parameters is notably lower for the ground surfaces.

Table 3.2. Surface roughness parameters for ground and milled TMBs with different thickness ratios

	R_a (μm)	SD_{R_a} (μm)	R_z (μm)	SD_{R_z} (μm)	R_y(μm)	SD_{R_y} (μm)
Machined	1.26	0.53	5.29	1.97	6.41	2.45
Ground	0.35	0.09	2.27	0.49	2.56	0.56

The test matrix used in the experimental study is given in Figure 3.3. The number of the samples in each group, the geometry of the samples, the type of machining process used for preparing the specimens, the smaller thickness, the larger thickness, and material are given in this table. As one can see, the specimens were cut from either Bare or Clad 2024-T3 sheets. The number of Clad specimens is limited and only used to investigate whether the pure aluminum layer (and its removal during machining operations) makes any difference in the mechanical behavior of machined TMBs. Both Clad and Bare sheets were originally 2 mm in thickness and were machined to the desired thickness (ratio). A wide range of thickness ratios, r , (from 1 and to 4) was used in the test matrix to reveal the effects of the thickness ratio on the mechanical behavior of TMBs. All specimens were grid marked by electrochemical etching with a 2 mm circular grid pattern. After tensile testing, the applied grid system was used for measurement of the local strains near the transition line and close to the failure site. The dimensions of the deformed circles were determined by using an accurate microscope and were used for calculation of the major and minor in-plane strains. Instead of using the single-point-measurement microscopy, a multi-point strain measurement method based on digital image processing was developed for the measurement of strains. In this method, a digital camera is used to capture a microscopic image of the target ellipse. Four different filters are applied to convert the initial image to a binary image. A boundary-detection algorithm is applied over the binary image so that the boundaries of the ellipse are detected. Then, the detected points of the boundary are fitted to an elliptic locus by using the least-squares method. The major and minor radii (or lengths of principal axes) of the fitted ellipse are used for calculation of the strains. This method significantly improves the accuracy and repeatability of the strain measurement. In the single-point-measurement, there is no guarantee that the measured major and minor radii belong to the optimal elliptical locus, while the multi-point-measurement method guarantees that the measured radii belong to the best possible ellipse that can be fitted to the boundaries of the captured ellipse. By using this method, the radii can be measured within an accuracy of 0.001 mm to 0.002 mm which for 2 mm circular-grid-pattern means 0.05% to 0.1% strain accuracy. The tensile tests were performed on a 250 kN Zwick/Roell static test machine. An extensometer was used for measurement of the longitudinal strain. A displacement rate of 2 mm/min in the elastic range and 5 mm/min in the plastic range was used for all the specimens.

3.2. Experimental results

Before performing the test, the actual dimensions of the specimens, including actual thickness, were measured. In Table 3.3. the nominal dimensions are given per test serie, but the actual specimen dimensions were used for calculation of the specimens' data like area, stresses, etc. In this table, the two significant digits (0.05 mm accuracy) are given for thickness values; because this is the accuracy which can be achieved safely by machining. The cross sections are different in the different zones of TMBs. However, the cross section area of the failure zone was used to determine the tensile strength of the specimens.

Table 3.3. Test matrix used in the experimental study.

		smaller thickness			larger thickness							
Series No.	material	t_2 (mm)	milling	grinding	t_1 (mm)	milling	grinding	r	geometry	No. samples	No. failure at TL	σ_{max}(MPa)
1	Bare	2.0	N	N	2.00	N	N	1.0	reg.	5	NA	484.6±3.9
2	Bare	1.80	Y	N	1.80	Y	N	1.0	reg.	5	NA	489.8±3.2
3	Bare	1.80	N	Y	1.80	N	Y	1.0	reg.	5	NA	490.8±1.0
4	Bare	1.80	Y	N	2.00	Y	N	1.1	trans.	3	0	480.8±3.4
5	Bare	1.80	N	Y	2.00	N	Y	1.1	trans.	3	0	486.5±0.7
6	Bare	1.60	Y	N	2.00	N	N	1.2	trans.	3	2	483.7±2.8
7	Bare	1.30	Y	N	2.00	N	N	1.5	trans.	3	1	471.7±2.8
8	Bare	1.15	Y	N	2.00	N	N	1.7	trans.	3	0	484.4±1.1
9	Bare	1.00	Y	N	2.00	N	N	2.0	trans.	3	1	480.4±0.4
10	Bare	0.80	Y	N	2.00	N	N	2.5	trans.	3	0	484.5±1.4
11	Bare	0.65	Y	N	2.00	N	N	3.1	trans.	3	0	490.7±0.2
12	Bare	0.50	Y	N	2.00	N	N	4.0	trans.	3	0	475.9±1.4
13	Bare	1.80	Y	N	2.00	N	N	1.1	long.	3	NA	485.4±3.2
14	Bare	1.60	Y	N	2.00	N	N	1.2	long.	3	NA	481.5±3.0
15	Bare	1.30	Y	N	2.00	N	N	1.5	long.	3	NA	488.5±1.3
16	Bare	1.15	Y	N	2.00	N	N	1.7	long.	3	NA	479.8±3.9
17	Bare	1.00	Y	N	2.00	N	N	2.0	long.	3	NA	487.7±2.1
18	Bare	0.80	Y	N	2.00	N	N	2.5	long.	3	NA	490.2±0.7
19	Bare	0.65	Y	N	2.00	N	N	3.1	long.	3	NA	485.9±0.8
20	Clad	2.00	N	N	2.00	N	N	1.0	reg.	5	NA	470.9±2.1
21	Clad	1.80	Y	N	1.80	Y	N	1.0	reg.	5	NA	481.3±2.6
22	Clad	1.80	N	Y	1.80	N	Y	1.0	reg.	3	NA	488.1±0.8

Results of the tensile tests are summarized in Table 3.3 and Table 3.4. Table 3.3 presents the tensile strength of the specimens and the failure location . Major and minor in-plane strains at the failure zone and transition line of some samples of the specimens are listed in Table 3.4. Table 3.4 implies that when failure has occurred away from the transition line, the strain level (ε_1) at the failure zone is higher than for the specimens which failed at the transition line. Furthermore, when failure has occurred away from the transition line, the strain level at the failure zone is significantly higher than the strain level at the transition line of the same specimen. It means that the strain is localized in a region at the failure zone. Figure 3.3 compares failure and transition zones of a specimen in which failure has occurred away from the transition line. From the differences in the elliptical shapes of the original circular grid elements, it is concluded that the strain level at the failure zone (Figure 3.3a) is much higher than the strain level at the transition line (Figure 3.3b).

Table 3.4. Major and minor in-plane principal strains at the failure and transition zones of some representative specimens.

				Transition line		Failure zone	
Series	Sample	r	Failure at TL	ε_1 (%)	ε_2 (%)	ε_1 (%)	ε_2 (%)
6	44	1.2	Yes	10.4	-9.4	10.4	-9.4
6	45	1.2	No	13.9	-6.4	25.8	-8.5
7	47	1.5	No	10.6	-6.1	23.0	-7.5
9	54	2.0	No	8.2	-5.7	21.2	-6.7
11	58	3.1	No	7.3	-5.8	18.1	-6.5
12	61	4.0	No	5.0	-5.3	16.1	-5.2

As is clear from Table 3.3, the thickness ratio does not have a significant impact on the tensile strength of TMBs. However, the tensile strengths of the non-machined Clad specimens are lower than the tensile strength of the non-machined Bare specimens. This is because a pure-aluminum layer is present on Clad specimens. The layer is applied on both sides of Clad sheets to improve sheet’s corrosion resistance. The thickness of the two layers together is about 10% of the nominal thickness. Since the strength values of the pure aluminum are much lower than those of the AA2024-T3 alloy, the tensile strengths of non-machined Clad specimens (470.9±2.1 MPa) are (7.7 MPa to 19.7 MPa) lower than of the bare specimens (484.6±3.9 MPa). However, by milling and grinding the tensile strength of the Clad specimens increases (to 481.3±2.6MPa for machining and 488.1±0.8MPa for grinding), because a part of pure aluminum is removed during the machining process. Although this slightly improves the tensile strength of TMB, the corrosion resistance of the machined surface will be worse than for the non-machined Clad sheet. The other point is that, all other conditions being equal, the tensile strengths of the ground specimens are slightly higher than the milled specimens for both Bare and Clad specimens (compare series number 2, 4, and 21 of Table 3.3 with respectively series number 3, 5, and 22 of the same table). This difference can be attributed to the smoother surface of the ground specimens (see Table 3.2) which makes the notch effect less severe when compared to the milled surfaces. Figure 3.4a and Figure 3.4b depict the failure zones of two milled specimens. From Figure 3.4a, it seems that the failure has exactly occurred at one of the notches created by the cutting tool. Figure 3.4b, displays a more detailed view of the failure zone and one can see the notches (grooves/surface roughness) in the left side of the picture, where the failure has occurred.

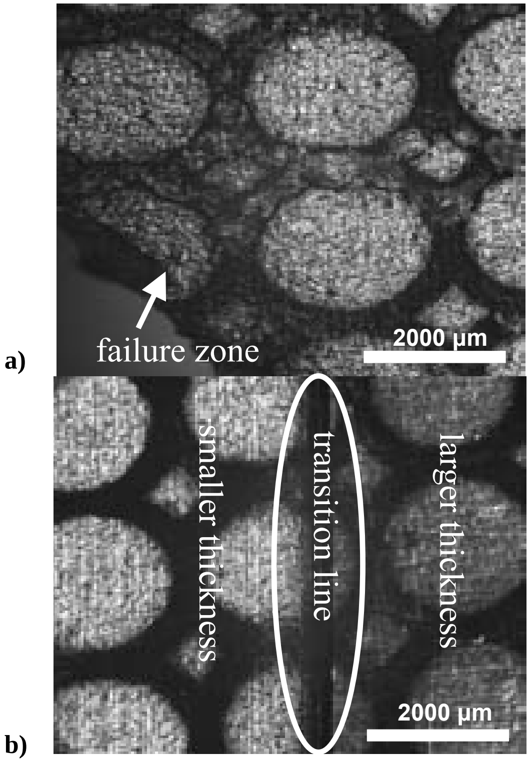

Figure 3.3. Strain levels at the failure zone (a) and transition zone (b) of one of the specimens in which the failure zone is away from the transition line (series no. 5, $r = 1.11$).

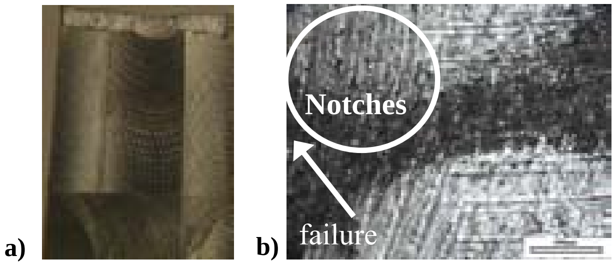

Figure 3.4. a) Failure zone of a milled specimen. The notches created by the cutting tool can be seen around the failure zone and part of the failure has taken place exactly on one of the footstep circular lines. b) A magnified view (x10) of the machined surface of a milled specimen in which small grooves caused by the cutting tool can be clearly seen (series no. 9, $r = 2$).

Because of the sudden change of the thickness at the transition line, stress concentrations happen at the transition line of the transverse specimens. Chan *et al* [4] studied the stress distribution at the transition line of tailor-made blanks with thickness ratios ranging from 1.11 to 2. They showed that as the thickness ratio increases, the stress concentration becomes more pronounced. They, as well as some other researchers [5-7], state that the stress concentration induce the failures at the transition zone. In Table 3.3, one can see that, for thickness ratios ranging from 1.2 to 2, four specimens fail at the transition line. This is in line with the cited literature and can be attributed to the stress concentration phenomenon. However, it is important to notice that most of the failures at the transition line happen for thickness ratios ranging from 1.2 to 1.5. Furthermore, no failure at the transition line was observed for thickness ratios larger than 2. The fracture surfaces were studied by using Scanning Electron Microscopy (SEM) and it was observed that the failure had happened by coalescence of voids. The dimples and tear edges, which are indicators of ductile fracture, were present on the fracture surfaces.

3.3. Numerical study

The tensile tests were simulated by using the commercial FEM software ABAQUS. Transverse and longitudinal geometries were modeled and dimensions shown in Figure 3.2a and thicknesses combinations given in Table 3.2 were used for parametric analyses. Three-dimensional solid (continuum) elements with three translational degrees-of-freedom and linear hexahedron (brick) geometry were used for discretization of the geometries. The reduced integration scheme with hourglass control was applied meaning that the elements had 8 nodes and only 4 integration points. The hexahedral elements were preferred over first-order tetrahedral elements because the hexahedral elements provide an equivalent accuracy at less cost and have a better convergence rate. Besides that, first-order tetrahedral elements are too stiff for stress analysis problems [8]. The reduced integration scheme could be used because of the fact that hour-glassing, which results in uncontrolled distortion of the elements when all calculated strains are zero at the integration point, was not an issue. In addition, application of the reduced integration scheme prevents the model from being locked when incompressible materials undergo plastic deformation. In the reduced integration scheme, a lower-order integration procedure is used to generate the element stiffness matrix while still a full integration is used to form the mass and distributed loading matrices. The computational expense of the reduced-integration elements is significantly less than the full-integration elements, specifically in the three-dimensional stress analysis.

Table 3.5. The material parameters used in the numerical study.

material	E (GPa)	σ_{y0} (MPa)	κ (MPa)	n
2024-T3	70	350	683	0.1283

Generally, second-order elements can more accurately capture the large stress gradients as in the case of stress concentrations. However, second-order elements do not combine well with von Mises and Hill plasticity because with developing plasticity, the incompressible nature of the von Mises and Hill plasticity calls for over-constraining (locking) of the material. One solution to this problem is to use the hybrid second-order elements. However, the hybrid elements substantially increase the computational cost of the simulation. Therefore, it was concluded that the first-order hexahedral element can provide the best accuracy and convergence rate at the minimum computational cost while fulfilling other conditions such as not being suspect to model-locking. Previous studies have shown that wherever solid elements are used in the FEM models of sheet metals, a large number of through thickness elements are required so that the stress and strain fields and specifically the bending behavior can be fully captured [9]. In the preliminary studies, it was observed that if a small number of through-thickness elements are used, the stress and strain fields can not be determined accurately, in particular near the transition line. Therefore, a large number of through the thickness elements (up to 25) were used in the FEM models. On the other hand, in order to maximize the accuracy of the results for brick elements, the element dimensions should be of similar size. Since the through-thickness dimension of the elements is very small, this means that a very large number of brick elements should be used. The structured meshing method was used and the mesh was optimized so that the number of elements was higher where larger stress and strain gradients were expected, e.g. near the transition zone. Optimization of the mesh improves the accuracy of the results while it keeps the computational cost manageable. Indeed, it is important to have a fine mesh at the transition line because that is where the stress concentrations happen and the stress values have to be accurately determined so that the stress concentration factors can be accurately calculated. A mesh sensitivity analysis was conducted to ensure that the results and the applied mesh are independent. In the mesh sensitivity analysis, the number of elements increased steadily and the stress values were recorded. It was observed that even for relatively small number of elements (7000- 12000 elements) the range of variations of the stress values is small (i.e. less than 4% of the nominal stress value). However, the models were considered to be mesh-independent only if by further increasing the number of elements, the stress values did not change by more than 0.5% of the nominal stress value.

The number of elements was kept constant (124400 for transverse specimens and 18690 for longitudinal specimens) while varying the thickness between different FEM models. An impression of the applied mesh near the transition line (for transverse specimens) is depicted in Figure 3.5a. The models were simulated by using an implicit solver (ABAQUS/Standard). Boundary conditions were set so that the simulation resembled the actual test conditions. All the translational degrees of freedom were constrained at one side of the specimens (clamping side) to approximate the clamping mechanism in the tensile test machine. At the other side (moving side) of the specimens, two translational degrees of freedom were applied, which were not lying along the loading direction, were constrained while no translational constraint was applied for movement along the loading direction. The tensile force was simulated by applying a ramp traction force over the clamping length at the moving side. Experimentally-obtained material parameters (see Table 3.5) were used in the FEM models. The Hollomon’s hardening rule and von Mises yield criterion were adopted.

a)

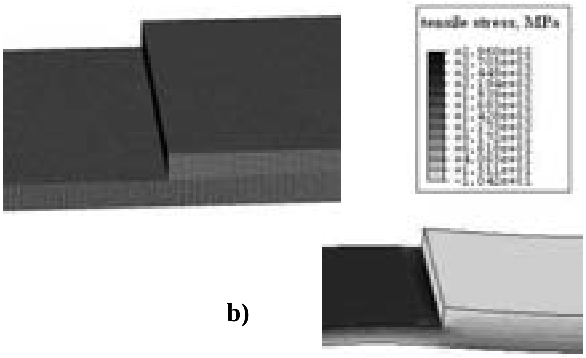

b)

Figure 3.5. a) The mesh distribution for transverse specimens. b) The Stress concentration at the transition line of the transverse specimens.

3.4. Simulations results

As previously stated, due to the existence of the thickness difference in the middle of the gauge length, the stress concentration phenomenon is expected to happen during the tensile testing of the transverse specimens. Numerical simulations confirmed that the stress concentration takes place at the transition line. Figure 3.5b shows the stress concentration phenomenon near the transition line. In order to be able to asses the stress concentration phenomenon quantitatively, a stress concentration factor, *K*, was defined as follows

$$K = \frac{\sigma_{\mathrm{max,TL}}}{\sigma_{\mathrm{nom}}} \tag{1}$$

In this study, the maximum tensile stress value is determined by FEM analysis of the tensile test and the maximum value is divided by the nominal stress (of the thin section) to determine the stress concentration factor in both elastic and plastic ranges. The concept of stress concentration factor in the plastic range has been used by some other researchers, see e.g. references [10-12]. In the elastic range, the stress concentration factor of a particular point is independent of the applied load. In contrast, the plastic stress concentration factor is dependent on the applied load. Figure 3.6 shows how the stress concentration factor changes when the applied load increases. It can be seen that in the elastic region, the stress concentration factor is constant and does not change with the applied load. However, after yielding, the stress concentration factor decreases as the maximum value of the calculated tensile stress increases. Although stress concentration factor vs. maximum tensile stress for only one thickness ratio is displayed in Figure 3.6, the same decreasing trend was observed for all other thickness ratios of the test matrix.

Figure 3.7 depicts how the stress concentration factor changes with the thickness ratio. As predicted by physical reasoning, the stress concentration factor increases with an increase of the thickness ratio up to a maximum value. Afterwards, the stress concentration factor decreases with an increase of the thickness ratio. The thickness ratio for which the maximum stress concentration factor takes place is weakly dependent on the tensile stress and varies from around 1.9 to 2.1. Therefore, there is a qualitative correlation between experimental and numerical results, because there is a thickness ratio for which maximum stress concentration factor takes place and there are some thickness ratios for which most failures at the transition line takes place. However, the experimental and numerical results are not in quantitative agreement since the thickness ratio for which the maximum stress concentration factor takes place ($r = 1.9 - 2.1$) is different from the thickness ratio for which the largest number of failures at the transition line is observed ($r = 1.2 - 1.5$). The discrepancy between the stress concentration analysis and experimental results stems from the point that there are two competing failure mechanisms: stress concentration and strain localization. Typical machining processes, like milling, have a constant accuracy (between 0.02 to 0.05 mm). This limited accuracy results in some thickness variations in the machined surfaces. According to the Marciniak-Kuczynski theory, very small variations of the thickness are responsible for the failure of sheet metals, because after a certain point strain is localized in the area with smaller thickness (imperfection zone) [13]. The strain localization mechanism is discussed in more detail in the next section, "discussions".

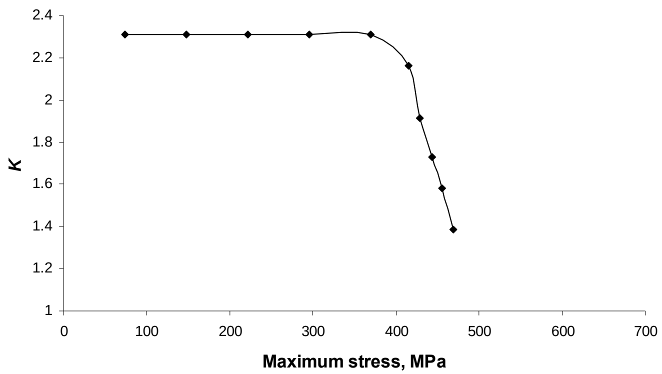

Figure 3.6. Numerically predicted stress concentration factor vs. maximum tensile stress for transverse TMBs (*r*=2)

Although the thickness difference was always compensated at the clamping length, the simulation results showed that there is a bending behavior in the tensile testing of machined TMBs. This behavior is present in both transverse and longitudinal specimens. Analyses showed that there are two different reasons for the bending behavior: stress concentration and the displacement of the neutral axis. The stress concentration phenomenon only exists in the transverse specimens. Displacement of the neutral axis is present in both transverse and longitudinal specimens. The effect of the neutral axis displacement is pronounced with the increment of the thickness ratio. For very small thickness ratios, this effect is negligible. Figure 3.8 depicts the maximum lateral displacement of a transverse specimen ($r = 1.05$) vs. maximum tensile stress. A very small thickness ratio is selected to eliminate the effect of the neutral axis displacement. Because of the stress concentration, upper thickness elements at the transition line deform more than the lower thickness elements (see also Figure 3.5b). Therefore, the specimen has to bend in order to be able to accommodate extra deformation of the upper thickness layers. The effect is pronounced when the maximum tensile stress reaches the yield stress (see Figure 3.8), since the upper thickness layers enter the plastic range while the lower thickness layers are still in the elastic range. Figure 3.8 shows this behavior and one can see that the maximum lateral deflection increases gradually up to the point where the yield stress (350 MPa) is reached. Then, just after the yielding point is reached, the maximum deflection increases suddenly and continues to increase rapidly, for higher maximum stress values.

Simulations of the tensile test of the longitudinal specimens showed that for very small thickness ratios there is no significant bending in the specimens. However, when the thickness ratio increases, the longitudinal specimens bend. Figure 3.9 shows how the maximum lateral deformation changes with the thickness ratio for transverse and longitudinal specimens. The data in this figure are given for a small nominal tensile stress (σ_{nom}=50 MPa) to minimize the effect of the stress concentration on the transverse specimens. It can be seen that, for both transverse and longitudinal specimens, as the thickness ratio increases, the maximum lateral deformation increases. While the lateral deformation increases with increasing r, the stress concentration factor decreases for $r > 2$. One can therefore conclude that the secondary bending due to the shifting of the neutral axis is much stronger than due to the stress concentration. Furthermore, it was found that, due to the bending behavior, tensile strain is not uniform in the gauge length. Indeed, for very large thickness ratios, the difference between the maximum and minimum strain values can amount up to 20-30% of the average strain value.

Table 3.6. Thickness variations for ground and milled surfaces, statistical parameters of the thickness variations, and random imperfection parameters.

r	processing	points	$\overline{t}_{2,act}$ (mm)	SD_{t_2} (mm)	f_1	f_2	f_3
1.11	milling	16	1.78	0.0106	0.9940	0.9880	0.9820
1.53	milling	16	1.24	0.0120	0.9903	0.9806	0.9709
2.00	milling	16	0.94	0.0131	0.9860	0.9721	0.9582
1.00	grinding	16	1.76	0.0141	0.9919	0.9838	0.9757

3.5. Discussions

Experimental studies showed that the thickness difference does not have a significant impact on the tensile strength (property related to the thinner gauge). The tensile strengths of not-machined Clad specimens were found to be slightly lower than the bare specimens. However, the tensile strengths of the machined Clad specimens (when Clad layer was removed) were of the same level of the tensile strengths of the Bare specimens. Furthermore, although the surface roughness of the ground surfaces ($R_z = 2.27\ \mu\mathrm{m}$) is notably lower than the surface roughness of the milled surfaces ($R_z = 5.29\ \mu\mathrm{m}$), the difference in the surface roughness caused only a slight difference in the tensile strength. Table 3.6 gives the thickness variations caused by the grinding process. One may notice that the thickness variations caused by the grinding process (SD_{t_2} =0.0141 mm) is not lower than the thickness variations caused by the milling process (SD_{t_2} =0.0106 to 0.0131 mm). Because, on one hand, grinding aluminum alloys is a difficult and costly process and, on the other hand, since the variations are marginal, it is suggested that milling should be used for production of aluminum TMBs.

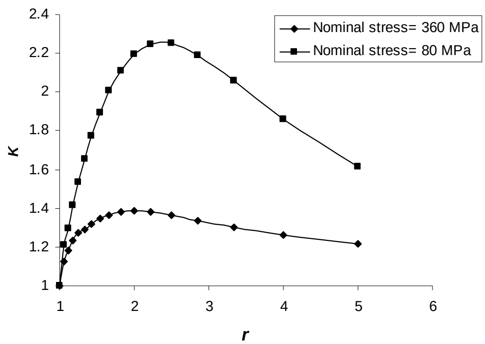

Figure 3.7. Numerically predicted stress concentration factor vs. thickness ratio for transverse TMBs.

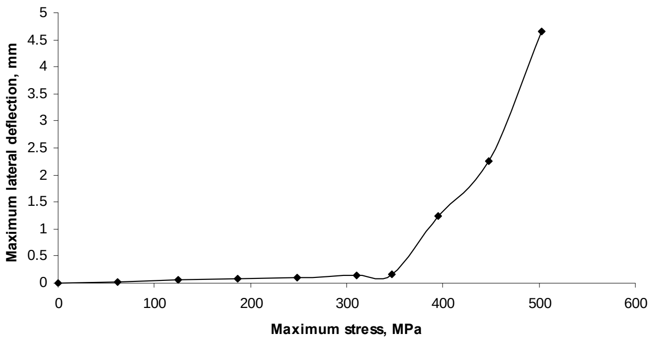

Figure 3.8. Numerically predicted maximum deflection vs. maximum tensile stress for transverse specimens ($r = 1.05$).

The numerical study showed that the stress concentration takes place at the transition line of the transverse specimens. A generalized stress concentration factor, which describes the stress concentration phenomenon in both elastic and plastic ranges, was used to show how the stress concentration factor changes with different parameters. Simulation results implied that the stress concentration factor decreases in the plastic region. This is important because the chance of failure due to stress concentration during forming process decreases. In addition, it was found that the stress concentration factor increases as the thickness ratio increases up to a thickness ratio for which the maximum stress concentration factor occurs. Beyond this maximum, the stress concentration factor decreases with an increase of the thickness ratio. This is in agreement with what is predicted with physical reasoning: For very large thickness ratios, the thicker part of the specimen remains almost undeformed and its relationship with the thinner part is similar to the relationship between a clamping point and a deforming object. The thickness ratio for which the maximum stress concentration factor occurs is weakly dependent on the maximum tensile stress and varies between $r = 1.9$ and $r = 2.1$. The experimental study also showed that the number of failures at the transition line increases as the thickness ratio increases up to the thickness ratios ($r = 1.2 - 1.5$) for which the maximum number of failures at the transition line happens. Further experimental study with a larger number of thickness ratios in this range ($r = 1.2 - 1.5$) is needed to determine the accurate value of the thickness ratio at which the maximum number of failures at the transition line takes place. Although there is a correlation between the experimental and numerical results, the thickness ratios for which the maximum number of failures at the transition line takes place are lower than the thickness ratios for which maximum stress concentration factors happen. This back-shifting of the thickness ratios from $r = 1.9 - 2.1$ for the numerical results to $r = 1.2 - 1.5$ for the experimental results needs to be explained. Indeed, there are two competing failure mechanisms: stress concentration and strain localization. The stress concentration failure mechanism was described in the previous sections. In 1967, Marciniak and Kuczynski postulated that the failure of the sheet metals is related to the small thickness variations [13]. In not-machined sheet metals, the thickness variations were assumed to be created during the manufacturing process of the sheets. This theory has received much attention and is used by many researchers for prediction of the limiting strains in sheet metal forming processes, see e.g. [14-16]. In this regard, an imperfection parameter, *f*, is defined as follows

$$f = \frac{t_b}{t_a} \tag{2}$$

It is assumed that failure in sheet metals happens when strain is localized in the imperfection zone (region b). When strain is localized in the imperfection zone, straining in that particular zone is significantly higher than the zone with uniform thickness (region a). In general, the lower the imperfection parameter, the more severe the strain localization phenomenon is, and the lower the failure strains are.

For machined surfaces, small thickness variations are caused also by the machining process. Accuracy of the machining processes is almost the same for all thickness ratios. Table 3.6 shows that the accuracy of the machining process (SD_{t_2}) is almost the same for all three given thickness ratios. However, for smaller thicknesses of the machined surfaces, the impact of the machining accuracy is higher than the machined surfaces with a larger thickness. This is because a given thickness variation causes a larger change in the imperfection parameter, *f*, when the nominal thickness is smaller. Therefore, for smaller thicknesses of the machined surfaces, i.e. larger thickness ratios, the strain localization phenomenon is more severe and failure strains would be lower. If it is assumed that the machining process causes a normal random distribution of the thickness variation in the machined surface, three random imperfection parameters, f_1, f_2, and f_3, can be defined as follows:

$$f_1 = \frac{\overline{t}_{2,act} - SD_{t_2}}{\overline{t}_{2,act}}, f_2 = \frac{\overline{t}_{2,act} - 2SD_{t_2}}{\overline{t}_{2,act}}, f_3 = \frac{\overline{t}_{2,act} - 3SD_{t_2}}{\overline{t}_{2,act}} \tag{3}$$

The theoretical basis for defining these three parameters is a property of every normal distribution. Due to that property, 65% of all random values of every normal distribution fall within one standard deviation of the average values, 95% fall within two standard deviations of the average values, and 99.7% fall within three standard deviations of the average value. Therefore, almost all values are within three standard deviations of the average value. This is clear from Table 3.6 that the random imperfection parameters decrease as the thickness ratio increases. The failure strains of some of the specimens for which the failure has taken place away from the transition line are given in Table 3.4. It can be seen that, in agreement with the predictions of the MK theory, as the thickness ratios increases, the absolute values of the major and minor failure strains decrease. Besides that, the strain values in the failure zone are higher than at the transition line in the specimens for which the failure has happened away from the transition zone. These evidences confirm that the strain localization phenomenon is more severe for larger thickness ratios. This may be the reason why the maximum number of failures at the transition line happens in a lower thickness ratio compared to the thickness ratio for which the maximum stress concentration factor occurs.

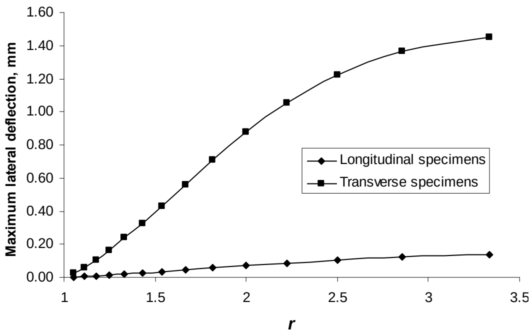

Figure 3.9. Numerically predicted maximum deflection vs. thickness ratio for both longitudinal and transverse specimens (σ_{nom} =50MPa).

The presented discussion can be summarized as follows. There are two competing failure mechanisms in the tensile testing of machined TMBs: stress concentration and strain localization. For small thickness ratios ($r \leq 1.1$), the stress concentration and strain localization are both small and each of them, or the local stress concentration caused by the notches created during the machining process, could cause the failure (on a random basis). For moderate thickness ratios ($r = 1.2 - 1.5$), the stress concentration failure mechanism is dominant. However, the strain localization is dominant for large ($r \approx 2$) and very large thickness ratios ($r > 2$). It is worthwhile to point out that, because of the dynamic loading conditions and

production issues, moderate thickness ratios are more likely to be used in real applications of machined tailor-made blanks.
Simulations showed that there is a bending behavior in both transverse and longitudinal specimens. For the longitudinal specimens, the bending behavior is due to the displacement of the neutral axis. For transverse specimens, there are two different reasons for the bending behavior: stress concentration and neutral axis displacement. Because of presence of the bending behavior, the stress and strain values are not constant in the transverse and longitudinal specimens. Indeed, it was found that the difference between maximum and minimum strain and stress values can amount up to 15% of the average values for $r = 2$, and up to about 20 to 30% of the average value for larger thickness ratios. In general, this percentage increases as the thickness ratio increase, because the bending behavior is pronounced with increment of the thickness ratio. The point that strain and stress values are not constant in the gauge length of TMBs is an important point for all kinds of tailor-made blanks in view of the fact that some widely used methods for measurement of the mechanical properties of the weld metal and heat-affected zones are based on the assumptions that strain and stress values are constant in certain regions of the longitudinal and transverse TWB specimens, respectively. The technique called rule-of-mixture uses these two assumptions to calculate the mechanical properties of the weld metal and heat-affected zones of welded tailor-made blanks, see references [17, 18] for a description of the method. Some researchers have used this method for calculation of the mechanical properties of welded TMBs with thickness ratios ranging from 1.11 to 2 [4, 19-23]. As previously mentioned, results of the simulations of machined TMBs are useful for other kinds of TMBs as well; because, in simulations of machined TMBs, the effects of the thickness difference are isolated from the other effects such as the welding effects. Therefore, the results obtained in the FEM analysis of machined TMBs are also applicable to the other kinds of TMBs in which a thickness difference is present. Validity of those two assumptions of the rule-of-mixture method was examined for different thickness ratios and it was found that although these assumptions are fairly accurate for small thickness ratios ($r = 1 - 1.3$), they are not accurate enough for thickness ratios about or more than 2. The numerical results are in agreement with findings of the other researchers who have shown that during the deformation of tailor-made blanks the stress and strain values are not uniformly distributed [4-7, 24]. However, the numerical values reported here should be considered only as qualitative indicators of the non-uniform stress and strain distribution. The quantitative measures of the non-uniformity have to be determined by using full-field strain analysis methods such as photo-elasticity or digital image correlation.

3.6. Conclusions

In this chapter, machined aluminum tailor-made blanks were studied from both numerical and experimental viewpoints. The most important conclusions of the study are summarized as follows:

- The thickness ratio does not have a significant impact on the tensile strength of machined TMBs.

- There are some thickness ratios ($r = 1.9 - 2.1$) for which maximum stress concentration factors happen in a numerical analysis.
- On one hand, all failures at the transition line happen for thickness ratios less than the thickness ratios for which the maximum stress concentration factors were predicted. On the other hand, the imperfection factor related to the thickness variations caused by the machining is greater for larger thickness ratios, meaning that the strain localization is more severe for the larger thickness ratios. Although the experimental evidence is not strong enough to draw a firm conclusion, these two phenomena might be related; because the more severe strain localization for larger thickness ratios could result in the strain localization failure be preceding the potential failure due to the stress localization.
- There are two competing failure mechanisms in the tensile testing of machined TMBs: stress concentration and strain localization. For moderate thickness ratios ($r = 1.2 - 1.5$), the stress concentration failure mechanism is dominant. The strain localization is predominant for large ($r \approx 2$) and very large thickness ratios ($r > 2$).
- The displacement of the neutral axis (in both transverse and longitudinal specimens) and stress concentration (in transverse specimens) cause a bending behavior in machined TMBs. The maximum deflection increases as the thickness ratio increases.
- Because of the bending behavior, the stress and strain values are not constant in the gauge length of machined TMBs and, hence, the rule-of-mixture method can only be used for welded tailor-made blanks with a relatively small thickness ratio.
- The effects of the machining processes are at least as important as the effects of the thickness difference.

3.7. References

[1] Sinke J, Stofregen MM, Straatsma E. Tailor made blanks for the aircraft industry: a pilot study. Netherlands Institute for Metals Research, 2005.
[2] Monaco A. Tailor made blanks for the aircraft industry. Faculty of Aerospace Engineering, vol. M.Sc.: Delft University of Technology(TU Delft), 2006.
[3] Sternad M. Front spar design with tailor made blanking. Faculty of Aerospace Engineering and Geodesy, vol. M.Sc.: University of Stuttgart, 2006.
[4] Chan LC, Cheng CH, Chan SM, Lee TC, Chow CL. Formability analysis of tailor-welded blanks of different thickness ratios. J. Manufac. Sci. Eng.-Trans. ASME 2005;127:743.
[5] Buste A, Lalbin X, Worswick MJ, Clarke JA, Altshuller B, Finn M, Jain M. Prediction of strain distribution in aluminum tailor welded blanks for different welding techniques. Canad. Metall. Quart. 2000;39:493.
[6] Ono M, Yoshitake A, Omura M. Laser weldability of high-strength steel sheets in fabrication of tailor welded blanks. Weld. Int. 2004;18:777.
[7] Uchihara M, Fukui K. Performance of tailor welded blanks using automotive highs trength steel sheets for practical use. Weld. Int. 2006;20:622.

[8] ABAQUS. ABQUS Theory Manual ver. 5.5. Pawtucket: Hibbitt, Karlsson & Sorensen Inc., 1995.
[9] Zhao KM, Chun BK, Lee JK. Finite element analysis of tailor-welded blanks. Fin. Elem. Anal. Des. 2001;37:117.
[10] Ishikawa H. Stresses in the plastic range around a circular hole in an infinite sheet subjected to equal biaxial tension. ZAMM 1975;55:171.
[11] Budiansky B, Managasarian L. Plastic stress concentration at a circular hole in an infinite sheet subjected to equal biaxial tension. J. App. Mech.-Trans. ASME 1960;27:59.
[12] Sherbourne AN, Haydl HM. Stress concentration in the plastic range. AIAA J. 1976;14:1628.
[13] Marciniak Z, Kuczynski K. Limit strains in the process of stretch-forming sheet metal. Int. J. Mech. Sci. 1967;9:609.
[14] Hiwatashi S, Van Bael A, Van Houtte P, Teodosiu C. Prediction of forming limit strains under strain-path changes: Application of an anisotropic model based on texture and dislocation structure. Int. J. Plasticity 1998;14:647.
[15] Banabic D, Comsa S, Jurco P, Cosovici G, Paraianu L, Julean D. FLD theoretical model using a new anisotropic yield criterion. J. Mater. Proc. Tech. 2004;157-58:23.
[16] Butuc MC, da Rocha AB, Gracio JJ, Duarte JF. A more general model for forming limit diagrams prediction. J. Mater. Proc. Tech. 2002;125:213.
[17] Wild PM, Abdullah K, Jeswiet JJ, Ghasempoor A. Tensile testing for weld deformation properties in similar gage tailor welded blanks using the rule of mixtures. J. Mater. Proc. Tech. 2001;112:91.
[18] Liu S, Chao YJ. Determination of global mechanical response of friction stir welded plates using local constitutive properties. Mod. Sim. Mater. Sci. Eng. 2005;13:1.
[19] Chan SM, Chan LC, Lee TC. Tailor-welded blanks of different thickness ratios effects on forming limit diagrams. J. Mater. Proc. Tech. 2003;132:95.
[20] Chan LC, Chan SM, Cheng CH, Lee TC. Formability and weld zone analysis of tailor-welded blanks for various thickness ratios. J. Eng. Mater. Tech.-Trans ASME 2005;127:179.
[21] Miles MP, Decker BJ, Nelson TW. Formability and strength of friction-stir-welded aluminum sheets. Metal Mater. Trans. A 2004;35A:3461.
[22] Ghoo BY, Keum YT, Kim YS. Evaluation of the mechanical properties of welded metal in tailored steel sheet welded by CO2 laser. J. Mater. Proc. Tech. 2001;113:692.
[23] Hetu L, Siegert K. Hydromechanical deep drawing of tailor welded blanks. Steel Res. Int. 2005;76:857.
[24] Chien WY, Pan J, Friedman PA. Failure prediction of aluminum laser-welded blanks. Int. J. Damage Mech. 2003;12:193.

3.8. Appendix A- Nomenclature

t_1	larger thickness in a TMB, mm
t_2	smaller thickness in a TMB, mm
r	ratio of larger thickness to smaller thickness in a TMB, dimensionless
ε_1	major in-plane principal strain, %
ε_2	minor in-plane principal strain, %
$\sigma_{\max}$	tensile strength, MPa
K	stress concentration factor, dimensionless

$\overline{t}_{2,act}$	average actual smaller thickness in a TMB, mm
SD_{t_2}	standard deviation of the actual smaller thickness, mm
R_a	average roughness, µm
SD_{R_a}	standard deviation of the average roughness, µm
R_z	mean roughness depth, µm
SD_{R_z}	standard deviation of the mean roughness depth, µm
R_y	maximum roughness, µm
SD_{R_y}	standard deviation of the maximum roughness, µm
t_a	thickness of the uniform zone in the M-K model, mm
t_b	thickness of the imperfection zone in the M-K model, mm
f	imperfection parameter used in the M-K model, dimensionless
σ_{nom}	nominal stress at the gauge length of the tensile test specimens, MPa
$\sigma_{\mathrm{max,TL}}$	maximum tensile stress value at the transition line, MPa
E	elastic modulus, GPa
σ_{y0}	initial yield stress, MPa
κ	strength coefficient in Hollomon's rule, MPa
n	strain hardening exponent in Hollomon's rule, dimensionless

Modified from: Zadpoor, A. A., Sinke, J., Benedictus, R., 2009," The mechanical behavior of adhesively bonded tailor-made blanks", International Journal of Adhesion and Adhesives, vol. 29 (5), pp. 558-571.

4. Adhesively bonded tailor-made blanks

Adhesive bonding is a promising alternative joining method for fabrication of tailor-made blanks in the aircraft industry. In this chapter, the mechanical behavior of adhesively bonded tailor-made blanks is studied from both experimental and numerical viewpoints. The transition line is defined as the boundary between two different thicknesses present in the TMB. Two different forming directions, one in parallel with the transition line and one perpendicular, are considered. Tensile testing of the specimens from each category is carried out and FEM models are used to simulate the mechanical behavior of the specimens during the test. It is shown that when loading direction is perpendicular to the transition line, metal failure is preceded by decohesion at the bond line. The adhesive layer is modeled by using the cohesive interface elements with the capability of simulating the damage initiation and evolution mechanisms of adhesives. The experimental and numerical results are compared and are shown to be in a good agreement. It is shown that the capacity of adhesively bonded TMBs for in-plane plastic straining is limited. It is therefore recommended that forming processes should be designed such that in-plane plastic straining is minimized.

The high-strength aluminum alloys that are used in production of structural parts in the aircraft industry are often not weldable and are sensitive to high welding temperatures. Reason is that high welding temperatures affect the microstructure created by heat-treatments of high-strength aluminum alloys. Besides that, welding adversely affects the formability of aluminum alloys, and it is difficult to weld dissimilar alloys. In contrast to welding, the adhesive bonding processes used in the aircraft industry do not include high temperatures and the mechanical properties of alloys are unchanged after bonding. Furthermore, dissimilar alloys can be bonded easily together and this removes many of the constraints a designer faces while attempting to achieve optimal material distribution within structural parts (by combining different materials and/or different sheet thicknesses).

Aircraft manufacturers have been using adhesive bonding as an efficient joining method for a long time. Among the advantages of adhesive bonding for the aircraft industry are the absence of stress concentrationw related to the weakening of the sheet that is present in other joining methods (such as riveting), high joint efficiency, and, as mentioned, the possibility of joining dissimilar materials. The idea behind adhesively bonded tailor-made blanks is to combine the advantages of adhesive bonding with the tailor-made blank concept such that the structural parts of aircraft

can be made lighter and/or more cost-effective without any compromise in (structural) performance.
A pilot study was carried out to investigate the feasibility of application of adhesively bonded TMBs [4]. Figure 4.1 shows some samples of the experimental parts manufactured during the pilot study. As annotated in this figure, these samples are produced either by rubber pad forming or press brake forming. Rubber pad and press brake forming are among the most widely used forming processes in the aircraft industry. The adhesive used in these experimental parts is the same as the one used in this current study (AF163-2k). The ratio of the larger to the smaller thickness in these parts is in the range of 1 to 2. The pilot study showed that though adhesive bonding is a promising candidate for production of TMBs in the aircraft industry, more information regarding the forming behavior of bonded TMBs is needed before practical application can be realized. The forming behavior, strain distribution, forming limits, and springback behavior of the blanks are not known yet, in particular for those issue close to the transition line. In addition to the above-mentioned issues, which adhesive TMBs have in common with monolithic sheets, there are some forming issues that are specific to adhesively bonded TMBs. Among these issues, the additional failure mode related to the adhesive, i.e. delamination, is of particular importance, because it sets another limit on the formability of bonded TMBs.

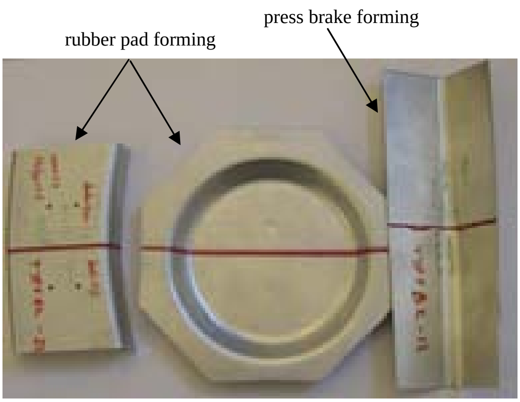

Figure 4.1. Samples of the adhesively bonded tailor-made blanks.

In this chapter, a combined experimental and numerical study of the mechanical behavior of adhesively bonded TMBs is presented. Some special tensile test specimens are designed to study the mechanical behavior of TMBs, determine the forming limits (in tension) for these TMB, and understand the (failure) behavior. The specimens can be categorized as either longitudinal or transverse. In the longitudinal samples, the loading direction is in parallel with the transition line whereas in the transverse samples, the loading direction is perpendicular to the transition line. A numerical study is also conducted to understand the physical mechanism behind the observed mechanical behavior of the specimens during tensile testing.

4.1. Experimental methods

The global geometry and dimensions of the tensile test specimens are shown in Figure 4.2a. The specimens can be categorized as either longitudinal or transverse. While in the longitudinal specimens, the loading direction is in parallel with the transition line (see Figure 4.2b), in the transverse specimen, the loading is perpendicular to the transition line (see Figure 4.2c). There are also some symmetric specimens which are made by bonding two transverse specimens with the back side to each other (see Figure 4.2d). The longitudinal and transverse specimens are used to study the in-plane straining limits of bonded TMBs when straining is in parallel with or perpendicular to the transition line, respectively. The symmetric specimens are a version of the transverse specimens in which the asymmetry with respect to the neutral line is eliminated.

Most of the forming processes used in the aircraft industry, including rubber pad forming and press brake forming combine stretching and bending. Depending on whether the major strain is perpendicular to or in parallel with the transition line, the stretching part of the deformation is similar to the deformation taking place in the tensile testing of the transverse or longitudinal specimens, respectively.

Both the base sheet and the upper sheet bonded on top of the base sheet were 2024-T3. The commercial adhesive AF163-2K from 3M was used to bond the upper sheet to the base sheet. The nominal thickness of the adhesive layer for all the specimens was 0.2 mm. In order to make the symmetric specimens out of the transverse specimens, a different cold-cured adhesive (EPX DP190 from 3M) was used so that any possible delamination of the two transverse specimens constituting the symmetric specimen does not happen at the same time as the expected delamination of the upper sheet from the base sheet and these two delamination mechanisms are distinguishable. In addition, the capability of the FEM model in distinguishing between these two failures could be examined. The surfaces of the sheets were carefully prepared prior to the application of the adhesive. The surface preparation procedure included cleaning (Alkali soap P3RST (Henkel), $\tau = 30$ min, $T = 60 - 80$ ^oC), pickling (CrO_3 + H_2SO_4 + demineralized H_2O, $\tau = 20$ min, $T = 60 - 65$ ^oC), anodizing (CrO_3 + demineralized H_2O, $\tau = 40$ min, $T = 38 - 42$ ^oC), and application of the primer (BR127 from Cytec). The degreasing, pickling, and anodizing processes were concluded by thorough rinsing of the surfaces. After drying and application of primer, the sheets were bonded, sealed in a vacuum bag, and cured in an autoclave. The heating rate of 2^o C/min was used to bring the temperature of the autoclave to 120^o C at which temperature the adhesive was cured for 90 min. The autoclave was subsequently cooled down with a cooling rate of 3^o C/min. The pressure of the autoclave was rapidly increased to 3 bar (= 0.3 MPa) and maintained for the whole curing cycle.

The thickness ratio of the specimens is defined as the ratio of the sum of the upper sheet and base sheet thicknesses to the base sheet thickness (the thickness of the adhesive is ignored). The thickness of the base sheet was 2 mm for all the specimens. Four different thicknesses of the upper sheet varying between 0.5 mm and 2.5 mm, as specified in Table 4.1, were used. Therefore, the thickness ratio varied between 1.25 and 2.25. For each set of the specimens (identified as one row in Table 4.1), six different samples were tested.

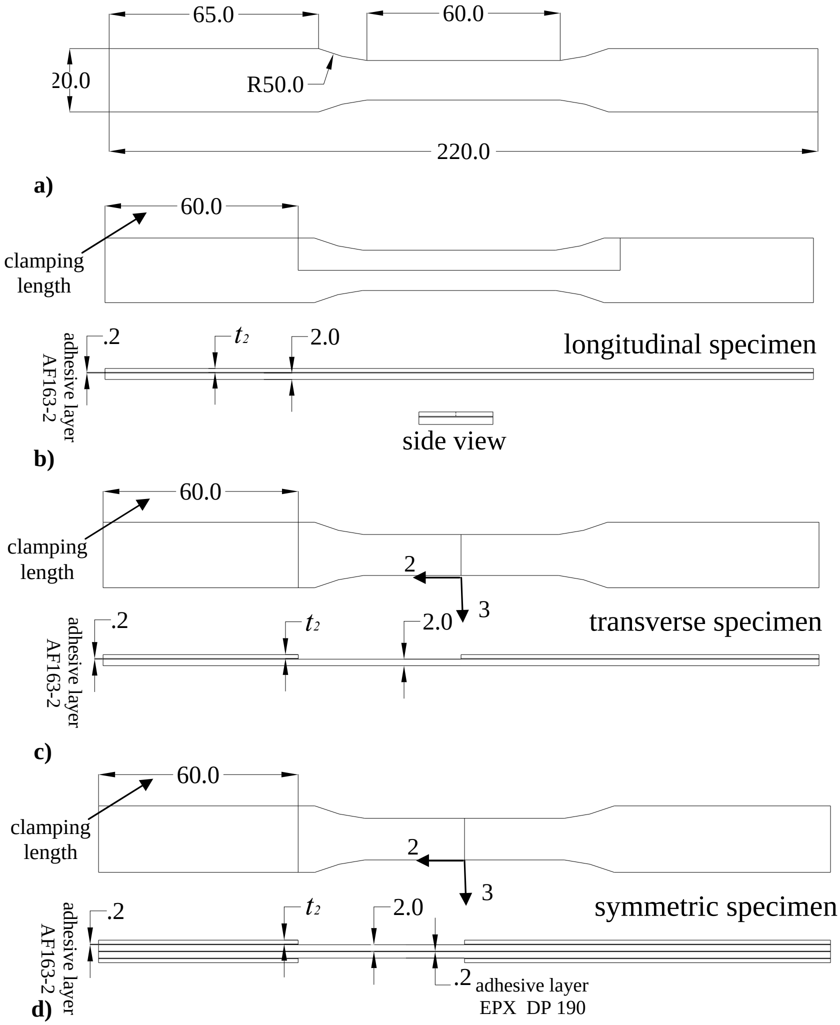

Figure 4.2. Schematic drawings of the dog-bone shape geometry (a), longitudinal specimens (b), transverse specimens (c), and symmetric specimens (d).

A brittle white-color coating was applied to the edge of the specimens so that the onset of delamination could be easily captured. During the tensile testing, a digital camera with special high-magnifying lens was used to capture the image of the area suspect to delamination. The timing of the camera was correlated with the timing of the static test machine meaning that the results could be traced back and the relation between the images and force/displacement values was established accordingly. A Zwick/Roell static test machine equipped with extensometer was used to perform the tensile tests at a constant deformation rate of 5 mm/min. The base metals were characterized with dedicated tensile testing. The results of the tensile tests were analyzed to determine the strain hardening and strength coefficients of the alloy. Six tensile test specimens were used to characterize the material (2024-T3) and to calculate the plasticity parameters. The material properties of 2024-T3 along with the parameters of the Hollomon's strain hardening law ($\sigma = K\varepsilon^n$) are listed in Table 4.2. The results were used as input for the numerical study to make sure that the actual material parameters are used for the simulation of the tensile tests.

Table 4.1. The test matrix for the tensile testing.

no.	$t_1 + t_2$ (mm)	t_1 (mm)	r	geometry
1	2+0.5	2	1.25	transverse
2	2+1.2	2	1.6	transverse
3	2+2	2	2	transverse
4	2+2.5	2	2.25	transverse
5	2+0.5	2	1.25	symmetric
6	2+1.2	2	1.6	symmetric
7	2+2	2	2	symmetric
8	2+2.5	2	2.25	symmetric
9	2+0.5	2	1.25	longitudinal
10	2+1.2	2	1.6	longitudinal
11	2+2	2	2	longitudinal
12	2+2.5	2	2.25	longitudinal

Table 4.2. The mechanical properties of 2024-T3.

material	E (GPa)	υ	σ_{y_0} (MPa)	K (MPa)	n
2024-T3	70	0.33	343	775.3	0.1787

4.2. Experimental results

The results of the tensile tests showed that for the transverse specimens, delamination occurs before metal failure regardless of the thickness ratio. The same phenomenon was observed for the symmetric specimens. However, no delamination was observed during the tensile testing of the longitudinal specimens. For all the transverse specimens, both transverse and symmetric, the delamination always started at the transition line where the thickness suddenly changed. The damage started as a crack at the thickness-step that later on propagated in loading direction such that the upper sheet separated from the base sheet. In the case of the symmetric specimens, the adhesive which bonded the two transverse specimens of the symmetric specimen failed before the delamination of the upper sheet at the thickness step. Figure 4.3 gives stroboscopic views of the delaminations of the transverse and symmetric specimens. The time of each sub-figure is given beneath it. The start of the delamination was defined as the point where the crack appeared at the thickness-step. The tensile forces at the start of the delamination were recorded. The recorded force values at the start of the delamination vs. thickness ratio for the symmetric and non-symmetric specimens will be compared with the numerical results.

Nominal yield stress (0.2% offset) and nominal ultimate strength of the samples are shown in Figure 4.4a and b, respectively. The nominal strains at the maximum forces are shown in Figure 4.4c. It should be noted that these values are nominal values as the stress and strain are non-uniformly distributed within the specimens and it is not possible to use one single stress or strain value as actual representative of the whole specimen. In the case of the longitudinal samples, the cross section area was constant throughout the gauge length. In contrast, the cross section area of the transverse and symmetric specimens varied along the gauge length. In those cases, the cross section area of the base sheet was used for calculation of the stresses. Note that the given nominal strain values at the maximum force is composed of two components. The first component is the strain up to the point where delamination occurs and the second component is the nominal strain taken place between delamination and sheet failure. The failure/limit strain of the TMB is the strain at the end of the first section and the remaining strain is sustained by the base sheet only. As is clear from Figure 4.4, neither the thickness ratio nor the loading direction has a significant impact on the nominal yield and ultimate strengths of the adhesively bonded TMBs. However, the nominal strain at the maximum load for the longitudinal specimens with thickness ratios up to 2 is slightly lower than that of the corresponding transverse specimens. This is due to the fact that the formability of the sheets with smaller thicknesses is less than the sheets with larger thicknesses [5]. The sheets with smaller thicknesses undergo more cold-rolling strain in order to be brought to the desired thickness and, thus, have less room for further deformation (see Chapter 9).

4.3. Numerical methods

The tensile tests were modeled by using a finite element model. The geometries and dimensions depicted in Figure 4.2 were implemented in the finite elements model. The von Mises yield function along with the Hollomon's strain hardening law ($\sigma = K\varepsilon^n$) was adopted to describe the plastic behavior of the aluminum sheets. The adhesive layer was modeled by using the cohesive interface elements. The formulation of the cohesive interface elements is described elsewhere [6]. We only discuss the constitutive equations used for modeling the mechanical behavior of the adhesives. The commonly used index notation is adopted throughout this chapter. The summation convention applies unless otherwise mentioned.

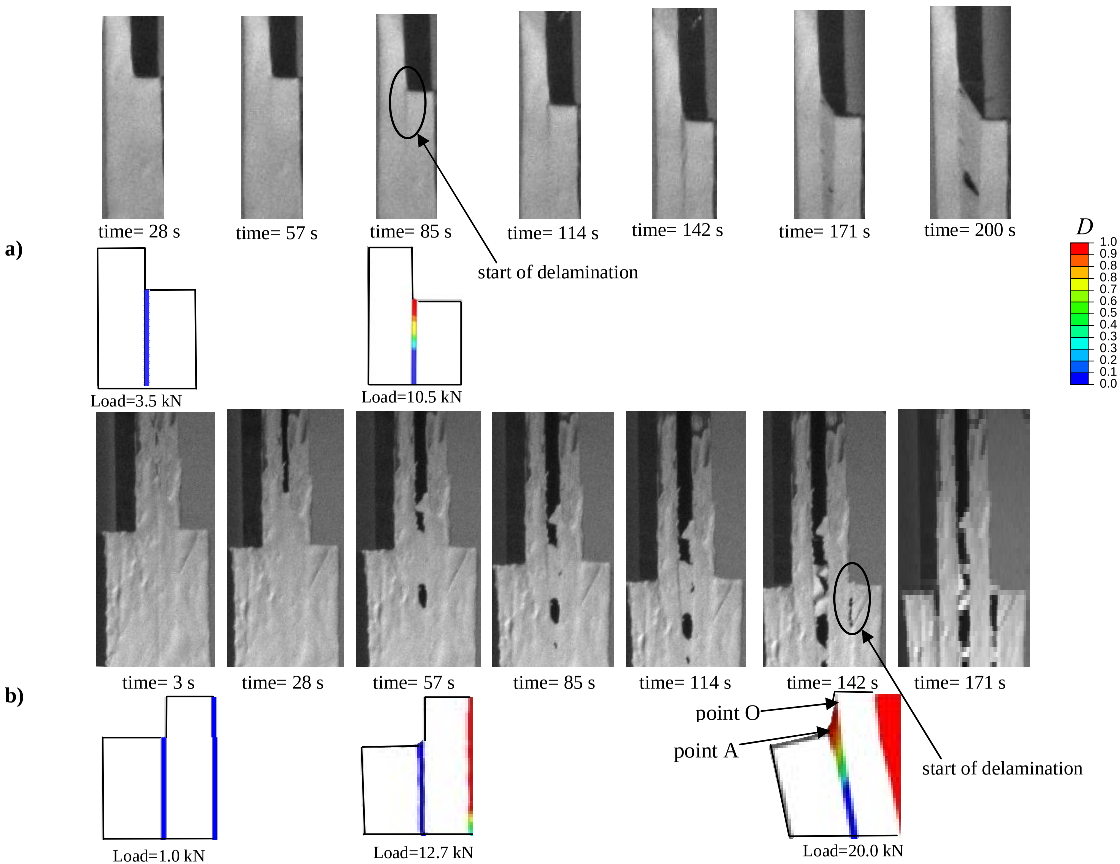

Figure 4.3. Stroboscopic pictures of the delamination behavior in the transverse (a) and symmetric specimens (b). The capturing time are given beneath the images. Numerically calculated values of the scalar damage variable are represented for some selected load steps.

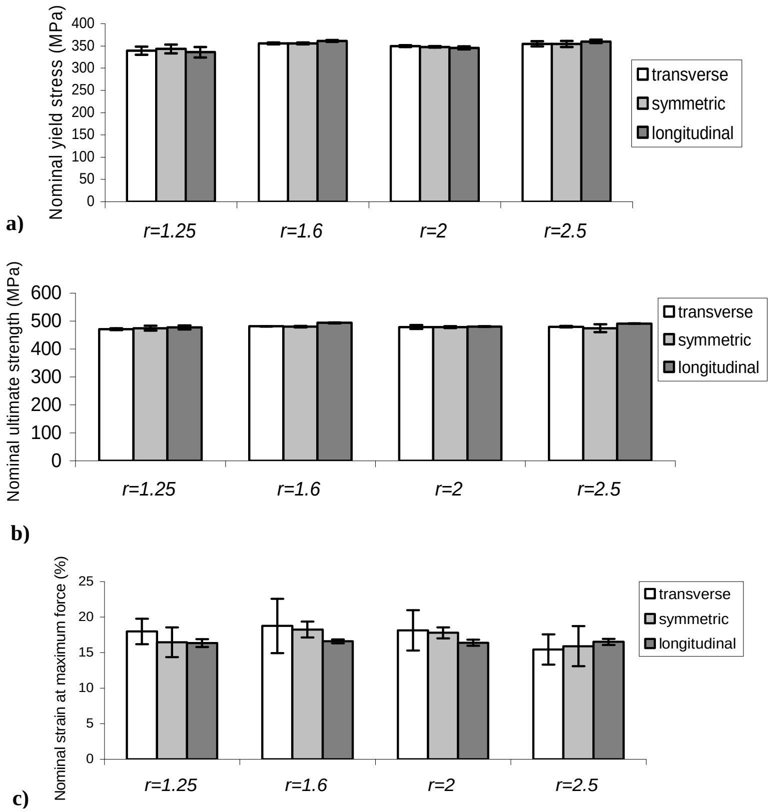

Figure 4.4. The nominal yield stress (a), nominal ultimate strength (b), and nominal strain at the maximum force (c) of the tensile test specimens.

Numerical delamination analysis can be carried out by using different techniques including the ones based on the Linear Fracture Mechanics approach [7] and virtual crack closure technique (VCCT) [8]. However, these approaches tend to be less efficient than a recently revived approach called cohesive interface technique [9]. The advantages of the cohesive interface technique over the VCCT for delamination analysis are discussed in reference [10]. The cohesive interface technique is a phenomenological approach for delamination analysis of adhesives which assumes that the fracture is a local process in the so-called cohesive zone. No preexisting crack is needed for the analysis of fracture behavior. The damage initiation and evolution phases are commonly combined together in one single bi-linear traction-separation law which relates traction (stress) to mode 1 and mode 2 nodal displacements (separations). The results are shown to be relatively insensitive to the exact shape of the traction-separation law provided that the correct interfacial strength and fracture energy values are used [9, 10]. For a review of the cohesive zone elements see [9]. The traction-separation elements are normally used only when the thickness of the adhesive is negligibly small as is the case in the current study (adhesive thickness= 0.2 mm). The adhesive layer is modeled by a series of interface elements which are tied to the adherends (from both sides). Only one element through the adhesive thickness should be used [11].

The bilinear traction-separation law assumes that the adhesive is linear-elastic up to the onset of damage. The elasticity equation of the cohesive interface material can be stated as follows

$$\hat{t}_i = K_{ij}\hat{\varepsilon}_j \ (i,j = 1,2,3) \tag{1}$$

where K_{ij} are the entries of the elasticity tensor and $\hat{t}_k$ is the traction in direction k. Separation strain in direction j, ε_j, is defined as

$$\forall j \in \{1,2,3\}, \hat{\varepsilon}_j = \frac{\delta_j}{T_0} \tag{2}$$

where T_0 and δ_j are respectively the adhesive thickness and separation in direction j.

Once the damage has commenced, the stiffness of the adhesive starts to degrade according to a specified damage evolution law. It is widely accepted that the quadratic stress criterion can properly predict the onset of damage [12]. The quadratic stress parameter, χ, can be expressed in terms of the tractions and ultimate strengths, $\sigma_{u,i}$, as

$$\chi = \left\{\frac{\langle \hat{t}_1 \rangle}{\sigma_{u,1}}\right\}^2 + \left\{\frac{\hat{t}_i}{\sigma_{u,i}}\right\}^2, i \in \{2,3\} \tag{3}$$

The Macaulay bracket used in Equation (3) means that the contribution of the mode 1 traction to the value of the quadratic stress parameter is nonzero only if the mode 1 traction is positive. The damage is assumed to start when χ reaches unity. Once the damage is started, the stiffness of the adhesive starts to decrease. The stress components of the damaged adhesive are influenced by the damage evolution as follows

$$\forall i \in \{1,2,3\}, \overline{\hat{t}_i} = (1-D)\hat{t}_i + D\varepsilon_{i23}H(-\hat{t}_i)\hat{t}_i \tag{4}$$

where D is the scalar damage variable, H is the Heaviside step function, and ε_{i23} is the Levi-Civita symbol. The scalar damage variable is 0 at the onset of damage and takes the maximum value, $D_{\max}$, (normally 1) at failure.

Figure 4.5 gives a schematic overview of the damage initiation and evolution processes. As previously pointed out, the behavior of the adhesive is assumed linear-elastic up to the point where the damage initiates. Equation (3) postulates that the damage initiates once the quadratic stress parameter exceeds unity. The damage initiation point is corresponding to the maximum traction value and is presented in Figure 4.5 at the common top of the two right triangles. After the damage is initiated, the stiffness of the adhesive is assumed to decrease as the separation increases. The decrease of the stiffness continues up to the point where the stiffness equals zero and the delamination is assumed to have occurred. The area of the triangle (in Figure 4.5) equals the fracture energy of the adhesive. As is clear from Figure 4.5, two components are necessary to fully describe the damage evolution phase of the adhesive. The first component is the energy released during the fracture process and the second component is ‘how the scalar damage variable evolves from

0 to $D_{\max}$'. The first component is a material property of the adhesive, which in the case of mixed-mode loading, is defined as a function of the single mode fracture energies. In the case of mixed-mode loading, the effective separation, δ_m, is used to describe the damage evolution. The effective separation is defined in terms of the separations in directions 1 to 3 as follows [6]

$$\delta_m = \left\{ \langle \delta_1 \rangle^2 + \delta_i^{\,2} \right\}^{\frac{1}{2}}, i = 2,3 \tag{5}$$

The second component of the damage evolution is how the scalar damage variable evolves from 0 to 1 and is based on the linear damage evolution assumption. According to this assumption, the scalar damage variable can be expressed as [6]

$$D = \frac{\delta_m{}^f \left(\delta_m{}^{\max} - \delta_m{}^0 \right)}{\delta_m{}^{\max} \left(\delta_m{}^f - \delta_m{}^0 \right)} \tag{6}$$

where $\delta_m{}^0$ and $\delta_m{}^{\max}$ are respectively the effective separation at the onset of damage and at the maximum effective separation. The failure effective displacement, $\delta_m{}^f$, can be calculated from the mixed-mode fracture energy, G_C, according to the following relation

$$\delta_m{}^f = \frac{2G_C}{\sigma_{u,m}} \tag{7}$$

where the effective traction at the damage initiation, $\sigma_{u,m}$, is given by

$$\sigma_{u,m} = \left\{ \langle \sigma_{u,1} \rangle^2 + \sigma_{u,i}{}^2 \right\}^{\frac{1}{2}}, i = 2,3 \tag{8}$$

The Benzeggagh-Kenane (BK) criterion assumes that the mixed-mode fracture energy, G_C, is a function of the single-mode fracture energies, G_{iC}, total energy release rate, G_T, and mode-mix ratio, G_{shear} / G_T, and is given by the following relationship [13]

$$G_{1C} + (G_{2C} - G_{1C}) \left(\frac{G_{\text{shear}}}{G_T} \right)^{\eta} = G_C \tag{9}$$

where

$$G_T = G_i, i = 1,\ldots,3 \quad \text{and} \quad G_{\text{shear}} = G_j, j = 2,3 \tag{10}$$

and η is a material parameter of the adhesive. The BK criterion is shown to be well fitting epoxy adhesives such as AF163-2K [14]. The mechanical properties of the adhesives are extracted from the manufacturer's datasheets and literature [15-17] and are listed in Table 4.3. The power, η, is a fitting parameter and was determined by minimizing the difference between the experimental and corresponding numerical results. However, the effect of this parameter on the predicted delamination loads was found to be minimal.

The models were simulated by using an implicit solver (ABAQUS/Standard). Boundary conditions were set such that the model resembled the actual test conditions. All the translational degrees of freedom were constrained at one side of the specimens (clamping side) to approximate the clamping mechanism in the tensile test machine. At the other side (moving side) of the specimens, the translational degree of freedom which was in the same direction as the tensile load was free and the other degrees of freedom were constrained. The tensile load was applied at the moving side. The geometries of the aluminum sheets were discretized by using the three-dimensional continuum elements with three translational degrees-of-freedom and linear hexahedron geometry. The reduced integration scheme with hourglass control was applied.

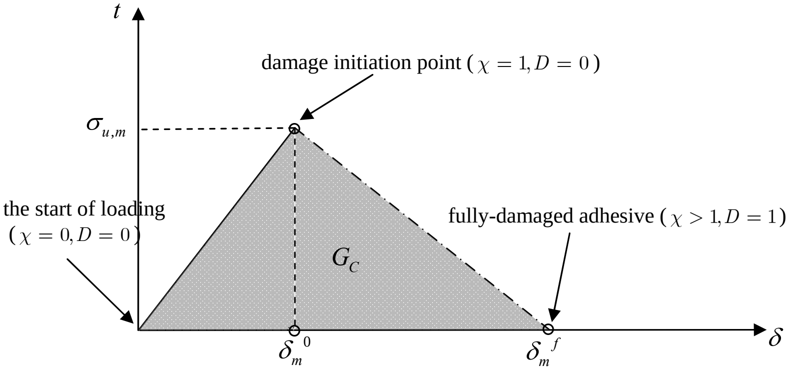

Figure 4.5. Schematic representation of the constitutive behavior, damage initiation, and damage evolution of the adhesive.

Table 4.3. The mechanical properties of the adhesives.

material	E (GPa)	G (GPa)	σ_{u1} (MPa)	σ_{u2} (MPa)	G_{1c} (J/m^2)	G_{2c} (J/m^2)	η
AF163-2K	1.1	0.4	48	48	4370	2248	0.12
EPX DP190	0.35	0.12	4.14	4.14	500	--	0.12

4.4. Numerical results and discussions

The numerical results are presented, discussed, and compared with the experimental results in the five following subsections. The first subsection reports the findings of the mesh-independency analysis. The second, third, and fourth subsections report the results of the numerical study and comparison with the experimental study for transverse, symmetric, and longitudinal specimens. The final subsection of this chapter concludes by presenting the design implications which result from this study. Unless otherwise stated, two following conventions apply to the results presented in the following subsections:

1. The presented quadratic stress function, scalar damage variable, and displacement ratio values relate to the element which failed first.
2. The lateral deflection values which are presented relate to the element which has the maximum lateral deflection in each load step. Therefore, not all the plotted deflection values are related to the same element.

A mesh independency analysis was conducted for each FEM model to ensure that the numerical results not affected by the applied mesh. Two samples of the mesh dependency analyses are presented here. In the first sample (Figure 4.6), the dependency of the predicted damage initiation and delamination loads on the applied mesh is investigated for a transverse specimen (series no. 1). In the second sample (Figure 4.7), the dependency of the force-displacement curve and lateral deflection on the applied mesh is studied for a longitudinal specimen (series no. 10). The quadratic stress function vs. applied tensile load is plotted in Figure 4.6a. This figure shows that for elements sizes less than 0.4 mm the calculated values of the function are very close to each other. Similarly, the scalar damage variable values shown in Figure 4.6b are very close to each other for element sizes less than 0.4 mm. The approximate size of the cohesive interface elements used in all of the forthcoming delamination analyses was fixed at 0.1 mm to guarantee full convergence (convergence tolerance=0.5%). One noteworthy point in Figure 4.6 is that the loads at the onset of damage and delamination are underestimated when a very coarse mesh is used. However, for moderately coarse and fine meshes, the onsets of damage and delamination loads are quite independent from the applied mesh.

Figure 4.7a shows that the force-displacement curve can be accurately determined even when a coarse mesh is used. However, capturing the bending behavior of the longitudinal samples (see Figure 4.7b) needs a relatively finer mesh. This is because a larger number of through-thickness continuum elements are needed to accurately simulate the bending behavior [18].

Figure 4.7b shows the maximum deflection among the elements of the model for several load steps. The figure must be considered as showing a collection of data points rather than presenting interpolated curves; because, as previously mentioned, the elements are not necessarily the same for all load steps. The location of the elements was checked to ensure that, for each individual load step, the location of the elements for which the results are presented is the same regardless of applied mesh.

In the forthcoming simulations of the longitudinal specimens, the approximate element size is fixed at 0.5 mm for which the results were fully converged (convergence tolerance=0.5%). The optimized meshes of the different types of specimens, which are used in the forthcoming FEM analyses, are presented in Figure 4.8.

Transverse specimens. Figure 4.9 depicts the numerically predicted values of the tensile load at the onset of damage, numerically predicted values of the delamination load, and the experimental values of the delamination load vs. the thickness of the upper sheet. The displacement ratio, ξ , is defined as the ratio of the mode 1 separation, δ_1 , to the mode 2 separation, δ_2 ,

$$\xi = \frac{\delta_1}{\delta_2} \tag{11}$$

The coordinate systems used for calculation of the displacement ratio are shown in Figure 4.2. Figure 4.10 shows the numerically calculated values of the displacement ratio vs. the applied tensile load for different thickness ratios.

As is clear from Figure 4.9, the load at the onset of damage drastically decreases as the thickness ratio increases. The experimentally-determined delamination load also decreases as the thickness ratio increases. The numerically-calculated delamination load first decreases as the thickness of the upper sheet increases from 0.5 mm to 1.2 mm but then remains almost constant for larger thickness ratios. The decrease in the delamination loads is much less than in the damage initiation loads. This trend is discussed later in this section by the help of calculated displacement ratio values. The experimental and numerical values of the delamination load show a good agreement.

a)

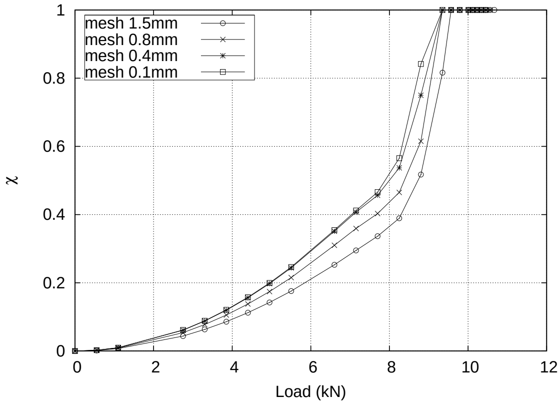

b)

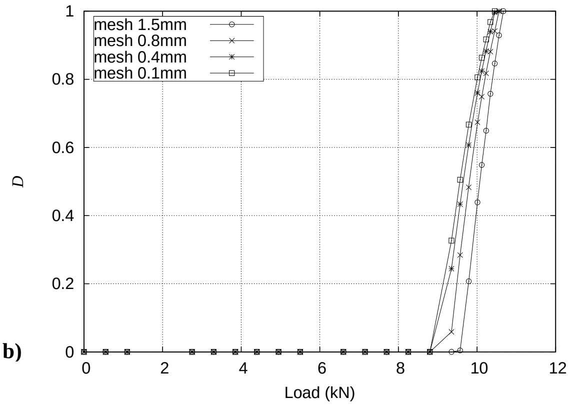

Figure 4.6. Analysis of the dependency of the quadratic stress function (a) and scalar damage (b) values from the size of the elements ($t_2 = 0.5$ mm).

The damage starts earlier in the specimens with the larger thickness ratios because the load carried by the upper sheet is larger for larger thickness ratios and, thus, the adhesive has to transfer a larger shear and tensile load to the base sheet at the transition line. In addition, a larger upper sheet thickness means higher out-of-plane bending, hence earlier adhesive damage. Therefore, the damage initiates much earlier for the specimens with larger thickness ratios.

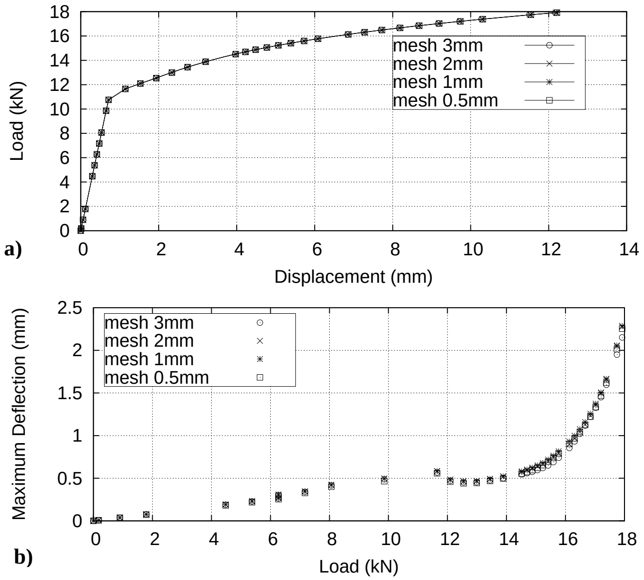

Figure 4.7. Analysis of the independency of the force-displacement curve (a) and lateral deflection (b) from the size of the elements for one sample longitudinal specimen ($t_2 = 1.2\,\mathrm{mm}$).

Figure 4.10 depicts the displacement ratio vs. tensile load. One can see that the absolute value of the displacement ratio is always small meaning that mode 2 is the dominant mode. Moreover, there is a disparity between the first part of the graphs where the displacement ratio is almost independent from the thickness ratio and the second part of the graphs where the specimens with larger thickness ratios exhibit larger displacement ratios. As the tensile load increases, the displacement ratio rapidly decreases to about -0.1 and is almost the same for the specimens with different thickness ratios. The displacement ratio remains constant up to the end of the first part of the loading curve, i.e. up to about 5 kN. In the second part of the loading curve, the displacement ratio values increases and becomes positive. Consider the right-handed coordinate systems shown in Figure 4.2c and points O and A annotated in the FEM results depicted in Figure 4.3b (tensile load=20.0 kN). The origin of the coordinate system is fixed at point O. The cohesive element placed between points A and O is the one which fails first. Before the start of the loading, the distance between points O and A is equal to the initial thickness of the adhesive. As the tensile load increases, point A displaces both along direction 1 and direction

2. The displacement along direction 2 is always negative. The displacement along direction 1 could be negative or positive depending if the adhesive is experiencing mode 1 compression or separation. The displacement ratio of point A is positive, if its displacement along direction 1 is also negative and the element is experiencing compression. The displacement ratio is negative if the displacement of point A along direction 1 is positive and the element is experiencing separation. Therefore, the positive values of the mode-mix ratio mean that the element experiences mode 1 compression and mode 2 separation during the second part of the loading curve. For loads substantially smaller than the damage initiation load, the contribution of mode 1 to the delamination is almost the same regardless of the thickness ratio. After the onset of damage, the contribution of mode 1 decreases and becomes much less. The decreasing trend is much faster for the specimens with larger thickness ratios. As a result, the difference between the damage initiation and delamination loads increases as the thickness ratio increases (see Figure 4.9). This indicates that as the thickness ratio increases, the damage initiation load should decrease much faster than the delamination load.

In the second part of the curves, the displacement ratio is larger for the specimens with larger thickness ratios. The compressive behavior in the second part of the loading curve (mostly between the yield point and delamination) was found to be due to the fact that the stress and strain components are much higher in the base sheet compared to the upper sheet and, thus, the base sheet tends to deflect (due to eccentricity) much more than the upper sheet. If the upper sheet is small in thickness, its overall stiffness is small and the lateral deflection of the upper sheet is large. Therefore, the adhesive layer experiences a smaller amount of compression. However, for very stiff upper sheets, as in the case of the specimens with large thickness ratios, the upper sheet is too stiff to deflect and the lateral deflection of the base sheet has to be compensated for by compression on the adhesive. This results in higher mode 1 compression of the adhesive in those specimens.

There is a bending behavior in the transverse specimens. This bending behavior is due to two reasons: out-of-axis loading and load transfer. The neutral axis is displaced due to the presence of the upper sheet. Consequently, the axis of application of the tensile load is not coincident with the neutral axis and out-of-plane bending takes place. In addition to this effect, there is an edge effect at the transition line from one thickness to the other. Since the load carried by the upper sheet has to be transferred to the base sheet at the transition line, the upper layer imposes a load to the base sheet through the adhesive. The load is composed of two components: the first component is aligned along the loading direction (direction 2 in Figure 4.2c) and is called the traction (shear) component. The second component is in thickness direction, which is normal to the plane of the specimen. The second component is called the lateral (peel) component and contributes to the bending of the specimen. The lateral deflections of the specimens are plotted in Figure 4.11. The figure shows that, in the first part of the loading curve, the lateral deflection is greater for the specimens with larger thicknesses. This is because a larger upper sheet thickness results in a greater load transfer and out-of-plane bending and, thus, a greater lateral deflection. In the last phase of the loading curves, the specimens with larger thicknesses are left behind by the specimens with smaller thicknesses.

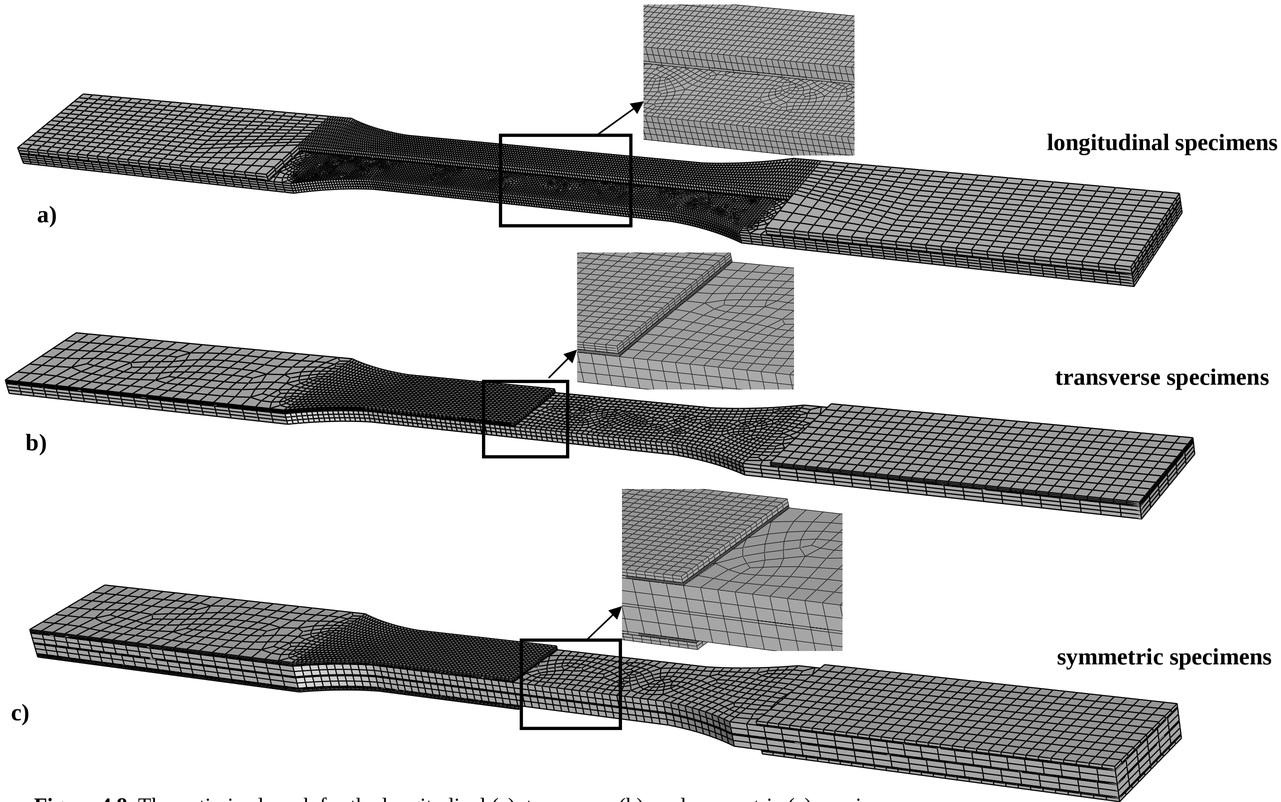

Figure 4.8. The optimized mesh for the longitudinal (a), transverse (b), and symmetric (c) specimens.

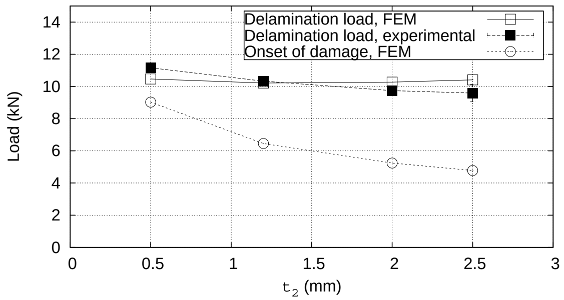

Figure 4.9. The experimental and numerical tensile loads at the delamination, and numerical value of the tensile load at the onset of damage for the transverse specimens.

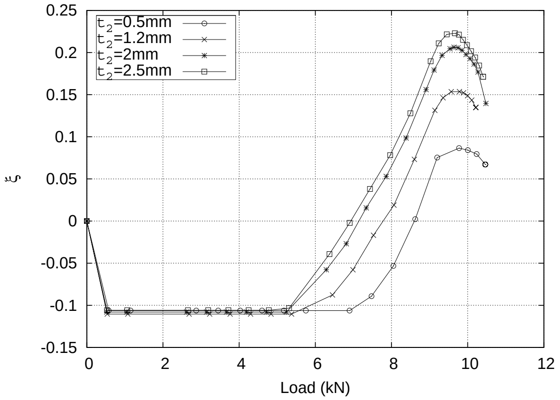

Figure 4.10. The numerically calculated displacement ratio vs. applied tensile load for the transverse specimens with different thickness ratios.

Similar to the trend seen in the study of the displacement ratio, this behavior has to do with the higher stiffness of the specimens with larger thickness ratios. At the final phase of the loading, the base sheet undergoes much more strain than the upper sheet meaning that while the base sheet is in the plastic range, the upper sheet is still in the elastic range. Therefore, the base sheet has the tendency to deflect more than the upper sheet. If the upper sheet is not stiff enough, the base sheet overcomes the resistance by the upper sheet and the lateral displacement values are higher. In the case of very stiff upper sheets, the deflection of the base sheet is constrained by the upper sheet and the specimens with larger thickness ratio are at one point left behind by the specimens with smaller thickness ratios.

One important result of the adhesively bonded tailor-made blanks is the plastic strain that specimens can undergo before delamination. The plastic strains of the base sheet at the onset of damage and at the delamination are shown in Figure 4.12. There are two remarkable points in this figure: first, the plastic strain at both delamination and onset of damage are small which means that adhesively bonded TMBs can not be strained much perpendicular to the transition line. For sufficiently large thickness ratios, the damage initiates even before the base sheet enters the plastic range meaning that no plastic straining of the sheet is possible without adhesive damage. Second, it is clear that the plastic strains at both onset of damage and delamination decrease as the thickness ratio increases. In practice, it is not sufficient to stay away from delamination load but care should be taken to stay away from the damage initiation load during the forming process. That is because the formed product will be used in load-carrying structural parts and a part with a damaged adhesive is not reliable for such an application. However, it should be noted that the calculated damage initiation load is based on the bilinear model. Real adhesives show (significant) plastic behavior, which is not necessarily detrimental. Taking the damage initiation load as the maximum allowable load may therefore be a conservative choice.

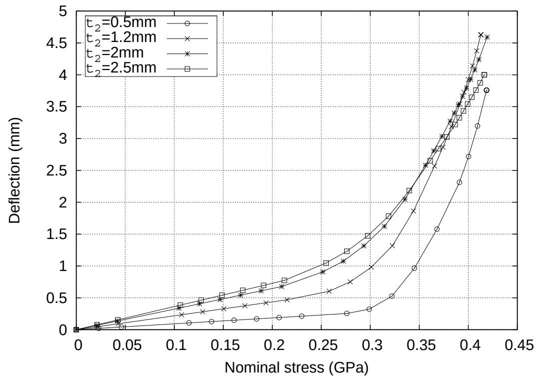

Figure 4.11. The lateral deflection vs. stress of the base sheet for the transverse specimens with different thickness ratios.

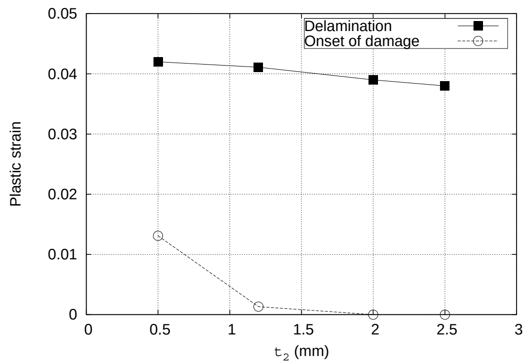

Figure 4.12. The numerical plastic strain of the base sheet of the transverse specimens at the onset of damage and at the delamination.

Symmetric specimens. The numerically-calculated loads at the onset of damage and at the delamination along with the experimentally-obtained delamination loads are shown in Figure 4.13. Similar to the transverse specimens, the load at the onset of damage decreases as the thickness ratio increases. The experimentally-determined delamination loads also decrease as the thickness ratio increases. The numerically-calculated delamination load first decreases as the thickness of the upper sheet increase from 0.5 mm to 1.2 mm and is almost constant as the thickness of the upper sheet increase from 1.2 mm to 2 mm and then again slightly decreases as the thickness of the upper sheet increases to 2.5 mm. Comparing Figure 4.13 and Figure 4.9, one can see that the delamination loads of the symmetric specimens are about twice (or slightly less than twice) of those of the transverse specimens. Similar to the transverse specimens, both the experimental and numerical results show that increasing the thickness of the upper sheet reduces the delamination loads to a less extent compared with the damage initiation loads. The mechanism causing this trend is similar to the mechanism observed for the transverse specimens and is described later using the calculated values of the displacement ratio.

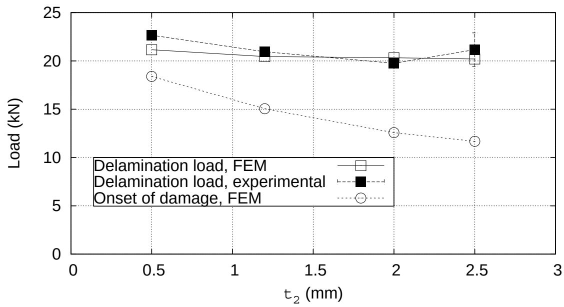

Figure 4.13. The experimental and numerical tensile loads at the delamination, and numerical value of the tensile load at the onset of damage for the symmetric specimens.

The simulation results of the symmetric specimens showed that the adhesive layer connecting the two base sheets is fully damaged before the delamination of the upper sheet. Just after failure of the connecting adhesive, the two base sheets behave somewhat similar to two separate transverse specimens and start to bend. However, the observed out of plane bending is to some extent different from the transverse specimens because the two separated parts influence the deformation of each other even if delaminated locally. This behavior can be seen in the numerical results presented in Figure 4.3b (time= 85 s, load=12.7 kN). As is clear from this figure, the connecting adhesive is fully damaged (D =1) and two base sheets are separated. This is in agreement with the experimental observations. A noteworthy point is that after destruction of the connecting adhesive and as the bonded transverse specimens start to separate, the load axis start to deviate from the neutral axis and the symmetric specimens can no longer be considered free from the out-of-plane bending.

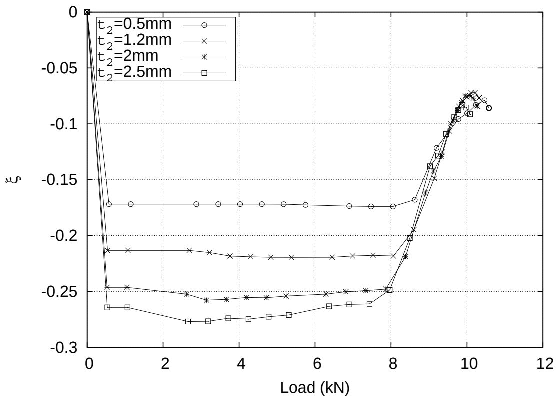

Figure 4.14. The numerically calculated displacement ratio vs. applied tensile load for the symmetric specimens with different thickness ratios

Figure 4.14 shows the displacement ratio vs. applied load for different thickness ratios. The absolute values of the displacement ratio are higher than in the case of the transverse specimens, meaning that the contribution of mode 1 to the delamination is higher for the symmetric specimens compared to the transverse specimens. That is because of the fact that in the symmetric specimens the base sheet remains unbent during the first phase of loading. The mode 1 separation of the upper sheet from the base sheet is therefore larger than in the case of the transverse specimens where the base sheet bends. The mode 1 separation of the upper sheet from the base sheet has to be withstood by the adhesive and the larger the separation is the more the adhesive is loaded in mode 1 and the greater the displacement ratio is. The curves showing the displacement ratio vs. tensile load can be divided into two parts. In the first part of the curves, i.e. up to about 8 kN (Figure 4.14), the base sheet is in the elastic range, displacement ratio is much dependent on the thickness ratio, and the contribution of mode 1 increases as the thickness ratio increases. That is because in the specimens with larger thickness ratios the load that has to be transferred from the upper sheet to the base sheet is greater. Therefore, the load transfer effect pronounces as the thickness ratio increases. However, in the second part of the curves, which begins from about 8kN tensile load and continues up to the end of the curves, the base sheet has entered the plastic range and the deflection is much more than in the elastic range (the connecting adhesive is also failed). Because of the different deflections of the upper and base sheets and in a way similar to the transverse specimens, the mode 1 separation declines. The effect of the bending in reducing the mode 1 separation is greater for the specimens with larger thickness ratio because the stiffness of the upper sheets is greater for those specimens. Since the specimens which have greatest loads to transfer also have the greatest influence of the bending, the displacement ratio of the specimens is similar in the second part of the curves. Therefore, the contribution of the mode 1 separation to delamination increases with the increment of the thickness ratio in the first part of the curves but is the same for all the specimens in the second part of the curves. The damage initiation takes place during the same time span as the first part of the displacement ratio curves takes place, meaning that the damage should initiate much earlier in the specimens with larger thickness ratio. The second part of the displacement ratio curves takes place in the same time span as the scalar damage variable evolves from 0 to 1. Because the contribution of the mode 1 separation is the same for all the specimens during this time span, the delamination loads are not much different between the specimens with different thickness ratios. Although the displacement ratios of the symmetric specimens increase in the second part of the curves, the final values are still negative meaning that the specimens are still in the mode 1 separation and not in compression as the transverse specimens are during the final part of their loading curves (compare Figure 4.10 and Figure 4.14). Since mode 1 compression, as implied by the Macaulay bracket in Equations 3, 6, and 10, does not contribute to delamination, the plastic strains of the transverse specimens at the onset of damage and at the delamination are greater than those of the symmetric specimens (Figure 4.15). Similar to the transverse specimens, the plastic strains at the onset of damage and at the delamination decrease as the thickness ratio increases.

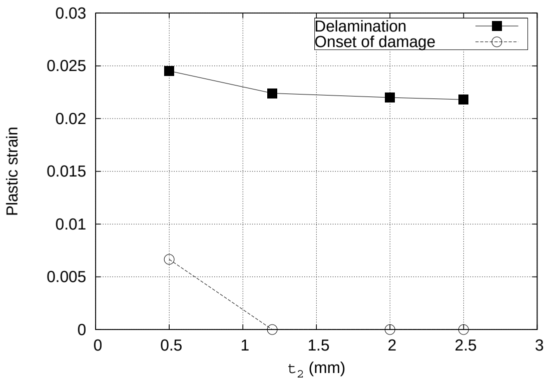

Figure 4.15. The numerical plastic strain of the base sheet of the symmetric specimens at the onset of damage and at the delamination.

The symmetric specimens enable examining the capability of the cohesive interface elements in capturing the two different delamination phases of the specimens. Both experimental (Figure 4.3b, time= 3 s) and numerical results (Figure 4.3b, load=1.0 kN) showed that there is no lateral deflection of the specimens up to the point where the connecting adhesive is destructed. When the connecting adhesive fails, the other adhesive is not failed yet. Figure 4.3b shows this behavior at time=57 s and 85 s. The numerically-calculated values of the scalar damage variable (D) are represented in Figure 4.3b as well. It is clear that while the connecting adhesive is calculated to have failed, the other adhesive is not yet reached the critical scalar damage variable value of 1 and is hence not failed. The connecting adhesive fails before the other adhesive because the fracture energy of the connecting adhesive is less than that of the adhesive used for making the thickness difference. Right after the failure of the adhesive, when the loading axis is still coincident with the neutral axis, the separate transverse specimens which constitute the symmetric specimens start to deflect laterally. In this case, the initiation of the bending behavior is due to the transfer of the tensile load from the upper sheet to the base sheet which imposes a bending force to the base sheet at the transition line.

Longitudinal specimens. The numerical stress-strain curve of a sample specimen ($t_2 = 1.2$ mm) is compared with the experimental results in Figure 4.16. The comparison between the numerical and experimental results shows that they are in good agreement which would be expected because this is, actually, the deformation of the aluminum alloy. For the longitudinal specimens, the adhesive had not been delaminated when the aluminum sheet failed. This was predicted by the FEM model. The simulations showed that, when the sheet fails, the maximum value of the quadratic stress function is close to zero throughout the gauge length. The maximum value of the quadratic stress function did not exhibit any significant dependency on the thickness ratio and remained negligible even for the largest thickness ratios.
Both experimental results discussed in the “experimental results” and numerical results presented above showed that there is no delamination in the gauge length of the longitudinal specimens. Furthermore, the force-displacement curves obtained from the experiments and numerical simulations agree with each other. Therefore, the model can both qualitatively and quantitatively predict the mechanical behavior of the longitudinal specimens except the cracking of the adhesive when the failure limit of the adhesive is exceeded (explained later in this section).

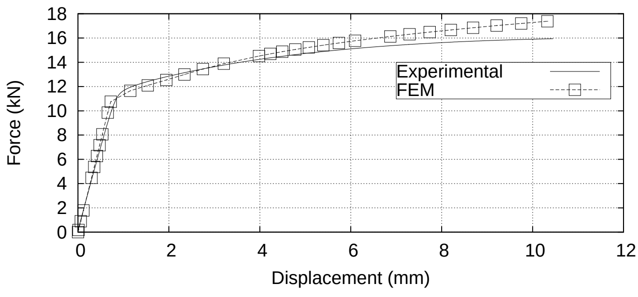

Figure 4.16. Comparison of the numerical and experimental force-displacement curves for a sample longitudinal specimen ($t_2 = 1.2$ mm).

In the longitudinal specimens, the out-of-axis bending is present but there is no load transfer from the upper sheet to the base sheet. Because of the displacement of the neutral axis, the longitudinal specimens experience out-of-plane bending. The lateral deflection of the specimens vs. tensile stress is depicted in Figure 4.17. A local peak is observed in the curves presented in this figure at around the yield point, i.e. 343 MPa. The appearance of this peak has to do with the fact that stress is non-uniformly distributed within the specimen and different parts of the specimen reach the yield point at different tensile loads. Therefore, some parts of the specimen enter the plastic range of the stress-strain curve earlier and tend to deform much more than the other parts of the specimen which are still in the elastic range. The difference between the deformations of the different areas of the specimen suppresses the increasing trend of the lateral deflection for some time until all the areas of the specimen are in the plastic range. Once all the areas are in the plastic range, the deflection starts to increase again.

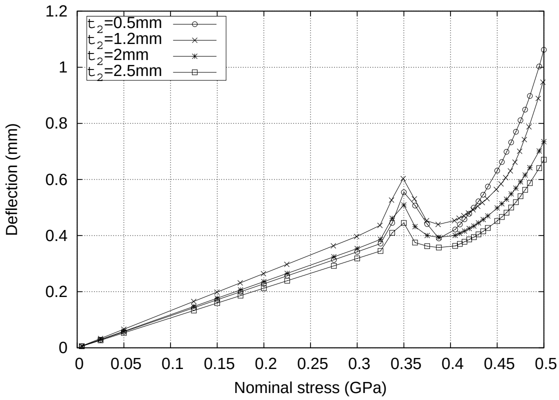

Figure 4.17. The lateral deflection of the longitude specimens vs. applied tensile stress for different thickness ratios.

The fact that there is no delamination of the adhesive regardless of the thickness ratio shows that the relative importance of the load transfer on the delamination behavior is much more than that of the bending behavior. The lateral deflection of the specimens in the final part of the loading curve shows a different trend from the transverse specimens. While for the transverse specimens, the lateral deflection increases as the thickness ratio increases, the lateral deflection of the longitudinal specimens is smaller for larger thickness ratios, particularly for the stresses above the yield stress. The out-of-plane bending of the longitudinal specimens is determined by the thickness of the upper layer. As the thickness of the upper layer increases, the magnitude of the out-of-plane bending moment increases. However, the thickness of the upper sheet also influences the moment of inertia of the cross section. The dependency of the moment of inertia on the thickness of the upper layer is cubic whilst the bending moment linearly relates to the thickness of the upper layer. As the thickness of the upper layer increases, the bending stiffness increases to a larger extent compared to the bending moment. Thus, the lateral deflection is less for the specimens with larger thickness ratios.

One important point to notice is that the ultimate strain of the AF163-2K adhesive is much less (3.4% [19] to 7.0% [16]) than that of the aluminum sheet, meaning that the adhesive fails along the gauge length, though this does not result in delamination, but it should be considered as adhesive failure. Therefore, straining in the directions parallel to the transition line is limited by the ultimate strain of the adhesive.

Design implications. The agreement of the experimental and numerical results in Figure 4.3, Figure 4.9, Figure 4.13, and Figure 4.16 proves that the FEM models with the cohesive interface elements can successfully predict the mechanical response and delamination behavior of adhesively bonded TMBs and can be used for the design of adhesively bonded TMBs.

Most applications of the adhesively bonded TMBs in the aircraft industry are anticipated to need thickness ratios between 1 and 2 with most applications concentrated in the thickness ratio range of 1 to 1.5. As discussed before, in-plane plastic straining of TMBs is limited by two different failure mechanisms depending on the direction of the major in-plane strain. If the major in-plane strain is perpendicular to the transition line, delamination takes place. In this case and for thickness ratios between 1 and 1.5, Figure 4.12 implies that the adherends can undergo between 0.5% (for t_2=1 mm) and 1.4% (for t_2=0.5 mm) plastic strain without damaging the adhesive. If the major in-plane strain is parallel with the transition line, the maximum plastic strain is independent from the thickness ratio and is dictated by the ductility of the adhesive. In the case of AF163-2K, the maximum ultimate strain is between 3.4% [19] and 7.0% [16]. Therefore, the maximum plastic strain that the adherends can undergo without damaging the adhesive is in this range regardless of the thickness ratio. For any other direction of the major in-plane strain with respect to the transition line, the maximum plastic straining is somewhere between these two extreme cases. One can therefore conclude that even in the most favorable case, the maximum in-plane plastic straining which can be achieved without damaging the adhesive is quite limited. Most forming processes used in the aircraft industry combine stretching and bending. The limited capacity of TMBs for in-plane straining is a limiting factor for application of the adhesively bonded TMBs in the processes where stretching is dominant. However, the TMBs can be more freely used in the processes where bending is the dominant deformation regime. One can, however, select a much more ductile or tougher adhesive so that the value of adhesively bonded TMB can be increased.

4.5. Conclusions

The mechanical behavior of the adhesively bonded tailor-made blanks was studied in this chapter from both numerical and experimental viewpoints. Following conclusions can be drawn from the study:

- The FEM model with cohesive interface elements can qualitatively and quantitatively predict the mechanical behavior of the specimens and the delamination of the adhesive.

- Delamination preceded the metal failure for the transverse and symmetric specimens.
- It was found that the tensile load at the onset of damage decreases as the thickness ratio increases.
- There was no delamination in the longitudinal specimens. The adhesive fails, however, due to the limited ductility of the adhesive compared with the aluminum alloy.
- In summary, if the in-plane straining is mainly in parallel with the transition line, the formability is limited by the ductility of the applied adhesive and it is recommended to use a more-ductile adhesive. If the in-plane straining is mainly perpendicular to the transition line, the formability is mainly controlled by the fracture energy of the adhesive and an adhesive with higher fracture energy must be preferred.
- The final conclusion is that the feasibility of the adhesive bonded TMB concept will improve significantly if a tougher or more suitable adhesive is selected.

4.6. References

[1] Shami SN, Good MC. Tailor Welded Blank Technology. Sixth International Conference on Manufacturing Engineering. Barton, ACT: Institution of Engineers, Australia, 1995.

[2] Meinders T, van den Berg A, Huetink J. Deep drawing simulations of Tailored Blanks and experimental verification. J. Mat. Proc. Tech. 2000;103:65.

[3] Zadpoor AA, Sinke J, Benedictus R. Mechanics of tailor-welded blanks: an overview. Key Eng. Mat. 2007;344:373.

[4] Sinke J, Stofregen MM, Straatsma E. Tailor made blanks for the aircraft industry: a pilot study. Netherlands Institute for Metals Research, 2005.

[5] Hosford WF, Duncan JL. Sheet metal forming: A review. JOM 1999;51:39.

[6] Camanho PP, Davila CG, de Moura MF. Numerical simulation of mixed-mode progressive delamination in composite materials. J. Comp. Mater. 2003;37:1415.

[7] Krueger R, Cvitkovich MK, O'Brien TK, Minguet PJ. Testing and analysis of composite skin/stringer debonding under multi-axial loading. J. Comp. Mater. 2000;34:1263.

[8] Rybicki EF, Kanninen MF. Finite-Element Calculation of Stress Intensity Factors by a Modified Crack Closure Integral. Eng. Fracture Mech. 1977;9:931.

[9] Yang QD, Cox B. Cohesive models for damage evolution in laminated composites. International Journal of Fracture 2005;133:107.

[10] Harper PW, Hallett SR. Cohesive zone length in numerical simulations of composite delamination. Eng. Fracture Mech. 2008;75:4774.

[11] ABAQUS. ABAQUS Analysis Manual ver. 6.6. Providence: ABAQUS Inc., 2006.

[12] Mohammadi S, Owen DRJ, Peric D. A combined finite/discrete element algorithm for delamination analysis of composites. Fin. Elem. Anal. Des. 1998;28:321.

[13] Benzeggagh ML, Kenane M. Measurement of mixed-mode delamination fracture toughness of unidirectional glass/epoxy composites with mixed-mode bending apparatus. Composites Science and Technology 1996;56:439.

[14] Comanho PP, Davila CG. Mixed-mode decohesion finite elements for the simulation of delamination in composite materials. NASA Technical Memorandum. Hampton Virginia: NASA Langley Research Center, 2002.

[15] Shimoda T, He J, Aso S. Study of cryogenic mechanical strength and fracture behavior of adhesives for CFRP tanks of reusable launch vehicles. Mem Fac. Eng. Kyushu Univ. 2006;66:55.
[16] Sargent JP. Durability studies for aerospace applications using peel and wedge tests. Int. J. Adhesion Adhesives 2005;25:247.
[17] Mathew J, Sankar B., Cattafesta L. Finite element modeling of piezoelectric actuators for active flow control applications. 39th AIAA Aerospace Sciences Meeting and Exhibition. Reno: AIAA, 2001.
[18] Zhao KM, Chun BK, Lee JK. Finite element analysis of tailor-welded blanks. Fin. Elem. Anal. Des. 2001;37:117.
[19] Bakker GJ. Road to failure: prediction of the strength and failure type of adhesively bonded single lap joints with the use of the finite element method. Faculty of Aerospace Engineering, vol. MSc. Delft: Delft University of Technology (TU Delft), 1995.

4.7. Appendix A- Nomenclature

t_1	Base sheet's thickness in a TMB, mm
t_2	Upper sheet's thickness in a TMB, mm
r	$(=(t_1+t_2)/t_1)$Thickness ratio of a TMB, dimensionless
E	Elastic modulus, GPa
σ_{y0}	Initial yield stress, MPa
K	Strength coefficient in the Hollomon's rule, MPa
n	Strain hardening exponent in the Hollomon's rule, dimensionless
δ_k	Separation in direction k, mm
T_0	Adhesive thickness, mm
$\hat{t}_k$	Traction in direction k, MPa
$\hat{\varepsilon}_k$	Separation strain in direction k, %
$\sigma_{u,i}$	Ultimate strength in direction k, MPa
χ	Quadratic stress parameter, dimensionless
$\bar{\hat{t}}_k$	Traction of the damaged adhesive in direction k, MPa
K_{ij}	Entry *ij* of the adhesive's elasticity tensor
D	Scalar damage variable, dimensionless
ε_{klm}	Levi-Civita (permutation) symbol, dimensionless
H	Heaviside step function, dimensionless
$D_{\max}$	Maximum scalar damage variable, dimensionless
G_{kC}	Mode k fracture energy, J/m^2
${\delta_k}^f$	Mode k separation at failure, mm
δ_m	Effective separation, mm
${\delta_m}^0$	Effective separation at onset of damage, mm
${\delta_m}^{\max}$	Maximum separation value, mm

G_C	Mixed-mode fracture energy, J/m^2
$\sigma_{u,m}$	Effective ultimate tensile strength, MPa
G_k	Mode k released fracture energy, J/m^2
η	A material parameter of the adhesive, dimensionless
ξ	Displacement ratio, dimensionless
$\langle\ \rangle$	Macaulay bracket
τ	Time, min
T	Temperature, ^{o}C

5. Dissimilar-alloy adhesively bonded TMBs

In this chapter, the mechanical behavior of adhesively bonded tailor-made blanks with dissimilar metallic adherends and their in-plane straining limits are studied using both experiments and FE models. The selected adhesive is AF163-2K (from 3M) and adherends are made from two dissimilar aluminum alloys, namely 2024-T3 and 7075-T6. The 7075-T6 adherend acts as a base adherend on top of which a 2024-T3 sheet is bonded. While the thickness of the base sheet (7075-T6) is the same for all specimens, the thickness of the upper sheet (2024-T3) varies between 0.5 mm and 2.5 mm. The transverse and longitudinal specimens, which were introduced in the previous chapter, are used in this chapter as well. The tensile tests are carried out and the three-dimensional deformations of the adherends are measured by digital speckle pattern correlation technique. It is shown that, in contrast with the case of similar metallic adherends (2024-T3), the upper sheet does not delaminate during the test and the failure mode is metal fracture. This is an important conclusion because delamination does not limit the in-plane straining capacity of this dissimilar-alloy type of adhesively-bonded tailor-made blanks. A mixed-mode cohesive interface model of the adhesive is made and is coupled with a distributed continuum damage model of the adherends to explain the observed behavior. It is shown that the mixed-mode cohesive interface model in combination with the distributed damage model can explain the behavior observed in the experiments.

In the previous chapter, the mechanical behavior of adhesively bonded TMBs with similar alloys (AA2024-T3) was studied. It was found that the capacity of TMBs for in-plane straining is limited due to two different failure modes of the adhesive. When the major straining direction was perpendicular to the transition line (from one thickness to the other), the metal failure was preceded by delamination. In the cases where the major straining direction was in parallel with the transition line, there was a chance of adhesive rupture due to the limited ductility of the adhesive. Cohesive interface theory was used to study and predict the delamination behavior of the TMBs and it was shown that the theory can successfully predict the onset of delamination.

In the current chapter, the in-plane straining limits of adhesively bonded TMBs with dissimilar alloys are studied. Table 5.1 presents the test matrix that is used in the study. The geometry of the transverse and longitudinal specimens is the same as the transverse and longitudinal specimens studied in the previous chapter. The mechanical behavior of the transverse specimens during the tensile testing is simulated with FEM. Cohesive interface theory is used to model the damage of the adhesive layer and distributed continuum damage theory is applied for the modeling of the damage of the metal sheets. The simulation results are discussed in comparison with the experimental results to highlight the physical mechanisms behind the observed behavior of the specimens.

Table 5.1. The test matrix used in this study.

no.	$t_1 + t_2$ (mm)	t_1 (mm)	r	geometry	samples
1	2+0.5	2	1.25	transverse	6
2	2+1.2	2	1.6	transverse	6
3	2+2	2	2	transverse	6
4	2+2.5	2	2.25	transverse	6
5	2+0.5	2	1.25	longitudinal	6
6	2+1.2	2	1.6	longitudinal	6
7	2+2	2	2	longitudinal	6
8	2+2.5	2	2.25	longitudinal	6

5.1. Experimental methods

The longitudinal and transverse specimens were composed of two sheets: the base sheet and the upper sheet which was bonded on the top of the base sheet. In all configurations (Table 5.1), the base sheet was made of a AA7075-T6 sheet, while the upper sheet was made of 2024-T3 sheets. The mechanical properties of both alloys, including the plasticity parameters according to the Hollomon's strain hardening rule, were determined through a dedicated tensile testing. A summary of the tensile test results is presented in Table 5.2. A commercial film adhesive, namely AF163-2K from 3M, was used to bond the upper sheet to the base sheet. The nominal thickness of the adhesive layer was 0.2 mm for all configurations. The mechanical properties of the adhesive and the surface preparation and bonding procedure were similar to what described in the previous chapter.

Table 5.2. The mechanical properties of adherend alloys: 2024-T3 and 7075-T6.

material	E (GPa)	ν	σ_{y0} (MPa)	K (MPa)	n
7075-T6	70	0.33	532	773	0.0808
2024-T3	70	0.33	343	775	0.1787

The tensile tests were carried out using a MTS machine at a constant deformation rate of 5 mm/min. The machine was synchronized with a three-dimensional Digital Image Correlation (DIC) camera system. The DIC system was composed of two high precision digital cameras that were first calibrated using a calibration grid. They were then used to continuously (more than 1 picture per second) capture the surface of the specimens during the tensile testing. The surface of the specimens (the side with thickness difference) was covered with a random spackle pattern. The displacement field was then calculated through correlating the random patterns of successive digital images and the strain field was determined accordingly.

5.2. Experimental results

The results of the experiments showed that there was no delamination whatsoever in any of the transverse or longitudinal specimens. That is in contrast with what was previously observed for adhesively-bonded TMBs with similar alloys (2024-T3). Figure 5.1a-c presents a summary of the tensile properties measured for the transverse and longitudinal specimens. The values presented in this figure should be considered as nominal stress and strain values, because the stress and strain distributions are highly non-uniform throughout the specimens and no single value can present the status of the whole specimen. The strain distribution will be discussed using the strain field measured by the DIC technique. In the case of the transverse specimens, the cross section area changes at the transition line. The cross section area of the base sheet was used for the calculation of the nominal tensile strength of transverse specimens. The cross section area of the longitudinal specimens is, however, constant throughout the gauge length. The force was divided by the total cross section area of the specimens to calculate the *nominal* stress values, even though we know that the stress values are not the same in the two different alloys.

One can see that the nominal tensile strengths of the transverse and longitudinal specimens are in most cases (except for $r = 2$) close to each other. However, the nominal tensile strength of the transverse specimens is always higher than that of the longitudinal specimens. That is due to the fact that in the case of transverse specimens, it is the base sheet that undergoes most of the deformation and given that the base sheet is made of a stronger (7075-T6) material, one would expect that the ultimate strength should be greater than in the case of the longitudinal specimens where both materials deform (almost) equally. Figure 5.1b-c show that the nominal strain at maximum stress and maximum nominal strain of longitudinal specimens increase as the thickness of the upper sheet increases from 0.5 to 2.5 mm.

The evolution of the tensile strain field on the thinner side of a sample transverse specimen is presented in Figure 5.2. Initially (up to 12.4 kN load), the strain is mainly concentrated in an area close to the transition line. As load increases, the strain concentration area widens in length and somewhat extends beyond the proximity of the transition line (load = 12.4-13.0 kN). A new area with high strain values (the imperfection area) starts to form well before reaching the maximum force (around 13.0-13.2 kN). The two areas of high strain values join together and form a large area of strain concentration around 13.2 kN load. As the load increases to 13.3 kN, the high strain area contracts and the strain value becomes quite high (max. 12.7%) after which the load drops and the shear band further sharpens, resulting in a maximum recorded strain of 38% just before the rupture.

Figure 5.3 presents the tensile strain field for a sample longitudinal specimen. As is expected from the geometry of the longitudinal specimens, the strain values are similar on the thinner and thicker sides of the specimen except for two high-strain locations: an area close to the edges of the gauge length and an imperfection area that is within the gauge length and shows somewhat higher strain values around 16.2 kN (and even before). The strain continues to localize in the imperfection area as the load increases to 17.7 kN. The maximum strain value exceeds the uniform strain level of 7075-T3 sheet around 17.7 kN-17.8 kN. Nevertheless, that same level of strain is still well below the ultimate uniform strain level of 2024-T3. Therefore, the 2024-T3 sheet supports the 7075-T6 sheet and postpones final rupture until the maximum strain exceeds the ultimate uniform strain level of 2024-T3 (around 18.0 kN) at which point the load starts to drop. The maximum strain profile then shifts towards the part containing the 2024-T3 sheet and specimen ruptures with a maximum recorded strain of around 34%.

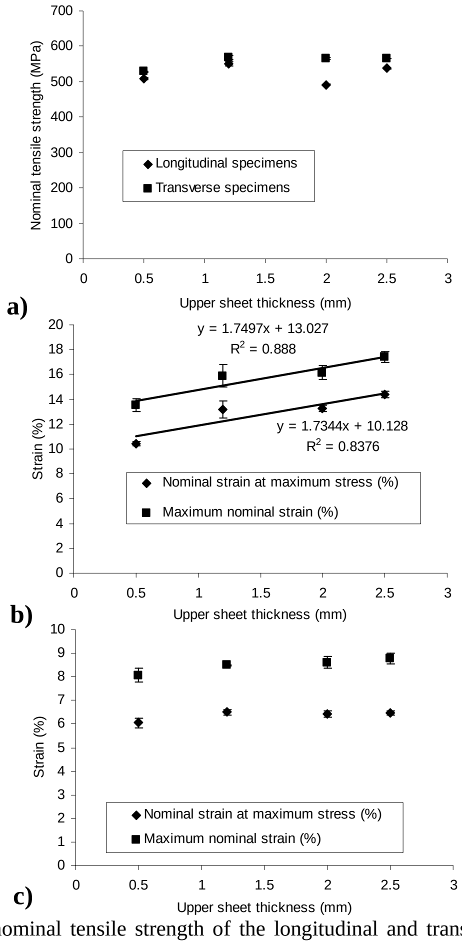

Figure 5.1. The nominal tensile strength of the longitudinal and transverse specimens vs. upper sheet thickness is presented in subfigure (a). Nominal strain at maximum stress and maximum nominal strain of the longitudinal (b) and transverse (c) specimens.

In the next section, a numerical model is presented for the mechanical behavior of the adhesive and sheet metal during the tensile testing of transverse specimens. The results of a similar model made for the longitudinal specimens are not presented and discussed, because the model did not deem necessary to explain the observed behavior of the longitudinal specimens.

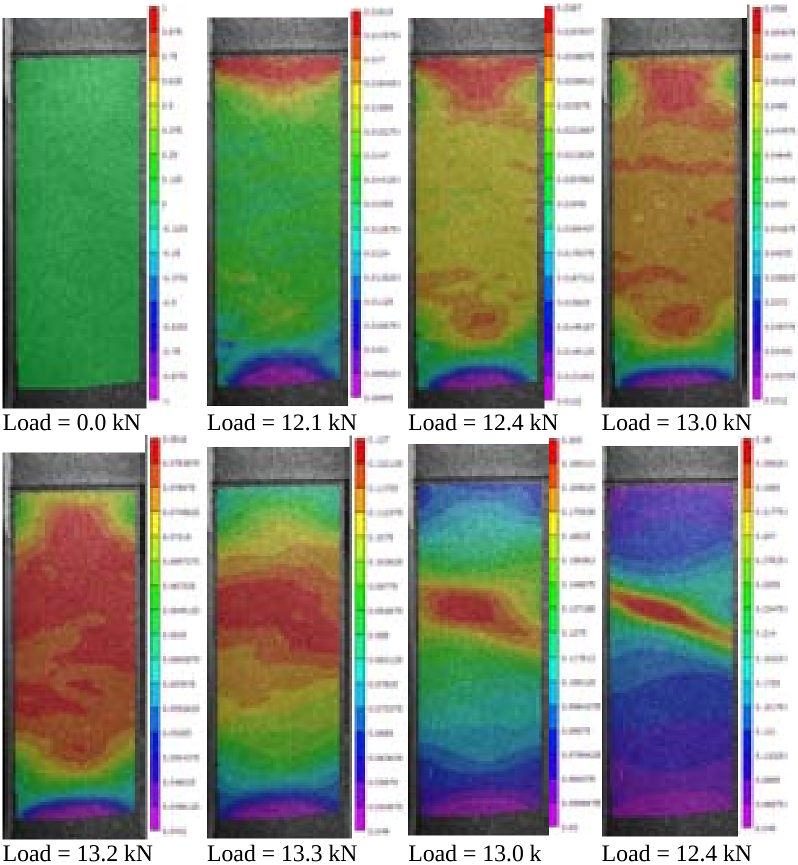

Figure 5.2. The evolution of the tensile strain field for a sample transverse specimen from configuration no. 1 ($r = 1.25$, Table 5.1).

5.3. Numerical methods

The modeling of the adhesively-bonded TMBs described in the experiments chapter can be divided into two parts: the modeling of the adhesive and the modeling of the adherends. The modeling of the adhesive was similar to the modeling of the adhesive in the previous chapter and will not be repeated here. This section therefore only discusses the modeling of the adherends.

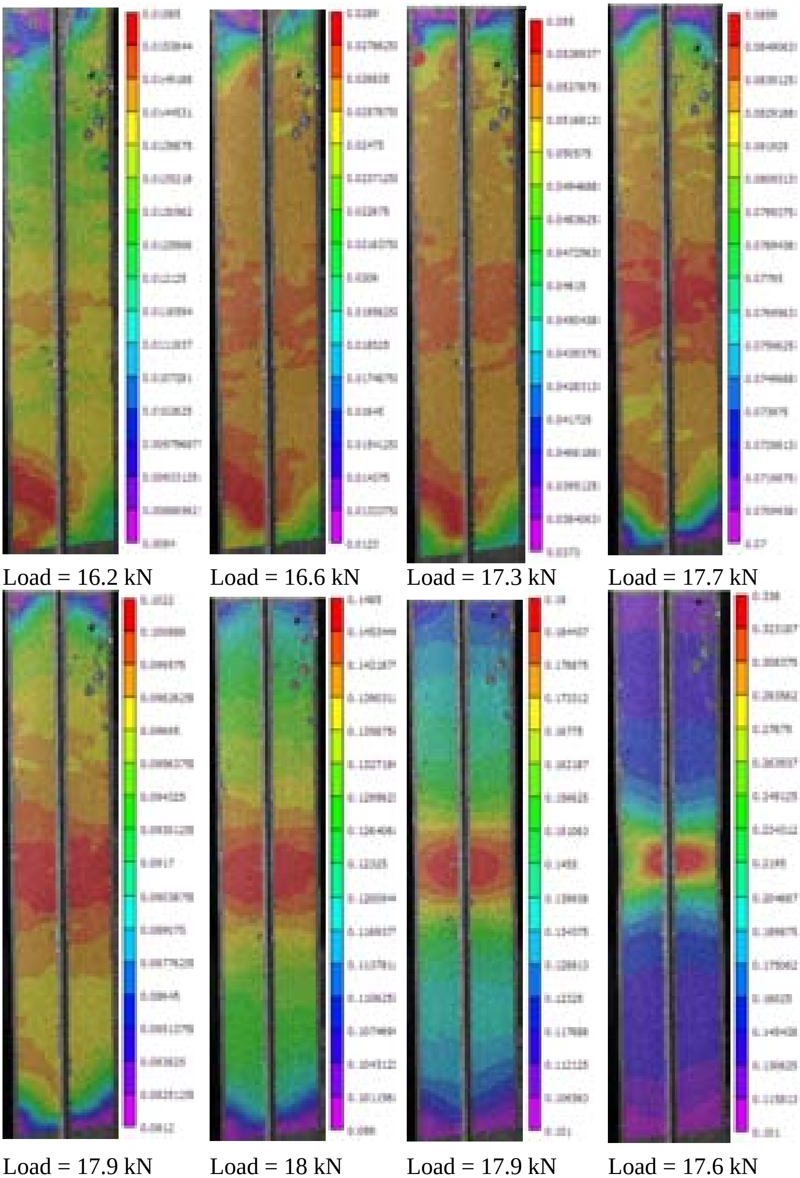

Figure 5.3. The evolution of the tensile strain field for a sample longitudinal specimen from configuration no. 6 ($r = 1.6$, Table 5.1). The thicker part is on the right side.

Two sets of models were built. The first set of models (model I) did not include the failure mechanism of the adherends and dealt only with the damage initiation and evolution of the adhesive. In the first set of models, the adherends (base sheet and upper sheet) were modeled using von Mises plasticity and Hollomon's isotropic hardening law. The second set of models (model II) included the modeling of the failure mechanism of the adherends as well. The base sheet of transverse specimens experiences significant plastic deformation and failure. However, the upper sheet does not fail in any of the studied cases. Therefore, a simple elastoplastic formulation based on von Mises plasticity and Hollomon's isotropic hardening law was used for the modeling of the upper sheet. The base sheet was modeled such that the effects of the shear band localization on the damage of the adhesive can be taken into account. An initial imperfection is often assumed to trigger the development of shear band [1-4]. The imperfection parameter, f_0, is defined as

$$f_0 = \frac{K_{b,0} t_{b,0}}{K_{a,0} t_{a,0}} = \frac{\hbar_{b,0}}{\hbar_{a,0}} \tag{1}$$

Where $K_{b,0}$ and $t_{b,0}$ are, respectively, the strength and thickness of the imperfection band and $K_{a,0}$ and $t_{a,0}$ are the same quantities this time for the uniform zone. In our simulations, the imperfection was modeled using a 10 mm long section with lower yield stress. The stress-strain curve of the uniform materials was scaled by the imperfection factor to obtain the stress-strain curve of the imperfection zone.

The velocity gradient and Cauchy stress tensors are typically known for the uniform zone and the task is to find the tensors in the imperfection zone. The velocity gradient, $\mathbf{L}$, is defined as

$$\mathbf{L} = \frac{\partial v_i}{\partial x_j} \hat{\mathbf{e}}_i \otimes \hat{\mathbf{e}}_j \tag{2}$$

and can be decomposed into a symmetric part, $\mathbf{D}$, which represents rate of deformation of the material particle, and an anti-symmetric part, $\mathbf{W}$, which represents the continuum spin of the material particle, as

$$\mathbf{L} = \mathbf{D} + \mathbf{W} \tag{3}$$

The compatibility condition at the interface of the imperfection zone requires that

$$L_{b,ij} = L_{a,ij} + \dot{c}_i n_j, \; i,j = 1,2 \tag{4}$$

where n_j s are the components of the unit normal to the imperfection zone and $\dot{c}_i$ are parameters to be determined during the solution process. Equation (4) can be decomposed into a symmetric part, D_{ij}, and anti-symmetric part, W_{ij}, as

$$D_{b,ij} = D_{a,ij} + \frac{1}{2}\left(\dot{c}_i n_j + n_i \dot{c}_j\right), \; i,j = 1,2 \tag{5a}$$

$$W_{b,ij} = W_{a,ij} + \frac{1}{2}\left(\dot{c}_i n_j + n_i \dot{c}_j\right), \; i,j = 1,2 \tag{5b}$$

Requiring equilibrium of the forces at the interface of the imperfection zone, one would get the following relationship

$$n_i \sigma_{b,ij} f = n_i \sigma_{a,ij} \tag{6}$$

These equations relate the state of stress and strain at the uniform zone to that of the imperfection and can be used to obtain the state of strain in the imperfection zone.

The damage of the sheet metal was modeled using a distributed continuum damage theory. A schematic description of the model is presented in Figure 5.4. According to this model, the material follows the normal elastoplastic path of deformation up to the point where damage initiates. The equivalent strain at the damage initiation point is assumed to be dependent upon stress triaxiality, η, and strain rate, $\dot{\varepsilon}$, and is given by a phenomenological damage function:

$$\varepsilon_{eq,c} = f(\eta, \dot{\varepsilon}) \tag{7}$$

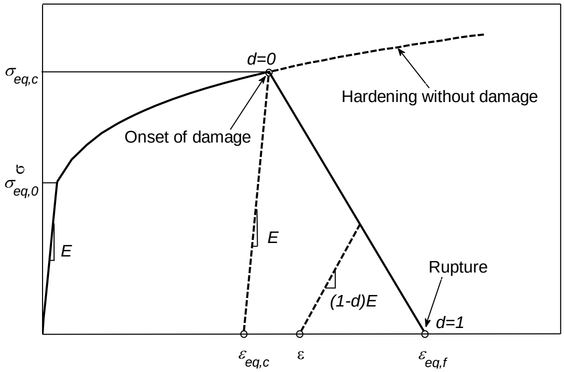

Figure 5.4. A schematic representation of the distributed damage model used for the modeling of metal failure in model II.

Different types of phenomenological functions have been previously used for the description of the failure of high strength aluminum alloys (see reference [4] and Chapter 8) and are shown to be able to predict the failure limits with an accuracy comparable with the accuracy of the physical models of ductile fracture. In the current study, the function is not of major importance because 7075-T6 is relatively strain-rate insensitive and the stress triaxiality value ($\eta \simeq 1/3$) varies only negligibly within the base sheet of the tensile test specimens and is almost the same regardless of the thickness ratio. Therefore, only a single parameter, $\varepsilon_{eq,c}$, is needed for the detection of the damage initiation point of transverse specimens. After the initiation of the damage, further application of the stress-strain curve would result in a strong mesh dependency due to the lack of any length scale, meaning that the released fracture energy keeps decreasing indefinitely as the element size decreases. The Hillerborg's proposal of introducing a length scale, L, was followed to alleviate the mesh dependency of the analysis results [5]. The definition of the length scale is dependent on the geometry and formulation of the element being used. For first- and second-order elements, the length scale is, respectively, one and one-half of a typical length across the element. It is recommended to use elements with an aspect ratio close to unity to eliminate any possible mesh dependency that may arise due to the difference between the elements that crack along different directions. By introducing the length scale, L, that is associated with an integration point, the released fracture energy (the area beneath the damage evolution curve in Figure 5.4) can be given by integrating over displacement, u, instead of integrating over strain:

$$G_f = \int_{\varepsilon_{eq,c}}^{\varepsilon_{eq,f}} L\sigma d\varepsilon_{eq} = \int_0^{u_{eq,f}} \sigma du_{eq} \quad (8)$$

In this study, it is assumed that the scalar damage variable, d , evolves linearly from 0 to 1:

$$\dot{d} = \frac{L\dot{\varepsilon}_{eq}}{u_{eq,f}} = \frac{\dot{u}_{eq}}{u_{eq,f}} \quad (9)$$

where

$$u_{eq,f} = \frac{2G_f}{\sigma_{eq,c}} \quad (10)$$

The failure of the material is assumed to have completed once d reaches 1.
The type of elements, loading, and boundary condition for models I and II were similar to what described in the previous chapter.

5.4. Numerical results

The results of the simulations of model I are presented in Figure 5.5-Figure 5.7. Figure 5.5a presents the experimentally-determined metal failure loads as well as the load at which the damage of the adhesive initiates, i.e. χ reaches unity. Two trends are clear from this figure: First, the changes in metal failure load are relatively insignificant and in most cases the sheet fails at around 14.0 kN. Second, the damage initiation load decreases as the thickness of the upper sheet, t_2 , increases. As a result of these two trends, the difference between the damage initiation and metal failure loads increases as the thickness of the upper sheet increases, meaning that the damage initiates at earlier stages for the specimens with larger thickness ratios. That is because the amount of load that is carried by the upper sheet increases as the thickness of the upper sheet increases and the adhesive is more heavily loaded at the transition line, where the portion of load that is carried by the upper sheet must flow from the upper sheet to the base sheet through the adhesive. Figure 5.5b shows the scalar damage variable of the adhesive, D , vs. the thickness of the upper sheet. All the values are calculated for 14.0 kN tensile load, i.e. around the metal failure load. One can see that the scalar damage variable is around 0.7 for the thickness ratio of 1.25, i.e. t_2 =0.5 mm. For other thickness ratios, the scalar damage variable is around 1, meaning that, according to model I, delamination should have occurred for the transverse specimens with a thickness ratio greater than 1.25. However, experiments showed that there is no delamination in any of the transverse specimens. This is due to the fact that the damage of the adherends is not included in model I. This issue will be revisited later in this section.
Figure 5.6 shows how the scalar damage variable evolves from 0 to 1 for the transverse specimens with different thickness ratios. The data points plotted in this figure are calculated using model I and a line is fitted to the data points. As is clear from this figure, the damage initiates earlier for specimens with larger thickness ratios. However, the slope of the increase is larger for specimens with smaller thickness ratios. That is because the fracture energy of the adhesive is the same regardless of the thickness ratio. Since damage initiates at smaller loads for the specimens with larger thickness ratios, the rate of increase of the damage variable

should be lower so that the released fracture energy, i.e. equal to the area beneath the traction-separation curve, is equal for all thickness ratios. Indeed, the calculated slope of the linear fit of the specimen with the smallest thickness ratio is more than three times of that of the specimen with the largest thickness ratio.

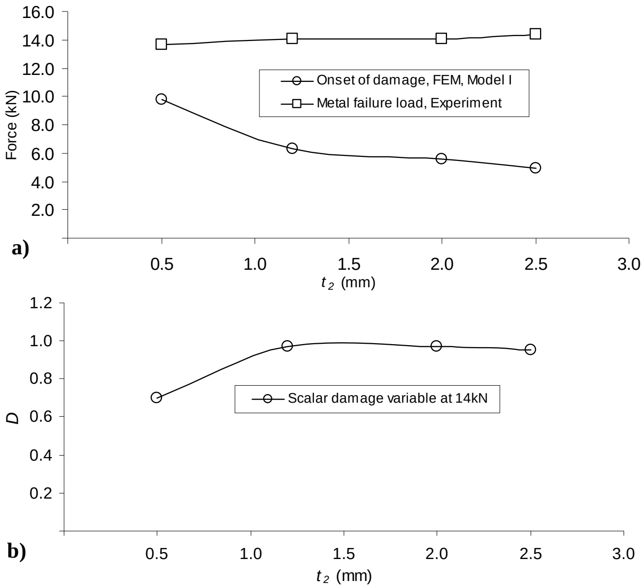

Figure 5.5. The tensile loads, respectively, at the damage initiation (FEM) and metal failure (experiments) points vs. the thickness of the upper sheet. b) The scalar damage variable calculated using model I for transverse specimens with different thicknesses of the upper sheet.

Figure 5.7 compares the strain field determined by model I with the experimentally-determined strain field for a sample transverse specimen. For a sufficiently small tensile load (13.2 kN), the maximum strain value calculated with the FEM model (3.1%) is in agreement with the maximum strain value measured in the experiments (2.9%). Moreover, the location of the maximum strain value is calculated to be in the proximity of the transition line and is quite close to the place where the maximum tensile strain is measured. As the tensile load increases to 13.6 kN, the maximum strain calculated with the FEM model (model I) mismatches the experimental values. In addition, the experimentally-determined location of the maximum strain starts to deviate from the transition line, whereas the location of the maximum strain calculated with the numerical model does not change. When the tensile load reaches 14.0 kN, the experimentally-determined maximum strain value is more than twice as much as the value determined with the FEM model (model I) and the location of the maximum value moves from the transition line to another location in the tensile specimen. The reason for the disagreement between the experimental results and the FEM results obtained with model I is the fact that the damage of sheet metal is not implemented in model I. Table 5.3 presents the results of the simulations carried out using model II for several sets of model parameters and a sample thickness ratio of 1.6 (similar results were obtained for other thickness ratios). The damage variables, D and d, and maximum strain value, $\varepsilon_{1,\max}$, are presented for the tensile load of 14.0 kN. It was observed that once the imperfection zone and damage initiation and evolution laws were implemented in the FEM model, the model was capable of predicting the right location of the maximum strain value.

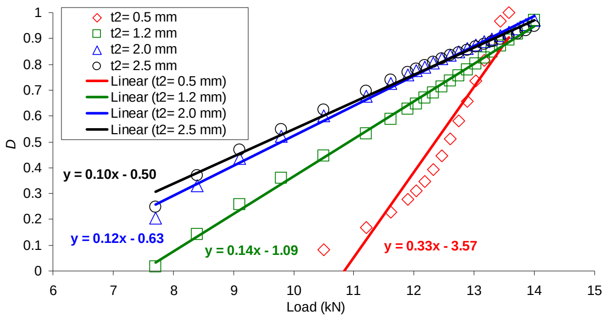

Figure 5.6. The evolution of the scalar damage variable of the adhesive calculated with model I for transverse specimens with different thickness ratios.

During initial stages, the maximum strain value was calculated to occur in the proximity of the transition line. However, the maximum strain value deviated from the transition line as the tensile load increased. The first four columns of Table 5.3 present the sets of parameters that were introduced to model II. The last three columns present the results of the FEM analysis. Two trends emerge from this table. First, the maximum calculated strain value, $\varepsilon_{1,\max}$ drastically increases when the damage of the sheet metal is implemented in the FEM model (compare the maximum tensile strain values in Figure 5.7 with the ones presented in Table 5.3). Second, the damage variables of the adhesive calculated with model II are significantly lower than the one calculated with model I, i.e. $D \simeq 0.95$. These two trends have to do with the fact that the presence of an imperfection zone in the FEM model means that the strain in the imperfection zone would be always higher than in the uniform zone. The ratio of the strain of the imperfection zone to that of the uniform zone would continue to increase. After a certain point, the strain is in the imperfection zone is so high that the maximum strain is not in the proximity of the transition line but within the imperfection zone. Therefore, the maximum strain values are higher in model II compared with model I, which does not include the imperfection zone. The localization of the strain in the imperfection zone also means that less deformation takes place at the transition line and, thus, the deformation of the adhesive is less.
A difficulty with model II is that it is difficult to identify the right model parameters for this model. Eight different sets of model parameters and their corresponding

simulations results are presented in Table 5.3. A technique that can be used for determination of the appropriate set of model parameters is to calibrate the model parameters such that the maximum strain value predicted by the FEM model is close to the maximum strain value measured in the experiments. An extensive series of simulations showed that the scalar damage variable calculated for the adhesive tends to be similar for the models that result in similar maximum strain values. The maximum strain values (10.5-10.8%) obtained using the parameters listed in the last three rows of Table 5.3 are close to the experimentally-determined maximum strain value (9.9%) for the same tensile load (14 kN- Figure 5.7). Therefore, it can be argued that the presence of the imperfection zone lowers the maximum scalar damage variable from $D \simeq 0.95$ for model I to $D \simeq 0.75$ for model II and that is the reason why delamination does not occur in reality for any of the tested specimens.

Table 5.3. The results of simulation of model II for different sets of model parameters (configuration 2).

no.	f_0	$\varepsilon_{eq,c}$	G_f (kJ/m^2)	D	d	$\varepsilon_{1,\max}$
1	0.97	---	---	0.88	0.00	5.1%
2	0.95	4%	20	0.85	0.01	6.2%
3	0.95	2%	50	0.85	0.01	6.3%
4	0.92	9%	30	0.80	0.00	8.4%
5	0.92	6%	30	0.80	0.01	8.5%
6	0.90	6%	50	0.75	0.01	10.8%
7	0.90	8%	50	0.76	0.01	10.6%
8	0.90	9%	30	0.76	0.01	10.5%

5.5. Discussions

The experimental and numerical results presented in the previous sections will be discussed in this section. The section is divided into two subsections each of which discusses the results concerning one single type of specimens, i.e. transverse or longitudinal.

Transverse specimens. As previously pointed out, when the base and upper sheet were similar and both were made of 2024-T3, delamination took place before sheet failure. The main questions that need to be answered by simulation are:

1. Why delamination does not occur when the base and upper sheet are different and the base sheet is made of 7075-T6?
2. What is the straining limit for adhesively-bonded tailor-made blanks with dissimilar alloys when the major straining direction is perpendicular to the transition line?

The data presented in Figure 5.5b shows that even if the ductile damage is not implemented in the FEM model, the delamination does not take place during the initial stages of plastic straining and it is only at about the fracture point that the adhesive's scalar damage variable, D, reaches unity. Therefore, even though the applied load is higher for the adhesively-bonded TMBs made of the stronger 7075-T6 base sheets, the damage of the adhesive is less than in the case of similar-alloy TMBs made of 2024-T3 base sheet. That is because 7075-T6 deforms much less than 2024-T3 before failure. However, lower ductility can not alone explain the experimental observation that delamination did not happen for any of the tested specimens, because according to model I the adhesive's scalar damage variable is just about 1 at the maximum load and one would normally expect the delamination to take place at least for some of the 24 tested specimens. Model II can explain why delamination never occurs. The presence of an imperfection zone results in localization of strain in the imperfection zone and not in the proximity of the transition line, where it would have otherwise happened. Therefore, the mode II loading of the adhesive, which is by far the dominant loading mode of the adhesive [6], decreases and the scalar damage variable of the adhesive is well below 1 at the metal failure point.

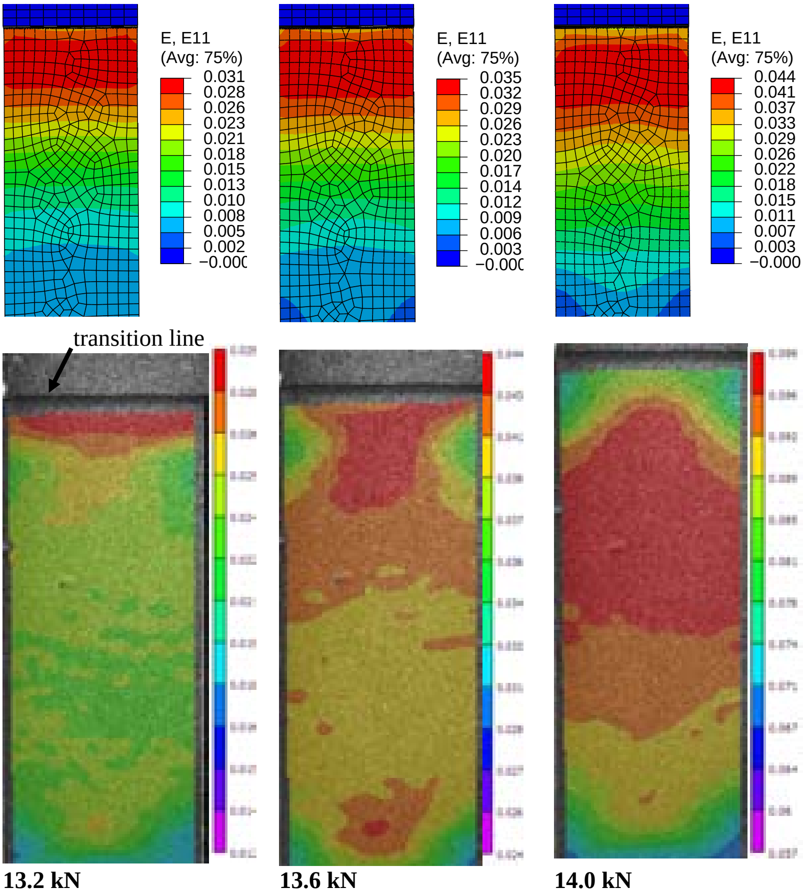

Figure 5.7. Comparison between the tensile strain field calculated with model I and the measured tensile strain field for a sample specimens from configuration 2 (Table 5.1).

The second question remains to be answered. Although model I and model II give a good qualitative description of the physical mechanism behind the observed behavior, a proper set of parameters are needed to achieve quantitatively reliable values of the scalar damage variable for the adhesive. Given that the cohesive interface model of the adhesive damage is shown to be able to give fairly accurate predictions of the delamination load [6], a quantitatively valid value for the scalar damage variable of the adhesive should be obtainable provided that the parameters of the metal failure model can be set accurately. However, the modeling of the shear band localization is a complicated process not only because of its somewhat stochastic nature but also due to the large number of involved parameters and the fact that a larger number of data points and, thus, a larger number of tests are needed for accurate identification of the model parameters. However, multiple simulations with different sets of model parameters, see e.g. Table 5.3, showed that the scalar damage variable of the adhesive at a given tensile load tends to be similar for various sets of model parameters, provided that the calculated maximum tensile strain and the location of the maximum strain are similar. This suggests that the maximum tensile strain measured using the DIC technique can be used to tune the FEM model and obtain at least a first approximation of the scalar damage variable of the adhesive. From practical viewpoint though, one may not need more than a first approximation. That is because the practical application of TMBs would probably require that the adhesive be undamaged, meaning that the scalar damage variable should be zero. Therefore, TMBs should be designed such that the adhesive is loaded up to the damage initiation point and not further. As the damage initiation point typically occurs well before the strain is localized in the imperfection zone, accurate determination of the parameters of the metal's damage model may be rendered unnecessary.

Longitudinal specimens. The experimental results presented in this chapter for TMBs with dissimilar alloys and the ones presented in the previous chapter for similar-alloy (2024-T3) TMBs have shown that delamination normally does not occur in the tensile testing of longitudinal specimens, regardless of the configuration of the base and upper sheets. However, the adhesive may still fail due to the limited ductility of the adhesive. The ultimate strain of AF163-2K is reported to be between 3.4% [7] and 7.0% [8]. For the case where both the base and upper sheets are made of 2024-T3, this means that the full tensile straining capacity of 2024-T3 (16-20%) can not be used in longitudinal TMBs and the straining limit is dependent on the ductility of the adhesive. In the case where the base sheet is made of 7075-T6 and is different from the upper sheet that is made of 2024-T3, the ultimate strain of 7075-T6 is close to the ultimate strain of the adhesive. Therefore, tailor-making does not significantly limit the forming window of the TMB as compared with the base metal. However, experimental results show that the straining limit of the longitudinal specimens increases as the thickness ratio increases. That is because the stiffness of the upper sheet that is made of 2024-T3 increases as the thickness ratio increases. Since the base and upper sheets tend to deform similarly in longitudinal specimens, the 2024-T3 sheet is still far from its softening point when strain starts to localize in the imperfection zone of the base sheet, which is made of 7075-T6 and is therefore much less ductile. The stiffer upper sheet helps to postpone the failure of the base sheet by limiting the deformation taken place within the imperfection zone of the base sheet. The limitation concerning the limited ductility of the adhesive still persists though. Therefore, it is suggested that the adhesives selected for TMBs with larger thickness ratios should be more ductile, if the entire straining capacity of the TMB is going to be used.

5.6. Conclusions

Adhesively-bonded TMBs with dissimilar alloys were studied in this chapter through experimenting as well as FEM simulation of the experiments. The base sheet and upper sheets were, respectively, made of 7075-T6 and 2024-T4. The experiments included tensile testing of the specially-designed specimens in two different conditions: when the loading direction was perpendicular to the transition line (transverse specimens) and when the loading direction was in parallel with the transition line (longitudinal specimens). Following conclusions can be drawn from the study:

- Unlike adhesively-bonded TMBs with similar-alloy adherends (2024-T3), there is no delamination in the tensile testing of adhesively-bonded TMBs with dissimilar alloys.
- The FEM simulations showed that due to the lower ductility of 7075-T6 compared with 2024-T3, there is a competition between the two failure mechanisms of TMBs, namely delamination of the adhesive and metal failure. Lower levels of tensile strain at the transition line as compared with similar-alloy (2024-T3) TMBs and localization of the strain in the imperfection zone of 7075-T6 are the reasons why metal failure occurs before delamination.
- Even if the damage initiation point of the adhesive is chosen as the straining limit of the adhesively-bonded TMBs, the reducation of the forming window caused by tailor-making is much less for the dissimilar-alloy TMBs than it is for similar-alloy (2024-T3) TMBs.
- The straining limit of longitudinal specimens increases as the thickness ratio increases. However, the straining limit caused by the limited ductility of the adhesive still persists. It is therefore recommended that more ductile adhesives should be used for TMBs with larger thickness ratios.

5.7. References

[1] Z. Marciniak and K. Kuczynski, "Limit strains in the process of stretch-forming sheet metal," *International Journal of Mechanical Sciences,* vol. 9, pp. 609-620, 1967.
[2] V. Tvergaard, "Material failure by void coalescence in localized shear bands," *International Journal of Solids and Structures,* vol. 18, pp. 659-672, 1982.
[3] H. Yamamoto, "Conditions for shear localization in ductile fracture of void-containing materials," *International Journal of Fracture,* vol. 14, pp. 347-365, 1978.

[4] A. A. Zadpoor, J. Sinke, and R. Benedictus, "Formability prediction of high strength aluminum sheets," *International Journal of Plasticity,* 2009.

[5] A. Hillerborg, M. Modéer, and P. E. Petersson, "Analysis of crack formation and crack growth in concrete by means of fracture mechanics and finite elements," *Cement and Concrete Research,* vol. 6, pp. 773-781, 1976.

[6] A. A. Zadpoor, J. Sinke, and R. Benedictus, "The mechanical behavior of adhesively bonded tailor-made blanks," *International Journal of Adhesion and Adhesives,* vol. 29, pp. 558-571, 2009.

[7] G. J. Bakker, "Road to failure: prediction of the strength and failure type of adhesively bonded single lap joints with the use of the finite element method," in *Faculty of Aerospace Engineering*. vol. MSc Delft: Delft University of Technology (TU Delft), 1995.

[8] J. P. Sargent, "Durability studies for aerospace applications using peel and wedge tests," *International Journal of Adhesion and Adhesives,* vol. 25, pp. 247-256, Jun 2005.

Modified from: Zadpoor, A. A., Sinke, J., Benedictus, R., Pieters, R., 2008,"Mechanical properties and microstructure of friction stir welded tailor-made blanks", Materials Science and Engineering A, vol. 494, pp. 281-290.

6. Friction stir welded blanks I

This chapter studies the microstructural features and mechanical properties of friction stir welds with dissimilar alloys and thicknesses. The welds are produced in five different thickness/material combinations from 2024-T3 and 7075-T6 sheets with different thicknesses. A parametric study is conducted to optimize the welding parameters such that the different configurations can be compared. The chapter is divided into two sections: microstructural features and mechanical properties. In the first section, study of the chemical composition and microstructure of the welds shows that a narrow chemical mixing zone is present in the dissimilar-alloy welds and that the stirring zone embodies the onion rings and exhibits heterogeneous texture for most configurations. Study of the hardness and tensile properties in the second section shows that an asymmetric softened region, which is harder at the advancing side and extends more into the retreating side, is formed in the stirring zone.

In this thesis, the study of the microstructural features and mechanical properties of FSW TMBs is presented in two chapters: the current and the next chapter. The current chapter studies five different weld configurations and deals with the microstructural features, hardness profiles, and global mechanical properties of those weld configurations. No configuration with simultaneously dissimilar thicknesses and alloys is studied in this chapter. The next chapter covers a wider range of possible TMB combinations (ten configurations) and includes all possible types of TMB configurations (including simultaneous difference in materials and thicknesses). While both chapters include a section on the microstructural features of the welds, the aspects of the microstructural features that are covered in the current chapter are not necessarily the same as the ones covered in the next chapter. The hardness profiles are presented in the current chapter. Local mechanical properties and fracture mechanisms are discussed in the next chapter. Hardness profiles are usually measured along a selected line perpendicular to the thickness direction. Because the hardness changes in the thickness direction [1], the measurement of the hardness along one single line can not faithfully present the mechanical properties of the whole cross section. Therefore, the measurement of local mechanical properties is needed to complement the hardness masurements.
Only a limited knowledge of the microstructural features and mechanical behavior of the FSW TMBs is available. Previous studies of welding of dissimilar materials can be categorized into three main categories. The first category considers FSW of different aluminum alloys. Welded materials are normally two different alloys from

two different aluminum series, e.g. 7075 and 2017 [2], 5052 and 2017 [2], 2024 and 6061 [3], and 2024 and 1100 [4]. The second category studies aluminum combined with a different metal, e.g. 6061 and copper [5], 2024 and silver [6], and 2024 and copper [4]. The third category includes the studies of FSW of two different metals or alloys other than aluminum alloys, e.g. copper and brass [7]. A comprehensive review of FSW of dissimilar materials is presented by Mishra [8]. The focus of the current chapter is the first category, dissimilar Al alloys as well as FSW of dissimilar thicknesses of the same alloy.

Successful FSW of different Al alloys needs special considerations. For example, it has been shown that welding a very soft aluminum to a very hard aluminum, results in poor mechanical properties of the weld [2]. Besides that, there is a debate on whether the stronger or weaker material should be placed at the advancing side during welding. While some studies prefer the first option [9], some others suggest the latter [10].

Although a loss of the tensile strength and ductility is observed in all FSWs, the mechanical properties at the weld zone are highly dependent on the welding parameters [8]. For the production of TMBs, the loss of the ductility is of particular importance as it limits the formability of the sheet assembly.

An additional difficulty when dealing with FSW TMBs is heterogeneity of the mechanical properties within the blank [11]. Four different zones can be distinguished in FSW blanks, the weld nugget, thermo mechanically-affected zone, heat-affected zone, and the base metal, all with different microstructures and mechanical properties [8]. In the case of FSW TMBs, the zones to be investigated are different on either side of the weld, increasing the complexity [12]. The microstructure and mechanical properties of the different zones are yet not well understood, especially when the materials or thicknesses are dissimilar. FSW sheets with different thicknesses, create additional technical difficulties. For example, Fratini *et al* suggested that the tool should have an angle with the plane of the blank [13].

The microstructural features and mechanical properties of FSW TMBs govern the behavior of FSW TMBs in such conditions as forming or in-service loading. Therefore, the engineering of the tailor-made blank structures and planning of the associated forming processes can not be realized without thorough knowledge of the mechanical properties and microstructural features of the different zones of the welds. The required information is not available yet for TMBs with dissimilar thicknesses. To address this need, this chapter studies and compares five different FSW configurations made of two alloys commonly used in the aircraft industry, 2024-T3 and 7075-T6. A parametric study is conducted towards optimization of the welding parameters so that the different weld configurations can be compared with each other.

After two introductory sections (introduction and welding procedure), the current chapter is organized into two main sections: microstructural features and mechanical properties. In the first section, the chemical composition and microstructure of the welds are studied. The second section is devoted to the hardness profiles and tensile properties of the welds. The results of these studies help the designers by, among the others, providing guidelines for appropriate distribution of large plastic strains in the

FSW TMBs so that the formability can be maximized. The results also reveal the effects of design parameters on the mechanical properties and help to understand relative importance of the phenomena like stress concentration, when the sheet thicknesses are dissimilar.

6.1. Welding procedure

Five different configurations were selected for the study (Table 6.1). The rolling direction of the sheets was in parallel with the welding direction. Prior to the welding, the oxide layer of the sheet strips was removed by grinding and subsequently the edges were cleaned with acetone. The welding machine was a fully-controlled 3-axis Cartesian FSW machine (ESAB Superstir FSA). Two different welding angles were used: the tool angle, $\alpha = 2^\circ$, which is the angle between the welding tool and the blank in the welding direction and the inclination angle, θ, which is the angle of the tool with the workpiece in the direction perpendicular to the welding direction. The inclination of the tool permits optimization of the contact area when FSW sheets have dissimilar thicknesses. The inclination angle was generated by tilting the clamping assembly. Due to the strong link between mechanical properties and welding parameters [8], a systematic approach to selecting appropriate welding parameters is needed. Within this study, welding parameters were selected by performing an extensive parametric study according to the procedure followed in the EADS welding center. Initially, an extensive set of welding parameter variations were selected in the range of commonly used settings. Parameters included in the parametric study were: rotational speed, welding feed, inclination angle (θ), and pin/shoulder diameters. The welding was carried out by using the selected variations and the resulting welds were examined to determine appropriate welding parameters.

Table 6.1. The material and thickness configurations used in the welding matrix.

#	material I	t_1	material II	t_2 (mm)	t_1 / t_2
1	2024-T3	2.0	2024-T3	2.0	1.0
2	2024-T3	2.0	2024-T3	1.2	1.7
3	2024-T3	2.5	2024-T3	2.0	1.3
4	2024-T3	2.0	7075-T6	2.0	1.0
5	7075-T6	2.0	7075-T6	2.0	1.0

Table 6.2. The welding parameters determined during the parametric study.

#	α	θ	shoulder diam.	pin diam. (mm)	rot. speed (min^{-1})	travel speed (mm/min)	control	force (kN)
1	2°	0	12	3	1200	400	position	8.0-9.0
2	2°	2.1°	6	3	1500	150	position	3.5
3	2°	2.1°	6	3	1500	150	position	3.7
4	2°	0	13	3	1200	400	position	9.5
5	2°	0	12	5	400	100	force	12.0

Four criteria were used to evaluate the welds. First, visual inspection: a continuous and visually defect-free weld seam was required to pass visual inspection. Secondly, the amount of the thickness-decrease should not be more than 0.2 mm. The third criterion was the minimum bending angle. Three samples of each weld, taken from the beginning, middle, and end of the weld, were prepared for the three-point bend test. The test was continued up to the onset of failure to compare the failure bending angles of the welds. The final criterion was related to the shape of the failure line in the bend test. If the failure occurred along a sharp straight line, the weld was considered to contain a defect. A good weld should fail along a wavy line, meaning that the weld seam is continuous. Besides the standard parameters, the relative placement of the sheets with respect to the tool rotation and movement was investigated in the cases where two different alloys were welded. The results from the performed bending test showed that the low strength material should be placed at the advancing side and the high strength material at the retreating side. In the case of the sheets with dissimilar thicknesses, the positioning of the pin is an important issue. By examining the resulting welds, it was revealed that the best results are obtained when the pin is shifted by 0.8 mm towards the thinner material. The final weld parameters were selected based on the parametric study and are listed in Table 6.2. The welds were produced by using these parameters. The welds for which the actual welding parameters deviated from the welding parameters presented in this table were discarded. After welding, the welds were naturally aged for a minimum of 45 days to ensure consistent and optimal mechanical properties.

6.2. Microstructural features

Experiments. Metallographic samples were cut from the welds and mounted, ground, and polished up to 1 μm and electrochemically etched using a Baker etching agent (5 g HBF_4 35% dissolved in 200 ml distilled water). An optical microscope with digital camera, polarization and ¼ lambda filters was used to capture the microstructure. Scanning electron microscopy samples were prepared similarly. For the welds from configuration number 4, the analysis of the alloying elements was carried out by using the energy dispersion spectrometer (EDS); beam energy = 15 kV, magnification 200x, count rate = 2000 s^{-1}.

Chemical composition. The EDS analysis was conducted for configuration 4 to reveal the chemical composition of the stirring zone. The line of measurement was in the middle of the cross section. The weight percent of Cu, Zn and Mg, the principal elements of the 2024 and 7075, vs. the distance from the weld centerline are depicted in Figure 6.1. On the 2024 side, the Cu and Zn contents vary slightly around the average values of 4.7% and 0.2%. Towards the 7075 side of the weld, there is a sudden change of the Cu and Zn content. The Cu and Zn contents reach values of 3.0 wt% and 3.2 wt% at about 0.5 mm to the right of the weld centerline on the 7075 side. The percentages continue to slightly vary around the average values of 1.8% and 5.9% on the 7075 side of the weld. Looking at the composition, two observations can be made. First, chemical mixing occurs in a narrow area in the order of 1 mm wide in the weld nugget. Larsson *et al* studied FSW of 5083 to 6082 [10] in which EDS analysis of the union rings showed only the composition of the two alloys without a chemical mixing zone. This is in line with our findings that the chemical mixing zone is very narrow. Second, the chemical mixing zone is shifted approximately 0.5 mm towards the retreating side (7075) with respect to the weld centerline. Another important observation in this test is the increased concentration of Mg in the WN/TMAZ area on the retreating side up to a distance of 4 mm from the weld centerline. The average Mg content in the 7075 alloy is shown as a dash-dotted line with the standard deviations as dashed lines in Figure 6.1. It must be noted that the Mg concentrations measured by EDS are below the lower limits of the nominal values for the 2024 (0.2 wt % less than the nominal value) [14] and 7075 (1.2 wt % less than the nominal value) [14]. This is a consequence of the lower accuracy of the EDS method for the light elements such as Mg. Despite this, the results are reproducible and the *qualitative* discussion still holds. It is clear that the extra Mg content seen in the right side of Figure 6.1 is significantly more than the standard deviation of the average values. No area with significantly less Mg content was identified in the centerline of the cross section. The EDS line-scanning of the alloying elements in thickness direction indicated a large variation of the Mg content over the thickness. Enrichment of the Mg and large through-thickness variations were also found by Khodir and Shibayanagi [15]. In the Zn-Mg-Cu system, increasing the Mg content, increases the tensile strength and decreases the ductility. This effect is pronounced as the Zn content increases [16]. Therefore, the variation of the Mg significantly changes the mechanical properties of the enriched area and makes it prone to failure during the forming process. This issue will be revisited in the section on the tensile properties of the welds.

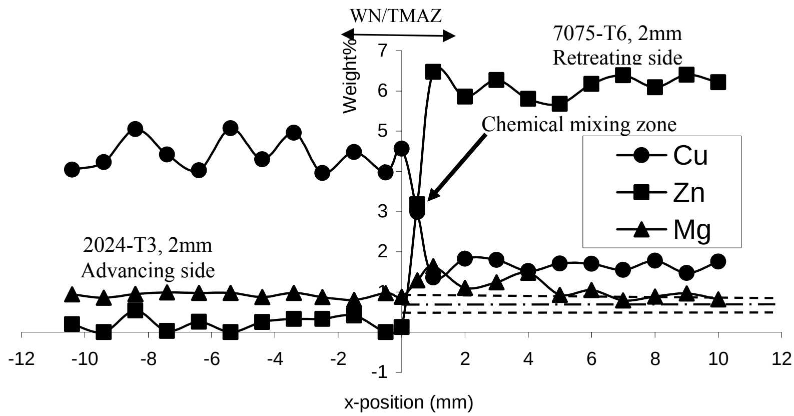

Figure 6.1. The alloying elements in the weld zone measured by SEM-EDS in the middle of the cross section of the weld samples from configuration. A narrow chemical mixing zone is detected to the right of the weld centerline.

Microstructure. The microstructures of the base metals are typical for the cold-rolled aluminum sheets with elongated grains in the rolling direction. Although the grain size was not the same for different thicknesses of the same material. Figure 6.2 shows the stirring zones of three samples of the welds with different configurations.

The size of the WN was found in all cases to be slightly greater than the pin diameter as found by other researchers [17]. The size of the TMAZ was measured to be about 0.4-0.5 mm for configurations number 1 to 4. For configuration number 5, the size of the TMAZ was very small. The classic "onion rings" structure has a different morphology (asymmetric vortex-shaped) for the dissimilar-alloy configuration, Figure 6.2c, than in the case of similar alloys as shown in Figure 6.2a and b, where the onion rings have a regular annular shape. The asymmetric vortex-shaped region is slightly to the right of the weld centerline and coincides with the chemical mixing zone. One of the features of the onion rings most often referred to is the decreasing distance between rings when progressing from the center towards the periphery [18]. While the onion rings structure in Figure 6.2a and b showed this feature, it is absent in configuration 4. There are two contradicting explanations how the onion rings are generated. First, Biallas *et al* [19] suggest that the onion rings are generated due to the reflection of the material flow from the cooler wall of the heat-affected zone, creating the necessity for through mixing of the two sides of the weld. A second hypothesis is provided by Threadgill [20] and Krishnan [18] according to which the onion rings are related to the forward motion of the welding tool making FSW simply an extrusion process in which a number of semi-cylinders are extruded by the welding tool [18]. In the current study, more evidence is found for the latter scenario. First, the results of the EDS analysis show a very narrow chemical mixing zone, smaller than what is expected based on the reflection of the material scenario. Second, in this scenario, the material behind the tool would have to be in the fluid state contradicting the observations reviewed in reference [8]. In fact, the FSW process is mostly considered (e.g. in [21]) to work as a localized cold-working process combining conventional metal working zones of pre-heat, plastic, extrusion, forging, and cool-down. This view supports the second scenario, which attributes the onions rings to the extrusion of the material.

Figure 6.3 shows a micrograph of a sample weld from configuration number 4 which is etched using the Kellers etching reagent. Due to the different etching times of the 2024 and 7075 for this reagent, the material extrusion during FSW can be revealed. This figure clearly shows the extent of the penetration of the extruded material into the base metal. The material from the 7075 sheet has smeared into the 2024 sheet up to a distance of 6 mm from the weld centerline. The extrusion occurs to a larger extent in the upper layers because the shoulder only superficially penetrates into the welded material. The crown shape of the stirring zone is specifically clear at a distance approximately equal to the pin radius. Therefore, the extrusion zone can be divided into two parts: the upper part, related to the shoulder and the lower part, which is limited by the pin diameter.

Figure 6.2a and b show that the welded sheets from the same-alloy configurations have two dominant grain orientations, one dominating in the advancing side and the other in the retreating side. This suggests that the large plastic deformations result in a preferred grain orientation. These are marked in Figure 6.2a and b.

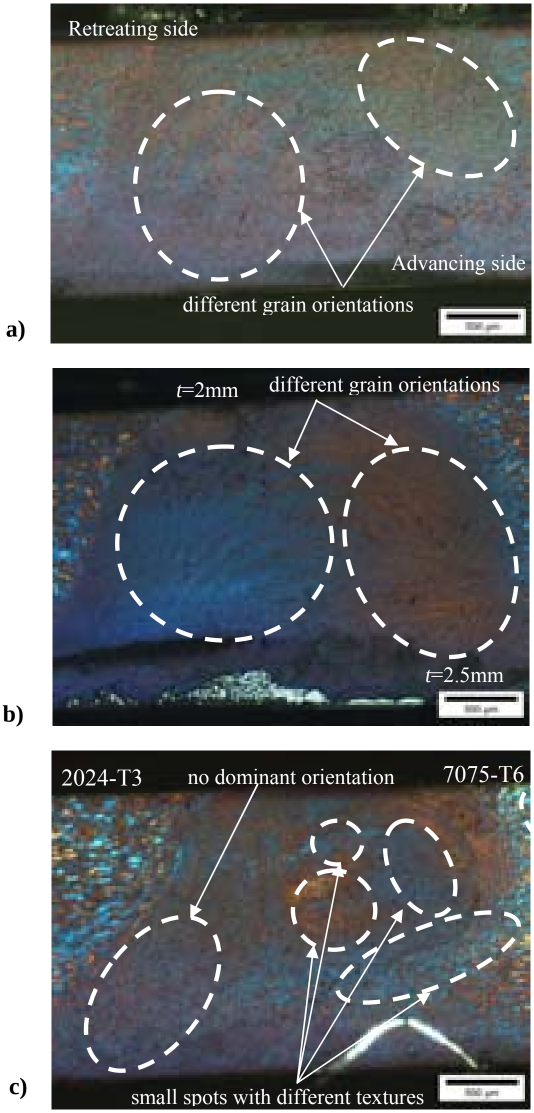

Figure 6.2. The microstructure of the stirring zones of the samples from configurations number 1(a), 3(b), and 4(c) observed by optical microscope (Baker etching reagent). Onion rings structures are present in subfigures a and b. The stirring zone tends to have a heterogeneous texture. A vortex-shape zone, which is coincident with the chemical mixing zone, is observed to the right of subfigure c.

Quantitative texture studies of the FSW have shown that the effects of the tool shoulder on texture evolution are limited to the upper surface of the sheet and the texture evolution in the weld nugget is largely due to the pin motion [22]. It was shown that the measured texture at the weld centerline is mainly composed of a shear component [22]. Due to different velocity fields, in the advancing side, the shear component rotates around the pin axis in the counter-clockwise direction and on the retreating side, the shear component rotates around the pin axis but in the clockwise direction resulting in two different orientations on either side of the weld [22].

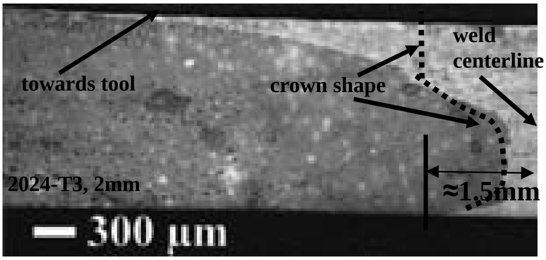

Figure 6.3. The stirring zone of a sample from configuration number 4 (Kellers etching reagent, 25x). The different etching responses of the 2024 and 7075 helps to reveal the material extrusion during FSW.

The dominant grain orientation is significantly different for configuration number 4 as shown in Figure 6.2c. While in Figure 6.2a and b there are two different grain orientations, in configuration 4, the grain orientation distribution is much more complicated. In the advancing side (2024), no dominant grain orientation can be recognized but on the retreating side there are sub-areas with a dominant grain orientation (Figure 6.2c). The individual rings within the “onion ring” structure observed in Figure 6.2a and b have different crystallographic orientations. This is in agreement with the findings of Prangnell and Heason [23]. The rings are apparently resulting from the periodic flow of material around the rear of the pin [23, 24]. The spacing between onion rings in Figure 6.2a and b is approximately equal to the tool advancement per revolution.

Another interesting feature of the welds is the gradient in grain orientation of single rings. In Figure 6.2b, for example, following each single ring, it can be seen that the orientation of the grains, within the ring, gradually changes progressing from the advancing side to the retreating side. The heterogeneous nature of the texture as well as the ring-shape structure of the texture is in agreement with the findings of previous researchers [25]. In summary, for the same-alloy configurations, the basic microstructural features of the weld zone are not much affected when the thickness ratio of the sheets changes. Furthermore, the microstructural features of the weld zone for the different-alloy configuration are different from those of the same-alloy configurations.

6.3. Mechanical properties

Experiments. The hardness measurement samples were mounted, ground, and polished up to 3 µm prior to the measurement. An automatic Vickers micro hardness indenter was used with a fixed load of 200 g. The distance between indentations was set between 0.2 mm to 0.4 mm depending on the expected complexity of the hardness profile. The tensile test specimens were prepared in two different conditions: as-welded and machined. For the as-welded samples, the samples were cut and machined to the standard dog-bone shape (gauge length: 70 mm, gauge width: 10mm). The top surface (the surface close to the welding tool) of the machined samples was milled to reach a uniform thickness throughout the specimen primarily because the typical roughness of the weld seam is too high for direct application in the aircraft structures, particularly under dynamic loading conditions. Moreover, the thickness difference in configurations 2 and 3 can result in stress concentrations at the transition line. The loading direction of the samples was perpendicular to the welding direction. Six samples were tested for each series of the specimens using a Zwick/Roell static test machine and a constant rate of 5 mm/min.

Hardness profiles. The hardness profiles of all weld configurations (measured along the line bisecting the thickness) are shown in Figure 6.4 to Figure 6.6. Clearly shown is that welding has created a highly heterogeneous hardness distribution which needs a detailed explanation. It has been widely accepted that the softening effect of FSW is due to dissolution and/or coarsening of the precipitates [8]. After welding, re-precipitation of the dissolved particles increases the hardness values [8]. The minima in the hardness profiles correspond to the areas in which re-precipitation is not possible due to lack of a super-saturation of precipitating elements [8]. Furthermore, the hardness profile is asymmetric for all configurations. Generally, the sheet at the advancing side has a higher hardness compared to the one at the retreating side, which has been observed in other studies as well [26], resulting from different deformations at both sides. The material at the advancing side is influenced more and for a longer time by the vortex velocity field because they have different directions on the retreating side but the same direction on the advancing side [27]. Therefore, the straining and grain refinement is more severe on the advancing side [27]. Moreover, the size of the HAZ in the advancing side is always smaller than at the retreating sides as can be seen in Figure 6.4 to Figure 6.6. This can be explained by analyzing the temperature profile around the weld centerline which has been shown to be asymmetric [27, 28]. The larger extension of the high-temperature iso-lines in the retreating side, as shown by Nandan *et al* [28], explains why the HAZ is 3 to 7 mm wider on the retreating side. In Figure 6.4 to Figure 6.6, a softened region is present in the WN due to the dissolution and precipitation of coarse particles at the high temperature during welding [8, 29]. For 7075, the hardness of the weld nugget (140 HV) is significantly less than that of the base metal (170 HV) but more than the minimum in the heat-affected zone (120 to 130 HV). In the hardness profile of 7075, two hardness minima can be observed on either side of the WN. The hardness profile of 2024 is much more complicated. A number of local hardness peaks and minima around the weld centerline can be observed. The hardness peaks near to or within the WN are about 150 HV, which is equal to the hardness of the BM. In these welds, the difference between the hardness values of the base metal and the local peaks is much less than in the case of the 7075 welds, as a result of the difference in the nominal natural aging times between 2000 and 7000 series alloys, a few days versus several years [30].

a)

b)

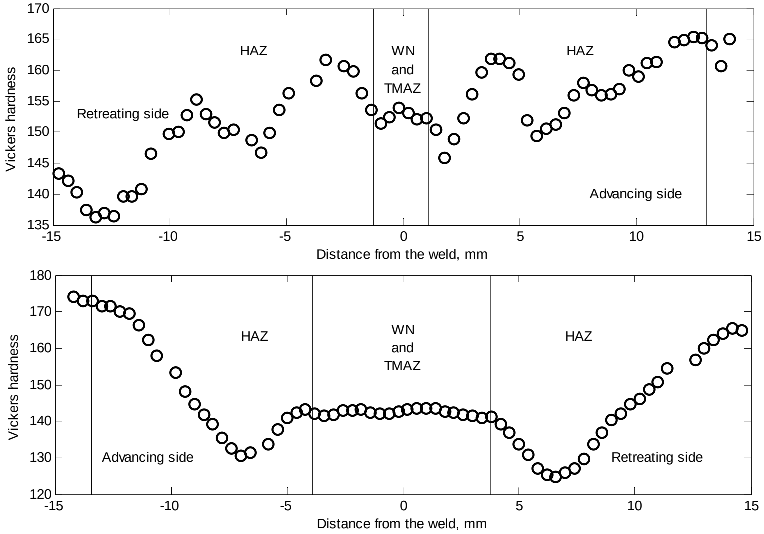

Figure 6.4. The microhardness profile for configurations number 1(a) and 5(b) measured by the automatic microindenter (load=200 g, indentations distance= 0.3 to 0.4 mm). The profile trends are different for the 2024 (a) and 7075 (b) and the hardness profiles are asymmetric with respect to the weld centerline.

The difference between the natural aging times alone can not explain the difference between the hardness profiles of the 2024 and 7075 and the dislocation densities have to be taken into account. It is shown that FSW has a major impact on the distribution of the dislocation density and creates a non-homogenous distribution of the dislocation density [31]. The mechanical properties of the 2024 are much more sensitive to the dislocation density distribution than those of the 7075. Therefore, it can be argued that the local peaks and minima in the hardness profiles of 2024 are related to the effects of the non-homogeneous dislocation density. Indeed, thermal modeling of FSW of the 2024 has shown that if the effects of the dislocation density are left out of the model, the predicted hardness profile is essentially similar to that of the 7075 [32]. Taking the effects of the non-homogenous dislocation density into account can improve the predicted hardness profile matching the actual hardness profile including the peaks and minima [32].

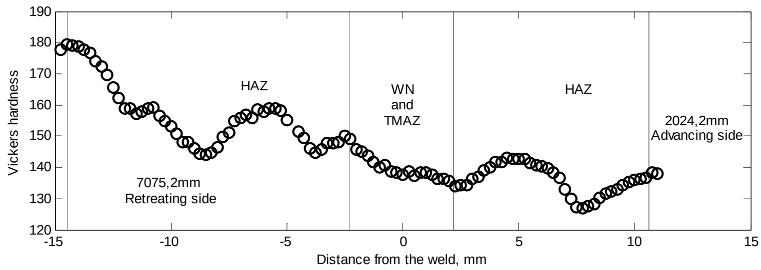

Figure 6.5. The microhardness profile for configuration number 4 (load=200 g, indentations distance= 0.2 mm).

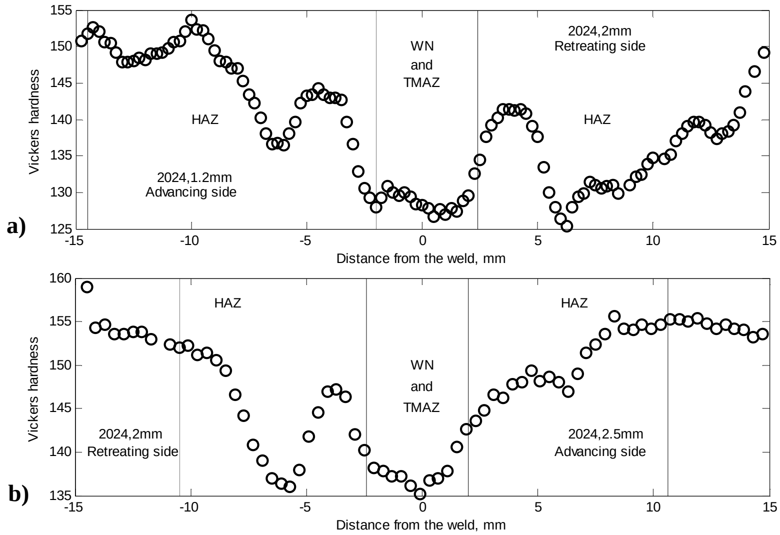

Figure 6.6. The microhardness profile for configurations 2 (a) and 3 (b) (load=200g, indentations distance= 0.2 to 0.3mm)

The hardness profile of the welds from configuration 4, Figure 6.5, shows that both sides of the weld are similar to that of the 2024 alloy. However, the hardness profile of the welds from configuration 4 can not be easily described because the effects of the chemical mixing and extrusion of two dissimilar alloys on the hardness profile of the weld are not known.
Ultimately, the FSW TMBs will be formed into their final shape. Therefore, the large variations of the hardness and mechanical properties within FSW blanks have to be analyzed from the formability point of view. According to the Marciniak-Kuczynski theory [33], any variation of the thickness or mechanical properties of the sheets results in localization of the strain in the imperfection zone. Therefore, the zones

with lower hardness may cause sheet metal instability and, as a result, premature failure.

Table 6.3. The summary of the tensile testing.

configuration			nr. 1		nr. 2		nr. 3		nr. 4		nr. 5	
			W[1]	M[2]	W	M	W	M	W	M	W	M
BM1[5]	σ_y (MPa)	AV[3]	418		418		418		418		533	
		SD[4]	2		2		2		2		2	
	$\sigma_{\max}$ (MPa)	AV	580		580		580		580		651	
		SD	3		3		3		3		2	
	$\varepsilon_{F_{\max}}$ (%)	AV	18.2		18.2		18.2		18.2		11.2	
		SD	0.1		0.1		0.1		0.1		0.2	
FSW	σ_y (MPa)	AV	379	384	416	307	409	322	411	399	478	477
		SD	3	2	4	16	45	14	4	1	4	4
	$\sigma_{\max}$ (MPa)	AV	424	483	530	382	471	384	442	441	513	511
		SD	13	4	4	9	15	13	14	4	10	3
	$\varepsilon_{F_{\max}}$ (%)	AV	7.4	10.4	10.0	4.1	7.7	5.5	6.5	6.9	7.6	7.1
		SD	0.79	0.75	0.89	0.36	1.4	0.84	0.7	0.62	0.42	0.16
BM1 - FSW	$\Delta\sigma_y$	MPa	-39	-34	-2	-111	-9	-97	-8	-19	-55	-56
		%	-9	-8	-1	-26	-2	-23	-2	-4	-10	-11
	$\Delta\sigma_{\max}$	MPa	-156	-97	-50	-198	-109	-196	-138	-139	-138	-140
		%	-27	-17	-9	-34	-19	-34	-24	-24	-21	-22
	$\Delta\varepsilon_{F_{\max}}$	%	-11	-8	-8	-14	-10	-13	-12	-12	-4	-4
		%	-59	-43	-45	-77	-58	-69	-64	-68	-33	-37
BM2[6]	σ_y (MPa)	AV	418		388		370		533		533	
		SD	2		0		2		2		2	
	$\sigma_{\max}$ (MPa)	AV	580		539		576		651		651	
		SD	3		0		2		2		2	
	$\varepsilon_{F_{\max}}$ (%)	AV	18		12.3		14.8		11.2		11.2	
		SD	0.1		0.3		0.6		0.2		0.2	
BM2 - FSW	$\Delta\sigma_y$	MPa	-39	-34	27	-81	39	-48	-122	-134	-55	-56
		%	-9	-8	7	-21	11	-13	-23	-25	-10	-11
	$\Delta\sigma_{\max}$	MPa	-156	-97	-9	-156	-105	-193	-209	-210	-138	-140
		%	-27	-17	-2	-29	-18	-33	-32	-32	-21	-22
	$\Delta\varepsilon_{F_{\max}}$	%	-11	-8	-2	-8	-7	-9	-5	-5	-4	-4
		%	-59	-43	-19	-66	-48	-63	-42	-48	-33	-37
failure location			WN	WN	WN:4 HAZ:1	WN	WN	WN	TMAZ (7075)	TMAZ (7075)	HAZ:5 BM:1	HAZ

Table Abbreviations
[1]**W**: As-Welded condition, [2]**M**: Machined condition, [3]**AV**: Average, [4]**SD**: Standard Deviation, [5]**BM1**: Base Metal I, [6]**BM2**: Base Metal II

Tensile properties. The results of the tensile tests are summarized in Table 6.3. For configurations 1 and 5, a small decrease in yield strength (8-10%) and a moderate decrease in the tensile strength (17-27%) is observed. However, the decrease in the elongation of configuration 1 (42-59%) is larger than that of configuration 5 (32-36%). Table 6.3 also shows that the mechanical properties of the as-welded specimens from configurations 2 and 3 are slightly lower than those of the base metals and failure almost always occurs in the weld nugget. However, the mechanical properties of the as-welded specimens are significantly better than those of the machined specimens. There are two basic active mechanisms in the tensile testing of the as-welded and machined specimens. First, due to presence of the thickness difference, the stress concentration occurs at the transition line from one thickness to the other [34]. Second, the thickness gradually changes from the smaller to the larger thickness as a result of the welding process. In fusion welding, the change of the thickness occurs over a length approximately equal to the thickness of the thinner sheet [35], while in FSW, this length is much larger and is determined by the shoulder diameter.

This gradual change has two implications. First, the stress concentration factor is lower for FSW than for fusion welding. Second, the most failure-prone zone (i.e. WN) has a larger thickness with respect to the thin sheet, resulting in a gradual change in stress along the gauge length during the tensile test. While the stress concentration lowers the mechanical properties, the gradual change of the thickness improves the mechanical properties of the as-welded specimens compared to the machined specimens. The tensile tests show that the gradual change of the thickness is more important. This is an important point from the manufacturing viewpoint where maximum possible formability is required, because the roughness of the as-welded blanks exceeds the maximum levels allowed by the aircraft-manufacture criteria [36] and, thus, machining seems to be unavoidable. However, a careful design of the machining process is needed such that the formability of the sheets is not much influenced.

Table 6.3 shows that the specimens from configuration 1 always fail in the middle of the weld nugget, while the specimens from configuration 5 almost always fail in the heat-affected zone. The failure locations of configuration 5 coincide with the hardness minima observed in Figure 6.4b, suggesting different failure mechanisms for these two configurations. Study of the failed specimens showed that with configuration 5, necking occurred before failure while no considerable neck development was observed in the specimens from configuration 1.

The yield and tensile strength as well as the ductility of the specimens from configuration 4 were slightly lower than those of the specimens from configuration number 1 and notably lower than those of the specimens from configuration 5. Failure occurred in the TMAZ zone (7075 side) near the areas where high Mg content was observed. High Mg content in Al-Cu-Mg systems lowers the ductility [16], resulting in the failure in the TMAZ (7075 side) away from the place where lowest hardness values were measured. No substantial necking developed in the fracture zone of the specimens from configuration 4. The results of the tests showed that the machining improves the straining limits and tensile strength of the specimens from configuration number 1 by 14% and 41%, respectively. This could be expected since the machining eliminates the notches from the weld seam and lowers its roughness. However, the difference between the tensile strength of the as-welded and machined specimens is negligible (0.2-0.4%) for configurations 4 and 5. Similarly, the elongation of the specimens from configurations 4 and 5 is only slightly (5.2% to 6.4%) different. Therefore, improvements of the mechanical properties by machining can only be observed for the welds from configuration 1. For configuration 5, this is the result of the failure location which is in the HAZ and improvement of the surface at the weld nugget does not influence the mechanical properties of the HAZ. For the welds from configuration 4, the failure was found mainly related to the embrittlement caused by the high Mg content and therefore the improvement of the surface at the weld nugget does not help to postpone the failure.

6.4. Conclusions

FSW of sheets with dissimilar alloys or dissimilar thicknesses was studied in this chapter. The microstructural features, chemical composition, hardness profiles, and mechanical properties were studied and compared. The main conclusion of the study is that the microstructural features and hence mechanical properties of the welds were significantly different from those of the same-alloy same-thickness welds. These variations may result in additional instability mechanisms and premature failure. Furthermore, the results show that for the different configurations of the 2024 sheets, the failure always occurs at the WN. Therefore, the machining and forming processes have to be carefully designed such that the weld line is kept away from the large-strain areas. Other conclusions which can be drawn from this work are as follows:

- The chemical mixing is limited in width (<1 mm). Mg has segregated the weld centerline at the 7075 side.
- The classical onion ring structure was observed in the WN. Subsequent rings have different grain orientations and the texture of the stirring zone tends to be heterogeneous.
- Dissolution and coarsening of the precipitates result in a softened region in the stirring zone. The hardness profile is asymmetric. Hardness values at the advancing side are higher than at the retreating side and the heat-affected zone is larger on the retreating side.
- The yield and tensile strengths as well as the elongation are decreased after FSW, but are strongly dependent on the weld configuration. The relative decrease in the yield and tensile strengths are lower than that of the elongation. Machining has a major impact on the measured properties (strength, etc) of the welds which is not always positive.
- Machining has a major impact on the elongation and other mechanical properties of the welds. Therefore, a careful design of the post-weld machining process is needed.

6.5. References

[1] R. S. Mishra and W. H. Murray, "Friction Stir Welding and Processing," Materials Park, Ohio: ASM International, 2007.

[2] S. H. Kazi and L. E. Murr, "Complex flow phenomena associated with friction-stir welding of aluminum alloys," in *Friction Stir Welding and Processing Conference*, Indianapolis, IN, 2001, pp. 139-150.

[3] Y. Li, L. E. Murr, and J. C. McClure, "Solid-state flow visualization in the friction-stir welding of 2024 Al to 6061 Al," *Scripta Materialia,* vol. 40, pp. 1041-1046, 1999.

[4] L. E. Murr, Y. Li, E. A. Trillo, and J. C. McClure, "Fundamental issues and industrial applications of friction-stir welding," *Materials Technology,* vol. 15, pp. 37-48, 2000.

[5] L. E. Murr, R. D. Flores, O. V. Flores, J. C. McClure, G. Liu, and D. Brown, "Friction-stir welding: Microstructural characterization," *Materials Research Innovations,* vol. 1, pp. 211-223, 1998.

[6] Y. Li, E. A. Trillo, and L. E. Murr, "Friction-stir welding of aluminum alloy 2024 to silver," *Journal of Materials Science Letters,* vol. 19, pp. 1047-1051, 2000.

[7] L. E. Murr, G. Sharma, F. Contreras, M. Guerra, S. H. Kazi, M. Siddique, R. D. Flores, D. J. Shindo, K. F. Soto, and E. A. Trillo, "Joining dissimilar aluminum alloys and other metals and alloys by friction-stir welding," in *TMS 2001 Annual Meeting Aluminum Automotive and Joining Symposia; New Orleans, LA; USA; 12-14 Feb.*, 2001.

[8] R. S. Mishra and Z. Y. Ma, "Friction stir welding and processing," *Materials Science and Engineering R-Reports,* vol. 50, pp. 1-78, Aug 31 2005.

[9] R. J. Lederich, J. A. Baumann, and P. A. Oelgoetz, "Friction Stir Welding of D357 castings and 2024 wrought products," in *Friction Stir Welding and Processing Conference*, Indianapolis, IN, 2001, pp. 71-81.

[10] H. Larsson, L. Karlsson, S. Stoltz, and E. Bergqvist, "Joining of dissimilar Al alloys by friction stir welding " in *Second International Symposium on Friction Stir Welding*, Gothenburg, Sweden, 2000.

[11] S. Liu and Y. J. Chao, "Determination of global mechanical response of friction stir welded plates using local constitutive properties," *Modelling and Simulation in Materials Science and Engineering,* vol. 13, pp. 1-15, Jan 2005.

[12] G. Buffa, L. Fratini, and R. Shivpuri, "Finite element studies on friction stir welding processes of tailored blanks," *Computers & Structures,* vol. 86, pp. 181-189, 2008.

[13] L. Fratini, G. Buffa, and R. Shivpuri, "Improving friction stir welding of blanks of different thicknesses," *Materials Science and Engineering A,* vol. 459, pp. 209-215, 2007.

[14] T. A. Association, *International Alloy Designations and Chemical Composition Limits for Wrought Aluminum and Wrought Aluminum Alloys (Teal sheets)*. Washington: The Aluminum Association, 2006.

[15] S. A. Khodir and T. Shibayanagi, "Friction stir welding of dissimilar AA2024 and AA7075 aluminum alloys," *Materials Science and Engineering B,* vol. 148, pp. 82-87, 2007.

[16] J. E. Hatch, *Aluminum: Properties and Physical Metallurgy*. Metals Park, Ohio: ASM International, 1984.

[17] A. P. Reynolds, "Visualisation of material flow in autogenous friction stir welds," *Science and Technology of Welding and Joining,* vol. 5, pp. 120-124, 2000.

[18] K. N. Krishnan, "On the formation of onion rings in friction stir welds," *Materials Science and Engineering A,* vol. 327, pp. 246-251, 2002.

[19] G. Biallas, R. Braun, C. Dalle Donne, G. Staniek, and W. A. Kaysser, "Mechanical properties and corrosion behaviour of friction stir welded 2024-T3," in *1st International Symposium on Friction Stir Welding*, Thousand Oaks, California, 1999.

[20] P. L. Threadgill, "Friction-Stir Welding-State of the Art," The Welding Institute (TWI) Report 678, 1999.

[21] W. J. Arbegast, "Modeling friction stir joining as a metal working process," in *TMS Annual Meeting*, San Diego, CA, 2003, pp. 313-327.

[22] Y. S. Sato, H. Kokawa, K. Ikeda, M. Enomoto, S. Jogan, and T. Hashimoto, "Microtexture in the friction-stir weld of an aluminum alloy," *Metallurgical and Materials Transactions A,* vol. 32, pp. 941-948, Apr 2001.

[23] P. B. Prangnell and C. P. Heason, "Grain structure formation during friction stir welding observed by the `stop action technique'," *Acta Materialia,* vol. 53, pp. 3179-3192, 2005.

[24] K. A. A. Hassan, P. B. Prangnell, A. F. Norman, D. A. Price, and S. W. Williams, "Effect of welding parameters on nugget zone microstructure and properties in high strength aluminium alloy friction stir welds," *Science and Technology of Welding and Joining,* vol. 8, pp. 257-268, Aug 2003.

[25] D. P. Field, T. W. Nelson, Y. Hovanski, and K. V. Jata, "Heterogeneity of crystallographic texture in friction stir welds of aluminum," *Metallurgical and Materials Transactions A,* vol. 32, pp. 2869-2877, Nov 2001.

[26] Y. S. Sato, S. H. C. Park, and H. Kokawa, "Microstructural factors governing hardness in friction-stir welds of solid-solution-hardened Al alloys," *Metallurgical and Materials Transactions A,* vol. 32, pp. 3033-3042, Dec 2001.

[27] P. Heurtier, M. J. Jones, C. Desrayaud, J. H. Driver, F. Montheillet, and D. Allehaux, "Mechanical and thermal modelling of friction stir welding," *Journal of Materials Processing Technology,* vol. 171, pp. 348-357, Feb 1 2006.

[28] R. Nandan, G. G. Roy, T. J. Lienert, and T. Debroy, "Three-dimensional heat and material flow during friction stir welding of mild steel," *Acta Materialia,* vol. 55, pp. 883-895, Feb 2007.

[29] T. S. Srivatsan, S. Vasudevan, and L. Park, "The tensile deformation and fracture behavior of friction stir welded aluminum alloy 2024," *Materials Science and Engineering A,* vol. 466, pp. 235-245, 2007.

[30] J. R. Davis, *Aluminum and Aluminum Alloys- ASM Speciality Handbook*. Materials Park, Ohio: ASM International, 1993.

[31] L. E. Murr, G. Liu, and J. C. McClure, "Dynamic recrystallization in friction-stir welding of aluminium alloy 1100," *Journal of Materials Science Letters,* vol. 16, pp. 1801-1803, Nov 15 1997.

[32] H. R. Shercliff, M. J. Russell, A. Taylor, and T. L. Dickerson, "Microstructural modelling in friction stir welding of 2000 series aluminium alloys," *Mecanique et Industries,* vol. 6, pp. 25-35, 2005.

[33] Z. Marciniak and K. Kuczynski, "Limit strains in the process of stretch-forming sheet metal," *International Journal of Mechanical Sciences,* vol. 9, pp. 609-620, 1967.

[34] M. Uchihara and K. Fukui, "Performance of tailor welded blanks using automotive highs trength steel sheets for practical use," *Welding International,* vol. 20, pp. 622-632, 2006.

[35] *ASM Handbook volume 6, Welding, Brazing, and Soldering*. US: ASM International, 1993.

[36] A. A. Zadpoor, J. Sinke, and R. Benedictus, "Experimental and numerical study of machined aluminum tailor-made blanks," *Journal of Materials Processing Technology*, vol. 200, pp. 288-299, 2008.

7. Friction stir welded blanks II

This chapter studies the properties of a wide range of friction stir welded joints with dissimilar aluminum alloys and/or thicknesses. Two aluminum alloys, namely 2024-T3 and 7075-T6, are selected for the study and are welded in ten different combinations of alloys and thicknesses. The welding parameters are optimized for the configurations and a systematic study of the effects of material and thickness combinations on the microstructural features, global and local mechanical properties, and fracture mechanisms of the welds is carried out. It is shown that the dissimilar materials are extruded into each other, the texture is heterogeneous in the weld zone, and that there is no significant diffusion of alloying elements between the alloys. For most configurations, the local and global mechanical properties decrease as the thickness ratio increases. The local yield strength and plasticity parameters substantially vary next to the weld centerline, hence requiring their implementation in FEM models. Machining to obtain a constant thickness significantly influences the mechanical properties of the welds. The fracture mechanism is found to be a mixture of ductile and brittle fractures and to qualify for the term “quasi-cleavage”.

FSW blanks exhibit highly heterogeneous microstructural features [1] and mechanical properties [2]. The link between heterogeneous microstructure and heterogeneous mechanical properties as well as the plasticity features of FSW TMBs must be known because any application of the technology requires availability of such data as input for material selection, structure design, and manufacture planning. There has been a vast body of research addressing the different aspects of FSW blanks including some studies of FSW blanks with dissimilar materials or different thicknesses. A summary of the studies on dissimilar-material FSW is presented in the Table 24 of reference [3]. The studies of FSW with dissimilar thicknesses are rarer, see e.g. [4]. Very limited knowledge of FSW blanks with simultaneously dissimilar alloys and thicknesses is available in the open literature. The main purpose of this chapter is to provide an integrated study of the different types of FSW TMBs and to contribute towards understanding how the thickness and material difference affects the microstructure and global and local mechanical properties of FSW TMBs. An extensive test matrix comprising ten different configurations (Table 7.2) is considered. The designed test matrix allows for the study of not only the independent effects of dissimilar thickness and dissimilar alloy but also their combined effects. Three different thicknesses of 2024-T3 and 7075-T6 sheets are used for welding. For each series, a parametric study is conducted to optimize the welding parameters. This is an important step to make the welds from different configurations comparable and to isolate the effects of the welding procedure from those of the TMB design parameters to the maximum possible extent. The microstructural features and the global and local mechanical properties of the welds as well as their fracture mechanism are presented. The grain morphology, material mixing and chemical composition, and qualitative evolution of the texture due to FSW have been studied. Although some researchers have previously studied the local mechanical properties of FSW blanks [2, 5, 6], the local mechanical properties of the welds with different materials and/or different thicknesses are not studied yet. Furthermore, there is a lack of data needed for the numerical simulation of the forming processes and formability prediction of FSW TMBs. Important examples of such data are the strain hardening exponents, strength coefficients, and anisotropy parameters. In Chapter 10, it will be shown that the implementation of the mechanical properties of the different weld zones is crucial for accurate FEM modeling of FSW TMBs. The data presented in this chapter partially fills the gap. The fracture surfaces of the welds are inspected with SEM and the fracture mechanism is discussed.

Table 7.1. The true properties of the base metals.

no.	material	t	σ_y	$\sigma_{\max}$	$\varepsilon_{F_{\max}}$	K	n
i	2024-T3	2.0	418±2	580±3	18.2±0.1	913±12	0.27±0.00
ii	2024-T3	1.2	388±0	539±0	12.3±0.3	700±5	0.13±0.00
iii	2024-T3	2.5	370±2	576±2	14.8±0.6	791±2	0.16±0.00
iv	7075-T6	2.0	533±2	651±2	11.2±0.2	773±3	0.08±0.00
v	7075-T6	1.2	557±1	655±2	10.2±0.4	778±3	0.08±0.00
vi	7075-T6	2.5	554±1	649±1	10.2±0.1	761±2	0.07±0.00

7.1. Materials and methods

Welding procedure. The details of the welding procedure were discussed in the previous chapter. Table 7.2 presents the weld parameters for all ten configurations studied in this chapter.

Experiments. Metallographic samples were cut from the welds and mounted, ground, and polished up to 1 μm and electrochemically etched using a Baker etching agent (5 g HBF4 35% dissolved in 200 ml distilled water). Optical microscopy with digital camera, polarization and ¼ lambda filters were used to visualize the microstructure. The grain morphology was studied through optical microscopy. The texture pattern was studied qualitatively taking advantage of the fact that grains with different crystallographic orientations reflect the polarized light differently.

The mechanical properties of the base metals were characterized through a dedicated series of tensile testing (Table 7.1). The dimensions of the tensile test specimens, throughout this study, are according to the full-size standard specimen as described in the ASTM E8 (metric) standard. The tensile test specimens of the welds were prepared in two different conditions: as-welded and machined. For the as-welded specimens, the weld samples were edge-milled to the standard full-size dog-bone shape as specified in ASTM E8 without any modification through the thickness. The machined specimens were not only milled at the edges to the same dog-bone shape, but also shaved on top to reach a uniform thickness all-over the specimen, thereby eliminating the thickness differences. The weld line was perpendicular to the loading direction for all the specimens. The specimens were tested at a constant deformation rate of 2 mm/min. A digital Image Correlation (DIC) system was used to measure the local mechanical properties of the machined specimens. Therefore, the top surface of the specimens was covered by a speckle ink pattern. A high-resolution digital camera capable of automatically photographing the area of interest at a frame rate of up to 7.5 Hz was used to record the morphology of the ink pattern during the tensile testing. The local strain values were calculated by correlating the random patterns in the successive images through a DIC program. The timing of the camera was synchronized with the timing of the test machine. Having the strain values and the corresponding force values, the local stress-strain curves were established. The offset yield strengths were calculated for each local stress-strain curve. The Hollomon's strain hardening equation ($\sigma = K\varepsilon^n$) was fitted to the plastic part of the local stress-strain curves to determine the local values of the strength coefficient, K, and the strain hardening exponent, n. The fracture surfaces of the tensile test specimens were inspected with Scanning Electron Microscopy (SEM). The chemical compositions of the alloys were examined using the Energy Dispersion Spectrometry (EDS) element mapping and spot measurement techniques. The backscatter mode of SEM was used to identify particles and intermetallics.

Table 7.2. The specification of the weld series and corresponding welding parameters.

no.	base metal I	base metal II	α	θ	d	D	ω	ν	F
1	2024-T3, 2mm	2024-T3, 2mm	2	0	12	3	1200	400	8.0-9.9
2	2024-T3, 2mm	2024-T3, 1.2mm	2	2.1	6	3	1500	150	3.5
3	2024-T3, 2.5mm	2024-T3, 2mm	2	2.1	6	3	1500	150	3.7
4	7075-T6, 2mm	7075-T6, 2mm	2	0	12	5	400	100	12.0
5	7075-T6, 2mm	7075-T6, 1.2mm	2	2.1	13	5	400	100	9.5-10.5
6	7075-T6, 2.5mm	7075-T6, 2mm	2	2.1	13	5	400	100	9-10
7	2024-T3, 2mm	7075-T6, 2mm	2	0	13	3	1200	400	9.5
8	2024-T3, 2mm	7075-T6, 1.2mm	2	2.1	13	5	400	100	9-10
9	7075-T6, 2.5mm	2024-T3, 2mm	2	2.1	13	5	400	100	10-11
10	2024-T3, 2.5mm	7075-T6, 2mm	2	2.1	13	5	400	100	8.5-9.5

Table nomenclature and abbreviations
$\boldsymbol{\alpha}$ (deg): weld angle, $\boldsymbol{\theta}$ (deg): inclination angle, $\boldsymbol{d}$ (mm): shoulder diameter, $\boldsymbol{D}$ (mm): pin diameter, $\boldsymbol{\omega}$ (min^{-1}): rotational speed, $\boldsymbol{v}$ (mm/min): travel speed, $\boldsymbol{F}$ (kN): tool force.

7.2. Results and discussion

Microstructural features. Two dissimilar alloys that are joined through FSW experience significant thermomechanical evolution including high strain rate vortices at elevated temperatures and (possibly) local melting that may result in their chemical mixing. There are two questions to be answered: firstly, does FSW result in chemical mixing? Secondly, do the alloying elements diffuse during FSW or not? Figure 7.1a depicts the microstructure of the stirring zone of a representative weld (configuration 8). As is clear from this figure and was observed for other configurations as well, there is a dividing line between the two alloys which implies that the alloys are not chemically mixed. This is in line with the findings of previous studies in which no or very limited chemical mixing was found [7-9]. Figure 7.1b presents the EDS mapping of Zn for the same representative weld. Since 7075-T6 has a significant amount (5.1-6.1%) of Zn and the Zn content of 2024-T3 is negligible (<0.254%), Zn element mapping can distinguish between the two alloys. The boundaries of Zn-rich zones are matching the observed microstructural lines, meaning that the dissimilar alloys are not chemically mixed (other weld configurations showed similar traits). Indeed, FSW has been suggested to work as a localized cold-working process combining conventional metal working zones of pre-heat, plastic (initial deformation), extrusion, forging, and cool-down. [10]. The dissimilar alloys are merely extruded into each other as can also be seen in Figure 7.4c and Figure 7.4f.

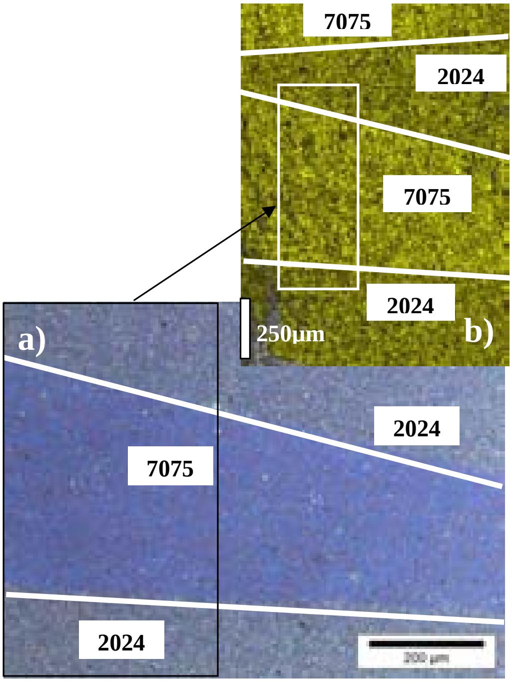

Figure 7.1. The microstructure (a) and EDS Zn element mapping (b) of the WN of a sample weld from configuration 8. The magnifications of subfigures (a) and (b) are 100x and 70x, respectively.

As for whether or not the alloying elements of dissimilar alloys diffuse into each other, there is a disagreement in the literature. While the studies of FSW of 7075 and 6065 [11] and 5083 and 6061 [12] suggest that there is no diffusion, a study of the

FSW of steel and 6013 showed slight diffusion from steel to 6013 [13] and a chemical compositions reported for the welding of 2024-T3 and 7075-T6 shows incomplete diffusion of the elements between the two alloys [7].

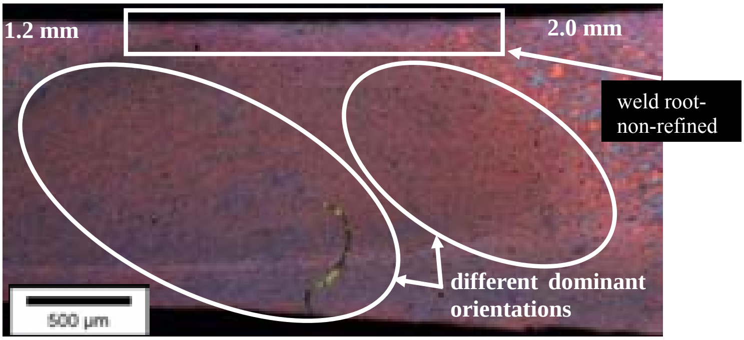

Figure 7.2. The microstructural features of the stirring zone of a sample weld from configuration 2 (magnification 25x).

The thermomechanical mixing of the weld material during the welding process not only extrudes the alloys and brings them close to each other, but also increases the temperature and velocity and lowers the viscosity, thereby increasing the diffusion rate. Whether or not significant diffusion takes place during FSW depends on two parameters: temperature and dwell time. These two parameters are dependent on the welding parameters and the mechanical properties of the base metals. The temperature would be higher if the base metals are harder, because higher tool force would be needed, resulting in more friction. The dwell time is longer if the travel speed of the tool is lower. The alloys used in this study are high strength aerospace alloys and are quite hard and the travel speed is sometimes quite low. Nevertheless, the EDS analysis of the welds with dissimilar alloys showed that there is no significant diffusion of alloying elements from one alloy to the other. Some spot measurements of the Mg, Zn, and Cu contents along a line perpendicular to the boundary between 2024-T3 and 7075-T6 in Figure 7.1a-b (and some similar figures) were carried out. They showed a sudden jump from the chemical composition of one alloy to the chemical composition of the other alloy without any sizable diffusion from one material to the other. A first approximation of the diffusion length ($= 2\sqrt{Dt}$) can be obtained using the Arrhenius equation ($D = D_0 \exp(-Q/RT)$) and the pre-exponential diffusion factors (D_0 =0.6E-6 – 2.0E-5 m^2/s) and activation energies ($Q =$ 100-120 kJ/mole) gathered in [14] for diffusion of Zn, Cu, and Mg in polycrystalline FCC Al. The peak temperatures ($T =$ 550-700 K) and dwell times ($t =$ 10-30 s) were estimated from the graphs presented in reference [15] and its cited references. The diffusion depth was accordingly estimated to be between 0.1-1.6 μm. These values should be used just as an order-of-magnitude indication, because some of the assumptions behind the equations do not hold in FSW. The estimated range of diffusion length is too small to be detected by EDS accurately.

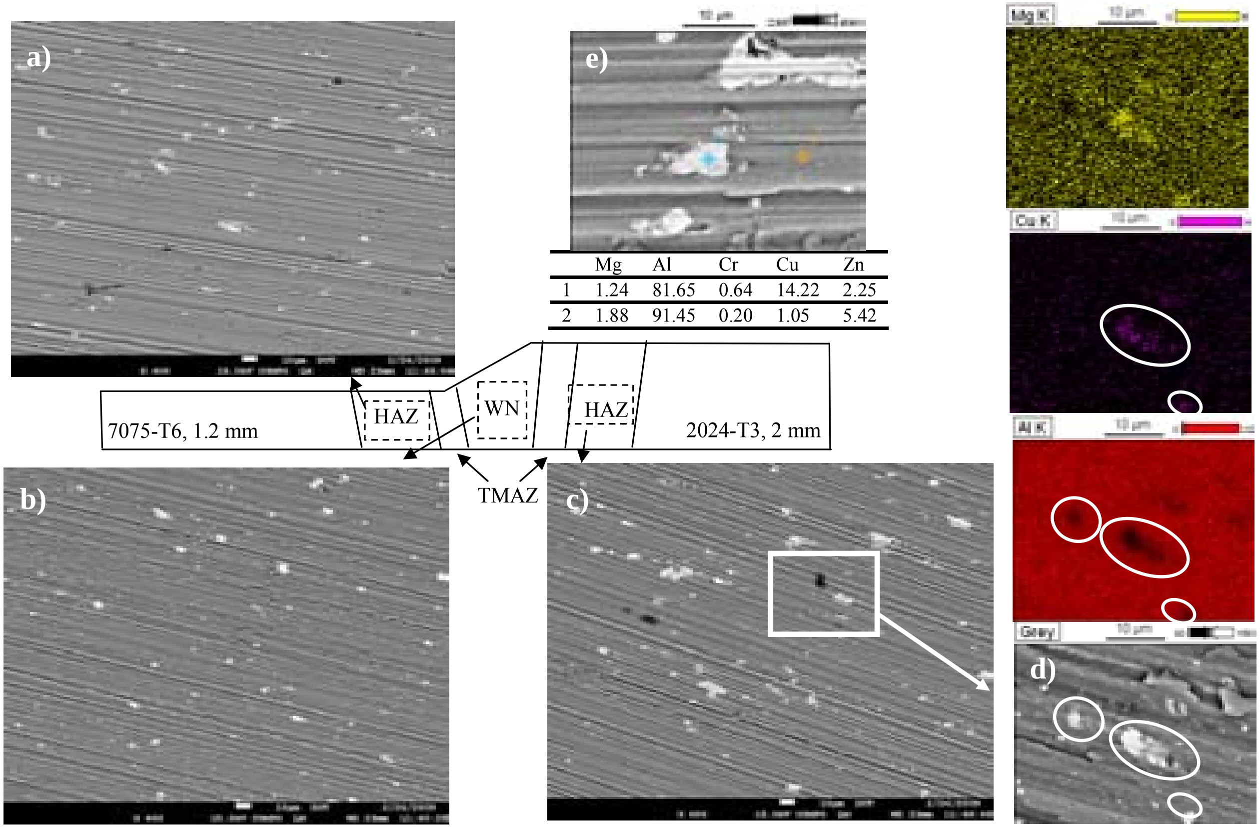

	Mg	Al	Cr	Cu	Zn
1	1.24	81.65	0.64	14.22	2.25
2	1.88	91.45	0.20	1.05	5.42

Figure 7.3. (previous page) The backscatter images of the HAZ of the 70705 (a) and 2024 (b) sides of a sample specimens from configuration 8 along with its WN (c). Two magnified views of the HAZ of the 2024 side (d) and 7075 side (e) is also provided. The EDS element mapping and spot element analysis are carried out for subfigures (d) and (e), respectively.

Figure 7.2c depicts the microstructure of the stirring zone of a sample weld from configuration 2. The grains are highly refined in the Weld Nugget (WN) through dynamic recrystallization (DRX). The classic onion rings structure can be detected in the figure. Interestingly, the dominant grain structure on the advancing side (2024-T3, 1.2 mm) is different from the one on the retreating side (2024-T3, 2 mm). This has to do with the different rotation fields of the shear component of the texture on the advancing and retreating sides. The texture of the WN is measured to be mainly composed of shear component [16]. On the advancing side, the rotation field created by the pin rotates the shear component in the counter-clockwise direction, while the shear component is rotated in the clockwise direction on the retreating side [16]. Therefore, the plastic deformation imposes preferred grain orientation on either side. For configurations 1-3, 4, and 7, the preferred orientation gradually changes from the advancing side towards the retreating side, because individual rings within the onion rings structure gradually change in texture going from the advancing side to the retreating side. For the other configurations, there were two different texture types, each of which related to one of the base metals (see Figure 7.1a, Figure 7.4c, and Figure 7.4f). As the pin partially penetrates into the materials, the grains are not well refined in the weld root (Figure 7.1c), meaning that the weld may be weaker in the root. This is reflected in the lower hardness of the weld root compared to the weld toe and its immediate neighborhood [17].
Figure 7.3 presents the morphology and chemical composition of the particles within the different zones of a sample weld from configuration 8. The high temperatures of FSW results in dissolution, coarsening, and re-precipitation of the precipitates [3]. As is clear from Figure 7.3a-c, there are relatively large number of large particles in the WN and the HAZs of both materials. The particles tend to be larger (up to 25 μm) in the HAZs compared to the WN (up to 10 μm). That may be due to the coarsening of the precipitates and could be the reason why the lowest strengths are measured within the HAZ. The number of smaller particles (500 nm-1 μm) is significant in the WN and the HAZ of the 2024 side, but there are not as many such particles in the HAZ of the 7075 side. Figure 7.3d presents EDS element maps for a few large particles in the HAZ of the 2024 side and shows that the particles are rich of Cu and Mg. In Figure 7.3e, the EDS spot measurement technique is used to compare the composition of two points: a point in the matrix and a point within a large particle. The point within the particle is clearly much richer in Cu and lacks Zn. These large intermetallics can potentially limit the plastic deformation by stopping various active slip systems.

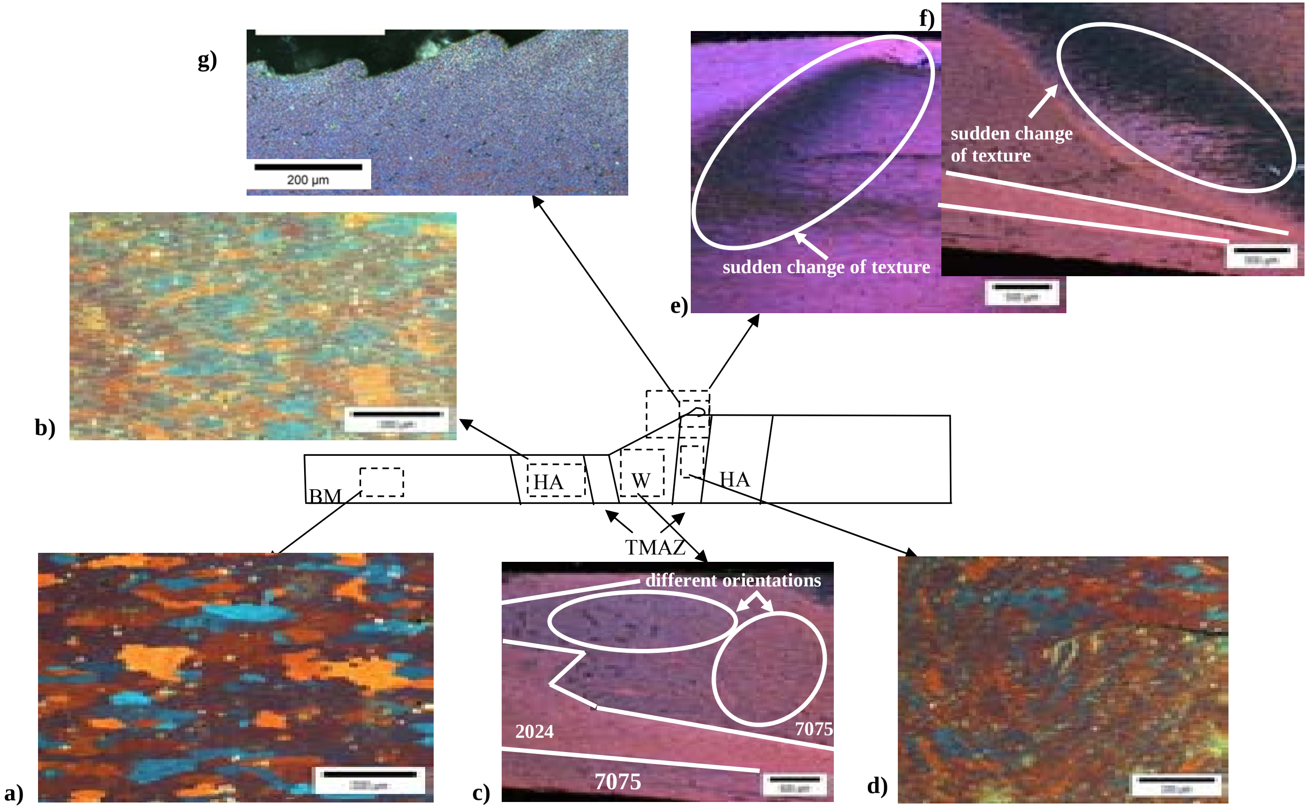
g)
200 µm
b)
e)
sudden change of texture
f)
sudden change
of texture
BM
HA
W
HA
TMAZ
a)
c)
different orientations
2024
7075
7075
d)

Figure 7.4. (previous page) A schematic representation of the different zones of the welds with dissimilar thicknesses and/or dissimilar alloys. Subfigures a-g depict some samples of the microstructural features observed for different weld configurations. (a)- base metal from configuration 2 (magnification 100x). (b)- HAZ from configuration 2 (magnification 100x). (c) stirring zone from configuration 9 (magnification 25x). (d) TMAZ from configuration 2 (magnification 100x). (e)-(f) WN and TMAZ from configuration 9 (magnification 25x). (g): weld burr from configuration 5 (magnification 100x).

Figure 7.4 consists of a schematic drawing of a typical weld accompanied by some sample micrographs representing various locations within the weld zone. The microstructural morphology of the base metals (Figure 7.4a) was consistent with the usual morphology of cold rolled sheets with grains elongated along the rolling direction. Figure 7.4b presents the grain morphology in the Heat-Affected Zone (HAZ) of a sample right next to the ThermoMechanically-Affected Zone (TMAZ). One can see that the grain size is comparable to that of the base metal; yet, the aspect ratio of the grains is somewhat smaller due to the high temperatures experienced during FSW. The mixing of two different alloys in the WN of the welds with dissimilar materials and dissimilar thicknesses is represented in Figure 7.4c, where it can be clearly seen that the two different materials are extruded into each other and form a WN with strongly heterogeneous texture. The 2024-T3 alloy is extruded into 7075-T6 and has its own distinctive grain orientation. The onion ring structure is still visible in the 7075 portion of the nugget. Within the 7075 portion, one can also see the difference between the dominant grain orientations of the advancing and retreating sides. The highly deformed grains in the TMAZ zone are shown in Figure 7.4d. Although the size of the grains is preserved, they are curled in accordance with the circular strain field created by the tool.
It was found that there is a sudden change of grain orientations on both sides of the WN in the dissimilar-thickness configurations (Figure 7.4e-f) such that the area with the suddenly changed texture surrounds the WN. Figure 7.4g shows the highly refined grains of weld burr that are refined through DRX. In summary, there is significant change of the chemical composition and grain orientation through the thickness.

Global mechanical properties. The global mechanical properties of the studied FSW TMBs as well as their failure locations are presented in Table 7.3. Comparing the values presented in Table 7.3 with the ones presented in Table 7.1, one can see that the thermomechanical evolution during the welding degrades the mechanical properties of the welds. Table 7.4 presents the differences between the mechanical properties of the welds and those of the base materials as well as the differences between the mechanical properties of the As-Welded (W-) and Machined (M-) specimens. As is clear from this table, the yield strengths of the different configurations decrease in the range of 7%-35% for W-specimens and in the range of 6%-39% for M-specimens. The range of the decrease of the ultimate strength is 2%-31% for W-specimens and 8-33% for M-specimens. In the case of the strain at maximum stress, the decreases are in the range of 0%-79% for W-specimens and 0%-60% for M-specimens. Two trends emerge from the values presented in Table 7.4. First, the columns presenting the difference between the W- and M-specimens (i.e. W-M columns) show that the yield and ultimate strengths of the M-specimens tend to be worse than the W ones. Secondly, the percentage loss of ductility is as much as the twice of the percentage loss of the strength. This is an important point given the fact that the sheets are to be plastically formed afterwards.

Table 7.3. The global mechanical properties of the base metals and FSW as well as failure locations.

no.	σ_y		$\sigma_{\max}$		$\varepsilon_{F_{\max}}$		failure location			
							W		M	
	W	M	W	M	W	M	zone	side	zone	side
1	360±4	336±4	555±19	434±9	19.2±2.8	12.3±4.6	WN/TM	---	WN/TM	---
2	315±6	315±20	569±18	428±17	13.3±1.9	9.9±0.6	WN/TM	II	TMAZ	II
3	389±2	347±4	476±35	444±4	8.9±2.4	8.1±0.1	WN/TM	II	WN/TM	I
4	490±9	418±8	551±4	522±8	9.5±0.3	7.8±0.2	HAZ	---	HAZ	---
5	440±3	408±12	449±3	514±15	4.0±0.4	7.2±0.2	HAZ	II	HAZ	I
6	444±1	393±11	510±4	502±12	5.9±0.0	7.9±0.1	HAZ	II	HAZ	II
7	365±2	353±7	528±5	504±16	13.0±0.7	12.8±0.7	HAZ	I	HAZ	I
8	437±2	339±6	480±4	534±5	3.9±0.0	7.3±0.2	HAZ	II	HAZ	I
9	361±2	349±6	454±5	433±13	7.5±0.1	7.4±0.4	HAZ	II	HAZ	II
10	416±4	330±13	519±4	468±18	7.3±0.1	12.1±0.7	HAZ	II	TMAZ	I

Table nomenclature and abbreviations
σ_y (MPa): Yield strength, σ_{max} (MPa)*:* Tensile strength, ε_{Fmax} (%)**:** strain at maximum force, **W**: as-welded condition, **M**: machined condition, **WN**: Weld Nugget, **HAZ**: Heat-Affected Zone, **TM(AZ)**: ThermoMechanically-Affected Zone.

There are four fundamental differences between W- and M-specimens. Firstly, there are local stress concentrations due to the roughness of the weld toe in the W-specimens, which are removed in the M-specimens by machining. Secondly, stress concentrations occur at the transition line from one thickness to another in the welds with dissimilar thicknesses. Again, it is removed in the M-specimens, where the upper surface is milled to give a uniform thickness throughout the specimen. Thirdly, there is a gradual thickness change in the W-specimens with dissimilar thicknesses (Figure 7.4), meaning that the thickness of the WN is somewhat larger than the thinner base metal. Therefore, stress in the WN/TMAZ is less than in the thinner base metal. If the weakest point happens to be within the WN/TMAZ, the failure would be earlier in the M-specimens, where the thickness of the WN/TMAZ is the same as the thinner base metal. In the fourth place, the penetration of the pin into the material is partial, meaning that the weld root is not as well consolidated as the rest of the weld (Figure 7.2). Therefore, the mechanical properties of the weld root are not as good as the rest of the weld cross section. Through thickness measurement of the hardness has shown that the minimum hardness is at the weld root [17]. The machining process removes some well-consolidated material from the top side of the weld and, thereby, enhances the ratio of the weld root material to the well-consolidated material. Among these four mechanisms, the first two work towards lowering the mechanical properties of the W-specimens in comparison with the M-specimen. The last two mechanisms work towards improving the mechanical properties of the W-specimens. The second and third mechanisms are active only for the configurations with dissimilar thicknesses, whereas the first and the last mechanisms are active for all configurations. The differences between the mechanical properties of the W- and M-specimens depend on the balance of these four active mechanisms. Table 7.4 presents the differences between the mechanical properties of the W- and M-specimens. As is clear from this table, the yield strength of the W-specimens is always higher than that of the M-specimens. The same holds for the ultimate strength, except for configurations 5 and 8. Configurations 5 and 8 are the ones with the highest thickness ratio ($r = 1.7$). Stress concentration due to the change of the thickness is the greatest for these two configurations. That may be the reason why the ultimate strength and the strain at maximum stress are better for the M-specimens from these two configurations. As for the strain at the maximum stress, the M-specimens deform to a larger extent only in the case of configurations 5, 6, 8, and 9, all of which have a thickness ratio greater than 1. One has to note that these are just static properties and the trends could change in the case of dynamic loading, where the local and global stress concentrations are more relevant.

The effects of the thickness ratio on the mechanical properties can be studied by comparing the configurations presented in Table 7.3. The strain at maximum stress for the configurations with dissimilar thicknesses is less than that of the same-thickness configurations. This holds not only for the W-specimens, but also for the M-specimens in which the stress concentration caused by the thickness difference does not play a role. A stronger statement can be made for the dissimilar-thickness configurations from 7075-T6 (configurations 4-6), and the dissimilar-thickness dissimilar-alloy configurations (configurations 7-10). For these two cases, the strain at maximum stress decreases as the thickness ratio increases. Therefore, when there is a forming component perpendicular to the thickness step, the formability of FSW TMBs tends to decrease as the thickness ratio increases. As a result of that, production of structural parts out of FSW TMBs with high thickness ratio would be more difficult. As for the yield strength and tensile strength, they generally tend to be lower for the configurations with dissimilar thicknesses. Although the statement holds firmly for the 7075-T6 configurations (configurations 4-6), it is not without exception for the 2024-T3 configurations (configurations 1-3) and dissimilar-alloy configurations (configurations 7-10).

The configurations with dissimilar alloys can be divided into two groups. First group includes the configurations for which the thickness of the 2024-T3 sheet is the same or smaller than the 7075-T6 sheet, namely configurations 7 and 9. Second group includes configurations 8 and 10 for which the thickness of the 7075-T6 is less than that of the 2024-T3 sheet. Table 7.3 shows that the failure always takes place in the 2024-T3 side for the first group, which is due to the lower strength of 2024-T3 compared with 7075-T6. For the second group, the failure takes place at the 7075-T6 side for the W-specimens, but it moves to the 2024-T3 side once the thickness is leveled by the machining. The mechanical properties of the first group are similar to those of the corresponding 2024-T3 configurations and those of the second group are similar to those of the corresponding 7075-T6 configurations. The mechanical properties of the second group approaches those of the corresponding 2024-T3 configurations once the machining process is applied. This is consistent with the microstructural observations indicating that the two alloys are not chemically mixed but are merely extruded into each other.

Table 7.4. The differences between the global mechanical properties of the W-and M-specimens and those of the base metals. The differences between the mechanical properties of the W- and M-specimens are presented as well. Each cell of the table contains the absolute difference value (bold) followed by the percentage value (italic).

no.	σ_y (MPa)					$\sigma_{\max}$ (MPa)					$\varepsilon_{F_{\max}}$ (%)				
	I-W	I-M	II-W	II-M	W-M	I-W	I-M	II-W	II-M	W-M	I-W	I-M	II-W	II-M	W-M
1	**58**,*14*	**82**,*20*	**58**,*14*	**82**,*20*	**24**,*7*	**25**,*4*	**146**,*25*	**25**,*4*	**146**,*25*	**121**,*22*	**-1.0**,*-5*	**5.9**, *32*	**-1.0**,*-5*	**5.9**, *32*	**6.9**,*36*
2	**103**,*25*	**103**,*25*	**73**,*19*	**73**,*19*	**0**,*0*	**11**,*2*	**152**,*26*	**-30**,*-6*	**111**,*21*	**141**,*25*	**4.9**,*27*	**8.3**, *46*	**-1.0**,*-8*	**2.4**, *20*	**3.4**,*26*
3	**-19**,*-5*	**23**,*6*	**29**,*7*	**71**,*17*	**42**,*1*	**100**,*17*	**132**,*23*	**104**,*18*	**136**,*23*	**32**,*7*	**5.9**,*40*	**6.7**, *45*	**9.3**,*51*	**10.1**,*55*	**0.8**,*9*
4	**43**,*8*	**115**,*22*	**43**,*8*	**115**,*22*	**72**,*5*	**100**,*15*	**129**,*20*	**100**,*15*	**129**,*20*	**29**,*5*	**1.7**,*15*	**3.4**,*30*	**1.7**,*15*	**3.4**,*30*	**1.7**,*18*
5	**93**,*17*	**125**,*23*	**117**,*21*	**149**,*27*	**32**,*7*	**202**,*31*	**137**,*21*	**206**,*31*	**141**,*22*	**-65**,*-14*	**7.2**,*64*	**4.0**,*36*	**6.2**,*61*	**3.0**,*29*	**-3.2**,*-80*
6	**110**,*20*	**161**,*29*	**89**,*17*	**140**,*26*	**51**,*1*	**139**,*21*	**147**,*23*	**141**,*22*	**149**,*23*	**8**,*2*	**4.3**,*42*	**2.3**,*23*	**5.3**,*47*	**3.3**,*29*	**-2.0**,*-34*
7	**53**,*13*	**65**,*16*	**168**,*32*	**180**,*34*	**12**,*3*	**52**,*9*	**76**,*13*	**123**,*19*	**147**,*23*	**24**,*5*	**5.2**,*29*	**5.4**,*30*	**-1.8**,*-16*	**-1.6**,*-4*	**0.2**,*2*
8	**-19**,*-5*	**79**,*19*	**120**,*22*	**218**,*39*	**98**,*2*	**100**,*17*	**46**,*8*	**175**,*27*	**121**,*18*	**-54**,*-11*	**14.3**,*79*	**10.9**,*60*	**6.3**,*62*	**2.9**,*28*	**-3.4**,*-87*
9	**193**,*35*	**205**,*37*	**57**,*14*	**69**,*17*	**12**,*3*	**195**,*30*	**216**,*33*	**126**,*22*	**147**,*25*	**21**,*5*	**2.7**,*26*	**2.8**,*27*	**10.7**,*59*	**10.8**,*59*	**0.1**,*1*
10	**-46**,*-12*	**40**,*11*	**117**,*22*	**203**,*38*	**86**,*1*	**57**,*10*	**108**,*19*	**132**,*20*	**183**,*28*	**51**,*10*	**7.5**,*51*	**2.7**,*18*	**3.9**,*35*	**-0.9**,*-8*	**-4.8**,*-66*

Table nomenclature and abbreviations. I-W: the difference between base metal I and the W-specimens, **I-M**: the difference between base metal I and M-specimens, **II-W:** the difference between base metal II and the W-specimens, **II-M:** the difference between base metal II and M-specimens, **W-M:** the difference between W- and M-specimens. The absolute value is presented first and is separated with a comma from the percentage value.

Table 7.5. The maximum and minimum values of the local mechanical properties of the welds from different configurations as well as the differences between the maxima and minima.

Series		1	2	3	4	5	6	7	8	9	10
σ_y	max	315	386	352	478	444	410	449	393	314	392
	min	275	327	247	314	308	290	294	247	259	257
	Δ	**40**,*14*	**59**,*17*	**105**,*35*	**165**,*42*	**135**,*36*	**120**,*34*	**155**,*42*	**146**,*46*	**55**,*19*	**135**,*42*
K	max	693	861	804	923	839	817	802	975	614	1172
	min	625	758	660	759	731	735	694	650	556	616
	Δ	**68**,*10*	**103**,*13*	**144**,*20*	**164**,*20*	**109**,*14*	**82**,*11*	**108**,*14*	**325**,*40*	**58**,*10*	**556**,*62*
n	max	.187	.237	.213	.195	.204	.208	.195	.230	.141	.206
	min	.138	.162	.152	.093	.110	.120	.092	.136	.124	.124
	Δ	**.050**,*31*	**.075**,*38*	**.061**,*34*	**.101**,*70*	**.094**,*60*	**.087**,*53*	**.103**,*71*	**.094**,*51*	**.017**,*13*	**.082**,*50*

Table nomenclature and abbreviations. Δ: The difference between the maximum and minimum values expressed both as the absolute value and percentage of the average (of the maximum and minimum values). The absolute value is presented first and is separated with a comma from the percentage value.

Interestingly, there is significant difference between the mechanical properties of the configurations 9 and 10. Although the same alloys are welded in these two configurations, the thicknesses of the sheets are different. After machining, the thicknesses are the same and one would therefore expect that the mechanical properties of the M-specimens from configurations 9 and 10 should be similar. However, the mechanical properties of the M-specimens from configuration 10 are significantly higher than those of the M-specimens from configuration 9. This can be explained in terms of heat input. The heat input of FSW can be estimated as [18]:

$$Q = \frac{4\pi^2 \alpha \mu P N R^3}{3V} \tag{1}$$

where the heat input efficiency, α, and friction coefficient, μ, can be assumed to be similar for configurations 9 and 10. Table 7.3 shows that the travel speed, V, rotational speed, N, and shoulder diameter, R, are the same for both configurations. However, the tool pressure, P, is higher for configuration 9, because it is the harder 7075-T6 that has to be squeezed by the tool's shoulder to make the gradual thickness change (from one material to the other). Since the other parameters (including the specific heat of the materials) tend to be similar, the temperature would be higher for configuration 9 compared to configuration 10, meaning that 2024-T3 material is subject to a more severe over-aging and precipitation coarsening in the case of configuration 9.

Local mechanical properties. The local mechanical properties including the yield strength, strength coefficients, and strain hardening exponents are presented in Figure 7.5 to Figure 7.7. Table 7.5 lists the maximum and minimum values of the local mechanical properties as well as the differences between the maxima and the minima. The local mechanical properties of FSW blanks are not widely available and the values presented in Figure 7.5 to Figure 7.7 are helpful in the FEM modeling of FSW blanks. One can see that the difference between the maximum and minimum values of the local yield strength is between 14 to 46% of the average of the maximum and minimum values. The difference is between 10 to 62% (10 to 20% for eight configurations) for the strength coefficient and between 13 to 71% for the strain hardening exponents. However, most Since the FSW blank would be formed into structural parts, it is important to be able to build accurate FEM models of FSW blanks. On one hand, the level of the difference between the maximum and minimum values is so large that one would wonder whether or not the FEM models would be accurate enough without implementing the local mechanical properties. On the other hand, the implementation results in more computationally expensive simulations which may or may not be justified by the extra accuracy obtained through the implementation of the local mechanical properties. Zadpoor *et al* have addressed this problem for FSW blanks with the same thicknesses and same materials and have shown that the implementation of the local mechanical properties substantially improves the capability of FEM models in predicting strain distribution and springback behavior [19]. The results of that study are presented in Chapter 10 of this thesis.

The difference between the maximum and the minimum values of the tensile strength are 14-35% for the 2024-T3 series and 35-42% for the 7075-T6 series. This is due to the natural aging of the 2024-T3 that recovers the strength of the locally-heated areas, whereas the artificially-aged 7075-T6 is not able to recover the strength to a comparable extent. Therefore, the determination of the local mechanical properties are even more important for artificially-aged alloys. The differences between the maximum and minimum values of tensile strength are quite high in the case of dissimilar-alloy configurations that are due to the large difference between the mechanical properties of 2024-T3 and 7075-T6.

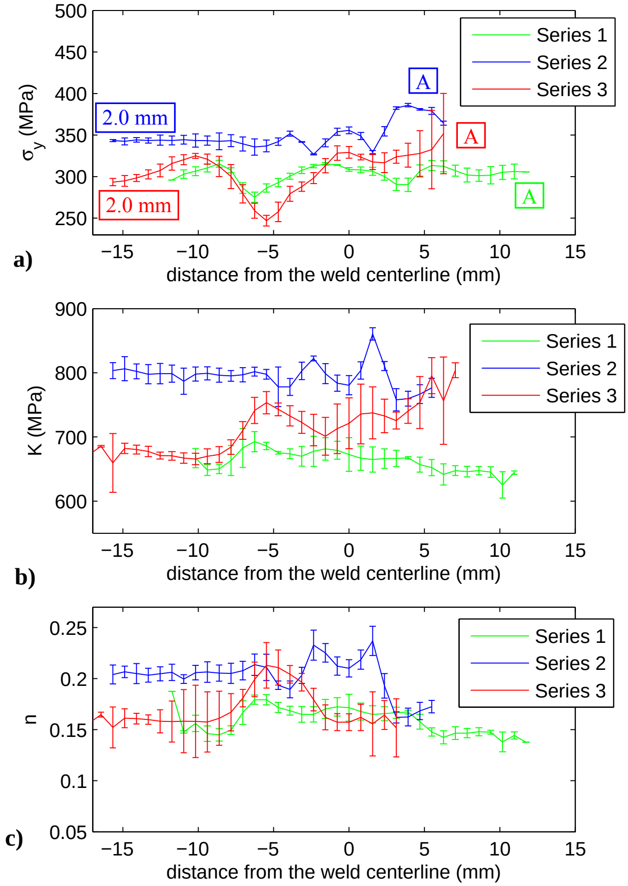

Figure 7.5. The local yield stress (a), strength coefficient (b), and strain hardening exponent (c) for configurations 1-3. The advancing side of each configuration is marked using an “A” mark.

One interesting point in Figure 7.5 to Figure 7.7 is that even for the configurations in which the sheet at the advancing side is similar to the one at the retreating side, the local mechanical properties are asymmetric around the weld centerline. The tensile strength tends to be higher on the advancing side than on the retreating side. This trend has been observed in other studies as well, e.g. [20-23], and may be due to different deformation histories on the advancing and retreating sides. The material on the advancing side is influenced to a greater extent by the vortex velocity field. That is because the circumventing and rotational velocity fields have different directions on the retreating side but are of the same direction on the advancing side. Therefore, the straining and grain refinement is more severe on the advancing side [23]. According to the Hall-Petch relationship, this would result in higher yield strengths.

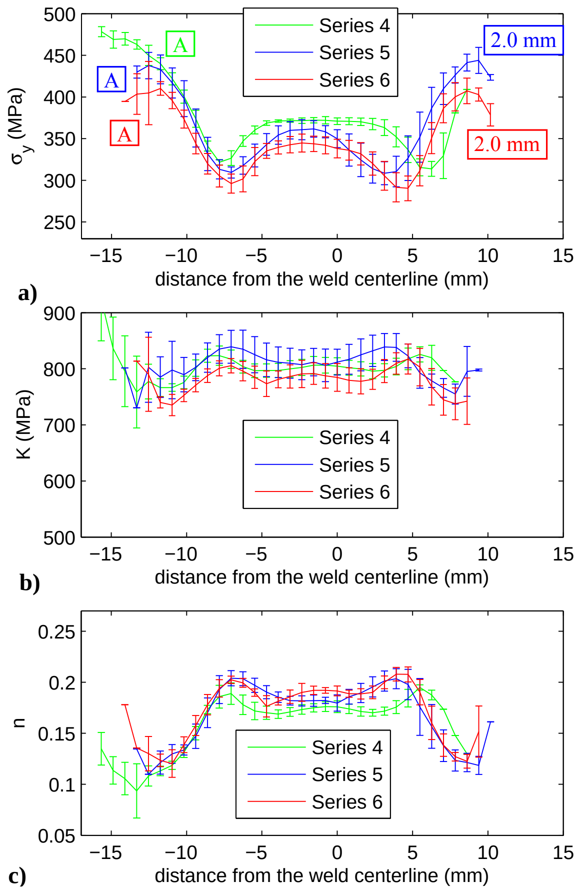

Figure 7.6. The local yield stress (a), strength coefficient (b), and strain hardening exponent (c) for configurations 4-6. The advancing side of each configuration is marked using an “A” mark.

Comparing Figure 7.5a and Figure 7.6a, one can see that the yield strength profiles are different for 2024-T3 and 7075-T6. While the 7075-T6 configurations exhibit a smooth distribution of the yield strength around the weld centerline with two minima on the either side of the weld, the yield strength profile is less smooth in the case of 2024-T3 configurations and includes several minima and maxima. Previous studies have shown that FSW has a major impact on the distribution of the dislocation density and creates a non-homogenous distribution of the dislocation density [24, 25]. It is known that in 2024-T3, dislocations can strongly interact with precipitates and act as preferred location for the nucleation of precipitates [26, 27]. Since the dislocations are heterogeneously distributed, the precipitate distribution would be heterogeneous as well. That may be the reason why several maxima and minima exist in the yield strength profile of 2024-T3. Indeed, thermophysical modeling of the FSW of 2024 has shown that if the effects of the dislocation density are left out of the model, the predicted hardness profile is essentially similar to that of 7075 [28]. Several other factors such as different temperatures and cooling rates (that could cause coarse precipitation) and different precipitation sequences in two alloys may be playing a role and further study is needed to determine which of these mechanisms is playing a major role.

The effect of the thickness ratio on the local yield strength (Figure 7.5a-Figure 7.7a) is different for the 2024-T3 configurations compared to the 7075-T6 configurations and dissimilar-alloy configurations. While the levels of the yield strength of the 7075-T6 and dissimilar-alloy configurations are relatively close to each other and tend to be higher for the same-thickness cases, the reverse holds for the 2024-T3 configurations. This may be described in terms of the heat input during the FSW as estimated with Equation (1). The equation can be simplified, if the friction coefficient and efficiency can be assumed to be similar for configurations from the same alloy:

$$Q = A\frac{FNR}{V}, A = \frac{4\pi\alpha\mu}{3} \quad (2)$$

Replacing for the parameters from Table 7.2, the heat input of the 2024-T3 configurations can be calculated as $Q_1 = 153A, Q_2 = 105A,$ and $Q_3 = 111A$, where the subscript denotes the configuration number. For the 7075-T6 configurations, the rotational speed and travel speed are the same and can be incorporated into A to give $A' = 4\pi\alpha\mu N / V$. The heat inputs of the 7075-T6 configurations can then be compared using only the tool force and shoulder diameter (Table 7.2): $Q_4 = 144A', Q_5 = 124A' - 137A',$ and $Q_6 = 124A' - 130A'$. As is clear from the calculated heat inputs, in the case of the 2024-T3 configurations, the required heat input increases as the thickness ratio increases. This might cause higher temperatures and, thus, more severe dissolution and coarsening of the precipitates and, thus, degradation of the mechanical properties. In the case of the 7075-T6 configurations, the heat input is similar for the three configurations and the local mechanical properties are close. However, one should note that Equation (1) is suggested for the same-thickness configurations. In the case of dissimilar alloys, the shoulder has to deeply penetrate into the material with larger thickness and this may result in higher heat input. That may be the reason why in the case of the harder

7075-T6 alloy, the level of the yield strength slightly decreases as the thickness ratio increases. Moreover, the heat capacities of sheets with different thicknesses are different and the same amount of heat input would not necessarily result in the same temperature profile.

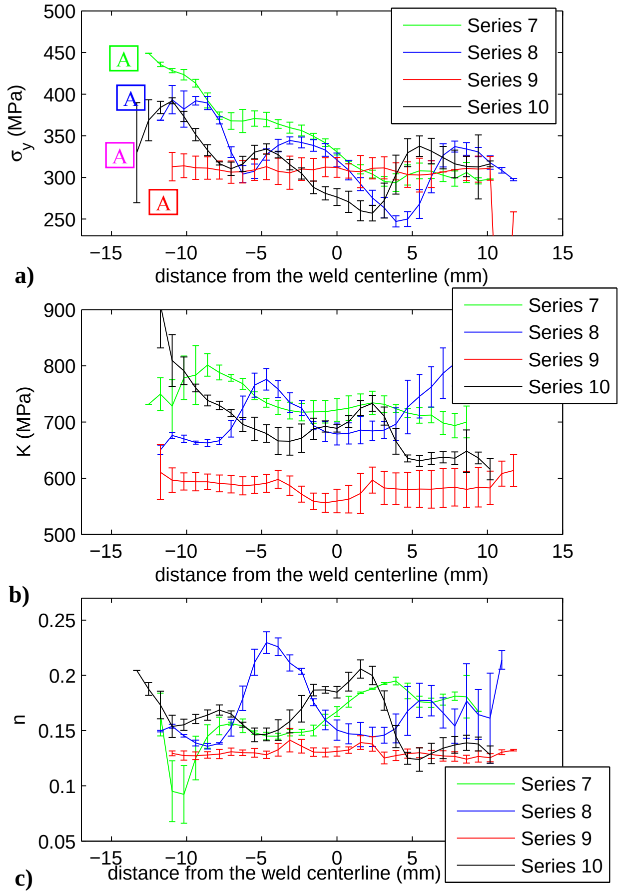

Figure 7.7. The local yield stress (a), strength coefficient (b), and strain hardening exponent (c) for configurations 7-10. The advancing side of each configuration is marked using an “A” mark.

The hardness profiles are often used to give a measure of the local mechanical properties of FSW. The hardness measurements are often carried out locally, for example, along the centerline of the cross-section. Since there is a significant change of the hardness values through the thickness [17], one would wonder if the local hardness measurements can give a reasonably valid picture of the local mechanical properties of the entire cross-section. The hardness profiles of the 2024-T3 configurations measured along the centerline of the cross-section were presented in the previous chapter [9]. Comparing Figure 7.5-Figure 7.7 with the previously-presented hardness profiles of the same welds, one can see that there are two fundamental differences between these two. First, the hardness profiles suggested that after natural aging, the yield strengths of the WN is almost the same as the base metal. Figure 7.5-Figure 7.7 show that the peak yield strengths in the WN are well below those of the base metals, if the entire weld is considered. Secondly, the hardness profiles suggest a trend for the dependency of the local mechanical properties upon the thickness ratio that is contradicting the trend suggested by the direct measurement of the local mechanical properties of the entire weld section. Therefore, the local measurement of the hardness profiles may not give a reasonably accurate picture of the distribution of the mechanical properties around the weld centerline and one has to resort to techniques such as DIC for that.

One of the mechanisms limiting the formability of FSW blanks is strain localization. According to the Marciniak-Kuczynski theory of localization bifurcation, the strain localization phenomenon is controlled by the imperfection parameter defined as:

$$f = \frac{K_2 t_2}{K_1 t_1} \tag{3}$$

where K_2 and t_2 are, respectively, the yield strength and thickness of the imperfection zone and K_1 and t_1 are the nominal values of the same quantities. The theory assumes that strain localization originates from areas with smaller thickness and/or lower yield strength whose strain paths are always ahead of the uniform zone. The localization takes place once the ratio of the strain of the imperfection zone to that of the strain zone approaches infinity. In the case of FSW blanks, the variations of the local yield strength observed in Figure 7.5-Figure 7.7 can give rise to such imperfections and cause pre-mature metal failure. An in-depth analysis of formability is needed to determine the relative importance of this phenomenon compared to other active failure mechanisms.

Fracture mechanism. Table 7.3 shows that the fracture locations of the same-alloy configurations is either in WN/TMAZ (for 2024-T3) or HAZ (for 7075-T6). In the latter group, the fracture location coincides with the minima of the yield strength profile (Figure 7.6a) where the material is softened due to the dissolution and coarsening of the precipitates. In the former group, however, the yield strength of the fracture site is not necessarily the lowest (Figure 7.5a). In contrast to the fracture of 7075-T6 which takes place in the HAZ, which is controlled by the softening of the material, and involves the significant development of a localized neck, the fracture of 2024-T3 occurs in the WN, which in some cases did not exhibit the significant development of a localized neck and is hypothesized to be controlled by lack of ductility.

Some samples of the inspected fracture surfaces are presented in Figure 7.8 and Figure 7.9. The ductile fracture mechanism is normally identified by dimples and tearing edges. The brittle fracture mechanism is identified by a relatively featureless fracture surface that may include cleavage facets, river patterns, and feather markings [29]. For the entire weld series listed in Table 7.1, the fracture surfaces exhibited the features of both ductile and brittle fracture mechanisms. However, there were two types of the mixture of the features of ductile and brittle fractures. In the first type, the fracture surfaces was predominantly occupied by the features of one single fracture mechanism (ductile or brittle) and the features of the other mechanism were scattered over the fracture surface. In the second type, the fracture surface was divided into two distinct regions: one overwhelmingly exhibiting the features of brittle fracture and the other demonstrating ductile or mixed ductile/brittle fracture. Figure 7.8 depicts some samples of the first type and Figure 7.9 some samples of the second type.

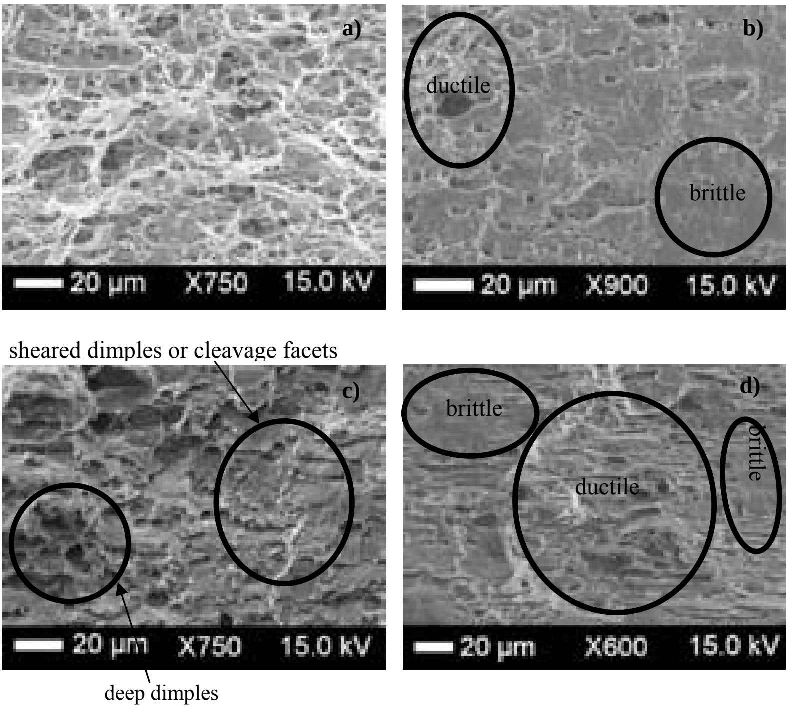

Figure 7.8. The fracture surfaces of some sample welds from configurations 2 (a-b), 1 (c), and 4 (d).

Figure 7.8a-b shows the fracture surface of a sample from configuration 2. In Figure 7.8a, it can be seen that the features of ductile fracture dominate the fracture surface. Figure 7.8b presents a different part of the fracture surface of the same specimen. A mixture of the features of ductile and brittle fractures is present in this figure. The area depicted in Figure 7.8b is almost featureless with some shallow dimples and some traits resembling cleavage facets scattered throughout the surface. However, these features can be considered to be sheared dimples as well.

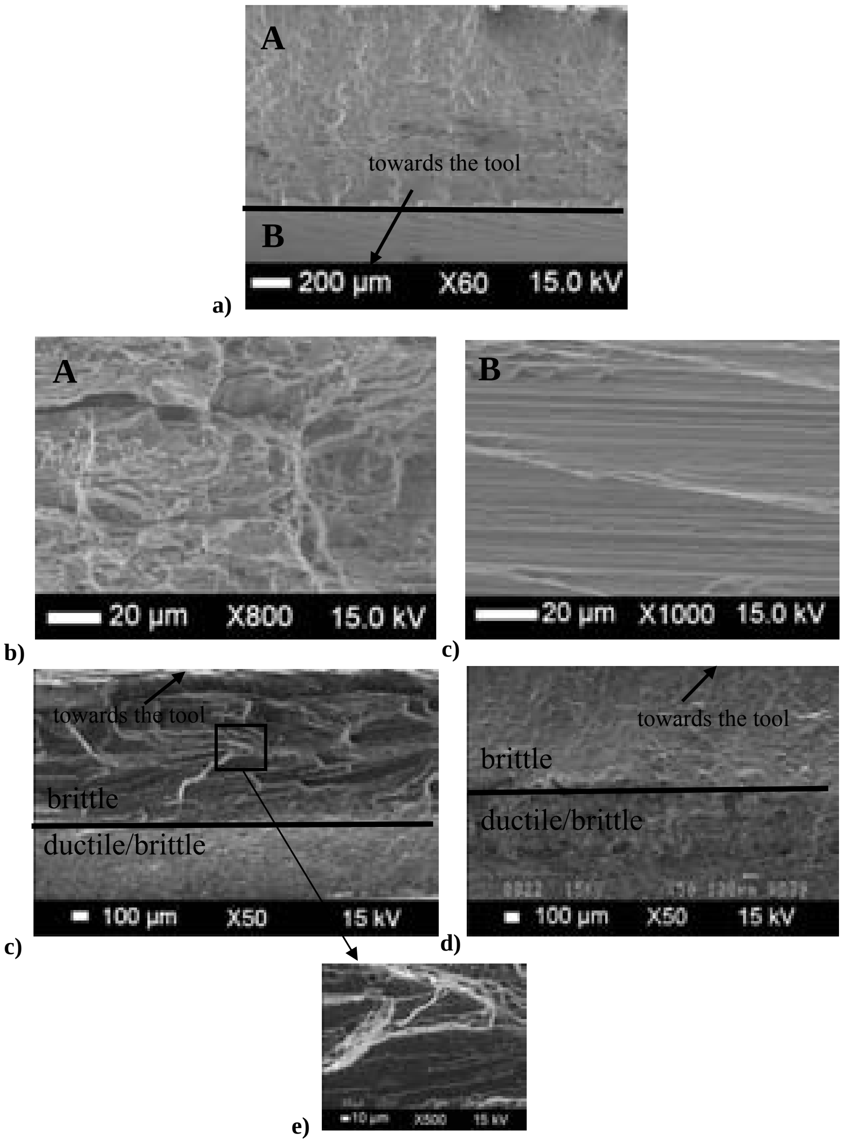

Figure 7.9. An overview of the fracture surface of a sample specimen from configuration 8 (a) along with two magnified views of the regions A (b) and B (c). Overviews of the fracture surface of two sample specimens from configurations number 2 (d) and 3 (e). A magnified view is provided for the brittle fracture region of the sample depicted in subfigure (d).

Figure 7.8c depicts the fracture surface of a sample from configuration number 1. The fracture surface is composed of areas which clearly exhibit the features of ductile fracture such as relatively deep dimples. However, there are some other areas in this figure which can be considered to be either sheared dimples or cleavage facets. Closer examination of these features revealed that they are more likely to be sheared dimples. In this scenario, the deep dimples relate to the start of the crack. After the initial phase of crack formation, the specimen experiences overloading and the dimples are sheared. Cavaliere *et al* observed a behavior similar to what depicted in Figure 7.8 [30] for same-thickness same-alloy FSWs. They concluded that the observed cleavage-like fracture is due to a non-optimal grain structure of the recrystallized material. In this scenario, the high strain rate acting on the material during welding causes boundary weakening in the Dynamically Recrystallized Zone (DXZ). A possible explanation for the first type of the mixing between the features of ductile and brittle fractures is that the dislocation movement is blocked by the many intermetallics (Figure 7.3) that are observed in the HAZ and WN. Voids can not nucleate and grow in the proximity of the particles, resulting in the fracture surface being divided.

Figure 7.9a gives an overview of a sample specimen from configuration 8. As is clear from this figure, the fracture surface is divided into two distinct regions with the upper one (region A- Figure 7.9b) showing a mixed ductile/brittle fracture and the lower one (region B- Figure 7.9c) not showing any sign of ductile fracture. The same kind of behavior was observed for some other configurations (Figure 7.9d-e). It was observed that the brittle regions (the regions similar to region B in Figure 7.9c) were on the side of the material that had been in contact with the shoulder of the tool. Moreover, the size of the brittle region was found to be dependent on the thickness ratio and increased as the thickness ratio increased. Comparing Figure 7.9d and Figure 7.9e one can see that the portion of the fracture surface showing brittle fracture is larger for configuration 2 (Figure 7.9d) for which the thickness ratio (1.7) is more than for configurations3, with thickness ratio of 1.2 (Figure 7.9e). Moreover, the division of the fracture surface was not observed in configurations for which the failure location was away from the domain of the influence of the tool's shoulder. These three observations suggest that the creation of the brittle region may be due to the significant penetration of the tool's shoulder into the sheets. As already pointed out, the shoulder has to deeply penetrate into the thicker sheet to create the gradual thickness change. The severe plastic deformation of the top side of the sheets during the welding process could be the reason why a brittle region is formed on that side of the sheets that has been in contact with the shoulder. Xu *et al* [31] and Elangovan and Balasubramanian [32] have also observed the dividing of the fracture surface into two regions for *same-thickness welds.* In contrary to our observations, they observed the cleavage-like fracture in the weld root and suggested that it is due to the poor consolidation of the metal at the weld root. Therefore, the thickness difference present in our experiments results in a different type of divisive feature than was reported in the literature.

As FCC materials, aluminum alloys are generally considered to fail only through ductile fracture mechanism and not cleavage [29]. That is because of the numerous active slip systems in FCC materials. However, cleavage is reported for FCC materials under special circumstances [29]. As discussed earlier, there are some features in the fracture surfaces of FSW specimens which resemble the cleavage fracture. Similar results have been reported by other researchers [30, 32-34]. In most cases, fracture surfaces showed the features of both ductile and brittle fractures. The term 'quasi-cleavage' can be used to describe the type of fracture observed in the testing of FSW blanks. According to the ASM Handbook of Fractography, "quasi-cleavage fracture is a localized, often isolated feature on a fracture surface that exhibits characteristics of both cleavage and plastic deformation" [29]. The term quasi-cleavage implies that the features of the fracture surface resemble, but are not, cleavage. Therefore, using the term quasi-cleavage for description of the mixed behavior of the fracture surfaces implies that the fracture mechanism is not necessarily changed to the low-energy fracture mechanism that propagates along well-defined low-index crystallographic directions and is known as cleavage. It is not clear if the fracture mechanism is actually changed or the features that resemble the cleavage fracture are merely signs of limited plastic deformation. It should be noted that the ideal cleavage takes place only under certain well-defined conditions such as single-crystalline microstructure and limited number of slip systems [29]. Most of the times, there is a combination of plastic and cleavage fractures. The division line between the terms cleavage and quasi-cleavage is somewhat arbitrary [29].

7.3. Conclusions

The microstructure and local and global mechanical properties of FSW TMBs were studied in this chapter. Following conclusion can be drawn from the study:

- Dissimilar materials are merely extruded into each other. There is no significant diffusion of the alloying elements between the alloys and they form a WN with strongly heterogeneous texture varying both through the thickness and around the weld line. There is a sudden change of texture around the weld nugget when thicknesses are dissimilar. Large intermetallic particles were observed in the HAZ and WN with different sizes and morphology in the different zones of the welds.
- Although all mechanical properties degrade after FSW, ductility is influenced to a greater extent. Both high thickness ratio and through-the-thickness machining tend to adversely affect the mechanical properties. The properties of FSW with dissimilar thicknesses are close to those of the weaker alloy. Many observed trends of the global and local mechanical properties may be explained using the heat input estimates.
- The local yield strength and plasticity parameters drastically vary around the weld centerline, requiring them to be implemented in the FEM models. The local properties are asymmetric around the centerline with the advancing side having higher properties.
- The fracture mechanism of FSW TMBs was found to be matching the definition of quasi-cleavage fracture. Depending on the material/thickness configuration of the weld, the features of the ductile and brittle fracture are either (1) quasi-randomly scattered over the fracture surface or (2) are

segregated with a sharp boundary separating the brittle fracture region from the area exhibiting ductile or mixed ductile/brittle fracture. While the brittle regions that are scattered may have been created due to the large intermetallic particles that block the dislocation movement and void nucleation and growth, the creation of the sharply separated brittle regions may be due to the deep penetration of the shoulder that is required due to the dissimilar thicknesses of the blanks.

7.4. References

[1] D. P. Field, T. W. Nelson, Y. Hovanski, and K. V. Jata, "Heterogeneity of crystallographic texture in friction stir welds of aluminum," *Metallurgical and Materials Transactions A,* vol. 32, pp. 2869-2877, Nov 2001.

[2] S. Liu and Y. J. Chao, "Determination of global mechanical response of friction stir welded plates using local constitutive properties," *Modelling and Simulation in Materials Science and Engineering,* vol. 13, pp. 1-15, Jan 2005.

[3] R. S. Mishra and Z. Y. Ma, "Friction stir welding and processing," *Materials Science and Engineering R-Reports,* vol. 50, pp. 1-78, Aug 31 2005.

[4] L. Fratini, G. Buffa, and R. Shivpuri, "Improving friction stir welding of blanks of different thicknesses," *Materials Science and Engineering A,* vol. 459, pp. 209-215, 2007.

[5] J. Yan, M. A. Sutton, and A. P. Reynolds, "Notch tensile response of mini-regions in AA2024 and AA2524 friction stir welds," *Materials Science and Engineering A,* vol. 427, pp. 289-300, 2006.

[6] R. W. Fonda and S. G. Lambrakos, "Analysis of friction stir welds using an inverse problem approach," *Science and Technology of Welding and Joining,* vol. 7, pp. 177-181, 2002.

[7] S. A. Khodir and T. Shibayanagi, "Friction stir welding of dissimilar AA2024 and AA7075 aluminum alloys," *Materials Science and Engineering B,* vol. 148, pp. 82-87, 2007.

[8] H. Larsson, L. Karlsson, S. Stoltz, and E. Bergqvist, "Joining of dissimilar Al alloys by friction stir welding " in *Second International Symposium on Friction Stir Welding*, Gothenburg, Sweden, 2000.

[9] A. A. Zadpoor, J. Sinke, and R. Benedictus, "The mechanical properties and microstructure of friction stir welded tailor-made blanks," *Materials Science and Engineering A,* vol. 494, pp. 281-290, 2008.

[10] W. J. Arbegast, "Modeling friction stir joining as a metal working process," in *TMS Annual Meeting*, San Diego, CA, 2003, pp. 313-327.

[11] P. B. Srinivasan, W. Dietzel, R. Zettler, J. F. dos Santos, and V. Sivan, "Stress corrosion cracking susceptibility of friction stir welded AA7075-AA6056 dissimilar joint," *Materials Science and Engineering A,* vol. 392, pp. 292-300, Feb 15 2005.

[12] I. Shigematsu, Y. J. Kwon, K. Suzuki, T. Imai, and N. Saito, "Joining of 5083 and 6061 aluminum alloys by friction stir welding," *Journal of Materials Science Letters,* vol. 22, pp. 353-356, Mar 1 2003.

[13] H. Uzun, C. D. Donne, A. Argagnotto, T. Ghidini, and C. Gambaro, "Friction stir welding of dissimilar Al 6013-T4 To X5CrNi18-10 stainless steel," *Materials & Design,* vol. 26, pp. 41-46, Feb 2005.

[14] Y. Du, Y. A. Chang, B. Huang, W. Gong, Z. Jin, H. Xu, Z. Yuan, Y. Liu, Y. He, and F. Y. Xie, "Diffusion coefficients of some solutes in fcc and liquid Al: critical

evaluation and correlation," *Materials Science and Engineering A,* vol. 363, pp. 140-151, 2003.

[15] Y.-M. Hwang, Z.-W. Kang, Y.-C. Chiou, and H.-H. Hsu, "Experimental study on temperature distributions within the workpiece during friction stir welding of aluminum alloys," *International Journal of Machine Tools and Manufacture,* vol. 48, pp. 778-787, 2008.

[16] Y. S. Sato, H. Kokawa, K. Ikeda, M. Enomoto, S. Jogan, and T. Hashimoto, "Microtexture in the friction-stir weld of an aluminum alloy," *Metallurgical and Materials Transactions A,* vol. 32, pp. 941-948, Apr 2001.

[17] R. S. Mishra and W. H. Murray, "Friction Stir Welding and Processing," Materials Park, Ohio: ASM International, 2007.

[18] Ø. Frigaard, Ø. Grong, and O. Midling, "A process model for friction stir welding of age hardening aluminum alloys," *Metallurgical and Materials Transactions A,* vol. 32, pp. 1189-1200, 2001.

[19] A. A. Zadpoor, J. Sinke, and R. Benedictus, "Finite element modeling and failure prediction of friction stir welded blanks," *Materials & Design,* vol. 30, pp. 1423-1434, 2009.

[20] Y. S. Sato, S. H. C. Park, and H. Kokawa, "Microstructural factors governing hardness in friction-stir welds of solid-solution-hardened Al alloys," *Metallurgical and Materials Transactions A,* vol. 32, pp. 3033-3042, Dec 2001.

[21] Y. S. Sato, H. Kokawa, M. Enomoto, and S. Jogan, "Microstructural evolution of 6063 aluminum during friction-stir welding," *Metallurgical and Materials Transactions A,* vol. 30, pp. 2429-2437, Sep 1999.

[22] Y. Li, L. E. Murr, and J. C. McClure, "Flow visualization and residual microstructures associated with the friction-stir welding of 2024 aluminum to 6061 aluminum," *Materials Science and Engineering A,* vol. 271, pp. 213-223, Nov 1 1999.

[23] P. Heurtier, M. J. Jones, C. Desrayaud, J. H. Driver, F. Montheillet, and D. Allehaux, "Mechanical and thermal modelling of friction stir welding," *Journal of Materials Processing Technology,* vol. 171, pp. 348-357, Feb 1 2006.

[24] L. E. Murr, G. Liu, and J. C. McClure, "Dynamic recrystallization in friction-stir welding of aluminium alloy 1100," *Journal of Materials Science Letters,* vol. 16, pp. 1801-1803, Nov 15 1997.

[25] W. B. Lee and S. B. Jung, "The joint properties of copper by friction stir welding," *Materials Letters,* vol. 58, pp. 1041-1046, Feb 2004.

[26] R. Ferragut and A. Somoza, "Positron, age-hardening and precipitation in predeformed 2024 (Al-Cu-Mg) alloy," *Physica Status Solidi (A) Applied Research,* vol. 175, 1999.

[27] C. Genevois, D. Fabrègue, A. Deschamps, and W. J. Poole, "On the coupling between precipitation and plastic deformation in relation with friction stir welding of AA2024 T3 aluminium alloy," *Materials Science and Engineering A,* vol. 441, pp. 39-48, 2006.

[28] H. R. Shercliff, M. J. Russell, A. Taylor, and T. L. Dickerson, "Microstructural modelling in friction stir welding of 2000 series aluminium alloys," *Mecanique et Industries,* vol. 6, pp. 25-35, 2005.

[29] A. I. H. Committee, *ASM Handbook: Volume 12: Fractography*. Materials Park: ASM International, 1987.

[30] P. Cavaliere, A. Squillace, and F. Panella, "Effect of welding parameters on mechanical and microstructural properties of AA6082 joints produced by friction stir welding," *Journal of Materials Processing Technology,* vol. 200, pp. 364-372, 2008.

[31] W. Xu, J. Liu, G. Luan, and C. Dong, "Temperature evolution, microstructure and mechanical properties of friction stir welded thick 2219-O aluminum alloy joints," *Materials & Design,* vol. In Press, Corrected Proof.

[32] K. Elangovan and V. Balasubramanian, "Influences of post-weld heat treatment on tensile properties of friction stir-welded AA6061 aluminum alloy joints," *Materials Characterization,* vol. 59, pp. 1168-1177, 2008.

[33] P. Cavaliere, A. D. Santis, F. Panella, and A. Squillace, "Thermoelasticity and CCD analysis of crack propagation in AA6082 friction stir welded joints," *International Journal of Fatigue,* vol. 31, pp. 385-392, 2009.

[34] S. Hong, S. Kim, C. G. Lee, and S.-J. Kim, "Fatigue crack propagation behavior of friction stir welded Al-Mg-Si alloy," *Scripta Materialia,* vol. 55, pp. 1007-1010, 2006.

Modified from: Zadpoor, A. A., Sinke, J., Benedictus, R., 2009,"Formability prediction of high strength aluminum sheets", International Journal of Plasticity, vol. 25(12), pp. 2269-2297.

8. Comparison of formability prediction theories

This chapter studies the theoretical formability prediction of high strength aluminum sheets. Four different modeling approaches are considered and compared with each other. The studied approaches are phenomenological ductile fracture modeling, physical modeling of ductile fracture mechanism based on a porous metal plasticity model, the Marciniak-Kuczynski model of sheet metal instability, and a combined porous metal plasticity and Marciniak-Kuczynski model. Three sets of experimental data are adopted from the literature to calibrate the studied models and to validate the predicted results. For phenomenological modeling, eight different phenomenological ductile fracture criteria are considered, calibrated, and compared with each other. The fracture loci predicted with the best performing ductile fracture criteria are compared both qualitatively and quantitatively with those predicted using the other modeling approaches. It is shown that the best phenomenological ductile fracture criteria are those proposed by Wilkins in the 1980s and a recent one proposed by Xue and Wierzbicki. However, the fracture loci predicted by these two criteria can be inaccurate if the number of calibration data points is small and over-fitting occurs. The Tresca ductile fracture criterion, which was suggested by the previous researchers to be a low-cost competitor to the most sophisticated phenomenological models, is found to show relatively poor performance when it comes to the quantitative comparison of prediction errors. Nevertheless, the Tresca and CrachFEM models are more robust against over-fitting and may be used when the number of calibration data points is small. The porous metal plasticity model is found to be successful in the range of small stress triaxialities ($1/3 < \eta < 1/\sqrt{3}$) but inaccurate for the high end of the stress triaxiality range ($1/\sqrt{3} < \eta < 2/3$). It is also shown that the Marciniak-Kuczynski model gives good predictions of the formability limits for high stress triaxiality values but is not as accurate for low values. Moreover, the combined Marciniak-Kuczynski and porous metal plasticity shows that the porous metal plasticity theory can accurately predict the fracture limits in the high end of the stress triaxiality range once it is combined with the Marciniak-Kuczynski theory.

Theoretical formability prediction is of practical importance because it eliminates the need for elaborate, time consuming, and expensive experiments which are normally needed to determine forming limits. Numerous models [1-8] have been developed for determining the Forming Limit Diagrams (FLDs) since the classic works of Swift [9] and Hill [10] on theoretical prediction of the diffuse and localized necking in the 60s. Banabic has given a classification of the most important classical methods used in the theoretical prediction of the FLDs [11]. Nevertheless, most of these models are applicable only to highly ductile materials such as mild steels and 5000 and 6000 series aluminum alloys. For such ductile materials, failure is typically related to sheet metal instability and that is why instability prediction theories such as the Marciniak-Kuczynski model [12] are extensively used for the prediction of the FLDs of these materials. However, the ever increasing push for lighter and more fuel-efficient vehicles has increased the attractiveness of materials with high strength to weight ratios (like Advanced High Strength Steels-AHSS) among car manufacturers. Besides that, high-strength 2000 and 7000 series aluminum alloys have been used in the aircraft industry for decades. The failure mechanism of these high strength materials is considered to be different from that of highly ductile materials. In such materials, other failure mechanisms such as void nucleation and growth and shear band localization compete with instability. Currently, there is no clear understanding of the role each of these mechanisms plays in limiting the formability of high strength materials. Therefore, even though various theories have been proposed for the prediction of the formability of high strength materials, it is not clear which one can provide the best predictions.

The main focus of the current study is the formability of high strength aluminum alloys. From the high strength aluminum alloys, the 2024-T3 alloy, which is commonly used in formed structural parts of aircraft, was selected for this study.

Four different classes of failure prediction theories have been applied to predict the forming limits of 2024-T3. The first category of the applied models is the category of phenomenological ductile fracture criteria. These criteria do not directly model the physical mechanism of ductile fracture but predict the onset of damage, based on a macroscopically defined damage accumulation function. These models have been used by some researchers for the prediction of failure of 2024-T3 [13-18].

The second category of prediction methods is the so-called Gurson-type models which are based on the porous metal plasticity theory first proposed by Gurson in 1977 [19]. These models are based on nucleation and growth of voids in the metal. The yield function is modified to account for the presence and evolution of the voids. The damage accumulates as the voids nucleate and grow and, at the same time, the yield surface contracts until a point is reached where the void volume fraction exceeds the failure threshold and the material is assumed to have failed. The Gurson type models have been applied by some authors for the formability prediction of stainless steel [20] and aluminum alloy 5182 [21]. For 2024-T3, the Gurson type models have been used for crack growth and damage tolerance analyses, e.g. in [22, 23]. There have not been many applications of the Gurson type models for the formability prediction of 2024-T3.

The third category of models is the Marciniak-Kuczynski (M-K) model which is used to predict sheet metal instability. This theory is based on the assumption of a pre-existing imperfection in sheets. During deformation, strain values in the imperfection zone are higher than in the uniform zone. Failure is assumed to take place once the ratio of the strain in the imperfection zone to that of the uniform zone

exceeds a critical value. Variants of the M-K theory have been used for prediction of the plastic failure of 2024-T3 by some researchers, see e.g. [24].
The fourth approach in the prediction of the formability of aluminum 2024-T3 is to combine the M-K theory with the Gurson type models. By doing so, both instability and ductile fracture are accounted for in one single model of failure. Although already applied to mild steels [25, 26] and 5000 and 6000 series aluminum alloys [27], the combined M-K and Gurson analysis has not been previously applied to the formability analysis of 2024-T3.
In this chapter, the four approaches are compared with each other to understand which of them can adequately predict the forming limits of high strength aluminum alloys like 2024-T3. Three different sets of experimental data are adopted from the literature to cover a relatively broad range of available experimental data. The models are calibrated by using the experimental data. The predicted forming limits are compared with each other and with the experimental data.

8.1. Experimental data

Three sets of experimental forming limits are adopted from the literature and are used for the calibration and validation of the different formability prediction theories. In chronological order, the data comes from studies of the formability of 2024-T3, carried out by Lee *et al* in 1995, 1997, and 1999 [17, 24, 28], Wierzbicki *et al* in 2005 [13], and Vallellano *et al* in 2008 [14].
In the studies by Lee and coworkers, the FLDs were determined using tensile and Erichsen cupping tests [17]. While the limiting strains for the positive strain ratios were determined using the Erichsen cup test, the left hand side of the FLD was determined by uniaxial tensile tests. A sheet thickness of 0.8 mm was used. The strain hardening coefficient was determined as $n = 0.21$ [17].
Wierzbicki *et al* used various tests to capture the failure limits of 2024-T3. The tests included round tensile testing (in three conditions of smooth, large notch, and small notch), flat-grooved tensile testing, cylinder upsetting (with three different diameter-to-height ratios), round notch specimen compression, flat dog-bone shape tensile testing, dog bone tensile testing, flat specimen tensile testing, pipe uniaxial testing, and solid bar tensile testing [13]. The above-mentioned tests were used to make the material fail at different stress triaxiality values, hence giving failure limits for a broad range of stress triaxialities. They also showed that the Hollomon's law ($\sigma = \tilde{K}\varepsilon^n$) fitted the measured hardening curve once the strength coefficient, $\tilde{K}$, and strain hardening exponent, n, were determined (as $\tilde{K} = 744$ MPa and $n = 0.153$).
Vallellano *et al* also used the Erichsen cupping test along with uniaxial tensile testing to determine the right hand side and left hand side of the FLDs, respectively [14]. The sheet material was 1.2 mm in thickness. Swift's strain hardening law ($\sigma = \tilde{K}(\varepsilon_0 + \varepsilon)^n$) was fitted to the experimental data points and its parameters were identified as $\tilde{K} = 814.04$ MPa, $\varepsilon_0 = 0.025$, and $n = 0.245$. No lubricant was used for the tests and the blank holding force was fixed at 40 kN.
Comparing the three sets of experiments that are mentioned above, one can see that the type of the experiments carried out by Wierzbicki *et al* [13] was different from the type of the experiments conducted by Lee *et al* [24] and Vallellano *et al* [14].

While the experiments performed by Wierzbicki and coauthors characterized the fracture process, the experiments carried out by Lee *et al* and Vallellano *et al* are cupping tests which normally characterize the necking limit. Therefore, one may argue that the three sets of the experimental data are inconsistent and cannot be directly compared with each other. There are two points which need to be noted in this regard. First, each of these three experimental datasets is considered independently and the four approaches studied in this paper are applied to each of the datasets. It is therefore possible to study each of the datasets both independently and in comparison with each other. Second, both Vallellano *et al* and Lee *et al* consider their data points as fracture limits and not necking limits. Vallellano *et al* [14] examined the fracture surface of their specimens using a microscope and observed that there was no localized necking at the fracture surface of any of the specimens. Moreover, the fracture zone of the specimens showed a through-thickness shear crack which continued from the top to the bottom of the cupping specimens. Finally, the cracks showed a faceted surface. Based on these three observations, they concluded that the obtained data points are fracture limits and not necking limits. Then, they used various phenomenological *ductile fracture criteria* to predict those fracture limits. Lee *et al* [17, 24] came to the same conclusion as Vallellano *et al*. They used a (continuum) ductile fracture criterion to predict the fracture limits as represented by their data points [17]. Therefore, even though they used cupping tests which result in necking limits for more ductile materials, necking is somehow precluded and the obtained failure limits are *indeed* fracture limits. The point that ductile fracture might preclude the necking process [14] is supported by the observations of other researchers who have reported no localized necking in deep drawing of 2024-T3 [16]. Indeed, Takuda and Hatta [16] came to the same conclusion as Vallellano *et al* and Lee *et al* and determined their fracture limits using a deep drawing experiment. Again, they used a phenomenological ductile fracture criterion to predict the fracture limits which were determined by their deep drawing test.

These three sets of experimental data will be presented in the forthcoming sections where they are used to validate the theoretically predicted fracture loci. Among the three experimental datasets, only the data provided by Wierzbicki *et al* is given in the equivalent strain-stress triaxiality space. The two other studies have given the fracture limits in the space of principal strains. For those two datasets, transformation from the space of principal strains to the equivalent strain-stress triaxiality space and vice versa is carried out by using the relationships provided in Appendix A. Plastic isotropy is assumed throughout this study. Assuming plastic isotropy facilitates this comparative study of the four different approaches considered in this chapter because not all the models studied here can take anisotropy into account. However, the *r*-value of most aluminum alloys including 2024-T3 is less than one, meaning that the yield surface is not as round as is suggested by the von Mises yield criterion. Therefore, transforming the experimental data points from the space of principal strains to the equivalent strain-stress triaxiality space could change the actual shape of fracture locus. In order to determine whether or not the transformation of the experimental data points from one space to the other influences the conclusions of this study, the four studied approaches were compared not only in the space of equivalent-strain-stress triaxiality but also in the space of principal strains. In order to compare the approaches in the space of principal strains, the predicted fracture loci were transformed to the space of principal strains. The experimental data points provided by Wierzbicki *et al* were also transformed to that space. It was not necessary to transform the data points provided by Vallellano *et al* and Lee *et al*. Comparing the fracture loci in the two spaces showed that transforming from one space to the other does not change the order of ranking of the different approaches studied in this paper. Appendix C presents the fracture loci in the principal strains space.

8.2. Phenomenological models

The phenomenological models of ductile fracture predict the onset of damage based on a macroscopically defined damage (accumulation) variable, D. This can be defined as

$$D = \wp(\sigma_{ij}, \varepsilon_{ij}{}^{p}) \tag{1}$$

Different phenomenological models use different damage evolution functions, $\wp$. The failure is assumed to take place once the damage variable reaches its critical value, D_c. Many different phenomenological damage initiation criteria are suggested by different researchers. In this study, eight different phenomenological fracture criteria are considered. These eight criteria are also used by Wierzbicki *et al* [13] for the failure prediction of 2024-T3. However, there are a number of differences between the study by Wierzbicki *et al* and the results presented here. First, Wierzbicki *et al* have used only one set of experimental data for the calibration and evaluation of the models. In this study, three different sets of experimental data (including the one presented by Wierzbicki *et al*) are used so that the whole range of stress triaxialities ($-1/3 < \eta < 2/3$) can be covered, particularly the high end of the range of stress triaxiality values (corresponding to positive strain ratios). The number of experimental data points presented by Wierzbicki *et al* is limited in this range of stress triaxialities. Second, the model calibration strategy used in this chapter is different from the one used by Wierzbicki *et al* in that they use only a fraction of their experimental data points for the calibration of individual models. This results in over-fitting of the models to that particular fraction of data and makes the models biased towards those data points. In the current study, the whole range of relevant experimental data points is used for the calibration of each individual model to eliminate bias and to be able to compare the models at their full predictive capacity. As a result of the different calibration strategies, even the fracture loci, predicted with the same models and calibrated using the same experimental dataset, are different in these two studies. Third, the comparison between different models is qualitative in the study by Wierzbicki *et al*. In this study, the models are compared both qualitatively and quantitatively. It will be shown that quantitative comparison between the models reveals some facts which can not be understood only with qualitative comparison. Finally, in this chapter, the equivalent strain at fracture is given as an explicit function of stress triaxiality for all the considered phenomenological models. Some of these explicit fracture loci are presented for the first time. Explicit presentation of the fracture loci not only facilitates functional comparison of the phenomenological models but also reveals the effects of different material parameters on the fracture limits and helps in understating the physical mechanism of failure.

Description of the phenomenological criteria. In this section, the phenomenological models used in this study are described. All the models are presented in the equivalent strain-stress triaxiality space. The values can be transferred to the principal strains space through the relationships given in Appendix A. The von Mises yield function and proportional loading assumption are adopted. Only the original and final formulations of each criterion are presented here. The intermediate formulations and the related mathematical elaborations are described in Appendix A, wherever non-trivial.

Constant Equivalent Strain (CES). This is the simplest phenomenological criterion which assumes that failure takes place at a constant equivalent strain, regardless of the stress triaxiality value. Therefore, the fracture locus is given by the following relationship

$$\varepsilon_{eq} = C_1 \tag{2}$$

Fracture Forming Limit Diagram (FFLD). By analyzing the available experimental fracture data points, Lee [29] suggested that the fracture locus in the principal strain space can be approximated by the following relationship

$$\varepsilon_1 + \varepsilon_2 = C_1 \tag{3}$$

Using the relationships given in Appendix A, it is straightforward to show that the FFLD criterion can be expressed in the equivalent strain-stress triaxiality space as

$$\varepsilon_{eq} = \frac{C_1}{\eta} \tag{4}$$

Maximum shear stress (Tresca). The maximum shear stress criterion, also known as Tresca criterion, postulates that the fracture takes place once the maximum shear stress reaches its critical value

$$\tau_{\max} = C_1 \tag{5}$$

In the equivalent strain-stress triaxiality space, the Tresca fracture locus is composed of two branches

$$\varepsilon_{eq} = \begin{cases} C_1 \left\{ \dfrac{\sqrt{2\left(-3\eta^2 + 2 - \aleph_1\right)}}{9\eta^2 - 4 + \aleph_1} \right\}^{\frac{1}{n}}, -\dfrac{1}{3} < \eta \le \dfrac{1}{3} \\ C_1 \left\{ \dfrac{\sqrt{2\left(-3\eta^2 + 2 - \aleph_1\right)}}{9\eta^2 - 2 - \aleph_1} \right\}^{\frac{1}{n}}, \dfrac{1}{3} < \eta \le \dfrac{2}{3} \end{cases} \tag{6}$$

where

$$\aleph_1 = \eta\sqrt{3\left(-9\eta^2 + 4\right)} \tag{7}$$

Johnson-Cook model. According to Johnson and Cook [30], for a given strain rate and temperature, the equivalent strain at fracture can be given as an exponential function of stress triaxiality as

$$\varepsilon_{eq} = C_2 \exp\left(C_3\eta\right) + C_1 \tag{8}$$

Xue-Wierzbicki model (X-W). The fracture criterion suggested by Xue and Wierzbicki [13] postulates that the fracture occurs once the integral of the modified plastic strain exceeds unity. The plastic strain is scaled by the factor, F, which is a function of stress triaxiality and the deviatoric state parameter, ξ, defined as [13]

$$\xi = \frac{27J_3}{2{\sigma_{eq}}^3} \tag{9}$$

Therefore, the fracture criterion can be stated as

$$\int_0^{\varepsilon_{eq,f}} \frac{d\varepsilon_{eq}}{F(\eta,\xi)} = 1 \tag{10}$$

The fracture criteria can be explicitly given as a function of the stress triaxiality as follows [13]

$$\varepsilon_{eq} = C_1 \mathrm{e}^{-C_2\eta} - (C_1\mathrm{e}^{-C_2\eta} - C_3\mathrm{e}^{-C_4\eta})(1 - \xi^{1/n})^n \tag{11}$$

where

$$\xi = \frac{-27}{2}\eta\left(\eta^2 - \frac{1}{3}\right) \tag{12}$$

Cockcroft-Latham model (CL). The fracture criterion suggested by Cockcroft and Latham [31] postulates that the fracture takes place once the accumulated equivalent strain multiplied by the major principal stress reaches its critical value

$$\int_0^{\varepsilon_{eq,f}} \sigma_1 d\varepsilon_{eq} = C_1 \tag{13}$$

The fracture locus can be given in the equivalent strain-stress triaxiality space as [13]

$$\varepsilon_{eq} = C_1 \frac{3\eta + \sqrt{12 - 27\eta^2}}{2\left(1 + \eta\sqrt{12 - 27\eta^2}\right)} \tag{14}$$

Wilkins model. According to Wilkins *et al* [32], the fracture takes place once the accumulated equivalent strain multiplied by a function of the entries of the stress tensor exceeds a critical value

$$\int_0^{\varepsilon_{eq,f}} \frac{(2 - A)^\mu}{(1 - a\sigma_H)^\lambda} d\varepsilon_{eq} = C_1 \tag{15}$$

where $A = \max(\sigma_2' / \sigma_1', \sigma_2' / \sigma_3')$ and a, λ, and μ are material constants. As detailed in Appendix A, the fracture locus in the equivalent strain-stress triaxiality space can be given by

$$\varepsilon_{eq} = \begin{cases} C_1\left(1 - \frac{2}{3}\eta\right)^{C_2}\left(3 - \frac{-3\eta^2 - 2 + \sqrt{-27\eta^4 + 12\eta^2}}{2(3\eta^2 - 1)}\right)^{(-109/50)}, \frac{-1}{3} \le \eta \le 0 \\ C_1\left(1 - \frac{2}{3}\eta\right)^{C_2}\left(\frac{3\eta^2 + 2 - 3\aleph_2}{3\eta^2 - \aleph_2}\right)^{C_3}, 0 < \eta \le \frac{1}{3} \\ C_1\left(1 - \frac{2}{3}\eta\right)^{C_2}\left(\frac{3\eta^2 - 4 + 3\aleph_2}{3\eta^2 - 2 + \aleph_2}\right)^{C_3}, \frac{1}{3} < \eta \le \frac{1}{\sqrt{3}} \\ C_1\left(1 - \frac{2}{3}\eta\right)^{C_2}\left(3 + \frac{-3\eta^2 + 2 + \sqrt{-27\eta^4 + 12\eta^2}}{2(3\eta^2 - 1)}\right)^{(-109/50)}, \frac{1}{\sqrt{3}} < \eta \le \frac{2}{3} \end{cases} \tag{16}$$

where

$$\aleph_2 = \eta\sqrt{-27\eta^2 + 12} \tag{17}$$

CrachFEM shear and ductile fracture models. In the CrachFEM model [33], it is argued that the fracture could happen due to either ductile fracture or shear fracture.

While the ductile fracture is due to void nucleation, growth, and coalescence and is identified by a rough fracture surface, the shear fracture is due to the shear band localization and is identified by an inclined fracture surface. Two different criteria are suggested for these two fracture mechanisms. The ductile fracture locus is given as the following sum of two exponential functions

$$\varepsilon_{eq,f}{}^{ductile} = C_1 \mathrm{e}^{(-C_2\eta)} + C_3 \mathrm{e}^{(C_2\eta)} \tag{18}$$

The shear fracture locus is stated as

$$\varepsilon_{eq,f}{}^{shear} = C_1 \mathrm{e}^{(-C_2\tilde{\theta})} + C_3 \mathrm{e}^{(C_2\tilde{\theta})} \tag{19}$$

where

$$\tilde{\theta} = \frac{\sigma_{eq}}{\tau_{\max}}(1 - 3k_s\eta) \tag{20}$$

Equation (19) gives an explicit description of the fracture locus in the equivalent strain-stress triaxiality space, provided that the variable $\tilde{\theta}$ can be explicitly expressed in this space. It is shown in Appendix A that the variable $\tilde{\theta}$ can be given as a function of stress triaxiality and material parameters as

$$\tilde{\theta} = \begin{cases} \dfrac{\sqrt{24}(-1 + 3k_s\eta)(-3\eta^2 + 2 - \aleph_3)}{9\eta^2 - 2 - \aleph_3}, -\dfrac{1}{3} < \eta \leq \dfrac{1}{3} \\ \dfrac{\sqrt{24}(-1 + 3k_s\eta)(-3\eta^2 + 2 - \aleph_3)}{9\eta^2 - 4 + \aleph_3}, \dfrac{1}{3} < \eta \leq \dfrac{2}{3} \end{cases} \tag{21}$$

where

$$\aleph_3 = \sqrt{3}\eta\sqrt{-9\eta^2 + 4} \tag{22}$$

Calibration of the phenomenological models. The models described in the previous section were calibrated using the three experimental datasets. Each individual model was calibrated four times, each time using one single experimental dataset. As described in the section on "experimental data", the experimental datasets included the data points provided by Lee *et al* in 1997 [24], Wierzbicki *et al* in 2005 [13], and Vallellano *et al* in 2008 [14]. However, the experimental data provided by Wierzbicki *et al* was used twice. Initially, all the data points were used for the calibration of the model. The second time, only data points with a stress triaxiality value between $1/3$ and $2/3$ were used for the calibration of the models. The data was analyzed in these two different conditions because the range of the measured stress triaxialities are much broader in this dataset and some of the data points are outside the range of the stress triaxialities important in the analysis of the sheet metal forming processes. The calibration process aimed at minimizing the sum of the squared prediction errors of the phenomenological models by tuning the parameters C_1 to C_4. The linear least squares method was used for the identification of the unknown parameters of all C^1-continuous fracture loci. The functions not satisfying the C^1-continuity condition were calibrated using the direct search nonlinear optimization theory. The calibration parameters along with the prediction error of the models are listed in Table 8.1. The prediction error is given in terms of Sum Squared Error (SSE) and Root Mean Squared Error ($RMSE$) as defined below

$$SSE = \sum_{i=1}^{m}(y_i - \hat{y}_i)^2, RMSE = \sqrt{\frac{SSE}{v}}, v = m - m_C \tag{23}$$

The fracture loci predicted by the phenomenological models are depicted in Figure 8.1a-d.

Discussion on the results. For each series of the experimental datasets, the error values related to the two best-performing models (minimum *RMSE* values) are typed in bold font whilst the ones related to the worst-performing models (maximum *RMSE* values) are underlined (Table 8.1). One can see that the best overall performances is exhibited by the X-W and Wilkins models while the FFLD and Tresca models show the worst overall performance. The *RMSE* of the FFLD model is in three out of four cases more than that of the CES, meaning that this model often behaves even worse than the CES. Even though the overall shape of the fracture locus predicted by Tresca model is quite similar to the ones predicted by X-W, Wilkins, and CrachFEMII, its performance is much worse, so much so that the *RMSE* of the Tresca model is in two cases even more than that of the CES. Therefore, a quantitative study of the errors leads us to a conclusion that is contrary to previous qualitative studies [13, 14]. Those previous studies have concluded that the Tresca model, despite its simplicity, can give quite accurate predictions of forming limits. The other important conclusion is that the $RMSE$ value is lower when the experimental data points are limited to the ones with large stress triaxiality. Therefore, one can argue that phenomenological models are even more appropriate for sheet metal forming applications than for general (bulk) forming purposes. Furthermore, the results of the study show that, aside from the Wilkins and X-W models which show superior performances, the other models are in many cases almost the same or even less accurate than the very simple CES criterion.

8.3. Porous metal plasticity theory

The Porous Metal Plasticity (PMP) theory deals with the physical mechanism of ductile fracture and directly works with nucleation, growth, and coalescence of voids. The porous metal plasticity models are also known as Gurson type models [19]. The von Mises yield function is modified to account for the presence and evolution of voids. The modified yield function can be stated as follows [34]

$$\Phi = \left(\frac{\sigma_{eq}}{\sigma_y}\right)^2 + 2\tilde{\alpha} f_{void} \cosh\left(-\tilde{\beta}\,\frac{3\sigma_H}{2\sigma_y}\right) - \left(1 + \tilde{\gamma} {f_{void}}^2\right) = 0 \qquad (24)$$

where $\sigma_{eq}, \sigma_H,$ and σ_y are respectively the effective Mises stress, hydrostatic pressure, and yield stress of the fully-dense matrix material. The parameter f_{void} is the ratio of the volume of voids to the total volume of the material and is called the void volume fraction. Three remaining parameters, namely $\tilde{\alpha}$, $\tilde{\beta}$ and $\tilde{\gamma}$, are experimentally-determined material parameters. It is assumed that there is an initial population of voids in the material which is represented by the initial void volume fraction, $f_{void,0}$. As the material deforms, voids nucleate, grow, and coalesce and the stress-carrying capacity of the material is lost, resulting in contraction of the yield locus.

Table 8.1. The parameters of the phenomenological ductile fracture models as determined by the calibration process and the values of the prediction error identifiers. The values given between parentheses relate to the case where a fraction of the data provided by Wierzbicki *et al* [13] for which *n*>1/3 is used for calibration of the models.

		CES	FFLD	Tresca	JC	X-W	CFEM I	CFEM II	CL	Wilkins
Lee *et al* 1997	C_1	.229	.099	9.10	21.280	.077	.003	-.020	.247	.07
	C_2	NA	NA	NA	-21.130	-3.389	6.759	.255	NA	-2.0
	C_3	NA	NA	NA	-.007	.127	1.549	.152	NA	-1.1
	C_4	NA	NA	NA	NA	-.889	NA	NA	NA	NA
	SSE	.101	0.376	.239	.086	.046	.058	.099	.105	.027
	$RMSE$	.054	<u>0.105</u>	<u>.084</u>	.052	**.038**	.042	.056	.056	**.029**
Wierzbicki *et al* 2005	C_1	.361(.347)	.002(.141)	14.33(12.45)	23.910 (-55.450)	.879(3.158e-5)	.284(-17.75)	-1.082(-.324)	.077(.369)	.35(0.57)
	C_2	NA	NA	NA	-23.530 (56.010)	1.494(-21.380)	.809(-.014)	1.997(1.472)	NA	1.3(4.9)
	C_3	NA	NA	NA	.005 (-.009)	.296(2.441)	.085 (18.32)	.009(.023)	NA	-1.3(1.8)
	C_4	NA	NA	NA	NA	.127(4.017)	NA	NA	NA	NA
	SSE	.166(.055)	1.945(.037)	.149(.051)	.141 (.032)	.105(0.015)	.140(0.032)	.110 (.038)	.708(.045)	.127(.025)
	$RMSE$	.113(.096)	<u>.387</u>(.079)	.107 (<u>.092</u>)	.113 (.089)	**.102**(**0.071**)	.113(0.089)	**.100** (<u>.097</u>)	<u>.233</u>(.087)	.108(**0.079**)
Vallellano *et al* 2008	C_1	.256	0.134	3.33	145.5	.096	.002	-.079	.283	.06
	C_2	NA	NA	NA	-145.3	-2.896	7.647	.337	NA	-2.7
	C_3	NA	NA	NA	-.000	.027	2.790	.164	NA	-1.4
	C_4	NA	NA	NA	NA	-3.426	NA	NA	NA	NA
	SSE	.022	.075	.033	.020	.003	.004	.021	.020	.003
	$RMSE$	.052	<u>.096</u>	<u>.064</u>	.058	**.025**	.026	.059	.050	**.022**

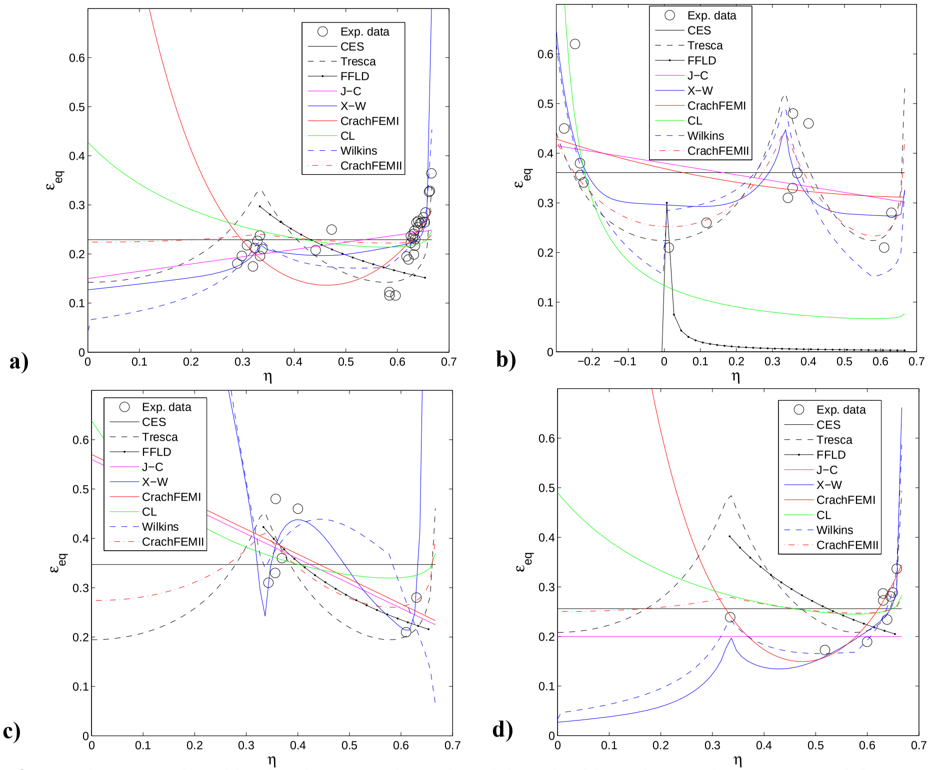

Figure 8.1. The fracture loci as predicted by the phenomenological models and calibrated using the experimental data given by Lee *et al* [24] (a), Wierzbicki *et al* [13] (b), Wierzbicki *et al* [13] using only the data points with large stress triaxiality (η>1/3) (c), and Vallellano *et al* [14].

These mechanisms of void evolution need to be accounted for in order to arrive at a realistic simulation of the ductile fracture mechanism. To account for the effects of void evolution and the resulting loss of the stress carrying capacity, the yield function can be rewritten as

$$\Phi = \left(\frac{\sigma_{eq}}{\sigma_y}\right)^2 + 2\tilde{\alpha} f_{void}^* \cosh\left(-\tilde{\beta}\frac{3\sigma_H}{2\sigma_y}\right) - \left(1 + \tilde{\gamma} {f_{void}^*}^2\right) = 0 \tag{25}$$

where the effective void volume fraction, f_{void}^*, is defined as a function of the void volume fraction, f_{void}, as follows

$$f_{void}^* = \begin{cases} f_{void}, \; f_{void} \le f_{void,c} \\ f_{void,c} + \dfrac{\overline{f}_{void,f} - f_{void,c}}{f_f - f_c}(f_{void,f} - f_{void}), \; f_{void,c} \le f_{void} \le f_{void,f} \\ \overline{f}_{void,f}, \; f_{void} \ge f_{void,f} \end{cases} \tag{26}$$

where

$$\overline{f}_{void,f} = \frac{\tilde{\alpha} + \sqrt{\tilde{\alpha}^2 - \tilde{\gamma}}}{\tilde{\gamma}} \tag{27}$$

The critical void volume fraction, $f_{void,c}$, is the void volume fraction at which the loss of stress carrying capacity starts. The material continues to loose its stress carrying capacity until the void volume fraction reaches the failure void volume fraction, $f_{void,f}$, at which the material fails.

The evolution of the void volume fraction is due to two contributing phenomena, namely void growth and void nucleation. Therefore, the time derivative of the void volume fraction can be calculated as

$$\dot{f}_{void} = \dot{f}_{void,gr} + \dot{f}_{void,nucl} \tag{28}$$

where subscripts ‘*gr*’ and ‘*nucl*’ stand for void growth and void nucleation, respectively. Based on the mass conservation law, the change in the void volume fraction due to void growth can be described as follows

$$\dot{f}_{void,gr} = (1 - f_{void})\dot{\varepsilon}^p : \mathbf{I} \tag{29}$$

The void nucleation dynamics is governed by the following relationship

$$\dot{f}_{void,nucl} = \tilde{A}\dot{\bar{\varepsilon}}_m{}^p \tag{30}$$

where

$$\tilde{A} = \frac{f_{void,N}}{s_N\sqrt{2\pi}}\exp\left[-\frac{1}{2}\left(\frac{\varepsilon_{eq}{}^p - \varepsilon_N}{s_N}\right)^2\right] \tag{31}$$

In Equation (31), it is assumed that the nucleation strain is normally distributed within the material with a mean value of ε_N and a standard deviation of s_N. The volume fraction of nucleated voids is denoted by $f_{void,N}$. Voids are assumed to nucleate only in tension.

Model calibration. The parameters of the porous metal plasticity model determined by Caputo *et al* for 2024-T3 were used ($f_{void,0}$=0.025, ε_N=0.09, s_N=0.045, $\tilde{\alpha}$=1.33, $\tilde{\beta}$=0.956, $\tilde{\gamma}$=1.77) [23]. Three remaining parameters needed to be determined during the calibration process. Accurate calibration of the PMP model is a complicated and computationally expensive process because advanced techniques are needed to go further than qualitative calibration procedures, which are mainly based on trial and error experiments, to reach the level of calibration accuracy that is necessary for quantitative comparison of different modeling approaches. In this study, a novel calibration technique based on artificial intelligence theories was used for calibration of the PMP model.

The complexity of the calibration procedure of the PMP models is due to two main reasons: the relatively large number of the calibration parameters (3 to 4 and sometimes even more) and the complicated morphology of the mappings from parameter space to fracture locus space. The mappings from parameter space to fracture locus space are needed because direct evaluation of the mathematical representation of the PMP model for every iteration of the optimization algorithm is difficult to implement and is very computationally expensive. Therefore, there are two main challenges in calibration of the PMP models: finding an efficient way of mapping the parameter space to the fracture locus and finding an efficient nonlinear optimization algorithm that is able to deal with the degree of morphological complexity that is seen in the mappings. The nonlinear optimization algorithm must satisfy the nonlinear constraints between the parameters and still keep sensibly progressing towards the global optimum without falling into the saddles surrounding local optima. Artificial Neural Networks (ANNs) were selected to establish the mappings. Pattern Search Algorithm, which belongs to the same family of meta-heuristic optimization algorithms as Genetic Algorithms, was selected for identifying the parameter values.

Artificial neural networks. ANNs are designed to mimic the functionality of biological networks of neurons. They are composed of the so-called artificial neurons which are the building blocks of ANNs and are arranged in layers. Figure 8.2a presents a schematic drawing of a typical ANN. As one can see in this figure, a typical ANN has a certain number of inputs, n_{in}, and a certain number of outputs, n_{out}. ANNs map the space of inputs to the space of outputs and are made of multiple layers. There are one input and one output layer in ANNs. The layers which are between the input and output layers are called hidden layers. Each hidden layer contains a number of artificial neurons. The numbers of neurons in the input and outputs layers are equal to the number of inputs and outputs of the ANN. The neurons that belong to the hidden layers are called hidden neurons. Each hidden layer could have as many hidden neurons as needed. The task of the input and output layers is to connect the ANN to the outside world and the processing task is all carried out in the hidden layers. As is demonstrated in Figure 8.2, various layers and neurons are strongly interconnected.

A representative neuron is depicted in Figure 8.2b. Every such neuron has a so-called activation function, f, such as the tang-sigmoid function. The neuron assigns weights, w_i s, to the signals, p_i s, that come to it through its incoming connections. The weighted signals are then summed up and biased (summed with b) and the result is introduced to the activation function. The scalar outcome of the function is sent out of the neuron through the outgoing connections of the neuron.

Application of ANNs requires that the parameters of neurons (weights, w_i , and biases, b) be tuned such that the mapping carried out by the ANN is the same as or very close to the desired mapping. The process of tuning the parameters of an ANN is called training. A training dataset composed of a number of inputs and their corresponding (target) outputs is needed for this purpose. The ANN is trained by a training algorithm such that, for the given set of inputs, the outputs of the ANN are very close to the target outputs.

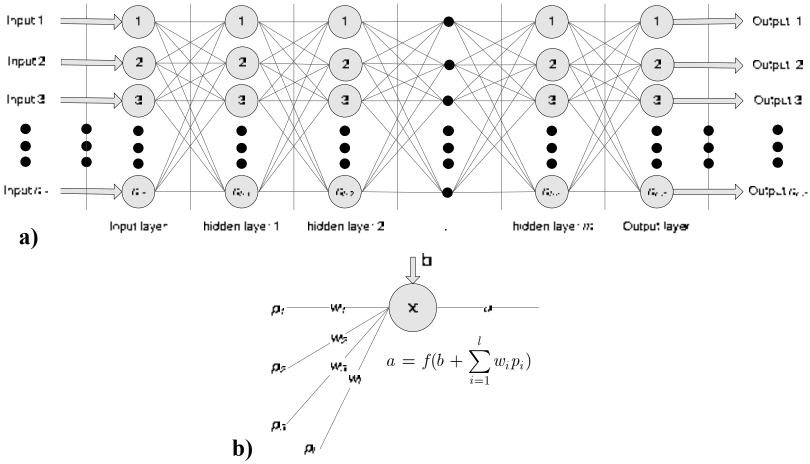

Figure 8.2. A schematic drawing of a typical artificial neural network (a) and a single neuron (b).

In this study, the intention is to use ANNs for representing the PMP model. The desired ANNs in this study represent the fracture loci that are predicted by the PMP model. One ANN is constructed for each of the three experimental datasets. The ANNs take four inputs including three characteristic void volume fractions, $f_{void,N}$, $f_{void,c}$, and $f_{void,f}$ and stress triaxiality, η . The equivalent strain at fracture is the output of the ANNs. As was already pointed out, three training datasets are needed to train the ANNs for the three experimental datasets. For each of the experimental datasets, the training dataset is generated by solving the PMP model for a large number of different combinations of void volume fractions, $f_{void,N}$, $f_{void,c}$, and $f_{void,f}$ and stress triaxiality value. The equivalent strains at fracture are calculated for each combination of the model parameters by using the PMP model. The considered combinations of the model parameters and their corresponding fracture limits are gathered in a training dataset. The model parameters are introduced to the training algorithm as the inputs of the ANNs and the training algorithm is applied to train the ANNs such that their predicted fracture limits are very close to the targeted fracture limits.

It is mathematically proven that a feedforward ANN with at least one hidden layer and sigmoid activation functions can approximate any continuous function independently from the dimension of the input space with an integrated square error of the order $O(1/n)$ [35]. Here, n is the number of the hidden neurons. The point that approximation error is independent from the dimension of the input space relieves the difficulty with the large number of the calibration parameters. Furthermore, every continuous function can be approximated to an arbitrary degree of accuracy which means that the ANNs are capable of successfully representing the complex morphology of the needed mappings.

Details of the parameter identification process. Three feedforward ANNs with one hidden layer and 120 hidden neurons activated with tang-sigmoid functions were used for the presentation of the mappings from the parameters space to fracture locus space. In order to generate the dataset needed to train the ANNs, the fracture limits were calculated for strain ratios ranging from -0.9 to 1.0 and a large set of parameter value combinations (7400 samples). Simulations were carried out using plane stress shell elements. The results were transformed from the principal strains space to the equivalent strain-triaxiality space using the relationships given in Appendix A. Training was carried out by using 90% of the training data points and by applying the quasi-Newtonian back-propagation method of Levenberg-Marquardt. Figure 8.3a shows the root mean square of the mapping error vs. the number of training iterations for one of the ANNs (the one related to the experimental dataset provided by Lee *et al* [24]). As is clear from this figure, the mapping error effectively decreases by 7 orders of magnitude within 100 iterations. The residual error is negligible for virtually all engineering purposes. The remaining 10% of the training data points was divided into two subsets (5% each) which were used for validation and testing of the trained ANN to see how the ANN performs for data points other than the ones used for its training. Figure 8.3b-d shows the results of the regression analysis for training, validations, and testing data points. Regression parameter, R, is defined as the linear correlation coefficient between the actual network outputs and targeted network outputs. A regression parameter of 1 means perfect correlation between the actual outputs and targeted outputs. One can see that the regression parameter, R, which is given on top of each subfigure, is very close to unity for all the three subsets of the training data meaning that the ANN can successfully present the complex morphology of the involved mappings.

Once the ANNs are constructed and successfully trained, a nonlinear optimization algorithm is needed to identify the input parameters of the ANNs such that the outputs of the ANNs are as close to the experimental data points as possible. Using the terminology of the optimization theory, it can be stated that the optimization algorithm should be able to minimize the objective function that in this study is defined as the $RMSE$. Therefore, the optimization algorithm is responsible for finding the void volume fractions, $f_{void,N}$, $f_{void,c}$, and $f_{void,f}$, that minimize the prediction error ($RMSE$) of the PMP model. In this study, the pattern search technique is used as the nonlinear optimization algorithm.

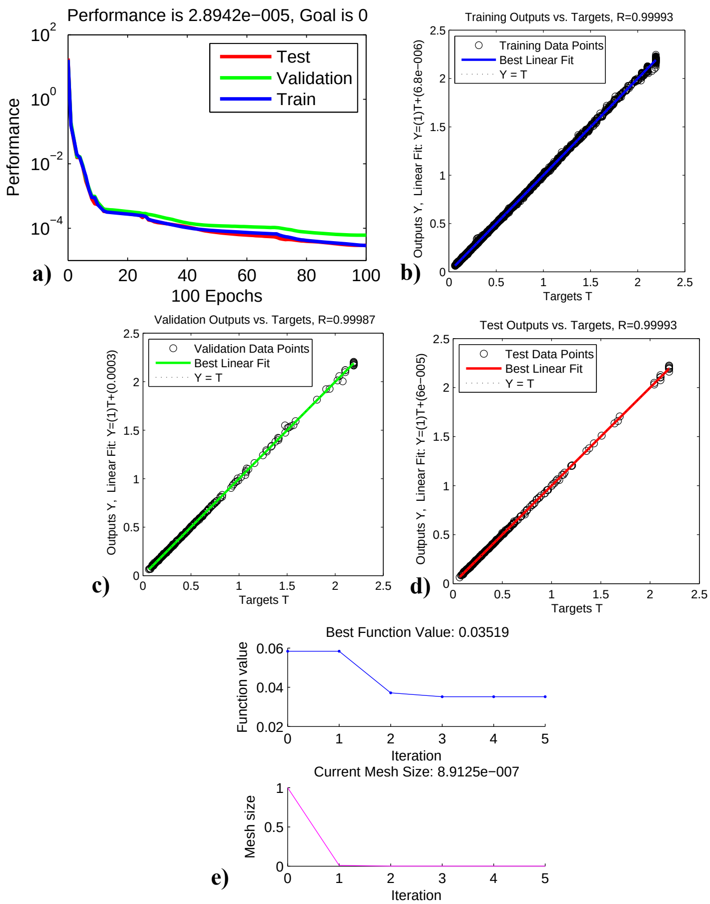

Figure 8.3. Training curve (a) and regression analysis of the training data points (b), validation data points (c) and test data points (d) performance of the artificial neural networks used for representation of the porous metal plasticity models. The performance of the pattern search algorithm used for optimization of the model parameters is depicted in subfigure (e) in terms of best function value (upper part) and mesh size (lower part).

The pattern search technique [36] is a type of direct search method which tries to optimize an objective function by applying some constraints. The constraints are the bound limits of the independent variables of the objective function. Based on the number of independent variables and a positive basis set, a set of vectors is defined, namely "pattern". Let the number of independent variable be n ; $2n$ vectors are used for a maximum positive basis, and $n+1$ vectors for a minimal positive basis. During each iteration, the pattern search algorithm applies this pattern to look for a set of points (mesh). The values of the objective function are calculated for all the points in that set and the process continues until a point is found which has an objective function value less than that of the successful point of the previous iteration. This point is used as the basis of comparison for the next iteration. The whole process will be stopped when either the objective function value or the mesh size is less than a small predetermined value. In this study, the minimum mesh size was 1×10^{-6}. Figure 8.3e depicts the objective function value and the mesh size vs. iteration. One can see that the algorithm shows a rapid convergence to the minimum possible objective function value within a few iterations. However, the objective function has to be evaluated several thousand times for each iteration. The model parameters were identified using the above-mentioned techniques and were used for determination of the corresponding fracture loci which are shown in Figure 8.4a-d. The parameter values along with the $RMSE$ and SSE values are annotated in each subfigure.

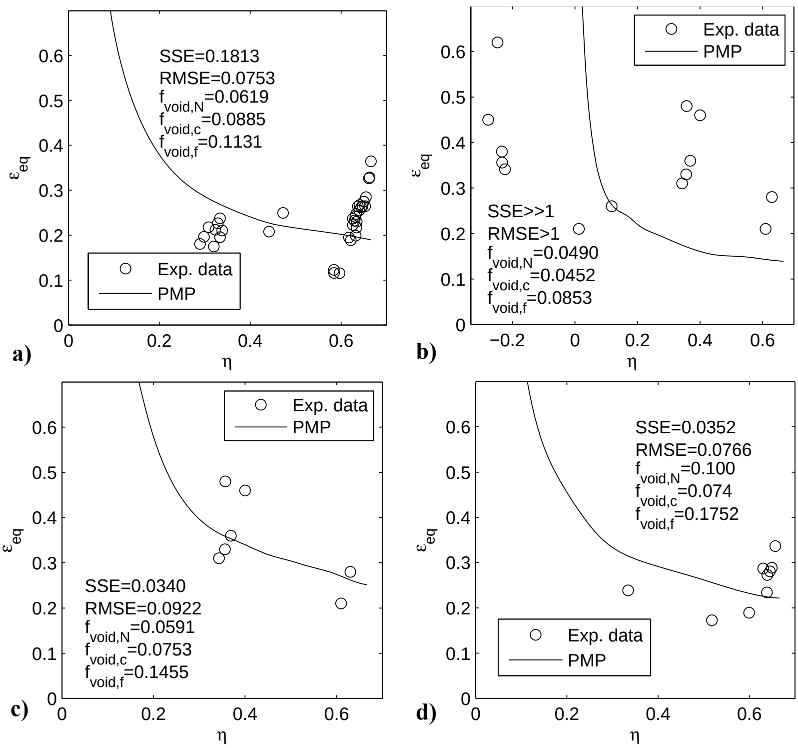

Figure 8.4. The fracture loci as predicted by the porous metal plasticity theory and calibrated against the experimental datasets provided by Lee *et al* [24] (a), Wierzbicki *et al* [13] (b), Wirezbicki *et al* [13] including only the data points with large stress triaxialities (c), and Vallellano *et al* [14] (d).

Discussion on the results. The fracture loci shown in Figure 8.4 are monotonic functions of the stress triaxiality. The equivalent strain at fracture decreases as stress triaxiality increases but there is no upward trend of the equivalent strain value at the end of the stress triaxiality range, i.e. for $\eta > 1/\sqrt{3}$. Therefore, the fracture loci are different from the conventional V-shape FLDs obtained for ductile materials, such as mild steels and low strength aluminum alloys. The $RMSE$ values obtained for the PMP model are generally greater than those of the best-performing phenomenological models such as X-W and Wilkins. The prediction error is again lower when the experimental data points are limited to the range of large stress triaxialities ($\eta > 1/3$).

8.4. Marciniak-Kuczynski theory

The Marciniak-Kuczynski (M-K) theory was developed for the prediction of sheet metal instability during forming processes [12]. In this theory, it is assumed that an initial imperfection is present in the metal sheet. The imperfection is modeled by a band of smaller thickness (see Figure 8.5 for a schematic presentation of the assumption). The initial imperfection can originate from what is actually a smaller thickness, a local variation of the strength, or a combination of both. The imperfection parameter, f_0, is defined as

$$f_0 = \frac{\underset{\sim}{K}_b t_{b,0}}{\underset{\sim}{K}_a t_{a,0}} \tag{32}$$

Originally, it was assumed that the imperfection zone is perpendicular to the major stress, σ_1, axis. This assumption can give the right-hand side of FLDs. In order to be able to produce both sides of FLDs, Hutchinson and Neale [37, 38] modified the assumption to allow the imperfection to lie at an angle, θ, to the σ_2-axis. The imperfection angle must be determined such that the limit strains are minimized. The angle for which the limit strains are minimized is dependent on the strain ratio. For proportional loading of planar isotropic materials, Hill's zero-extension angle can be used for calculation of forming limits [39].

During a biaxial straining process, the imperfection zone deforms more than the uniform zone. Therefore, the strain path of the imperfection zone is continuously ahead of the strain path of the uniform zone. At a certain point when strain localization occurs, the difference between the strain paths of the imperfection and uniform zones begins to increase drastically. In M-K analyses, the strain paths of both zones are traced and a criterion is used for detection of the high degree of discrepancy which is presumed to be an indicator of strain localization. Once strain localization is detected, sheet metal is assumed to have failed.

Formulation of the M-K theory. Consider Figure 8.5 in which a schematic presentation of the geometry of the model is given. The following conditions are assumed: 1. Plane stress condition applies and there is an initial imperfection in the sheet metal with an initial imperfection parameter equal to f_0. 2. Initial imperfection axis is initially oriented at a θ angle to the minor principal stress, the σ_2-axis. 3.

Damage phase is excluded and the constant volume assumption can be used meaning that

$$\varepsilon_{33,b} = -\left(\varepsilon_{11,b} + \varepsilon_{22,b}\right), \dot{\varepsilon}_{33,b} = -\left(\dot{\varepsilon}_{11,b} + \dot{\varepsilon}_{22,b}\right)$$
$$\varepsilon_{33,a} = -\left(\varepsilon_{11,a} + \varepsilon_{22,a}\right), \dot{\varepsilon}_{33,a} = -\left(\dot{\varepsilon}_{11,a} + \dot{\varepsilon}_{22,a}\right) \tag{33}$$

The compatibility condition can be stated as

$$\varepsilon_{tt,b} = \varepsilon_{tt,a}, \dot{\varepsilon}_{tt,b} = \dot{\varepsilon}_{tt,a} \tag{34}$$

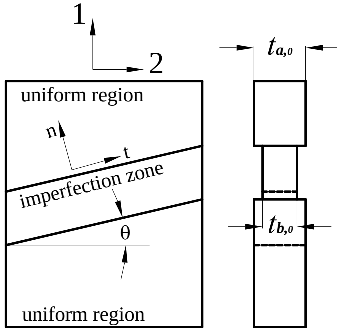

Figure 8.5. A schematic presentation of the imperfection assumption used in the M-K theory.

The force equilibrium condition can be formulated as

$$\sigma_{nn,b} f = \sigma_{nn,a}, \sigma_{nt,b} f = \sigma_{nt,a} \tag{35}$$

In each time step, the parameters of the imperfection zone in that particular time step should be used in the calculations. Transformation of the stress and strain tensors of the uniform zone from the anisotropy (1-2-z) coordinate systems to the groove's coordinate system (t-n-z) is performed by using the coordinate rotation matrix

$$_{ntz}\boldsymbol{\sigma} = \mathbf{T}\,_{12z}\boldsymbol{\sigma}\mathbf{T}^{\mathrm{T}} \qquad _{ntz}\boldsymbol{\varepsilon} = \mathbf{T}\,_{12z}\boldsymbol{\varepsilon}\mathbf{T}^{\mathrm{T}} \tag{36}$$

where

$$\mathbf{T} = \begin{bmatrix} \cos\theta & \sin\theta & 0 \\ -\sin\theta & \cos\theta & 0 \\ 0 & 0 & 1 \end{bmatrix}, {}_{12z}\boldsymbol{\varepsilon} = \begin{bmatrix} \varepsilon_{11} & 0 & 0 \\ 0 & \varepsilon_{22} & 0 \\ 0 & 0 & -\left(\varepsilon_{11} + \varepsilon_{22}\right) \end{bmatrix}, {}_{12z}\boldsymbol{\sigma} = \begin{bmatrix} \sigma_{11} & 0 & 0 \\ 0 & \sigma_{22} & 0 \\ 0 & 0 & 0 \end{bmatrix} \tag{37}$$

Evolution of the angle θ is described by using the following equation

$$\tan\left(\theta + \delta\theta\right) = \tan\left(\theta\right)\frac{1 + \delta\varepsilon_{11,a}}{1 + \delta\varepsilon_{22,a}} \tag{38}$$

Evolution of the imperfection parameter, f, takes place according to the following equation

$$f = f_0 \exp\left(\varepsilon_{33,b} - \varepsilon_{33,a}\right) \tag{39}$$

Hill's zero extension angle can be given for the von Mises yield function as [39]

$$\theta = \frac{\pi}{2} - \frac{1}{2}\cos^{-1}\left(\frac{1+\beta}{1-\beta}\right), \beta = \frac{\varepsilon_2}{\varepsilon_1} \tag{40}$$

The strain increments in the uniform material are imposed based on the loading scenario, i.e. proportional loading. The strains in the imperfection zone are then calculated from the strain values in the uniform zone using the above-mentioned equations. The critical ratio of the strain increment in the region b to that of the region a was considered 10. The Hollomon's hardening rule and von Mises yield criterion were adopted.

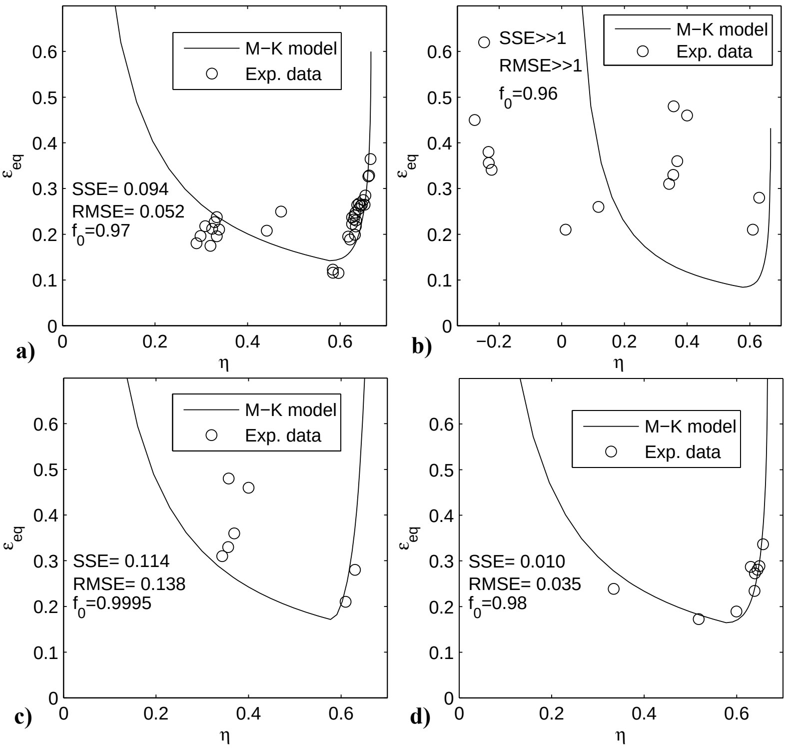

Figure 8.6. The fracture loci as predicted by the M-K theory and calibrated against the experimental datasets provided by Lee *et al* [24] (a), Wierzbicki *et al* [13] (b), Wirezbicki *et al* [13] including only the data points with large stress triaxialities (c), and Vallellano *et al* [14] (d).

Calibration of the M-K model. For each set of the experimental data points, a high resolution scanning of the applicable domain of imperfection parameters was carried out. A code developed for the solution of the M-K model was used to generate the data needed to calibrate the model. A second code was developed to fit a cubic spline interpolant to the fracture loci calculated during the data generation phase and to identify the initial imperfection parameter based on the direct search nonlinear optimization theory. The initial imperfection parameter was identified by minimizing the $RMSE$. Figure 8.6a-d shows the fracture loci, as predicted by the calibrated M-K model, and compares them with the experimental data points. For each experimental dataset, the identified imperfection parameter, SSE, and $RMSE$ are annotated in the corresponding subfigures.

Discussion on the results. One can see that while the M-K model can give a fairly good prediction of forming limits for the experimental datasets provided by Lee *et al* (1997) and Vallellano *et al* (2008), it shows a poor agreement with the experiments of Wierzbicki *et al* (2005). However, the agreement is much better if only the data points with large stress triaxialities are used for calibration and comparison of the model (Figure 8.6c). If plotted in the principal strain space, the shapes of the fracture loci are similar to the classical V-type shape of the FLDs of mild steels and ductile aluminum alloys. In the equivalent strain-stress triaxiality space and near to the high end of the stress triaxialities ($\eta > 1/\sqrt{3}$), the fracture envelopes show a sharply increasing trend which is in agreement with the trend exhibited by the experimental data points, particularly the ones provided by Lee *et al* [24] and Vallellano *et al* [14]. However, the theoretical fracture loci severely deviate from the fracture limits in the range of small stress triaxialities ($1/3 < \eta < 1/\sqrt{3}$).

8.5. Combined porous metal plasticity and Marciniak-Kuczynski model

The final approach studied in this chapter, hereafter referred to as MK-PMP, is a combination of the porous metal plasticity (PMP) and Marciniak-Kuczynski theories to account for both physical mechanisms of ductile fracture and sheet metal instability. It is assumed that: 1.There is an initial imperfection in the metal 2. The material in uniform and imperfection zones contain a population of initial voids that are subject to further nucleation, growth and coalescence as deformation takes place. Figure 8.7 presents a schematic drawing of the model. For a given strain ratio, β, the uniform zone (zone *a*) was proportionally strained in increments. For each strain increment, the elastoplastic equations of deformation were first integrated in zone *a*. Given the stress and state variables at time t and imposing the strain increment, $\Delta\varepsilon$, the stress and state variables at time $t + \Delta t$ were calculated by using the backward Euler integration scheme proposed by Aravas [40]. A summary of the method as applied to the current model is presented in the next subsection. Compatibility and force equilibrium conditions were used to relate the stress and strain values calculated for zone *a* to those of zone *b*. The complete stress and strain tensor of zone *b* was then calculated by the compatibility and equilibrium conditions required. For each time increment, the void volume fractions of both the uniform and imperfection zones were modified using Equations (29)-(32).The evolution of the yield locus was governed by Equations (27) and (28). Once the void volume fraction of the imperfection zone reached the failure void volume fraction, $f_{void,f}$, the sheet was assumed to have failed and the strain values in the uniform zone were recorded as forming limits.

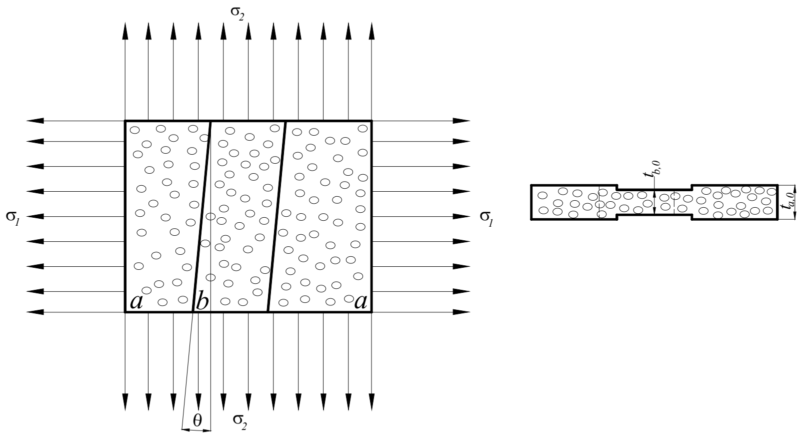

Figure 8.7. Schematic drawing of the combined PMP and M-K model

The analysis in this section includes only the positive strain ratio, i.e. $\beta > 0\ (\eta > 1/\sqrt{3})$, for two reasons: First, the PMP model has been shown to act quite satisfactorily for small stress triaxialities ($1/3 < \eta < 1/\sqrt{3}$) and given that the PMP model is essentially a special case of the MK-PMP model (with $f_0 = 1$) one knows that the MK-PMP model can give accurate prediction of fracture limits for that range of stress triaxialities. Second, the minimizing imperfection angle, θ, which is given based on Hill's zero extension assumption by Equation (41) for the von Mises yield function is different for other yield functions including the Gurson-type yield function used in this study [41]. In such cases, the minimizing angle is normally determined by scanning the space of the imperfection angle with a fine resolution and by solving the M-K equations for all the imperfection angles. One recent study has shown that a resolution of at least 1 degree is necessary to assure accurate results [41]. Therefore, the already high computational expense of the training data generation phase is multiplied by a factor of 90 resulting in several thousands hours of computation time for each series of the experimental datasets which is formidably high and out of reach.

Numerical formulation of the model. The elastoplastic equations governing the deformation of the uniform and imperfection zones were incrementally solved using the backward Euler integration scheme proposed by Aravas [40]. A summary of this method is presented here. It is assumed that the stress and state variables are known at time t and the strain increment $\Delta\varepsilon$ is imposed according to the proportional loading assumption. The stress and state variables at time $t + \Delta t$ need to be determined such that the flow rules, yield function, and the evolution equations of the state variables are satisfied.
The strain increment $\Delta\varepsilon$ is composed of elastic and plastic components

$$\Delta\varepsilon = \Delta\varepsilon^p + \Delta\varepsilon^e \tag{41}$$

The elasticity equation can be written as

$$\boldsymbol{\sigma} = \mathbf{C} : (\varepsilon^e|_t + \Delta\varepsilon - \Delta\varepsilon^p) = \boldsymbol{\sigma}^e - \mathbf{C} : \Delta\varepsilon^p \tag{42}$$

where the elastic predictor, $\boldsymbol{\sigma}^e$, is defined as

$$\boldsymbol{\sigma}^e = \mathbf{C} : (\varepsilon^e|_t + \Delta\varepsilon) \tag{43}$$

and the linear elastic tensor, $\mathbf{C}$, is given as

$$C_{ijkl} = 2G\delta_{ik}\delta_{jl} - (K - \frac{2}{3}G)\delta_{ij}\delta_{kl} \tag{44}$$

where G and K are respectively the shear and bulk moduli and are obtained from Young's modulus, E, and Poisson's ratio, υ, as

$$G = \frac{E}{2(1+\upsilon)}, K = \frac{E}{3(1-2\upsilon)} \tag{45}$$

All the variables are evaluated at time $t + \Delta t$ unless otherwise implied. As is implied by Equation (42), the stress at time $t + \Delta t$ is decomposed into two terms, the first of which can be directly calculated using Equation (43). In order to calculate the second term, the yield condition and flow rule should be considered:

$$\Phi(\boldsymbol{\sigma}, \varepsilon_{eq}{}^p, f_{void}{}^*) = 0 \tag{46}$$

$$\Delta\varepsilon^p = \Delta\lambda\frac{\partial\Phi}{\partial\boldsymbol{\sigma}} = \underbrace{-\Delta\lambda\frac{\partial\Phi}{\partial\sigma_H}}_{\Delta\varepsilon_{\sigma_H}}\frac{1}{3}\mathbf{I} + \underbrace{\Delta\lambda\frac{\partial\Phi}{\partial\sigma_{eq}}}_{\Delta\varepsilon_{\sigma_{eq}}}\underbrace{\frac{3}{2\sigma_{eq}}\boldsymbol{\sigma}'}_{\mathbf{n}} \tag{47}$$

By eliminating the increment of the plastic multiplier, $\Delta\lambda$, between $\Delta\varepsilon_{\sigma_H}$ and $\Delta\varepsilon_{\sigma_{eq}}$, one can write

$$\Delta\varepsilon_{\sigma_H}\frac{\partial\Phi}{\partial\sigma_{eq}} + \Delta\varepsilon_{\sigma_{eq}}\frac{\partial\Phi}{\partial\sigma_H} = 0 \tag{48}$$

Replacing for $\Delta\varepsilon^p$ from Equation (47) into Equation (42), the stress tensor can be expressed as

$$\boldsymbol{\sigma} = \boldsymbol{\sigma}^e - K\Delta\varepsilon_{\sigma_H}\mathbf{I} - 2G\Delta\varepsilon_{\sigma_{eq}}\mathbf{n} \tag{49}$$

Because the flow rule is independent from the third invariant of the stress tensor and given the linear elastic isotropy of the material, $\mathbf{n}$ is coaxial with the elastic deviatoric stress, $\mathbf{S}^e$, and can be determined as [40]

$$\mathbf{n} = \frac{3}{2\sigma_{eq}}\boldsymbol{\sigma}'^e \tag{50}$$

Therefore, the problem of integrating the governing equations of deformation reduces to the problem of consistent determination of the $\Delta\varepsilon_{\sigma_H}$ and $\Delta\varepsilon_{\sigma_{eq}}$ by using Equations (46) and (48). In these two equations, σ_H and σ_{eq} are defined as

$$\sigma_H = \sigma_H{}^e + K\Delta\varepsilon_{\sigma_H}, \sigma_{eq} = \sigma_{eq}{}^e - 3G\Delta\varepsilon_{\sigma_{eq}} \tag{51}$$

Equations (46) and (48) were solved by using the Newton's method.

Calibration of the model. The calibration method is essentially the same as described in the section on porous metal plasticity theory. Artificial neural networks along with a pattern search algorithm were used to identify the model parameters for which the predicted fracture loci were closest to the experimental data points. The only difference is that the number of parameters is increased from 3 to 4 because the initial imperfection parameter, f_0, also needs to be determined. Even though only one additional parameter is present in the MK-PMP model, the associated computational cost of the calibration process is significantly higher than that of the PMP model because of the multiplicative nature of the process. The required training data was generated by solving the coupled equations of the M-K and PMP theories and was used for training three ANNs which were finally used to determine the optimal model parameters through the Pattern Search algorithm. The final values of the model parameters identified during the calibration process and corresponding fracture loci are shown in Figure 8.8. The SSE and $RMSE$ values are annotated in subfigures of Figure 8.8 for all the three experimental datasets, except for $RMSE$ value of the experimental dataset provided by Wierzbicki *et al* [13]. It could not be calculated due to the small number of the data points.

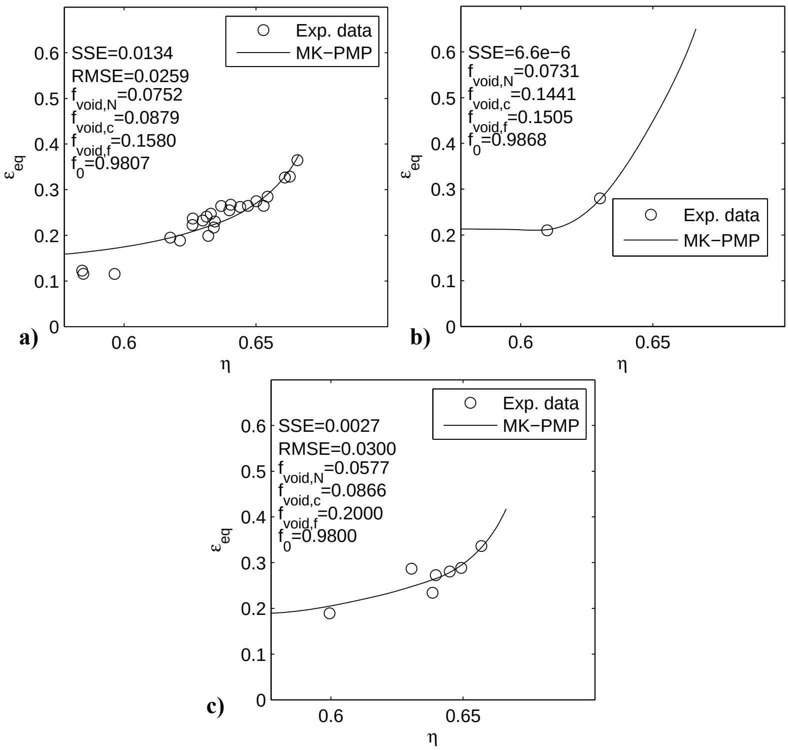

Figure 8.8. The fracture loci as predicted by MK-PMP model and calibrated against the experimental datasets provided by Lee *et al* [24] (a), Wierzbicki *et al* [13] (b), and Vallellano *et al* [14] (c).

Discussion on the results. Figure 8.8a-c shows that the combined MK-PMP model can give accurate prediction of the fracture loci for all three different experimental datasets. The $RMSE$ values are much better than the ones for the PMP model and are either better or comparable with the $RMSE$ values of the most successful phenomenological models, i.e. Wilkins and X-W models. The main reason is the upward trend of the fracture loci in the high end of the stress triaxiality values which was not present in the fracture loci predicted with the PMP model.

8.6. Comparative discussion on the results

In the previous sections, four different approaches for the theoretical prediction of the formability were studied for high strength aluminum 2024-T3. The prediction results provided by each of these four approaches are discussed in this section both independently and in comparison with the other approaches. The modeling approaches are compared with each other both qualitatively and quantitatively. In the qualitative comparison, the ability of the fracture loci in following the trend of the experimental data is examined. In the quantitative comparison, the prediction error of different modeling approaches will be compared with each other. The *RMSE* value is the most suitable measure for such a study because it is independent, not only from the number of experimental data points, but also from the models' degrees of freedom (see Equation (23)).

The study of the phenomenological fracture criteria showed that while some of them are very accurate, some others give unacceptably inaccurate results. Therefore, it is important to choose the right phenomenological criterion. Comparing the prediction error of eight different phenomenological models, it was revealed that the Wilkins and X-W models provide the fracture loci which match the experimental data points best. Figure 8.1c shows that when the number of experimental data points is small and the data points cover a relatively small fraction of the range of stress triaxialities, the Wilkins and X-W models are over-fitted to the experimental data points. As a result, the fracture loci deviate from the experimental data points outside the range of triaxiality for which the models are calibrated. The over-fitting does not take place for two other comparable models, namely CrachFEMII and Tresca. Therefore, one can conclude that the Wilkins and X-W models are the most accurate models when the number of experimental data points is large enough and the data points cover a significant portion of the stress triaxialities. The Wilkins and X-W are, nevertheless, prone to over-fitting when the number of experimental data points is relatively small. CrachFEMII and Tresca are less prone to over-fitting and are more useful for such cases. The worst overall performance (quantitative) was shown by FFLD and Tresca. Previous qualitative studies of different phenomenological fracture criteria had suggested that the Tresca fracture criterion can, despite its simplicity, provide accurate predictions comparable with what is provided by the most sophisticated phenomenological models [13-15, 18]. However, a remarkable conclusion of this study is, that despite the fact that the fracture loci predicted by the Tresca fracture criterion are similar in shape to the best-performing models, it can not keep its promise when it comes to quantitative comparisons. This is an example of why a qualitative study of the fracture loci is not sufficient and one has to pursue a quantitative study in order to be able to compare the models. The is true for the comparison of the different theoretical approaches.

An important difference between the fracture loci predicted by the best-performing phenomenological fracture criteria on one side and the fracture loci predicted by the physical models (including M-K, PMP, and MK-PMP) on the other side is the shape of the fracture loci. While the phenomenological fracture loci are composed of multiple branches and are not smooth, the fracture loci predicted by the physical models are single-branched and smooth. Of particular interest is the behavior of the fracture loci at $\eta = 1/3\ (\beta = -1/2)$. One can see that the Wilkins and X-W fracture loci (as well as the CrachFEMII and Tresca) are not smooth at this point and show a different behavior than the ones predicted by the physical models. However, there are not enough experimental data points to analyze which of these two trends is actually observed in the experiments. This lack of experimental data points is partly because of the limited practical importance of that part of the fracture loci. Due to the fact that the stress tensor in the region of small stress triaxialities ($\eta < 1/3\ (\beta < -1/2)$) includes one large compressive entry, which can result in wrinkling during forming processes, small stress triaxialities are rarely used in actual sheet metal forming practice.

The fracture loci predicted with the porous metal plasticity model are quite accurate in the range of relatively small stress triaxialities ($1/3 > \eta > 1/\sqrt{3}$), but cease to remain accurate once large values of stress triaxiality are approached. In the porous metal plasticity model, the equivalent strain at fracture decreases as stress triaxiality increases and there is no increase of the equivalent strain value at fracture for the high end of the stress triaxiality values. The physical reason behind this behavior is the fact that the large compressive stress in the low end of the stress triaxiality values retards the nucleation of the voids, as described by Equation (32). As the stress triaxiality value increases, the large compressive component declines and the retarding effect of the compressive stress component declines accordingly, which results in lower equivalent strain values at fracture. A further increase in the stress triaxiality value turns the already small compressive stress component positive. Biaxial straining accelerates the nucleation mechanism and the equivalent strain at fracture decreases even more profoundly and that is why the fracture loci predicted by the porous metal plasticity model do not show any upward trend in the high end of the stress triaxiality values.

The fracture loci predicted with the Marciniak-Kuczynski theory are accurate at the high end of the stress triaxiality values but are not as accurate in the range of small stress triaxialities. That is mainly due to the special sharp decreasing trend of the equivalent strain in the very low end of the stress triaxiality values. Physically speaking, development of the neck, which is an indicator of sheet metal instability, is very limited in high strength aluminum alloys such 2000 and 7000 series and the fracture of sheet metal, often occurs suddenly. Takuda and Hatta [16] showed that the fracture of the 2024 alloy sheets is without any visible sign of localized necking. Other researchers have not observed any clear indication of the localized necking in the fracture zone of 2024-T3 metal sheet [15] either. However, some authors have used the M-K theory for theoretical formability prediction of the 2024-T3 alloy [24].

Therefore, the physical relevance of the Marciniak-Kuczynski theory to the theoretical prediction of the formability of the 2024-T3 is disputable. This might be the reason why this method is not successful in the low end of the stress triaxiality values.
Chien *et al* [27] describe that there is experimental evidence for the fact that a combined mechanism governs the fracture of aluminum metal sheets. This combined mechanism is composed of localized necking and ductile fracture mechanisms which both contribute to the fracture of the material. The results of our study show that once combined with the M-K theory, the porous metal plasticity approach can give very accurate predictions for the fracture loci of 2024-T3. The upward trend of the fracture loci in the high end range of stress triaxialities, which was missing in the fracture loci predicted with the PMP theory, is present in the fracture loci predicted with the combined MK-PMP theory. The prediction error identifiers are the least for this approach. Therefore, one concludes that neither PMP nor M-K theories can successfully predict the fracture loci of the 2024-T3 alloy. However, once both approaches are combined, an accurate prediction becomes possible.
From computational expense standpoint, the MK-PMP and PMP approaches are respectively the first two most computationally expensive methods. The computational expense of the phenomenological models is comparable with the M-K theory and is much lower than those of the MK-PMP and PMP methods. Besides that, the implementation of the MK-PMP theory is far more complicated than any phenomenological model. Moreover, the prediction accuracies of the best performing phenomenological models are comparable with the MK-PMP model. Therefore, it can be concluded that the Wilkins and X-W are strong candidates for the practical application of the theoretical formability prediction theories. However, one has to be aware of the over-fitting problem that might arise if the number of available data points is small and the data points do not cover a sufficiently large portion of the stress triaxialities which might be encountered in the desired application. In those cases, CrachFEMII and Tresca fracture criteria tend to show a better performance than X-W and Wilkins.

8.7. Conclusions

Four different formability prediction theories were used to study the formability of high strength aluminum metal sheets. The modeling approaches included eight different phenomenological ductile fracture criteria, a Gurson-type porous metal plasticity model, the Marciniak-Kuczynski model, and a combined porous metal plasticity and Marciniak-Kuczynski model. Following conclusions can be drawn from the study:

- The phenomenological ductile fracture criteria proposed by Wilkins in the 80s and a recent criterion proposed by Xue and Wierzbicki are the best performing phenomenological ductile fracture criteria, provided that the number of experimental data points used for calibration of these models is large enough and the data points cover a significant portion of stress triaxialities that are relevant for the analysis. In the cases where the number of experimental data points is limited, the Wilkins and X-W models are prone to over-fitting. The CrachFEMII and Tresca did not exhibit over-fitting and are more appropriate for such cases.

- The Tresca fracture criterion which was previously suggested to be a low-cost single-parameter replacement for the sophisticated phenomenological models was found to provide inaccurate prediction values, although the trend of the fracture locus is reasonably accurate.
- The porous metal plasticity approach predicts the fracture loci more accurately in the low end of the stress triaxiality values, but the model cease to remain accurate once the large stress triaxiality values are approached.
- The Marciniak-Kuczynski model accurately predicts the fracture limits in the high end of the stress triaxialities, but is not as accurate in the low end.
- The combination of the porous metal plasticity with the Marciniak-Kuczynski model improves the quality of the predictions of the porous metal plasticity model in the high end of the stress triaxiality values.
- The computational cost of the phenomenological fracture modeling and Marciniak-Kuczynski models are minimal while the combined porous metal plasticity and Marciniak-Kuczynski (MK-PMP) and porous metal plasticity (PMP) are the most computationally expensive approaches.
- Comparing the computational cost and accuracy of the different studied modeling approaches, one concludes that the accuracy of the best-performing phenomenological ductile fracture models is comparable with the most sophisticated physical models such as combined porous metal plasticity and Marciniak-Kuczynski models while their computational cost is way less than the physical models.

8.8. References

[1] C. John Neil and S. R. Agnew, "Crystal plasticity-based forming limit prediction for non-cubic metals: Application to Mg alloy AZ31B," *International Journal of Plasticity,* vol. In Press, Corrected Proof, 2008.

[2] J. W. Signorelli, M. A. Bertinetti, and P. A. Turner, "Predictions of forming limit diagrams using a rate-dependent polycrystal self-consistent plasticity model," *International Journal of Plasticity,* vol. 25, pp. 1-25, 2008.

[3] T. B. Stoughton and X. Zhu, "Review of theoretical models of the strain-based FLD and their relevance to the stress-based FLD," *International Journal of Plasticity,* vol. 20, pp. 1463-1486, 2004.

[4] K. Yoshida and T. Kuwabara, "Effect of strain hardening behavior on forming limit stresses of steel tube subjected to nonproportional loading paths," *International Journal of Plasticity,* vol. 23, pp. 1260-1284, 2007.

[5] K. Yoshida and N. Suzuki, "Forming limit stresses predicted by phenomenological plasticity theories with anisotropic work-hardening behavior," *International Journal of Plasticity,* vol. 24, pp. 118-139, 2008.

[6] B. Haddag, F. Abed-Meraim, and T. Balan, "Strain localization analysis using a large deformation anisotropic elastic-plastic model coupled with damage," *International Journal of Plasticity,* vol. In Press, Accepted Manuscript, 2009.

[7] X. Sun, K. S. Choi, W. N. Liu, and M. A. Khaleel, "Predicting failure modes and ductility of dual phase steels using plastic strain localization," *International Journal of Plasticity,* vol. In Press, Accepted Manuscript, 2009.

[8] J. M. Allwood and D. R. Shouler, "Generalised forming limit diagrams showing increased forming limits with non-planar stress states," *International Journal of Plasticity,* vol. In Press, Corrected Proof, 2009.

[9] H. W. Swift, "Plastic Instability under Plane Stress," *Journal of the Mechanics and Physics of Solids,* vol. 1, pp. 1-18, 1952.

[10] R. Hill, "On discontinuous plastic states, with special reference to localized necking in thin sheets," *Journal of the Mechanics and Physics of Solids,* vol. 1, pp. 19-30, 1952.

[11] D. Banabic, "Forming limits of sheet metal," in *Formability of Metallic Materials: Plastic Anisotropy, Formability Testing, Forming Limits*, D. Banabic and K. Pöhlandt, Eds. Berlin: Springer-Verlag, 2001, pp. 173-214.

[12] Z. Marciniak and K. Kuczynski, "Limit strains in the process of stretch-forming sheet metal," *International Journal of Mechanical Sciences,* vol. 9, pp. 609-620, 1967.

[13] T. Wierzbicki, Y. B. Bao, Y. W. Lee, and Y. L. Bai, "Calibration and evaluation of seven fracture models," *International Journal of Mechanical Sciences,* vol. 47, pp. 719-743, Apr-May 2005.

[14] C. Vallellano, D. Morales, and F. J. Garcia-Lomas, "A study to predict failure in biaxially stretched sheets of aluminum alloy 2024-T3," *Materials and Manufacturing Processes,* vol. 23, pp. 303-310, 2008.

[15] C. Vallellano, C. Guzman, and J. Garcia-Lomas, "Failure prediction in stretched sheets of aluminium 2024-T3," *Materials Science Forum,* vol. 526, pp. 91-96, 2006.

[16] H. Takuda and N. Hatta, "Numerical analysis of the formability of an aluminum 2024 alloy sheet and its laminates with steel sheets," *Metallurgical and Materials Transactions A,* vol. 29, pp. 2829-2834, 1998.

[17] C. Y. Tang, W. Shen, and T. C. Lee, "Damage-based criterion for fracture prediction in metal forming processes: a case study in Al 2024T3 sheet," *Journal of Materials Processing Technology,* vol. 89-90, pp. 79-83, 1999.

[18] C. Vallellano, C. Guzman, and F. J. Garcia-Lomas, "Prediction of ductile failure in the stretch-forming of AA2024 sheets," in *AIP Conference Proceedings*, 2007, pp. 135-140.

[19] A. L. Gurson, "Continuum theory of ductile rupture by void nucleation and growth, 1. Yield criteria and flow rules for porous ductile media.," *Journal of Engineering Materials and Technology- Transactions of the ASME,* vol. 99, pp. 2-15, 1977.

[20] E. Doege, T. El-Dsoki, and D. Seibert, "Prediction of necking and wrinkling in sheet-metal forming," *Journal of Materials Processing Technology,* vol. 50, pp. 197-206, 1995.

[21] Z. T. Chen, M. J. Worswick, N. Cinotti, A. K. Pilkey, and D. Lloyd, "A linked FEM-damage percolation model of aluminum alloy sheet forming," *International Journal of Plasticity,* vol. 19, pp. 2099-2120, 2003.

[22] J. Kim, G. Zhang, and X. Gao, "Modeling of ductile fracture: Application of the mechanism-based concepts," *International Journal of Solids and Structures,* vol. 44, pp. 1844-1862, 2007.

[23] F. Caputo, G. Lamanna, and A. Soprano, "stochastic design improvement of a stiffened flat panel," in *Proceedings of ICAD 2006*, Florence, Italy, 2006.

[24] W. B. Lee, W. H. Tai, and C. Y. Tang, "Damage evolution and forming limit predictions of an A12024-T3 aluminium alloy," *Journal of Materials Processing Technology,* vol. 63, pp. 100-104, 1997.

[25] H. M. Huang, J. Pan, and S. C. Tang, "Failure prediction in anisotropic sheet metals under forming operations with consideration of rotating principal stretch directions," *International Journal of Plasticity,* vol. 16, pp. 611-633, 2000.

[26] H. S. Son and Y. S. Kim, "Prediction of forming limits for anisotropic sheets containing prolate ellipsoidal voids," *International Journal of Mechanical Sciences,* vol. 45, pp. 1625-1643, 2003.

[27] W. Y. Chien, J. Pan, and S. C. Tang, "A combined necking and shear localization analysis for aluminum sheets under biaxial stretching conditions," *International Journal of Plasticity,* vol. 20, pp. 1953-1981, 2004.

[28] C. Y. Tang and W. B. Lee, "Anisotropic damage of the 2024T3 aluminum alloy," *Scripta Metallurgica et Materialia,* vol. 32, pp. 767-772, 1995.

[29] Y. W. Lee, "Fracture prediction in metal sheets," in *Department of Ocean Engineering*. vol. PhD thesis: Massachusetts Institute of Technology, 2004.

[30] G. R. Johnson and W. H. Cook, "Facture characteristics of three metals subjected to various strains, strain rates, temperatures and pressures," *Engineering Fracture Mechanics,* vol. 21, pp. 31-48, 1985.

[31] M. G. Cockcroft and D. J. Latham, "Ductility and the workability of metals," *Journal of the Institutes of Metals,* vol. 96, pp. 33-39, 1968.

[32] M. L. Wilkins, R. D. Streit, and R. J. E., "Cumulative-strain-damage model of ductile fracture: simulation and prediction of engineering fracture tests," Lawrence Livermore National Laboratory 1980.

[33] H. Hooputra, H. Gese, H. Dell, and H. Werner, "A comprehensive failure model for crashworthiness simulation of aluminium extrusions," *International Journal of Crashworthiness,* vol. 9, pp. 449-463, 2004.

[34] V. Tvergaard, "Effect of yield surface curvature and void nucleation on plastic flow localization," *Journal of the Mechanics and Physics of Solids,* vol. 35, pp. 43-60, 1987.

[35] A. R. Barron, "Universal approximation bounds for superpositions of a sigmoidal function," *IEEE Transactions on Information Theory,* vol. 39, pp. 930-945, 1993.

[36] R. Lewis and V. Torczon, "Pattern search algorithms for bound constrained minimization," *SIAM Journal on Optimization,* vol. 9, pp. 1082-1099, 1996.

[37] J. W. Hutchinson, K. W. Neale, and A. Needleman, "Sheet necking-II. time-independent behavior," in *Mechanics of Sheet Metal Forming,* D. P. Koistinen and N. M. Wang, Eds. New York: Plenum, 1978, pp. 111-126.

[38] J. W. Hutchinson, K. W. Neale, and A. Needleman, "Sheet Necking-III. Strain-Rate Effects," in *Mechanics of Sheet Metal Forming*, D. P. Koistinen and N. M. Wang, Eds. New York: Plenum, 1978, pp. 269-283.

[39] K. S. Chan, D. A. Koss, and A. K. Ghosh, "Localized Necking of Sheet at Negative Minor Strains," *Metallurgical Transactions A,* vol. 15, pp. 323-329, 1984.

[40] N. Aravas, "On the numerical integration of a class of pressure-dependent plasticity models," *International Journal for Numerical Methods in Engineering,* vol. 24, pp. 1395-1416, 1987.

[41] A. A. Zadpoor, J. Sinke, and R. Benedictus, "Optimization of computational procedures for full modell strain path dependent analysis of forming limits," in *Proceedings of International Deep Drawing Research Group Conference (IDDRG 2008)*, Olofström, Sweden, 2008, pp. 419-428.

8.9. Appendix A

In this appendix, the theoretical basis of the formulas derived for the phenomenological fracture models are described. The assumptions used in this analysis are as follows:

1. Plane stress conditions are satisfied.
2. The yield locus is described by the von Mises yield function.
3. Strain hardening is isotropic and Hollomon's strain hardening law is applicable.
4. The sheet metal is proportionally loaded.
5. The volume remains constant during plastic deformation, i.e. $\varepsilon_1 + \varepsilon_2 + \varepsilon_3 = 0$.

Therefore, the basic relations can be written as

$$\sigma_{eq} = \sqrt{\sigma_1{}^2 + \sigma_2{}^2 - \sigma_1\sigma_2}, \varepsilon_{eq} = \sqrt{\frac{2}{3}\left(\varepsilon_1{}^2 + \varepsilon_2{}^2 + \varepsilon_3{}^2\right)} \quad \text{(A.1)}$$

$$\sigma_y = \tilde{K}\varepsilon_{eq}{}^n \quad \text{(A.2)}$$

$$\alpha = \frac{\sigma_2}{\sigma_1}, \beta = \frac{\varepsilon_2}{\varepsilon_1} \quad \text{(A.3)}$$

Based on the normality condition, the flow rule can be written as

$$d\varepsilon_{ij} = d\lambda \frac{\partial \sigma_{eq}}{\partial \sigma_{ij}} \quad \text{(A.4)}$$

From Equations (A.1) and (A.3), one can write the equivalent and hydrostatic stresses as

$$\sigma_{eq} = \sigma_1\sqrt{\alpha^2 - \alpha + 1} \quad \text{(A.5)}$$

$$\sigma_H = \frac{\sigma_1 + \sigma_2 + \sigma_3}{3} = \frac{1+\alpha}{3}\sigma_1 \quad \text{(A.6)}$$

Therefore, stress triaxiality is simply given by

$$\eta = \frac{\sigma_H}{\sigma_{eq}} = \frac{1+\alpha}{3\sqrt{\alpha^2 - \alpha + 1}} \quad \text{(A.7)}$$

Deviatoric stress is defined as

$$\sigma_i' = \sigma_i - \sigma_H \quad \text{(A.8)}$$

According to the Levy-Mises flow rule we have

$$\frac{d\varepsilon_i}{\sigma_i'} \triangleq \text{const.} \quad \text{(A.9)}$$

Equations (A.3), (A.8), and (A.9) give that

$$\alpha = \frac{2\beta + 1}{\beta + 2}, \beta = \frac{2\alpha - 1}{2 - \alpha} \quad \text{(A.10)}$$

Replacing for α in Equation (A.7) from Equation (A.10), one would have

$$\eta = \frac{\beta + 1}{\sqrt{3\left(\beta^2 + \beta + 1\right)}} \quad \text{(A.11)}$$

Solving Equation (A.11) for β we arrive at

$$\beta = \frac{\left(-3\eta^2 + 2\right) \pm \sqrt{-27\eta^4 + 12\eta^2}}{6\eta^2 - 2} \quad \text{(A.12)}$$

Using Equation (A.3) and applying the constant volume condition, Equation (A.1) can be written as

$$\varepsilon_{eq} = \varepsilon_1 \sqrt{\frac{4}{3}\left(\beta^2 + \beta + 1\right)} \tag{A.13}$$

Transformation from the principal strains space to the equivalent strain-stress triaxiality space and vice versa can be carried out using Equations (A.3) and (A.11-13).

Maximum shear stress (Tresca) model

In this section of appendix A, the explicit formulation of the fracture locus as predicted by Tresca phenomenological fracture criterion is derived.

According to the Tresca fracture model

$$\tau_{\max} = C_1 \tag{A.14}$$

But

$$\tau_{\max} = \max\left(\frac{\sigma_1 - \sigma_2}{2}, \frac{\sigma_1 - \sigma_3}{2}, \frac{\sigma_2 - \sigma_3}{2}\right) \tag{A.15}$$

and the plane stress condition applies, hence $\sigma_3 = 0$. Therefore, one can write

$$\tau_{\max} = \max\left(\frac{\sigma_1 - \sigma_2}{2}, \frac{\sigma_1}{2}, \frac{\sigma_2}{2}\right), \sigma_1 > \sigma_2 \Rightarrow \tau_{\max} = \max\left(\frac{\sigma_1 - \sigma_2}{2}, \frac{\sigma_1}{2}\right) \tag{A.16}$$

Two cases are possible here

Case 1:

$$\frac{\sigma_1 - \sigma_2}{2} > \frac{\sigma_1}{2} \Rightarrow \sigma_2 < 0 \tag{A.17}$$

Case 2:

$$\frac{\sigma_1 - \sigma_2}{2} \leq \frac{\sigma_1}{2} \Rightarrow \sigma_2 \geq 0 \tag{A.18}$$

Using Equations (A.5) and (A.7), one can obtain the range of triaxialities for which each of the cases apply

$$\sigma_2 \geq 0 \Rightarrow \frac{\alpha \sigma_{eq}}{\sqrt{1 + \alpha^2 - \alpha}} \geq 0 \Rightarrow 1 \geq \alpha \geq 0, \eta = \frac{1 + \alpha}{3\sqrt{1 + \alpha^2 - \alpha}} \Rightarrow \frac{2}{3} \geq \eta \geq \frac{1}{3} \tag{A.19}$$

$$\sigma_2 < 0 \Rightarrow \frac{\alpha \sigma_{eq}}{\sqrt{1 + \alpha^2 - \alpha}} < 0 \Rightarrow -2 \leq \alpha < 0, \eta = \frac{1 + \alpha}{3\sqrt{1 + \alpha^2 - \alpha}} \Rightarrow \frac{-1}{3} \leq \eta < \frac{1}{3} \tag{A.20}$$

For case 2 ($-1/3 \leq \eta < 1/3$), the fracture locus can be obtained by replacing for σ_1 and η from Equations (A.5) and (A.7)

$$\tau_{\max} = \frac{\sigma_1 - \sigma_2}{2} = \frac{1 - \alpha}{2}\sigma_1 = \frac{(1 - \alpha)\sigma_{eq}}{2\sqrt{1 + \alpha^2 - \alpha}} \tag{A.21}$$

Using the Hollomon's strain hardening law given in Equation (A.2), the final form of fracture locus for case 1 can be presented as

$$\varepsilon_{eq} = C_1 \left\{\frac{\sqrt{2\left(-3\eta^2 + 2 - \aleph_1\right)}}{9\eta^2 - 4 + \aleph_1}\right\}^{\frac{1}{n}}, \aleph_1 = \eta\sqrt{3\left(-9\eta^2 + 4\right)} \tag{A.22}$$

For case 1 ($1/3 \leq \eta < 2/3,$), the fracture locus can be obtained in a similar way as

$$\tau_{\max} = \frac{\sigma_1}{2} = \frac{\sigma_{eq}}{2\sqrt{1+\alpha^2-\alpha}} \tag{A.23}$$

which by applying Equations (A.2) and (A.7) can be written in its final form as

$$\varepsilon_{eq} = C_1\left\{\frac{\sqrt{2\left(-3\eta^2+2-\aleph_1\right)}}{9\eta^2-2-\aleph_1}\right\}^{\frac{1}{n}} \tag{A.24}$$

CrachFEM shear model

The ChrachFEM shear fracture model can be explicitly given in the space of the equivalent strain-stress triaxiality provided that the variable $\tilde{\theta}$ in CrachFEM can be given so. The variable $\tilde{\theta}$ is defined as

$$\tilde{\theta} = \frac{\sigma_{eq}}{\tau_{\max}}(1-3k_s\eta) \tag{A.25}$$

Equivalent strain can be replaced for from Equation (A.5) and the other term $\tau_{\max}$ is the same as obtained for the Tresca model and can be replaced for from equations (A.22) and (A.24) for the same two cases as the Tresca fracture criterion. By doing so, the variable $\tilde{\theta}$ is finally obtained as

$$\tilde{\theta} = \begin{cases} \dfrac{\sqrt{24}(-1+3k_s\eta)(-3\eta^2+2-\aleph_3)}{9\eta^2-2-\aleph_3}, -\dfrac{1}{3} < \eta \le \dfrac{1}{3} \\ \dfrac{\sqrt{24}(-1+3k_s\eta)(-3\eta^2+2-\aleph_3)}{9\eta^2-4+\aleph_3}, \dfrac{1}{3} < \eta \le \dfrac{2}{3} \end{cases}, \aleph_3 = \sqrt{3}\eta\sqrt{-9\eta^2+4} \tag{A.26}$$

Wilkins model

The Wilkins model gives the fracture point as the point where the following integral first reaches the critical value C_I.

$$\int_0^{\varepsilon_{eq,f}} \frac{(2-A)^{\mu}}{(1-a\sigma_H)^{\lambda}}\, d\varepsilon_{eq} = C_1 \tag{A.27}$$

where

$$A = \max\left(\frac{\sigma_2'}{\sigma_1'}, \frac{\sigma_2'}{\sigma_3'}\right) \tag{A.28}$$

If α>0 (β>-1/2), the deviatoric stresses, given in Equation (A.8), can be written in terms of the major principal stress and stress ratio as

$$\sigma_1' = \left(\frac{2-\alpha}{3}\right)\sigma_1, \sigma_2' = \left(\frac{2\alpha-1}{3}\right)\sigma_1, \sigma_3' = \left(\frac{-\alpha-1}{3}\right)\sigma_1 \tag{A.29}$$

Equation (A.29) can be rewritten by replacing for α from Equation (A.10) as

$$\sigma_1' = \left(\frac{1}{\beta+2}\right)\sigma_1, \sigma_2' = \left(\frac{\beta}{\beta+2}\right)\sigma_1, \sigma_3' = \left(\frac{-\beta-1}{\beta+2}\right)\sigma_1 \tag{A.30}$$

We then have

$$A = \max\left(\beta, \frac{-\beta}{\beta+1}\right) \tag{A.31}$$

By solving the inequality associated with Equation (A.31), the term $(2-A)^{\mu}$ can be obtained for the first two branches of the model envelope as follows

$$(2-A)^{\mu}=\begin{cases}(2-\beta)^{\mu},\beta\geq 0\\ \left(\dfrac{3\beta+2}{\beta+1}\right)^{\mu},\dfrac{-1}{2}\leq\beta<0\end{cases}\tag{A.31}$$

If $\alpha<0(\beta<-1/2)$, the deviatoric stresses can be written as

$$\sigma_1'=\left(\frac{1}{\beta+2}\right)\sigma_1,\sigma_2'=\left(\frac{-\beta-1}{\beta+2}\right)\sigma_1,\sigma_3'=\left(\frac{\beta}{\beta+2}\right)\sigma_1\tag{A.32}$$

and subsequently

$$A=\max(-\beta-1,-\frac{\beta+1}{\beta})\tag{A.33}$$

The term $(2-A)^{\mu}$ for the two other branches of the envelope is obtained as

$$(2-A)^{\mu}=\begin{cases}\left(\dfrac{3\beta+1}{\beta}\right)^{\mu},-1\leq\beta<\dfrac{-1}{2}\\ (3+\beta)^{\mu},-2\leq\beta<-1\end{cases}\tag{A.34}$$

The boundaries of the branches in Equations (A.31) and (A.32) can be expressed in terms of stress triaxiality by solving the quadratic equation resulting from replacing the boundary values in Equation (A.13). Equation (A.27) can be rewritten by replacing for σ_H from Equation (A.6) and for β from Equation (A.12) and the explicit form of the Wilkin's fracture envelope is formulated as

$$\varepsilon_{eq}=\begin{cases}C_1\left(1-\dfrac{2}{3}\eta\right)^{C_2}\left(3-\dfrac{-3\eta^2-2+\sqrt{-27\eta^4+12\eta^2}}{2(3\eta^2-1)}\right)^{(-109/50)},\dfrac{-1}{3}\leq\eta\leq 0\\ C_1\left(1-\dfrac{2}{3}\eta\right)^{C_2}\left(\dfrac{3\eta^2+2-3\aleph_2}{3\eta^2-\aleph_2}\right)^{C_3},0<\eta\leq\dfrac{1}{3}\\ C_1\left(1-\dfrac{2}{3}\eta\right)^{C_2}\left(\dfrac{3\eta^2-4+3\aleph_2}{3\eta^2-2+\aleph_2}\right)^{C_3},\dfrac{1}{3}<\eta\leq\dfrac{1}{\sqrt{3}}\\ C_1\left(1-\dfrac{2}{3}\eta\right)^{C_2}\left(3+\dfrac{-3\eta^2+2+\sqrt{-27\eta^4+12\eta^2}}{2(3\eta^2-1)}\right)^{(-109/50)},\dfrac{1}{\sqrt{3}}<\eta\leq\dfrac{2}{3}\end{cases}\tag{A.35}$$

where

$$\aleph_2=\eta\sqrt{-27\eta^2+12}\tag{A.36}$$

8.10. Appendix B- Nomenclature

D	Damage accumulation variable, dimensionless
σ_{ij}	Stress tensor entries, MPa
ε_{ij}	Strain tensor entries, dimensionless
ε_i	Principal strains, dimensionless
σ_i	Principal stresses, MPa
C_i	Parameters of the phenomenological fracture models, various dimensions
η	Stress triaxiality, dimensionless
$\tau_{\max}$	Maximum shear stress, MPa

n	Strain hardening exponent, dimensionless
J_3	Third invariant of the deviatoric stress tensor, MPa^3
ξ	Deviatoric stress parameter, dimensionless
a	Material parameter, GPa^{-1}
μ	Material parameter, dimensionless
λ	Material parameter, dimensionless
σ_H	Hydrostatic stress, MPa
k_s	Material parameter, dimensionless
SSE	Sum of squared error, dimensionless
$RMSE$	Root mean squared error, dimensionless
m	Number of experimental data points, dimensionless
m_C	A model's degrees of freedom, dimensionless
y_i	The equivalent strain at fracture as predicted by a fracture model, dimensionless
$\hat{y}_i$	Experimental value of the equivalent strain at fracture, dimensionless
σ_y	Yield stress, MPa
σ_i'	Deviatoric stress tensor entries, MPa
f_{void}	Void volume fraction, dimensionless
$\tilde{\alpha}, \tilde{\beta}, \tilde{\gamma}$	Material parameters, dimensionless
f^*_{void}	Effective void volume fraction, dimensionless
$f_{void,c}$	Critical void volume fraction, dimensionless
$f_{void,f}$	Void volume fraction at fracture, dimensionless
$\dot{f}_{void}$	Time derivative of void volume fraction, sec^{-1}
$\dot{f}_{void,gr}$	Time derivative of void volume fraction due to void growth, sec^{-1}
$\dot{f}_{void,nucl}$	Time derivative of void volume fraction due to void nucleation, sec^{-1}
$f_{void,N}$	Void volume fraction due to void nucleation, dimensionless
s_N	Mean value of void volume fraction due to void nucleation, dimensionless
ε_N	Standard deviation of void volume fraction due to void nucleation, dimensionless
f	Imperfection parameter in the M-K theory, dimensionless
$\underset{\sim}{K}$	Local yield stress, MPa
t	Sheet thickness, mm
$\mathbf{T}$	Transformation tensor from the principal to the groove's coordinate system, dimensionless
θ	Angle of the groove with the minor principal stress direction, rad

β	Strain ratio, dimensionless
α	Stress ratio, dimensionless
$\tilde{K}$	Strength coefficient, MPa
$\dot{\lambda}$	Plastic multiplier, dimensionless
$\mathbf{C}$	Elasticity tensor, GPa
δ_{ij}	Kronecker delta function, dimensionless
G	Shear modulus, GPa
K	Bulk modulus, GPa
E	Young's modulus, GPa
υ	Poisson's ratio, dimensionless
$\boldsymbol{\sigma}'$	Deviatoric stress tensor, MPa

Subscripts

eq	Equivalent value
0	Initial value of the variable
a	The value in the uniform zone
b	The value in the imperfection zone
ntz	The coordinate system of the groove
$12z$	The coordinate system of the principal stresses

Superscript

p	Plastic deformation
e	Elastic deformation

8.11. Appendix C

In this appendix, the fracture loci predicted with different types of formability prediction theories are presented in the space of principal strains.

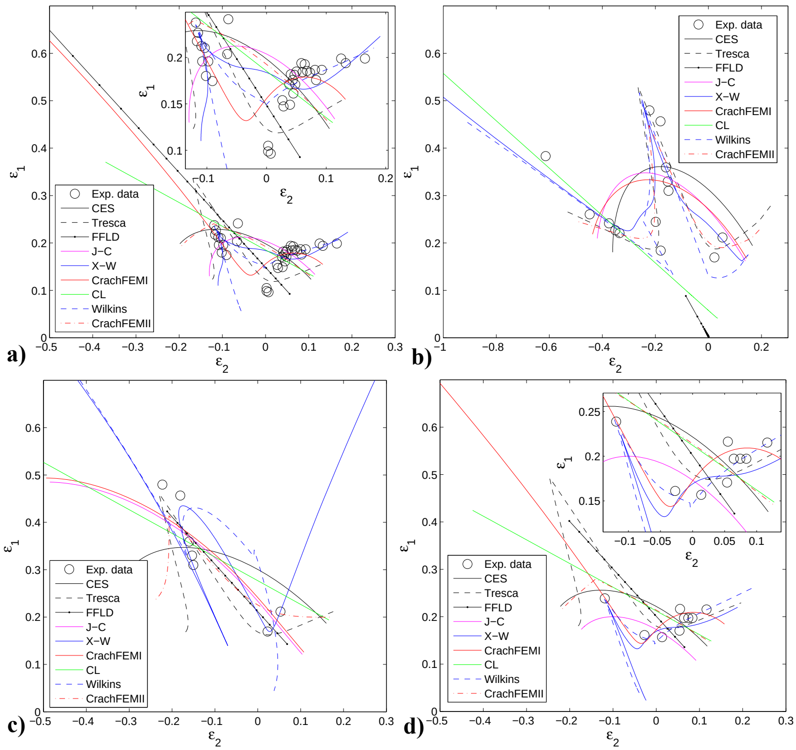

Figure C.1. The fracture loci as predicted by the phenomenological models and calibrated using the experimental data given by Lee *et al* [24] (a), Wierzbicki *et al* [13] (b), Wierzbicki *et al* [13] using only the data points with large stress triaxiality (η>1/3) (c), and Vallellano *et al* [14] (d).

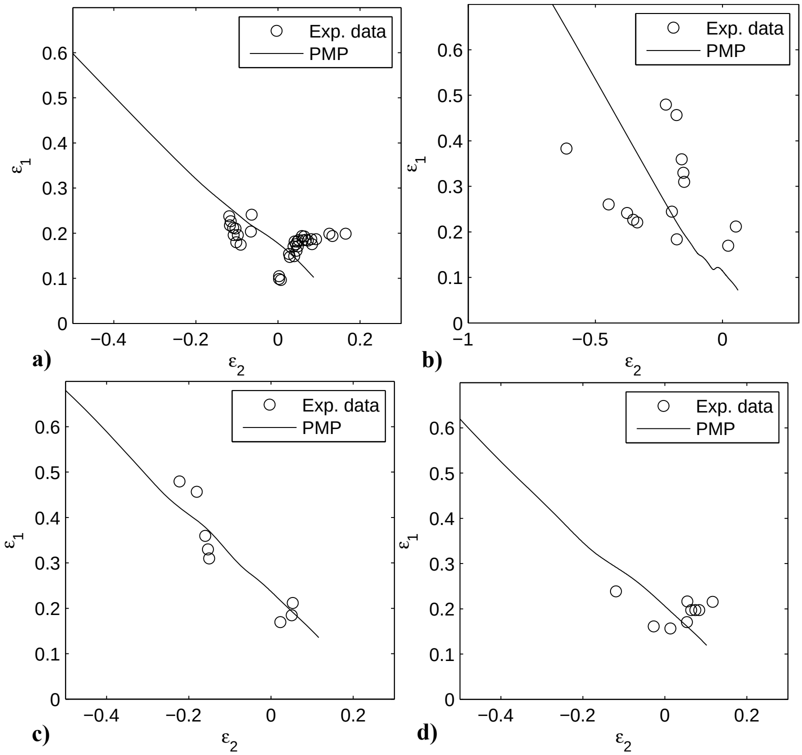

Figure C.2. The fracture loci as predicted by the porous metal plasticity theory and calibrated against the experimental datasets provided by Lee *et al* [24] (a), Wierzbicki *et al* [13] (b), Wirezbicki *et al* [13] including only the data points with large stress triaxialities (c), and Vallellano *et al* [14] (d).

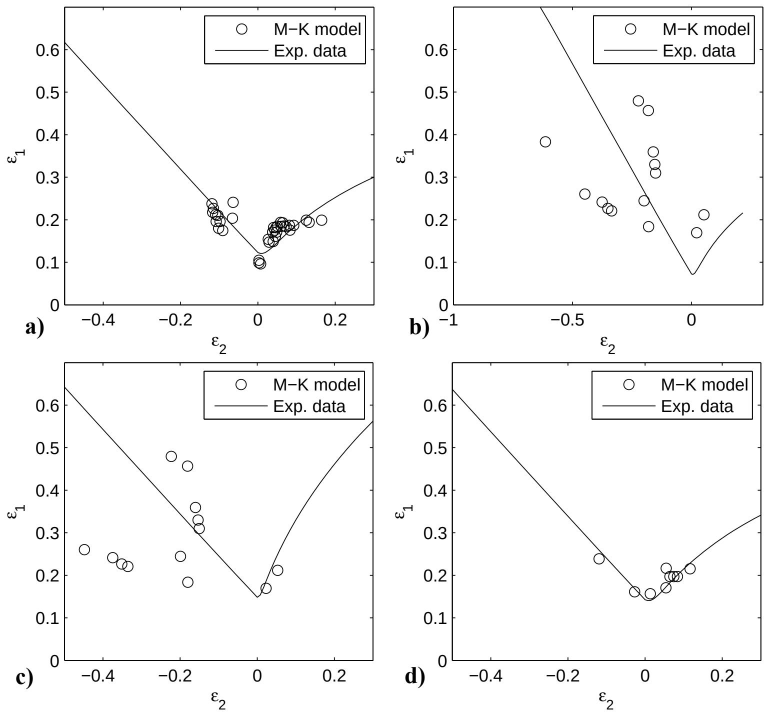

Figure C.3. The fracture loci as predicted by the M-K theory and calibrated against the experimental datasets provided by Lee *et al* [24] (a), Wierzbicki *et al* [13] (b), Wirezbicki *et al* [13] including only the data points with large stress triaxialities (c), and Vallellano *et al* [14] (d).

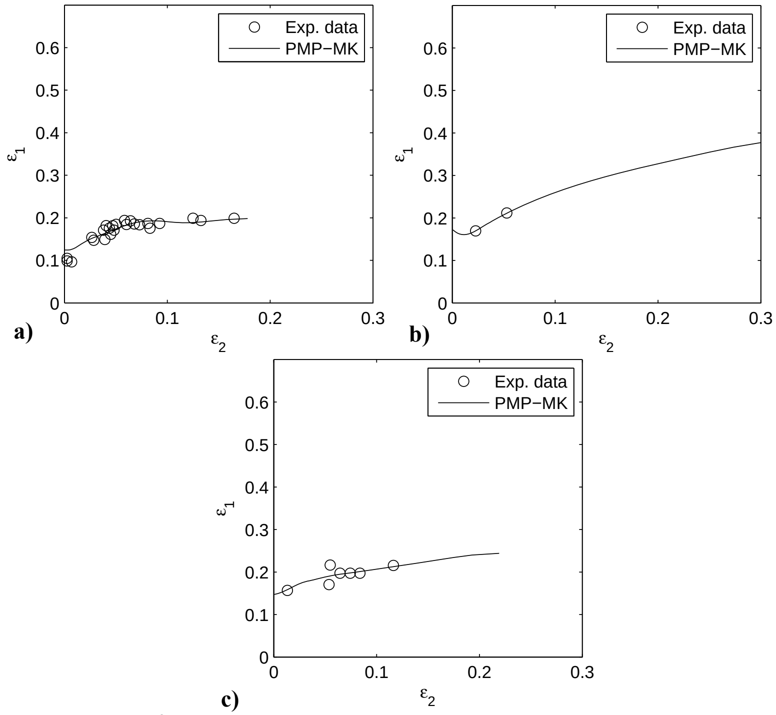

Figure C.4. The fracture loci as predicted by MK-PMP model and calibrated against the experimental datasets provided by Lee *et al* [24] (a), Wierzbicki *et al* [13] (b), and Vallellano *et al* [14] (c).

Modified from: Zadpoor, A. A., Sinke, J., Benedictus, R., 2009, "The effects of thickness on the formability of 2000 and 7000 series high strength aluminum alloys", Key Engineering Materials, vol. 410-411, pp. 459-466.

9. Effects of thickness on formability

This chapter studies the effects of sheet thickness on the forming limits of high strength aluminum alloys commonly used in the aircraft industry. The selected materials are 2024-T3 and 7075-T6 representing 2000 and 7000 series aluminum alloys. Two sets of experiments are carried out to identify the effects of sheet thickness on the forming behavior of these alloys. The first set of the experiments is tensile testing. The tensile properties of sheets with different thickness and different materials including the plasticity parameters are determined in the first set of experiments. The second set of the experiments is air bending. The minimum bending radius of the different series of materials is determined in the second set of experiments. The results of the tensile testing and air bending are studied both separately and in comparison with each other to identify the trends and to understand the mechanisms governing the observed trends. It is shown that the behavior of the studied alloys is to some extent different from the behavior of more ductile aluminum alloys and mild steels.

The forming limits of sheet metals tend to be dependent on, among other parameters, the thickness, [1-3]. Therefore, any accurate description of forming limits needs to take the thickness effect into account. How much the forming limits are affected by sheet thickness depends on the material being tested. For example, it is well known that the measured formability of draw quality mild steels increases as the sheet thickness increases [1-4]. This effect is believed to be partly a measurement effect. The shape of the localized neck, which is formed just before fracture, is the same geometrical regardless of the thickness. Because the size of the circular grids used for measurement of the strains is not changed for larger sheet thicknesses, the circles become closer to the center of the localized neck as sheet thicknesses increases and larger strains are recorded [4]. The explanation is confirmed by the experiments in which both grid size and sheet thickness increased. The experiments showed that failure strains are only slightly dependent on sheet thickness if both grid size and sheet thickness are increased [4].

The other possible reason for higher formability of the sheets with larger thicknesses is the relative effect of imperfections on strain localization [3-5]. According to the Marciniak-Kuczynski theory [6], the failure of sheet metals during forming is related to the localization of strains caused by local thickness imperfections. In the Marciniak-Kuczynski theory, the imperfection parameter is defined as the ratio of the thickness of the imperfection zone to that of the uniform sheet. The larger the imperfection parameter is, the sooner the strain is localized and the smaller the

forming limits are. Assuming that the imperfections created during the production of sheet metals are of the same absolute size regardless of sheet thickness, the effect of the imperfection on the imperfection parameter of the sheets with smaller thicknesses is larger than on sheets with larger thicknesses.
Finally, Ress [3] argues that the improvement of formability as a result of increase in sheet thickness increase might be connected to the effect of the grain size on the yield stress (Hall-Petch relationship).
The neck shape gets sharper as the strain rate sensitivity parameter, *m*, decreases [4]. Therefore, aluminum alloys which are normally much less sensitive to the strain rate are expected to exhibit less dependency on the thickness. Experimental observations supported this theory for 6000 series aluminum alloys used in the automotive industry [4]. However, the failure mechanism of mild steel and 5000 and 6000 series aluminum alloys is different from the 2000 and 7000 series high strength aluminum alloys which are widely used in the aircraft industry [7]. While sheet metal instability is the prevailing failure mechanism of the former group of alloys, ductile fracture appears to govern the failure of the latter group. Therefore, the effects of sheet thickness on the formability of the second group of alloys could be quite different from the first group.
The effects of sheet thickness on formability are important not only in the conventional sheet metal forming, but also in the so-called tailor-made blanks technology (particularly when the formability is significantly dependent on the sheet thickness). The metal sheets which constitute tailor-made blanks have different thicknesses and/or material properties and, thus, deform differently. The forming limits of tailor-made blanks are also influenced by the welding, joining, or machining process used to create the variations. Therefore, the formability of the resulting tailor-made blank is different from base metals and needs to be determined.
In the study of the formability of tailor-made blanks, we have different sheet zones with different thicknesses. We also have a transition from the thinner sheet to the thicker sheet. In order to understand the contribution of the different factors that influence the formability, it is important to isolate each of these effects and study them separately. Therefore, one of the goals of the current study is to study the independent effect of sheet thickness on the formability of high strength aluminum alloys. Two different alloys, namely 2024-T3 and 7075-T6 from 2000 and 7000 series are selected for the study. Two sets of experiments are designed in accordance with the type of the forming processes normally used in the aircraft industry to study these effects. The first series of the tests is tensile testing which is used to determine the plastic behavior of the materials. The second series of the tests is press brake forming which represents the bending processes used in the aircraft industry either in the form of press brake or rubber pad forming.

9.1. Methodology

In order to investigate the effects of sheet thickness on the mechanical properties and forming behavior of these two alloys, 2024-T3 and 7075-T6 sheets with four different thicknesses were selected for the study. The thicknesses of the 2024-T3 sheets were 1.2, 2.0, 2.5, and 3.2 mm. The thicknesses of the 7075-T6 sheets were 0.5, 1.2, 2.0, and 2.5 mm.

Two series of tests were carried out on each series of the materials: tensile testing and air bending. The tensile test specimens were machined such that the loading direction was in parallel with the rolling direction of the sheets. Figure 9.1a shows a drawing of the tensile test specimen. Six samples from each series of the specimens were tested using a Zwick/Roell static test machine at a constant deformation rate of 5 mm/min. The uniform strain along the gauge length was measured using an extensometer ($L_0 = 50$ mm). Hollomon's strain hardening law ($\sigma = K\varepsilon^n$) was fitted to the plastic part of the stress-strain curve and the strain hardening exponent, n , and strength coefficient, K , were determined accordingly.

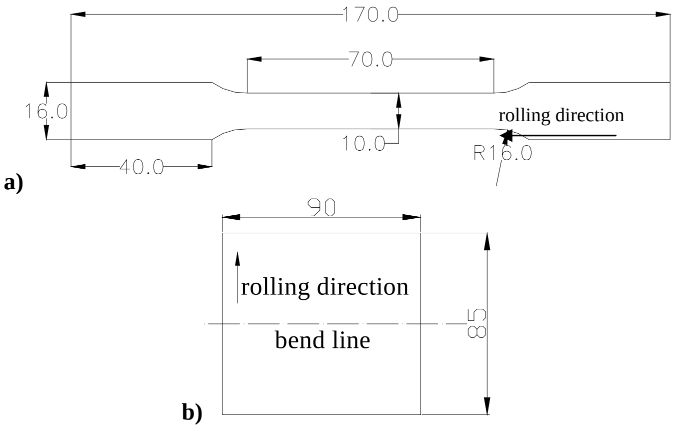

Figure 9.1 The geometry of the tensile test (a) and air bending (b) specimens.

According to the ASTM standard E290-97a for bend testing of materials, the width of air bending specimens has to be at least 8 times the sheet thickness to ensure plane strain conditions. However, some studies have shown that the minimum bending radius is dependent on the bend width for width-to-thickness ratios less than 16 [8]. In order to ensure that the minimum bending radius is independent from bend width, large width-to-thickness ratios in the range of 27 to 170 were used for the bending specimens. The air bending specimens were cut from the sheets in rectangular shapes with a length of 85 mm and width of 90 mm. The bend line was perpendicular to the rolling direction. Figure 9.1b presents a schematic drawing of the air bending specimens. The edges of the specimens were grinded to remove notches and irregularities that could cause crack initiation and premature failure of the specimens during air bending. A press brake with V-type dies and punches with different bending radii were used to bend the specimens to a bend angle of 90^{o}. For sheet thicknesses between 0.6 and 2.5 mm, die opening has to be 6 times the sheet thickness and for sheet thicknesses between 3 and 8 mm, die opening has to be 8 times the sheet thickness [9]. These guidelines were followed for the selection of the dies. For each series of materials, the minimum radius over which the specimen could be safely bent (without crack) was determined with an accuracy of 0.2-0.4 mm.

9.2. Experimental results

Figure 9.2 and Figure 9.3 present the results of the tensile tests vs. sheet thickness for 2024-T3 and 7075-T6 sheets, respectively. The presented values include yield strength, σ_y, ultimate strength, σ_u, strain at maximum stress, $\varepsilon_{\sigma_{\max}}$, ultimate strain, $\varepsilon_{\max}$, strain hardening exponent, n, and strength coefficient, K. Table 9.1 shows to what extent the tensile properties of the materials change with sheet thickness. The average value, maximum value, minimum value, and the difference between the maximum and minimum values of all tensile test parameters are listed in this table. In the last column, the difference between the strain hardening exponent and the strain at maximum stress is also included.

From the second set of experiments, the minimum bending radius of the specimens is plotted vs. sheet thickness in Figure 9.4a and Figure 9.5a. The minimum bending ratio, $\hat{R}$, is defined as the ratio of the minimum bending ratio to the sheet thickness:

$$\hat{R} = \frac{R}{t_0} \tag{1}$$

where R and t_0 are the minimum bending radius and (nominal) initial sheet thickness. The minimum bending ratios vs. sheet thickness are plotted in Figure 9.4b and Figure 9.5b. Linear equations are fitted to the experimental data points shown in Figure 9.4 and Figure 9.5 and fitting parameters are annotated in these figures.

9.3. Discussions

Figure 9.2, Figure 9.3 and Table 9.1 show that both stress and strain characteristics of the specimens change with sheet thickness. However, the dependency of the strain characteristics is stronger than that of the stress characteristics. While the differences between the minimum and maximum values of the yield and tensile strengths are between 2 to 13% of their average values, the difference between the minimum and maximum values of the strain at maximum stress and ultimate strain are between 15 to 36% of their average values (Table 9.1). It should be noted that the differences between the sheets with different thicknesses are not all systematic differences and, for example, the batch scatter of the properties also plays a role.

For 2024-T3, the strain at maximum stress and ultimate strain increased as sheet thickness increased from 1.2 to 2 mm and then slightly decreased as the thickness increased further to 2.5 mm. From 2.5 mm to 3.2 mm, the strain at maximum stress again slightly decreases while the ultimate strain slightly increases. However, the variations in the ultimate strain and strain at maximum stress that are observed after 2 mm are of the same order of magnitude as the scatter of the values. One can therefore conclude that as sheet thickness increases from 1.2 mm to 2 mm, the strain limits of the specimens increase. The strain values remain more or less the same if the thickness is further increased. The same pattern is observed for the strain hardening exponent. Table 9.1 shows that the difference between the minimum and maximum values of the ultimate strain and strain at maximum stress are quite significant and between 18 to 21%. A similar value (28%) is calculated for the variation of the strain hardening exponent. All these observations suggest that the elongation of the 2024-T3 specimens in tensile testing is about 20% higher for sheets with larger thicknesses.

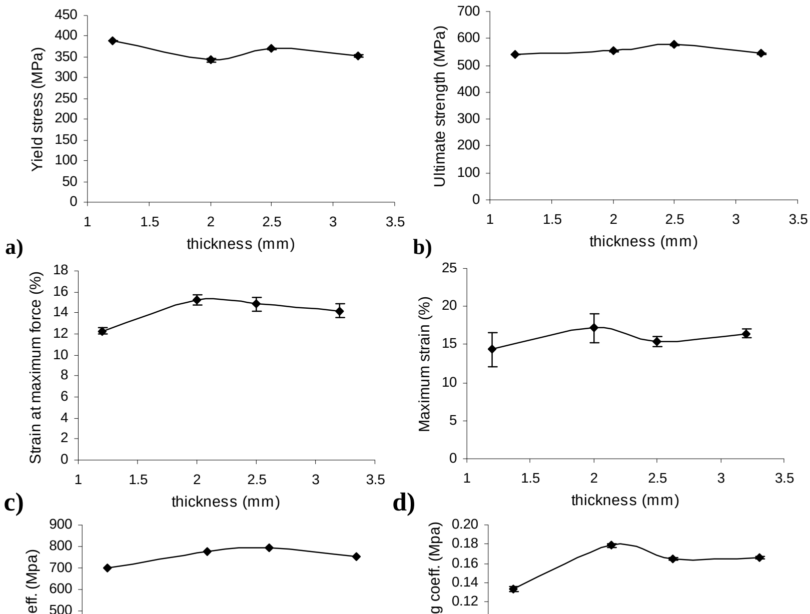

Figure 9.2. The results of the tensile testing of the 2024-T3 sheets with different thicknesses-yield stress (a), ultimate strength (b), strain at maximum stress (c), ultimate strain (d), strength coefficient (e), and strain hardening exponent (f) are all plotted vs. sheet thickness.

For 7075-T6, the strain at maximum stress and ultimate strain increase as sheet thickness increases from 0.5 to 2.0 mm. Both the strain at maximum stress and maximum stress slightly decrease as sheet thickness increases from 2.0 to 2.5 mm. Nevertheless, the change in the ultimate strain from 2.0 mm to 2.5 mm is of the same order of magnitude as the scatter of the results. Therefore, it can be concluded that as the sheet thickness increase from 0.5 to 2.0 mm, the strain values increase but remain more or less the same or even slightly decrease if the sheet thickness is further increased. The same pattern is observed for the strain hardening exponent. As is clear from Table 9.1, the increases in the strain at maximum stress and strain hardening exponent are close to each other (between 11 and 15%) but are much less than the increase in the ultimate strain (36%). Nevertheless, there is a clear increasing trend in all the formability indicators as sheet thickness increases. Interestingly, the maximum values of the formability indicators are recorded at the sheet thickness of 2 mm for both 2024-T3 and 7075-T6. It is not clear whether or not this is a coincidence or it has to do with the manufacturing process of the sheets.

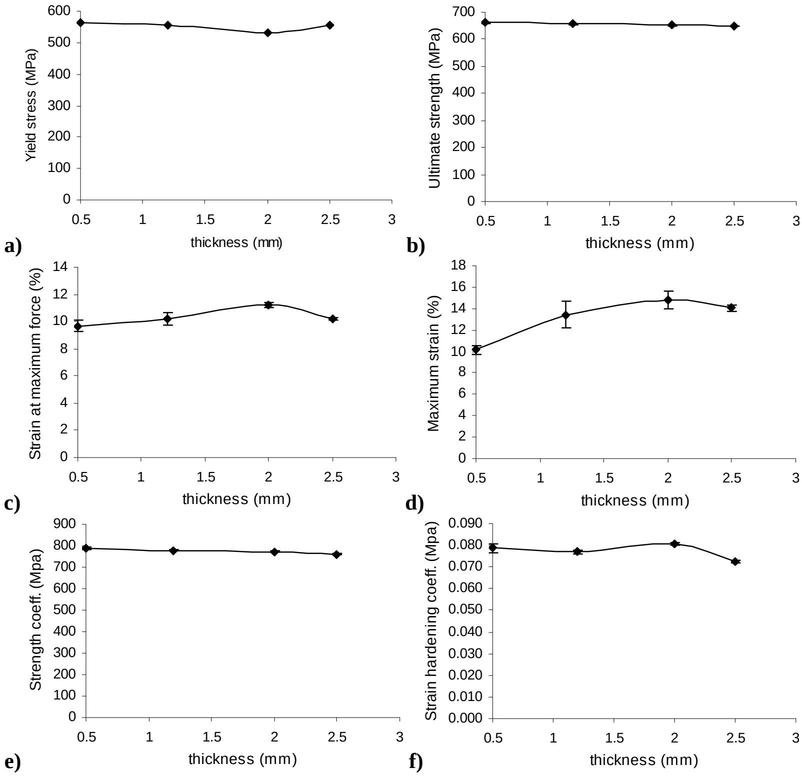

Figure 9.3. The results of the tensile testing of the 7075-T6 sheets with different thicknesses- yield stress (a), ultimate strength (b), strain at maximum stress (c), ultimate strain (d), strength coefficient (e), and strain hardening exponent (f) are all plotted vs. sheet thickness.

One relevant question is why do the strain values increase as sheet thickness increases? In order to answer this question, one may compare Figure 9.2a and Figure 9.3a with Figure 9.2c-d and Figure 9.3c-d. The comparison shows that in most cases, when the yield strength decreases, the values of the strain at maximum stress and ultimate strain increase. Figure 9.6 shows the dependency of the strain at maximum stress and ultimate strain on the yield strength for both 2024-T3 and 7075-T6. Linear equations are fitted to the data points and the parameters of the linear equations as well as the R^2 values are annotated in this figure. Figure 9.6 clearly shows that the strain at maximum stress and ultimate strain decrease as the yield strength increases. The observed trend suggests that the dependency of the tensile properties on sheet thickness has to do with the work hardening of the sheets during the rolling process. The thickness of sheets is gradually decreased from, say, 4 to 6 mm to the desired thickness through a cold rolling process. Therefore, sheets with smaller thickness pass through more cold rolling phases and undergo more deformation and have a smaller remaining formability.

Table 9.1. Dependency of the tensile properties on the sheet thickness.

		σ_y (MPa)	σ_u (MPa)	$\varepsilon_{\sigma_{\max}}$ (%)	$\varepsilon_{\max}$ (%)	K (MPa)	n	$(n-\varepsilon_{\sigma_{\max}})/n$
2024-T3	avg.	363	553	14.1	15.8	755	0.161	12%
	max	389	576	15.2	17.2	791	0.179	15%
	min	343	539	12.3	14.3	700	0.134	8%
	(max-min)/avg.	13%	7%	21%	18%	12%	28%	---
7075-T6	avg.	552	654	10.3	13.1	775	0.077	34%
	max	562	660	11.2	14.8	788	0.081	41%
	min	533	649	9.7	10.1	761	0.073	23%
	(max-min)/avg.	5%	2%	15%	36%	4%	11%	---

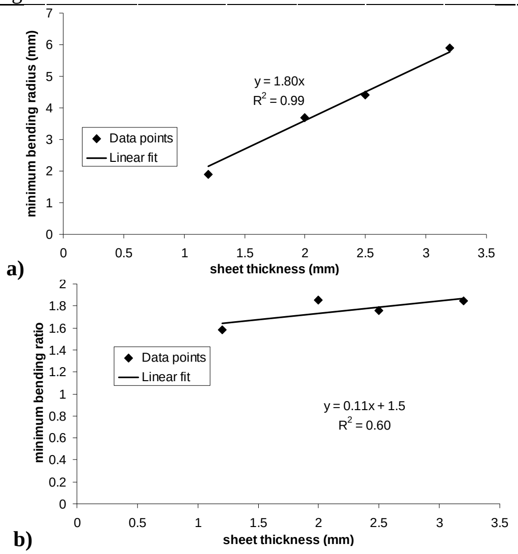

Figure 9.4. Minimum bending radius (a) and minimum bending ratio (b) of the specimens vs. specimen thickness- 2024-T3.

According to the Swift diffused necking theory [10], the strain at maximum stress should be equal to the strain hardening exponent. The last column of Table 9.1 presents the deviations of the values measured during the tensile testing from the prediction of the Swift theory. Interestingly, there is a clear difference between the 2024-T3 sheets and 7075-T6 sheets. While deviation from the Swift theory is a mere 8 to 15% for 2024-T3, it is much more and between 23 and 41% for 7075-T6. Moreover, it was observed that the deviation increases monotonically from 23 to 41% as sheet thickness increases from 0.5 to 2.5 mm. These observations suggest that the prevailing mechanism in the failure of 7075-T6 might be different from the one predicted by the Swift theory, i.e. instability.

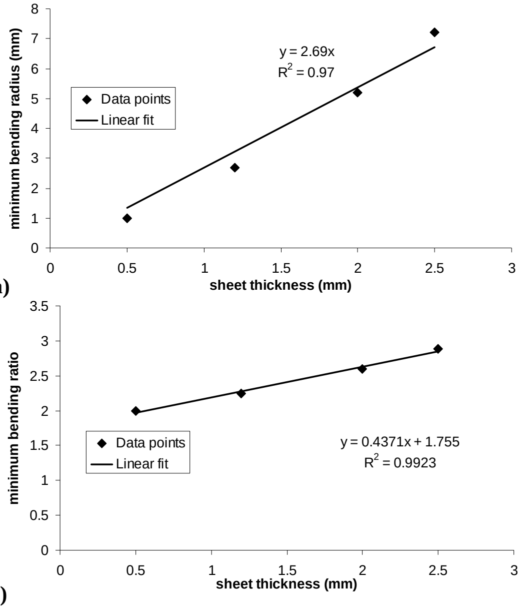

a)

b)

Figure 9.5. Minimum bending radius (a) and minimum bending ratio (b) of the specimens vs. specimen thickness- 7075-T6.

Figure 9.4a and Figure 9.5a show that the minimum bending radius of the sheets from both alloys increases as sheet thickness increases. By comparing the linear fits presented in Figure 9.4a and Figure 9.5a with the measured data points, one can see that the minimum bending radii are well approximated by the linear fits. This is in agreement with the linear dependency of the minimum bending radius upon sheet thickness predicted by Leu [11] through a modeling approach. The slope of the linear equation predicting the minimum bending radius of 7075-T6 is much greater than that of the equation predicting the minimum bending radius of 2024-T3 which is an indication of the less bendability of 7075-T6 compared with 2024-T3. Similar to the minimum bending radius, the minimum bending ratio increases as the sheet thickness increases. This is in agreement with the values of the minimum bending ratios given in ASM Handbook [8] for different materials and different thicknesses.

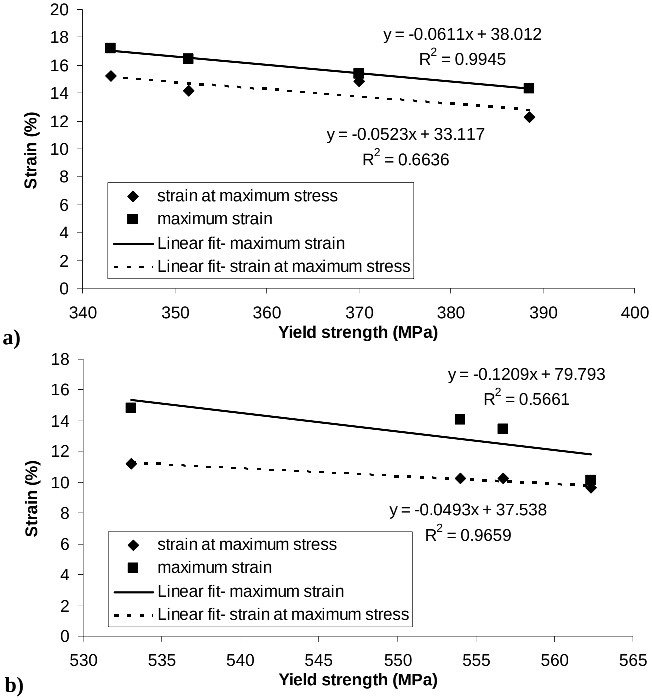

Figure 9.6. Strain at maximum stress and ultimate strain vs. yield strength for 2024-T3 (a) and 7075-T6 (b).

According to Wang *et al* [12], the ultimate strain on the convex surface of the bended specimens can be related to the inner bending radius, R_i, and sheet thickness, t, as:

$$\varepsilon_{\max} = \frac{1}{2}\ln\left(1 + \frac{t}{R_i}\right) \tag{2}$$

The inner bending radius is equal to the radius of the punch. Using Equation (2) and the minimum bending radii presented in Figure 9.4a and Figure 9.5a, the ultimate strain of the sheets with different thicknesses can be calculated. Figure 9.7 shows the calculated strain values vs. sheet thickness for 2024-T3 and 7075-T6.

As is clear from Figure 9.7, the failure strain of both 2024-T3 and 7075-T6 decreases as the sheet thickness increases. This is in agreement with the findings of Demeri [13] for AK steel, DP 80 steel, and HSLA-F50 steel. He showed that the forming limits of these materials increase as sheet thickness increases only if the dominant deformation regime is stretching and not bending. When deformation mode is mostly bending, forming limits decrease as sheet thickness increases. The important question is that ‘what does make bending different from (nearly) in-plane forming operations and causes this difference?’ There are various mechanisms which may contribute to the observed trend. First, it has been shown that the forming limits increase, if non-planar stress components are added to the stress state of a deforming sheet [14]. In particular, the forming limits are shown to increase as the normal stress increases [14-16]. In air bending, the normal stress acting on the concave side of the specimen increases as the bending radius decreases. Since the minimum bending radius of sheets with smaller thicknesses is smaller than the ones with larger thicknesses, the normal stress at minimum bending radius is higher for sheets with smaller thicknesses. Therefore, the forming limits of sheets with smaller thicknesses are lifted to a larger extent through the effect of normal stress, meaning that forming limits should decreases as the sheet thickness increases.

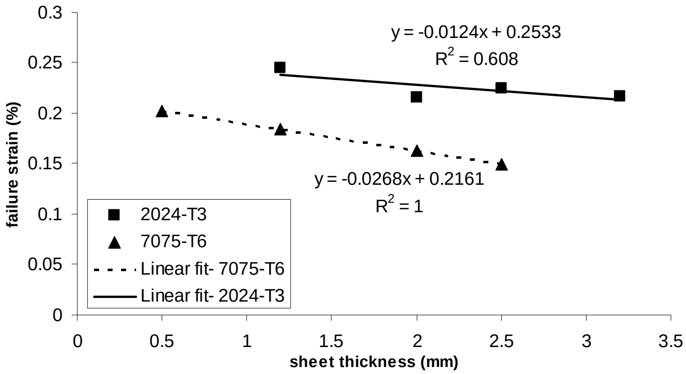

Figure 9.7. Failure strain vs. sheet thickness for 2024-T3 and 7075-T6.

The second mechanism is through-the-thickness stress gradient which is present in bending processes but not in deep drawing. It is suggested that the through-the-thickness strain gradient might be contributing to the early failure of the sheets with larger thicknesses [13], because gradients stabilize the deformation and postpone the onset of necking. In accordance with the Marciniak-Kuczynski’s theory of instability [6], necking originates from an imperfection zone with a slightly smaller thickness and/or slightly weaker material. During the deformation, the strain is continuously (slightly) larger in the imperfection zone compared with the uniform zone until a point is reached where the strain is localized in the imperfection zone. When a through-the-thickness stress gradient exists, the localization of the strain in the imperfection zone may be postponed. That is because the portion of the thickness that is experiencing compressive stress prevents the other portion of the thickness (that is experiencing tensile stress) from undergoing very large deformations. Indeed, Morales *et. al.* suggest that failure takes place once not a single fiber but a certain material volume is damaged [17].

Comparing the strain values presented in Figure 9.7 with the strain values measured during the tensile testing (Figure 9.2 and Figure 9.3), one can see that the failure strains are higher in the case of air bending than in tensile testing even though air bending takes place in the plane strain condition which normally has the lowest forming limit. This observation supports the idea that instability is suppressed in the case of air bending and the recorded values of failure strains are, indeed, fracture limits and not instability limits.

In addition to the effects of the through-thickness strain gradient and normal stress, the larger punch force needed for forming of sheets with larger thicknesses may play a role. As sheet thickness increases, the required punch force also increases. Since air bending is a three-point bending process, the contact forces of the blank with die also increase. Therefore, friction forces increase and additional stretching is added to the tensile strain induced by bending meaning that sheets with larger thicknesses experience more stretching than the ones with smaller thicknesses. As a result, the minimum bending ratio should increase as the sheet thickness increases.

9.4. Conclusions

The effects of sheet thickness on the formability of two high strength aluminum alloys, namely 2024-T3 and 7075-T6, were studied in this chapter. Tensile testing and air bending experiments were conducted to determine the effects of sheet thickness on the tensile and bending properties of the studied alloys. Following conclusions can be drawn from the study:

- For both 2024-T3 and 7075-T6, the strain at maximum stress and ultimate strain of the sheets tend to increase as sheet thickness increases up to 2 mm after which the strain values remain almost the same or slightly decrease.
- The yield strengths of sheets with different thicknesses are found to be correlated with the values of the ultimate strain and strain at maximum stress suggesting that the dependency of the strain values on sheet thickness partly might have to do with the cold rolling process used for production of sheet metals.
- In agreement with the prediction of the Swift theory of diffuse necking, the values of the strain at maximum stress were comparable to the strain hardening exponent for 2024-T3. However, there was a significant deviation from the prediction in the values measured for 7075-T6 suggesting that the mechanism governing the failure is not “instability”.
- The minimum bending radius linearly increases as the sheet thickness increases.
- Unlike stretching processes, the failure strain of sheets in air bending decreases as sheet thickness increases.

9.5. References

[1] R. Narayanasamy, M. Ravi chandran, and N. L. Parthasarathi, "Effect of annealing on formability of aluminium grade 19000," *Materials and Design,* vol. 29, pp. 1633-1653, 2008.

[2] V. Karthik, R. J. Comstock Jr, D. L. Hershberger, and R. H. Wagoner, "Variability of sheet formability and formability testing," *Journal of Materials Processing Technology,* vol. 121, pp. 350-362, 2002.

[3] D. W. A. Rees, "Factors influencing the FLD of automotive sheet metal," *Journal of Materials Processing Technology,* vol. 118, pp. 1-8, 2001.

[4] W. F. Hosford and J. L. Duncan, "Sheet metal forming: A review," *JOM-Journal of the Minerals Metals & Materials Society,* vol. 51, pp. 39-44, Nov 1999.

[5] J. E. Bird and J. L. Duncan, "Strain hardening at high strain in aluminum alloys and its effect on strain localization," *Metallurgical Transactions A,* vol. 12, pp. 235-241, 1981.

[6] Z. Marciniak and K. Kuczynski, "Limit strains in the process of stretch-forming sheet metal," *International Journal of Mechanical Sciences,* vol. 9, pp. 609-620, 1967.

[7] A. A. Zadpoor, J. Sinke, and R. Benedictus, "Comparative Study of the Formability Prediction Models for High-Strength Aluminum Alloys," in *9th International Conference on Technology of Plasticity (ICTP 2008),* Gyengju, South Korea, 2008, pp. 1258-1263.

[8] A. I. H. Committee, *ASM Handbook: Volume 18: Mechanical Testing and Evaluation*. Materials Park: ASM International, 2000.

[9] H. Kurtaran, "A novel approach for the prediction of bend allowance in air bending and comparison with other methods," *International Journal of Advanced Manufacturing Technology,* vol. 37, pp. 486-495, 2008.

[10] H. W. Swift, "Plastic Instability under Plane Stress," *Journal of the Mechanics and Physics of Solids,* vol. 1, pp. 1-18, 1952.

[11] D. K. Leu, "A simplified approach for evaluating bendability and springback in plastic bending of anisotropic sheet metals," *Journal of Materials Processing Technology,* vol. 66, pp. 9-17, 1997.

[12] C. Wang, G. Kinzel, and T. Altan, "Mathematical modeling of plane-strain bending of sheet and plate," *Journal of Materials Processing Technology,* vol. 39, pp. 279-304, 1993.

[13] M. Y. Demeri, "The stretch-bend forming of sheet metal," *Journal of Applied Metal Working,* vol. 2, pp. 3-10, 1981.

[14] J. M. Allwood and D. R. Shouler, "Generalised forming limit diagrams showing increased forming limits with non-planar stress states," *International Journal of Plasticity,* vol. 25, pp. 1207-1230, 2009.

[15] P. D. Wu, J. D. Embury, D. J. Lloyd, Y. Huang, and K. W. Neale, "Effects of superimposed hydrostatic pressure on sheet metal formability," *International Journal of Plasticity,* vol. 25, pp. 1711-1725, 2009.

[16] L. M. Smith, R. C. Averill, J. P. Lucas, T. B. Stoughton, and P. H. Matin, "Influence of transverse normal stress on sheet metal formability," *International Journal of Plasticity,* vol. 19, pp. 1567-1583, 2003.

[17] D. Morales, A. Martinez, C. Vallellano, and F. J. Garcia-Lomas, "Bending effect in the failure of stretch-bend metal sheets," *International Journal of Material Forming,* vol. In press, 2009.

Modified from: Zadpoor, A. A., Sinke, J., Benedictus, R., 2008,"Finite element modeling and failure prediction of friction stir welded blanks", Materials & Design, vol. 30(5), pp. 1423-1434.

10. FEM modeling and failure prediction of FSW blanks

The main objective of the current chapter is to study whether or not the implementation of the details of the different weld zones in FEM models of FSW TMBs is feasible and useful. Finite element modeling of friction stir welded blanks needs a compromise between accuracy and feasibility. On one hand, there are a number of zones with significantly different mechanical properties in a friction stir welded tailored blank whose mechanical and geometrical properties, if implemented, make the FEM models complicated and computationally expensive. One the other hand, the implementation of the different zones in the FEM model might make a significant contribution to the accuracy of the simulation results. In this chapter, the effects of the implementation of the weld details on the accuracy of the failure prediction, strain distribution, and springback behavior of FSW TWBs are studied for two benchmark problems, namely the limiting dome height test and the S-rail problem. The effects of the weld detail implementation on the simulation time are also considered. The Marciniak-Kuczynski theory is used for prediction of the forming limit diagrams of the different zones of the studied FSW TWBs. The M-K imperfection parameters are obtained by fitting the theoretical FLDs to the experimental tensile test failure limits. It is shown that the implementation of the weld detail results in more accurate strain field and springback predictions. Furthermore, the added computational cost caused by the implementation of the weld details is in many cases reasonable.

While the laser beam welding is often the first choice for steel sheets, it is so for aluminum alloys, primarily because of its high (welding) temperatures and surface reflection it produces. The high (welding) temperatures of laser beam welding eliminate the effects of the pre-applied heat treatments of the high-strength aluminum alloys that are used in the aircraft industry. In turn, the welding temperatures of the friction stir welding are moderate and the effects of the welding temperatures on the mechanical properties of the aluminum alloys are limited. Roughly speaking, fusion welding averages one defect in each 8.4m whereas there are some reports of 2.5 km continuous friction stir welding without any defect [1]. Further, due to the high strength to weight ratios of aluminum alloys, the automotive industry is becoming more and more interested in aluminum alloys, see e.g. [2]. Some researchers have already studied the applications of the friction stir welded aluminum, specifically 5000 and 6000 series, for the automotive industry applications, see e.g. [3-6].

One of the important challenges of the FEM modeling of TWBs is modeling the weld area, because it needs a compromise between accuracy and feasibility. On one hand, implementation of the mechanical properties of the different zones might significantly improve the accuracy of the finite element model, but on the other hand, such implementation will add to the computational cost of the problem. For theoretical formability prediction, there is an additional complexity, because not only the mechanical properties but also the forming limit diagrams of the different zones are different.

Table 10.1. The specifications of models used in this paper to study the LDH test and S-rail problem.

model no.	case of study	WN	HAZ
1	LDH test	no	no
2	LDH test	yes	no
3	LDH test	yes	yes
4	S-rail	no	no
5	S-rail	yes	no
6	S-rail	yes	yes

Limited information about the FEM modeling of FSW TWBs is available in the literature. This chapter tries to provide answers for the questions regarding the FEM modeling of the weld zone in FSW TWBs. Two different problems, namely limiting dome height test and the S-rail problem, are used as study cases. The LDH and S-rails problems are, respectively, good examples of the cases in which accurate prediction of the strain field and springback are important. In this chapter, some FEM models of these two problems are validated by using the NUMISHEET 96 benchmark data. After validating the models, the monolithic sheets are replaced with two friction stir welded blanks. The Marciniak-Kuczynski theory is used to determine the FLDs of the base metal, weld nugget, and heat-affected zone based on the imperfection parameters obtained by fitting the theoretical FLDs to the results of the tensile tests. Six different models as specified in Table 10.1 are built, simulated, and compared. First three models are related to the LDH test and the last three ones are related to the S-rail problem. From degree-of-heterogeneity viewpoint, the above-mentioned models can be categorized as completely-heterogeneous models (models no. 3 and 6) in which the mechanical properties of both the weld nugget and heat-affected zones are implemented, moderately-heterogeneous models (models no. 2 and 5) in which only the mechanical and geometrical properties of the weld nugget are implemented, and homogenous models (models no. 1 and 4) in which no weld detail is implemented and the blank is considered to be monolithic. The effects of asymmetry of the weld nugget and heat-affected zones around the centerline on the strain distribution and springback behavior of the blanks are also studied. Simulation results and computational time are compared between different models.

10.1. Limiting dome height test

The limiting dome height test is one of the most commonly used formability tests. In this test, a 101.6 mm (4 inch) diameter hemispherical punch is used to form rectangular blanks with a specific length and varying widths. The punch's travel at the onset of the failure is recorded as the dome height. Different widths are used to generate different strain ratios. The minimum value of the dome height is called limiting dome height and is deployed as a measure of formability. The clamping of the blanks during the forming should be carefully controlled by means of a large blank holding force and/or drawbeads. For a detailed description of the test and reporting procedures see ASTM standard E2218 or ISO standard 12004.

The limiting dome height test was assigned as one of the benchmark problems of the NUMISHEET 96 conference. A detailed description of the problem was provided by the organizers [7]. In this chapter, the same geometry, material, and parameters as of the NUMISHEET 96 benchmark problem are used. Drawings of the blank and die-set geometries are shown in Figure 10.1. A constant length of 180 mm and width of 100 mm is used for all simulations. The thickness of the blank is 1 mm. The blank is made of draw quality mild steel (IF). The material properties of the IF steel are given in the NUMISHEET 96 documents. The origin of the coordinate system is supposed to be coincident with the intersection point of the blank's diagonals. As specified by the NUMISHEET 96 documents, the friction coefficient for the contact between the punch and the blank is 0.11.

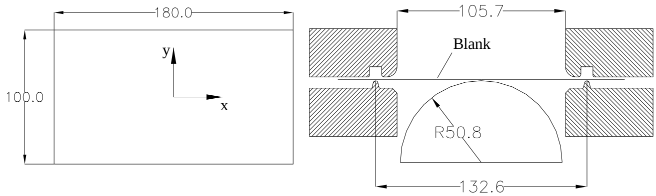

Figure 10.1. Geometry of the die set and the blank used in the FEM simulations of the LDH test.

Two FEM models of the LDH test were built by using two commercial FEM packages ABAQUS and PAM-STAMP. The Hollomon's hardening law and Hill48 yield criterion were adopted. The blank was discretized by using shell elements. Simulations were carried out on a Dell Precision^{TM} 690 workstation. The simulation results of two models were found to be consistent with each other.

In this section, a comparison is made between results of the current models of the LDH test and NUMISHEET 96 benchmark data. The punch travel was set to 0 at the beginning of the punch's contact with the blank. All the simulation results are presented for a constant punch travel of 30 mm. Figure 10.2a to c compare the punch force, major principal in-plane strain along the x-axis, and minor principal in-plane strain along the x-axis calculated for the current model with the benchmark data. In the current and following sections, the same terminology as of the NUMISHEET 96 is used to refer to the different sets of the benchmark data [7]. The names starting with E (e.g. EB2-02) stand for the experimental data, and names starting with S (e.g. SB2-02) stand for the simulation benchmark data. From Figure 10.2a to c, it is clear that the simulation results of the current model are in a good agreement with the experimental and numerical benchmark data. Therefore, the FEM models of the LDH test are considered to be valid and are used for further studies. In the following section, the FEM model of the S-rail problem will be discussed. Most of the specifications of that model are the same as what is used for the LDH test. Any point of discrepancy will be emphasized.

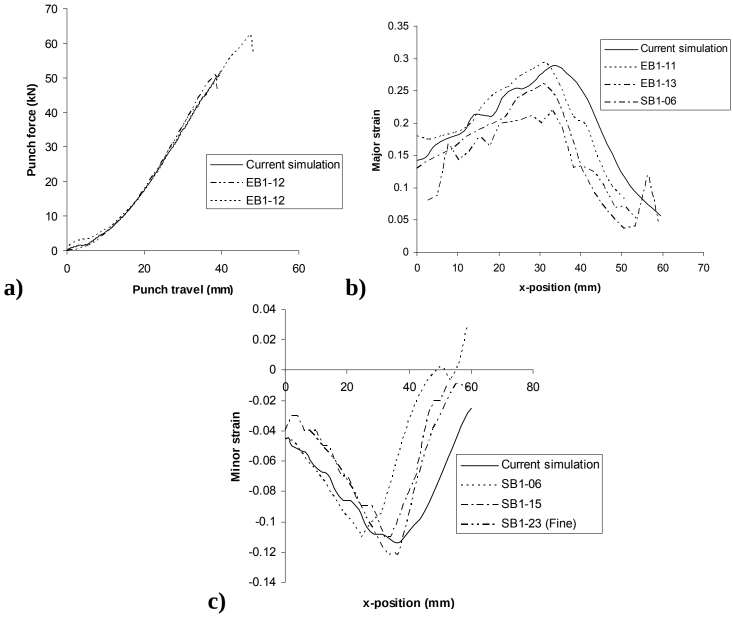

Figure 10.2. Comparison between the current simulation and NUMISHEET 96 benchmark data a) Punch force vs. punch travel b) Major principal strains (along x-axis) c) Minor principal strains (along x-axis).

10.2. S-rail problem

The S-rail problem was also assigned as one of the benchmark problems in the NUMISHEET 96 conference. The geometries of the blank and die are schematically depicted in Figure 10.3. Key points (A to J), that are described in the NUMISHEET 96 documents and will be used for comparison purposes, are marked in this figure. The S-rail problem is a prototype of the problems in which springback is an important issue. This problem is used by many researchers to study the springback behavior and its FEM model, see e.g. [8-10]. All the material and process parameters are similar to the LDH test model (material=IF, thickness=1 mm, friction coefficient=0.11, element type=shell, yield criterion=Hill1948, and hardening law= Hollomon). The blank holding force was set to 200 kN. A FEM model of this problem was built by using the PAM-STAMP package. The simulations were carried out in three stages, namely holding, stamping, and springback. The origin of the right-hand coordinate system used for presentation of the results is coincident with the key point A up to the end of the stamping stage. After springback, the origin of the coordinate system is transferred to the new position of the point A. Similarly, the x-axis is aligned along the AC line up to the end of the stamping stage and is, then, rotated to align along the new AC line (after springback). Figure 10.4a to c compare the results of the current model with the benchmark data. Figure 10.4a compares the punch force vs. punch travel for different sets of the benchmark data with the simulation results of the current model. Figure 10.4b makes a comparison between coordinates of the key points C, F, and H (after stamping and before springback) computed for the current model and those of the benchmark data. Finally, Figure 10.4c makes a comparison between coordinates this time for the distances from points A to C (AC), A to H (AH), and A to F (AF) after springback. It is clear from Figure 10.4a to c that the simulation results of the current model are in a good agreement with the experimental and numerical benchmark data and the FEM model of the S-rail problem is considered valid.

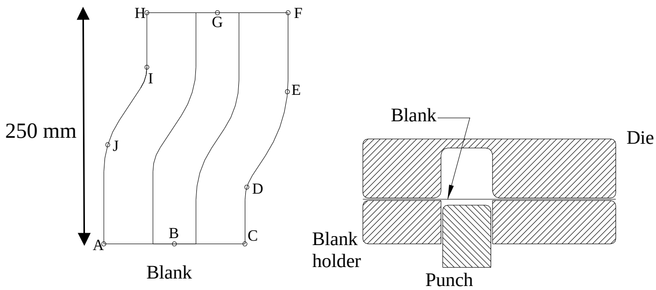

Figure 10.3. Geometry of the die set and the blank used in the FEM simulations of the S-rail problem.

10.3. Friction stir welded blanks

The original blanks used in the previous sections were replaced with two friction stir welded blanks. The schematic drawing of the blanks are given in Figure 10.5a and b. Before friction stir welding, both sheets were considered to be made of the aluminum alloy 2024-T351, as a common alloy in the aircraft industry. Since we are looking for the independent effects of the welding, all the sheet strips were considered to be of the same thickness (1 mm) so as the effects of the welding are isolated from the thickness effects.

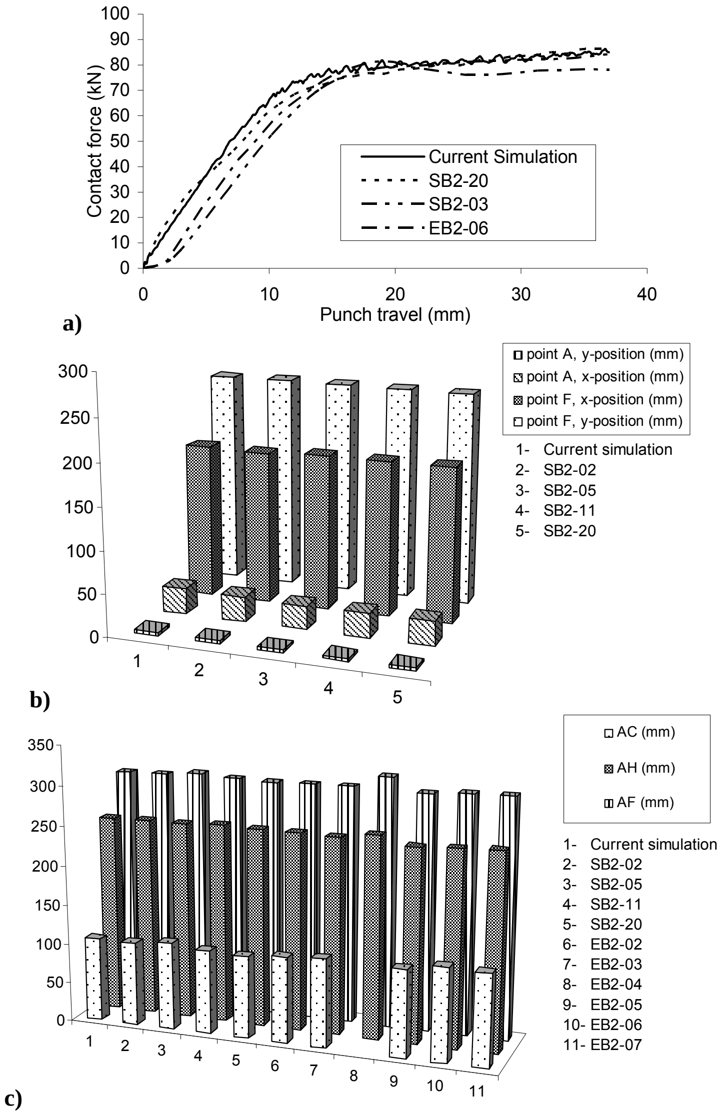

Figure 10.4. Comparison between the current simulation and NUMISHEET 96 benchmark data a) Contact force vs. punch travel b) x-position of the point A, y-position of the point A, x-position of the point F, and y-position of the point F at the maximum punch travel (before springback) c) Lengths AC, AH, and AF (after springback).

There are at least seven regions in a friction stir welded blank. Figure 10.6 depicts the regions schematically. It should be noted that not all friction stir welds have the same shape of weld nugget and HAZ. For an overview of the different possible shapes in FSW see reference [11]. However, the same seven regions are present in all friction stir welds. Figure 10.6 is a general representative shape that is used in this study. The mechanical properties of the different zones of a friction stir weld are different. If the first and the second base metals are the same, the number of zones reduces to four. It is worthwhile to point out that even if the first and the second base metals are the same, the weld nugget is asymmetric about the weld centerline. This asymmetry is due to the fact that the blank that is placed on the advancing side of the weld experiences different welding conditions compared to the blank placed on the retreating side.

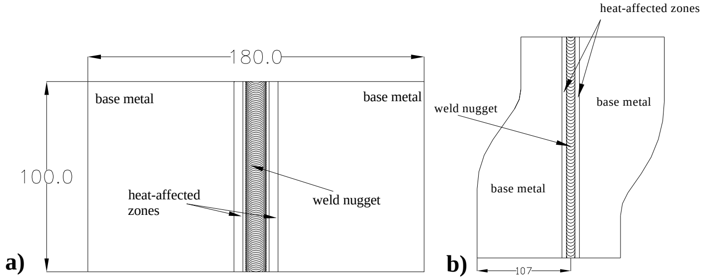

Figure 10.5. Drawings of the friction stir welded blanks used in the simulations of the LDH test (5a) and S-rail problem (5b).

Table 10.2 The mechanical properties and widths of the zones in the friction stir welded blank.

property	BM	HAZ	WN
E (GPa)	77	78	78
σ_y (MPa)	380	258	313
n	0.172	0.227	0.196
K (MPa)	760	754	730
width (mm)	NA	4.8	14.8
ε_{max}	17%	8.6%	

The experimental results used in this study are adopted from two related works reported in references [12, 13]. Accordingly, we have made three assumptions about the FSW blanks. First, it is assumed that the weld nugget and heat-affected zones are symmetrical about the weld centerline. Second, following Liu and Chao [12], the thermomechanically-affected zones are incorporated into the weld nugget. Finally, also following Liu and Chao [12], the point that the boundaries of the weld nugget and heat-affected zones are inclined was not considered in the FEM modeling of the FSW blanks. Experimentally-obtained mechanical properties and widths of the different zones were adopted from the literature [12]. Table 10.2 gives the mechanical properties and widths of the weld zones. Six different models, as

detailed in Table 10.1, are considered in this study. Three models, out of six, are related to the LDH test and the other three are related to the S-rail problem.
The first assumption regarding the symmetry of the WN and HAZs around the weld centerline is not entirely true. In reality, the conditions experienced by the material on the advancing side are different from the conditions experienced by the material on the retreating side. That is because of the different velocity profiles in the advancing and retreating sides. In the advancing side, the tangential component of the rotating tool velocity is in the same direction of the translational velocity of the tool-holder and these two velocities are, thus, summed up. In the retreating side, instead, these two velocities are in the opposite directions and are subtracted from each other, resulting in smaller overall velocity. Therefore, the straining and grain refinement is more severe in the advancing side [14]. Due to more severe strain hardening and grain refinement, the material in the advancing side has a higher strength compared to the material in the retreating side. The magnitude of this asymmetry was studied in previous experimental studies [15, 16]. The local stress-strain curves of the weld material were measured using the digital image correlation technique. The curves were used to determine the ratio between the strength and strain hardening coefficients of the weld material (both WN and HAZ) in the advancing side to those of the weld material in the retreating side. The measurements revealed that the asymmetry is rather limited in the WN ($K_{advanc}/K_{retreat} = 1.0246$, $n_{advanc}/n_{retreat} = 1.0226$) and more severe in the HAZ ($K_{advanc}/K_{retreat} = 1.0583$, $n_{advanc}/n_{retreat} = 1.1600$). The effects of relieving the symmetry assumption on the strain distribution and springback behavior of FSW TWBs are studied in the forthcoming paragraphs. In asymmetric cases, the strength and strain hardening coefficients of the WN and HAZ in the advancing and retreating side are calculated by using the above-mentioned ratios between the coefficients. The values presented in Table 10.2 are considered to be the average of the coefficients in the advancing and retreating sides.

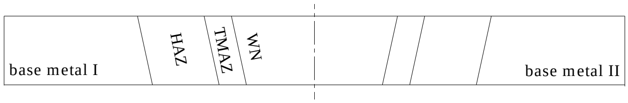

Figure 10.6. Schematic cross section of a typical friction stir weld.

10.4. Failure prediction

As previously pointed out, the forming limits of the different zones of FSW TWBs are much different and the FLDs used for identification of the failure in the forming of FSW TWBs need to be determined for each single zone. Experimental determination of the different zones of FSW TWBs is a difficult and error-prone process primarily because of the narrow widths of the WN and HAZ. Therefore, the Marciniak-Kuczynski method is used in this study for theoretical prediction of the FLDs. Different versions of the M-K theory have been already used by other researchers for failure prediction of the alloy (AA 2024) used in this study [17] and also for different types of the TWBs [18, 19]. The theory has been shown to be capable of successfully predicting the failure limits of the cases studied. The formulation of the Marciniak-Kuczynski theory was discussed in Chapter 8. The sheet was assumed to have been failed when the strain increment severity factor (the ratio of the strain increment in the region *b* to that of the region *a*) reached 10. The Hollomon's hardening rule and von Mises yield criterion were used in this study. The imperfection angle is assumed identical to the Hill's zero-extension angle. In the following section, first the imperfection parameters for the M-K model are determined based on the results of the tensile tests. The forming limits are then calculated by using the determined imperfection parameters. These FLDs are used to predict the forming limits in the FEM modeling of the LDH test and the S-rail problem.

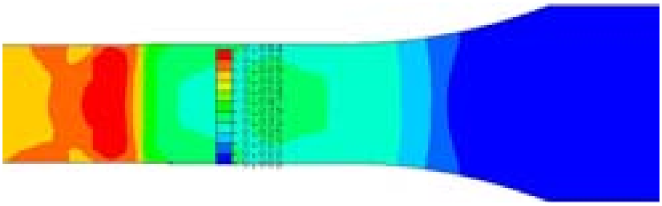

Figure 10.7. Local values of the major in-plane strain for half of the tensile test specimen.

The tensile tests are used for determination of the M-K model's imperfection parameters. The mechanical properties given in Table 10.2 were used to model the base metal, weld nugget, and heat-affected zones. The global elongation of the specimen was set at the same value as the experiments. The model was simulated to calculate the local strain values that correspond to the applied global elongation. Figure 10.7 shows the local strain values of the friction stir welded tensile test specimen at the applied global failing elongation. The calculated strain values of the WN were first compared with the experimental local strain values (from [12, 13]) to make sure that the FEM model is valid and accurate. The results of the FEM model were found in a very good agreement with the experimental values measured by using the digital image correlation technique [12, 13]. Once the model was validated, the calculated major and minor in-plane strain values of the WN and HAZ were extracted from the FEM model and were used to calculate the exact strain ratio and estimate the conservative straining limits of the different zones of the FSW TWB. Then, a nonlinear optimization algorithm, namely direct search, was used to solve the M-K model and identify the imperfection parameters for which the FLDs predicted by the M-K model match the local strain values calculated by the FEM model at the exact calculated strain ratio. Once the nonlinear optimization algorithm converged (convergence tolerance= 0.02% strain) and the FLDs predicted by the M-K model matched the experimental results, the FLDs were calculated for different zones of the FSW TWB, namely base metal, WN, and HAZ. The identified imperfection parameters as well as the predicted FLDs are depicted in Figure 10.8. It is clear that the forming limits of the WN and HAZ are much smaller compared with the BM but relatively close to each other. These FLDs will be used in the following sections for prediction of the failure during the simulation of the LDH test and S-rail problem.

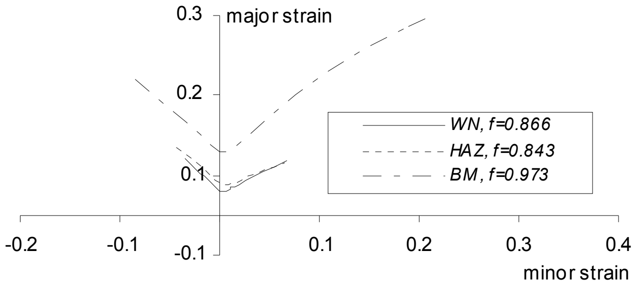

Figure 10.8. The imperfection parameters and FLDs of the different zone of the friction stir weld.

10.5. Simulation results

The FLDs determined in the previous section were used as input for the FEM packages. For each element, *i*, of the FEM model, a damage initiation parameter, χ_i, was defined as follows

$$\chi_i = \frac{\varepsilon_{i,1}}{\varepsilon_{1,FLD}} \tag{1}$$

where $\varepsilon_{i,1}$ and $\varepsilon_{1,FLD}$ stand for the major in-plane strain of the element *i* and the major in-plane strain of the FLD for the same strain ratio as the element *i*, respectively. The strain path of the element *i* crosses the FLD once the damage initiation parameter, χ_i, reaches unity. As previously stated, three different models with three different levels of weld details were considered for each case of the study. Although the first and second model did not include the mechanical properties of some zones of the FSW blank, the FLDs used for prediction of the damage of different zones were always identical to what obtained in the previous section. The independency of the simulation results from the applied mesh was studied to ensure convergence of the results and the element size was selected based on the convergence study. For example, the results of the mesh dependency study for the LDH test showed that by 7 folds change in the element size (from circa 5 mm to circa 0.75 mm) the punch travel at the onset of failure changed by 0.4 mm (≈5% of the converged value) while showing a clear convergence trend and the results converged within 0.1 mm tolerance ($\approx$1% of the converged value) at 1 mm (approximate) element size. The simulation results for each case of the study (LDH or S-rail) are presented in the either following subsections.

Simulation results for the LDH test. The monolithic blank was replaced by a friction stir welded blank. Other specifications of the model were not changed. The simulations were carried out for the three aforementioned models related to the LDH test (models 1 to 3). The first aim of the simulation was to detect the onset of failure. This was necessary because the formability of the FSW TWB is much less than that of the BM and, thus, the strain distribution of the models must be compared at a punch travel for which the comparison makes sense, i.e. at a punch travel about or less than the maximum punch travel. Table 10.3 gives the Dome Height (DH) at the onset of failure and the zone at which the failure first takes place. The maximum damage initiation parameter values of the other zones are also given. The minimum value of the punch travel (i.e. 7.6 mm) is used as the punch travel at which the strain values and calculation times from different models are compared with each other. The calculation time was not much affected by implementation of the weld details. Figure 10.9a to c depict the major in-plane strain, minor in-plane strain, and the damage initiation parameter along the x-axis (x=0 to 40 mm, y=0), respectively. The major and minor in-plane strains along the y axis (x=0, y=0 to 50 mm) are shown in Figure 10.10a and b. As previously mentioned, the effects of asymmetry (for model 3 and due to differences between advancing/retreating sides) of the mechanical properties of the weld metal around the weld centerline were also studied by simulating the deformation of the asymmetric FSW blank during the LDH test. Figure 10.11 presents the strain distribution of the asymmetric case at 5 mm punch travel and compares the results with the symmetric case to reveal the effects of asymmetry on the strain distribution. These simulation results will be discussed later in the “discussions” section.

Table 10.3. Summary of the failure prediction simulation results for models 1 to 3.

	model 1	model 2	model 3
DH (mm)	11.0	7.6	8.0
failure location	WN	WN	HAZ
$\chi_{i,max}$ @ BM	0.39	0.17	0.16
$\chi_{i,max}$ @ WN	1	1	0.87
$\chi_{i,max}$ @ HAZ	0.83	0.49	1

Simulation results for the S-rail problem. Similar to the LDH test, the simulations were carried out for three different models of the S-rail problem (models 4 to 6). Simulations were carried out in two phases. The first phase was devoted to determination of the maximum punch travel for different models. Therefore, the first phase consisted of only holding and stamping stages. Once the maximum punch travels were determined, the smallest one was used to simulate the models in the second phase, in which the simulations included holding, stamping, and springback stages. The first phase of the simulations showed that the failure punch travels for models 4, 5, and 6 are 7.3 mm, 7.6 mm, and 6.0 mm, respectively. The failure location was detected at the HAZ for all the three models. The results of the second phase of simulations are presented in Figure 10.12 to Figure 10.14. These figures show distribution of the x, y, and z displacements caused by the elastic recovery throughout the friction stir weld blank. For the holding and stamping stages, the simulation time was found almost independent from the level of the weld details in the models. However, the simulation time of the springback stage increased up to 120% when more weld details were implemented in the FEM model. The effects of weld metal asymmetry (for model 6) on the springback behavior of FSW TWBs were studied as well. The simulations were repeated for an asymmetric weld metal (both WN and HAZ were asymmetric) as described in the section on friction stir welded blanks. The simulation results are presented in Figure 10.12 to Figure 10.14 (subfigure (d) of the figures).

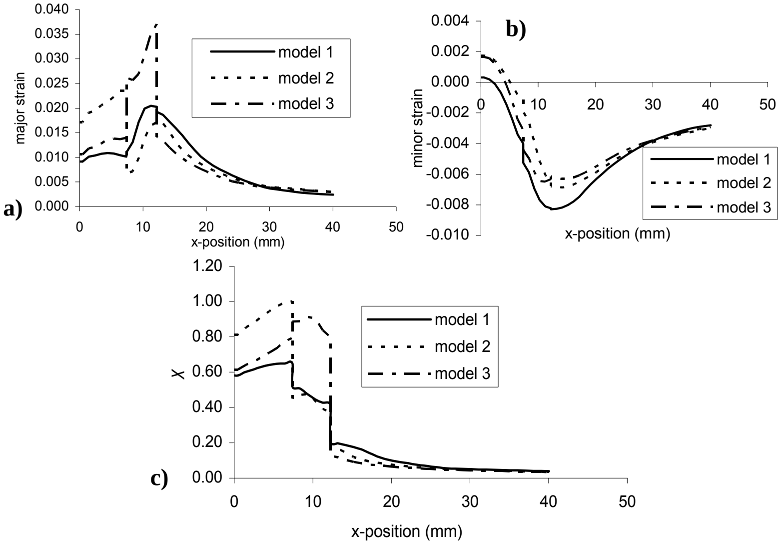

Figure 10.9. The major in-plane strain (a), minor in-plane strain (b), and damage initiation parameter (c) along the blank's x-axis.

10.6. Discussions

The results of the simulation show that the failure for all models occurs in either WN or HAZ. The simulation results show that omitting the mechanical properties of the weld zone can result in 38% overestimation of the dome height in the LDH test and 27% overestimation of the maximum punch travel in the S-rail problem. The maximum damage initiation parameters of the WN and HAZ are very close at the onset of damage for models 1 and 3, which shows that as long as the mechanical properties used for modeling these two zones are not much different, the damage initiation parameter of these two zones are quite similar and hence, statistically speaking, the failure might occur in either zone. This is in agreement with the findings of other researchers [4, 20, 21]. Interestingly, the predicted DH of model 2 is even less than model 3. This is due to different mechanical properties of the HAZ in these two models which results in larger straining of the weak WN zone in model 2 compared to model 3 in which the large strains are distributed between the weak zones of both WN and HAZ. Although the maximum punch travel of models 2 and 3 are close, it is not the case for models 5 and 6, which shows that generally speaking, it is not sufficient to implement the mechanical properties of the WN, but that the properties of the HAZ must be implemented as well.

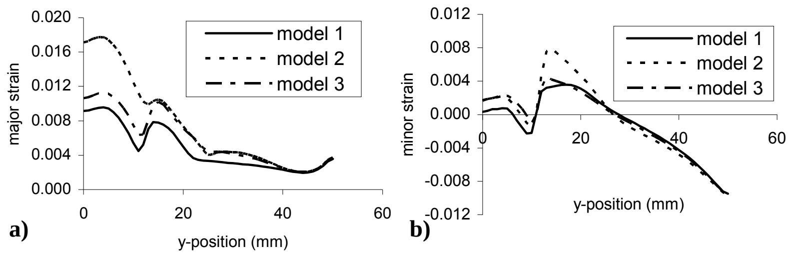

Figure 10.10. The major in-plane strain (a) and minor in-plane strain (b) along the blank's y-axis.

It is clear from Figure 10.9 and Figure 10.10 that the implementation of the weld details can significantly influence the simulated strain distribution of the friction stir welded blank being tested in a LDH test setup. However, the differences between three models (models 1 to 3) are not of the same magnitude for major and minor in-plane strains; neither are the differences homogeneously distributed within the blank. While there is practically no difference between contact forces of the three different models, the major in-plane strains tend to vary drastically from model 1 to model 3. However, the minor in-plane strains are less different for the different models when compared to the major in-plane strains. The other important point, as already mentioned, is that the differences between these three models are not uniform within the blank. In general, a higher level of discrepancy between the models can be seen in the central region of the blank and the differences are minimal at the blank's edge (see Figure 10.9 and Figure 10.10). Indeed, the heterogeneity of the studied FSW blank is limited to the local variation of the mechanical properties of the weld nugget and heat affected zones. Therefore, one expects that the impact of the heterogeneity is much less for the areas away from the weld's centerline. The point that the differences are much higher in the central region (of the blank) is an important point. The importance is due to the three following facts. First, the highest strains take place in the central region of the blank specifically in the HAZ zone (see Figure 10.9 and Figure 10.10). Second, in the LDH test of the blanks with a large width, as in the case of the studied blank, the failure normally happens in the central region of the blank. Thus, an accurate prediction of the strain distribution near the central region is crucial for an accurate prediction of the failure strains and, hence, the limiting dome height. Finally, the forming limit diagrams of the weld nugget and heat-affected zone are different from that of the base metal. More often than not, the formability of the weld nugget and HAZ is less than that of the base metal and in many cases (see e.g. [5]) the failure happens in the HAZ. The failure is more likely to happen in the HAZ for heat-treated aluminum alloys; because the favorable mechanical properties of the alloy are degraded due to the moderately high temperatures of the friction stir welding. In contrary to the heat-treated aluminum alloys, non-heat-treatable alloys develop slightly better mechanical properties after welding due to the grain refinement during the friction stir welding.

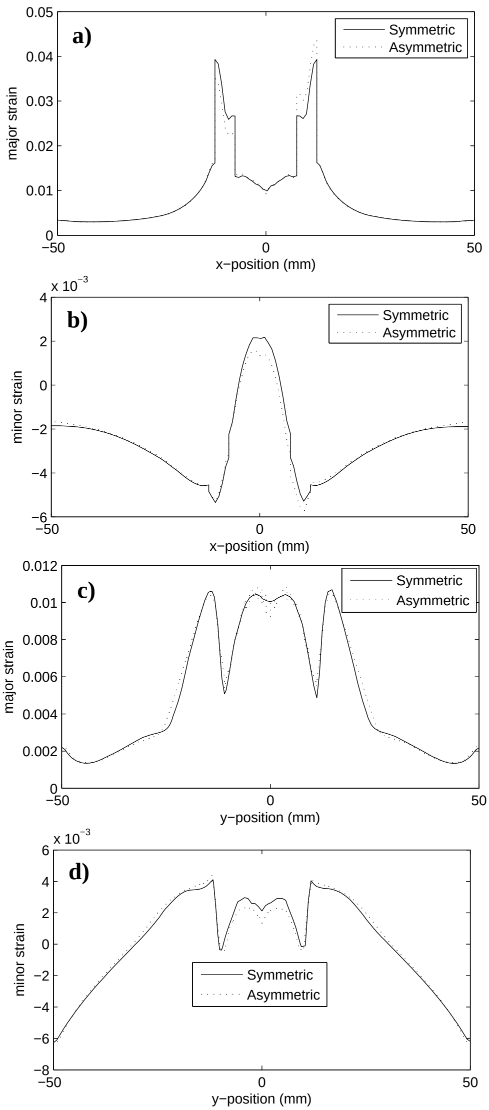

Figure 10.11. The major (a) and minor (b) in-plane strain strains along x –axis and major (c) and minor (d) in-plane strain along y-axis.

Since the alloy used in this study (2024-T351) is a heat-treated alloy commonly used in the aircraft structures, it is important for the FEM model to be able to provide an accurate prediction of the strain field in the central region of the blank. One may also notice that the peak major in-plane strain takes place in almost the same place for models 1 and 3 (see Figure 10.9a). However, the peak strain takes in a different place, i.e. the weld nugget, for model 2. This can be attributed to the fact that while the weld nugget is only moderately weaker than the base metal, a significant degradation of the mechanical properties happens in the heat-affected zones due to the exposure of the heat-affected zones to high welding temperatures.

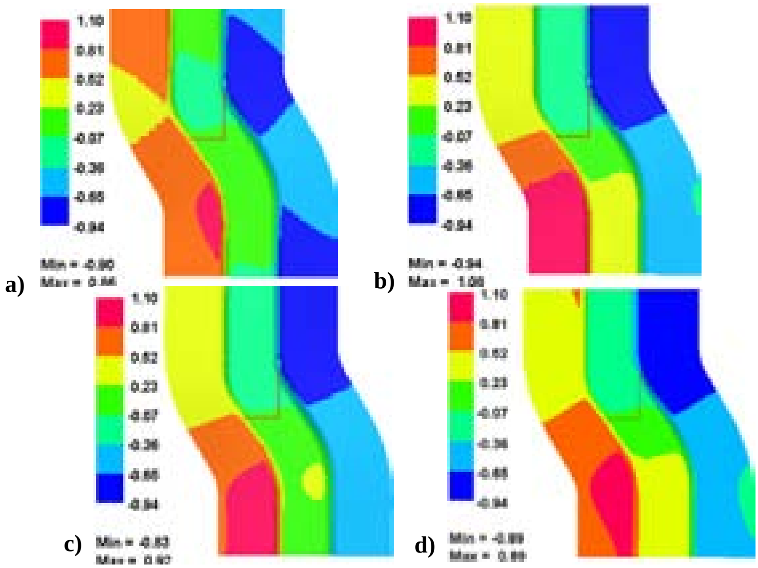

Figure 10.12. The x-displacement after elastic recovery for models 4(a), 5 (b), 6 (c) and asymmetric weld model (d).

In fact, although the welding temperatures in the friction stir welding are much lower than the fusion welding processes, the welding temperatures are high enough to cause a considerable degradation of the mechanical properties in the heat-affected zones of the welded blank. Figure 10.10a shows the maximum major in-plane strains along the weld centerline. In this figure, the strains are higher for model 2 compared to model 1; because, in model 2 the mechanical properties of the weld nugget are implemented in the FEM model. However, despite presence of an even weaker region in model 3, i.e. HAZ, the strains for model 3 are lower than model 2 (although yet higher than model 1). As already mentioned, in model 3, the straining mainly takes place in the HAZ zone and that is why the strains in the weld centerline are lower than model 2, in which straining is mainly taking place in the weld nugget. The springback behavior of the studied friction stir welded blank in the S-rail problem (see Figure 10.12 to Figure 10.14) also confirms that the implementation of the weld details in the FEM model makes a significant contribution to the accuracy of the FEM model. However, it is clear from these figures that the implementation of the weld details does not have a uniform impact on accuracy of all components of the elastic recovery displacements. Another important conclusion of the simulation results is that though there is a significant difference between the simulation results of model 4 on one side and models 5 and 6 on the other side, the differences between models 5 and 6 are minimal (particularly for x and z displacements). This means that the implementation of the mechanical properties of the weld nugget has a greater impact on the accuracy of the springback prediction than the subsequent implementation of the HAZ. This can be attributed to the smaller widths of the heat-affected zones compared to the weld nugget.

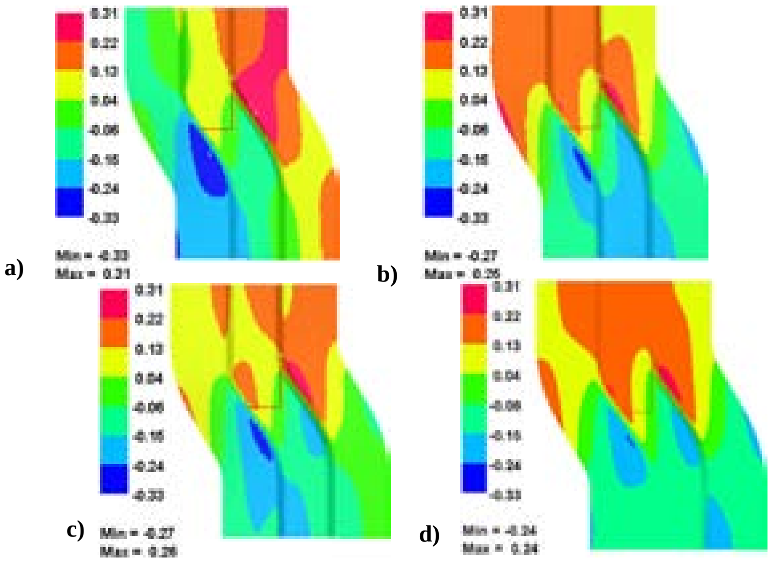

Figure 10.13. The y-displacement after elastic recovery for models 4(a), 5 (b), 6 (c) and asymmetric weld model (d).

Previous researchers have shown that the implementation of the mechanical properties of the weld zone (including the weld seam and HAZ) does not have a considerable impact on the accuracy of the springback behavior prediction of the laser-welded steel blanks [22]. This is apparently because the weld metal in laser welded blank has both a higher strength and a higher stiffness. Higher strength and stiffness have contrary impacts on the springback displacement and each one neutralizes/levels the impact of the other [22]. Furthermore, the width of the weld seam in the laser welded blanks is much less than the width of the weld nugget in friction stir welded blanks. Therefore, implementation of the weld details in the FEM model does not contribute significantly to accuracy of the springback behavior prediction of the laser welded blanks. In the case of the friction stir welded blanks, the elastic modulus of the weld nugget and heat-affected zones are almost the same as the base metal [12]. However, the strengths of the weld nugget and heat-affected zones are significantly lower than that of the base metal. In addition, the widths of the weld nugget and heat-affected zones are considerable. These factors result in the fact that implementation of the weld details has a considerable impact on accuracy of the springback prediction in friction stir welded blanks.

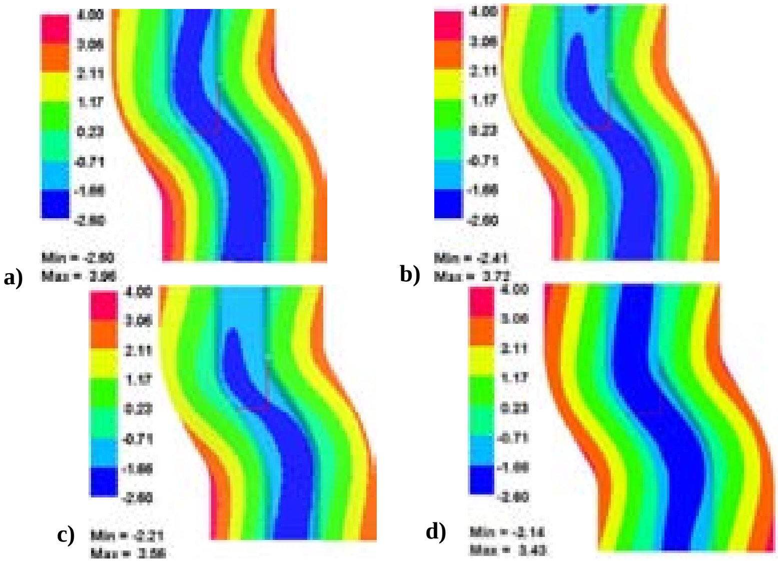

Figure 10.14. The z-displacement after elastic recovery for models 4(a), 5 (b), 6 (c) and asymmetric weld model (d).

The simulation times of models 1 to 3 were not much different. Likewise, there was no difference between the simulation times of models 4 to 6 up to the end of the stamping stage. However, the simulation time of the springback stage increased more than 120% with the implementation of the weld details in the FEM models. Therefore, it can be stated that the computational time of the simulations without springback stage is not much affected by the implementation of the weld details.
However, the simulation time of the springback stage is significantly dependent on the level of the weld details implementation. This point and the fact that the difference between the springback behaviors of models 5 and 6 are rather small brings us to the conclusion that as long as only the springback behavior is considered (e.g. in some springback-compensation die-design iterations), it might be worthwhile to compromise on the level of the weld details implementation (and accuracy) to land on a more computationally-feasible simulation However, the implementation of the mechanical properties of the heat-affected zones is crucial for the accurate determination of the strain field and the detection of the onset of failure. Therefore, in all other applications, the mechanical properties of the heat-affected zones should be implemented in the FEM models.

Figure 10.11 shows that the asymmetry of the weld metal mechanical properties around the weld centerline locally affects the strain values but does not change the overall strain distribution pattern. The peak strain values predicted by model 3 and those predicted by the asymmetric model were less than 10% (relative) different. For some applications, this level of difference is significant and needs to be taken into account. Therefore, implementation of the weld line asymmetry in the FEM model would make the model more accurate. However, there are two important barriers to this implementation. First, the number of required material parameter doubles. The material parameters are not always easy to obtain and one might have to run extra experiments to obtain the values of the extra parameters. Second, once the weld asymmetry is taken into account, it is not possible to take advantage of the model symmetry anymore. It is a common practice in the FEM modeling to reduce the full FEM model to a fraction of it taking advantage of the model symmetry. The model reduction significantly reduces the computational expense of FEM simulation. But, it is not possible to use the model reduction technique in modeling of asymmetric FSW TWBs, meaning that the computational expense is significantly increased. Figure 10.12d to Figure 10.14d show that the elastic recovery displacements are a few percents to about 10% (relative) different between model 6 and the asymmetric weld model. However, the differences are greater for the x- and y-displacements compared to the z-displacement. The z-displacement is only about 3.5% different between the symmetric and asymmetric models. Because the difference between the springback behavior of the symmetric and asymmetric models is rather small and the computational time of the springback stage increase more than 120% with implementation of the weld details, the feasibility of implementation of the weld asymmetry has to be carefully studied for each application.

The effects of the welding residual stresses were not considered in the study. That was because of three main reasons. First, the peak residual stresses in friction stir welding, even when thick plates with dissimilar high-strength alloys are welded together, is much less than that of the fusion welding processes [23]. Second, in many applications, the blanks have to be heat-treated after welding so as the residual stress can be relived. Finally, any implementation of the residual stress is in most cases formidably expensive; because the computational cost as well as the amount of the material data is substantially increased when the welding residual stress is implemented in the FEM model.

10.7. Conclusions

The failure prediction and FEM modeling of the friction stir welded blanks was studied in this chapter by using two different study cases, namely LDH test and S-rail problem. The forming limit diagrams of the different zones within the friction stir welded blanks were determined by using the M-K theory. Then, for each case of the study, three different models implementing different levels of the weld details were built, simulated, and compared. Following conclusions are drawn from the simulation results:

- Implementation of the weld details makes a significant contribution to the accuracy of the prediction of the failure, strain field and springback behavior.
- Both weld nugget and heat-affected zone have to be implemented in the FEM model so as the failure and strain field can be accurately captured. However, implementation of the mechanical properties of only the weld nugget is sufficient for reasonably accurate predictions of the springback behavior.
- The additional computational time caused by implementation of the weld details is in all cases small for up to the stamping stage. The simulation time of the springback stage might drastically (more than 120%) increases by implementation of the weld details.
- Implementation of the weld asymmetry in the FEM models makes them even more accurate. However, the difference between the strain values and elastic recovery displacements predicted by the symmetric and asymmetric models are often less than 10%.

10.8. References

[1] Hansen M. A cooler weld. Mech. Eng. 2003;125:D10.

[2] Davies RW, Oliver HE, Smith MT, Grant GJ. Characterizing Al tailor-welded blanks for automotive applications. JOM 1999;51:46.

[3] Sato YS, Sugiura Y, Shoji Y, Park SHC, Kokawa H, Ikeda K. Post-weld formability of friction stir welded Al alloy 5052. Mater. Sci. Eng. A 2004;369:138.

[4] Miles MP, Decker BJ, Nelson TW. Formability and strength of friction-stir-welded aluminum sheets. Metal Mater. Trans. A 2004;35A:3461.

[5] Buffa G, Fratini L, Merklein M, Staud D. Investigations on the mechanical properties and formability of friction stir welded tailored blanks. Key Eng. Mat. 2007;344:143.

[6] Vaidya WV, Horstmann M, Seib E, Toksoy K, Kocak M. Assessment of fracture and fatigue crack propagation of laser beam and friction stir welded aluminium and magnesium alloys. Adv. Eng. Mater. 2006;8:399.

[7] NUMISHEET 1996 benchmark documents available at http://rclsgi.eng.ohio-state.edu/~lee-j-k/Numisheet96/. 1996.

[8] Yoshida F, Uemori T, Abe S. Modeling of large-strain cyclic plasticity for accurate springback simulation. Key Eng. Mat. 2007;340-341 II:811.

[9] Kim J, Lee W, Kim D, Kong J, Kim C, Wenner ML, Chung K. Effect of hardening laws and yield function types on spring-back simulations of dual-phase steel automotive sheets. Metal. Mater. Int. 2006;12:293.

[10] Lee MG, Kim D, Kim C, Wenner ML, Chung K. Spring-back evaluation of automotive sheets based on isotropic-kinematic hardening laws and non-quadratic anisotropic yield functions, part III: Applications. Int. J. Plasticity 2005;21:915.

[11] Khaled T. An outsider looks at friction stir welding. Federal Aviation Administration 2005.

[12] Liu S, Chao YJ. Determination of global mechanical response of friction stir welded plates using local constitutive properties. Mod. Sim. Mater. Sci. Eng. 2005;13:1.

[13] Lockwood WD, Tomaz B, Reynolds AP. Mechanical response of friction stir welded AA2024: experiment and modeling. Mater. Sci. Eng. A 2002;323:348.

[14] Heurtier P, Jones MJ, Desrayaud C, Driver JH, Montheillet F, Allehaux D. Mechanical and thermal modelling of friction stir welding. J. Mat. Proc. Tech. 2006;171:348.
[15] Zadpoor AA, Sinke J, Benedictus R. The mechanical properties and microstructure of friction stir welded tailor-made blanks. Mater. Sci. Eng. A 2008.
[16] Zadpoor AA, Sinke J, Benedictus R. The effects of friction stir welding on the mechanical properties and microstructure of 7000 series aluminium tailor-welded blanks Int. J. Mater. Forming 2008;In press.
[17] Zeng XH, Barlat F. Effects of Texture Gradients on Yield Loci and Forming Limit Diagrams in Various Aluminum-Lithium Sheet Alloys. Metal. Mater. Trans. A 1994;25:2783.
[18] Chien WY, Pan J, Friedman PA. Failure prediction of aluminum laser-welded blanks. Int. J. Damage Mech. 2003;12:193.
[19] Davies RW, Grant GJ, Khaleel MA, Smith MT, Oliver HE. Forming-limit diagrams of aluminum tailor-welded blank weld material. Metal Mater. Trans. A 2001;32A:275.
[20] Miles MP, Melton DW, Nelson TW. Formability of friction-stir-welded dissimilar-aluminum-alloy sheets. Metal Mater. Trans. A 2005;36A:3335.
[21] Miles MP, Pew J, Nelson TW, Li M. Comparison of formability of friction stir welded and laser welded dual phase 590 steel sheets. Sci. Tech. Weld. Join. 2006;11:384.
[22] Zhao KM, Chun BK, Lee JK. Finite element analysis of tailor-welded blanks. Fin. Elem. Anal. Des. 2001;37:117.
[23] Prime MB, Gnaupel-Herold T, Baumann JA, Lederich RJ, Bowden DM, Sebring RJ. Residual stress measurements in a thick, dissimilar aluminum alloy friction stir weld. Acta Mater. 2006;54:4013.

11. Bendability of machined TMBs

Machining is among the techniques that can be used for creation of the needed thickness variations in TMBs. This chapter studies the bendability of machined tailor-made blanks. A high strength aluminum alloy, namely 2024-T3, is selected for the study. Air bending experiments are conducted to determine the minimum bending radius of TMBs with different thickness ratios. It is shown that the production of the machined TMBs with large thickness ratios is complicated by the release of the rolling induced residual stresses. Therefore, the TMBs with large thickness ratios are pre-strained prior to the machining process. In addition to the experiments, the forming limits are determined using a theoretical approach and the experimentally-determined forming limits are compared with the theoretically-determined ones. It is concluded that the minimum bending radius slightly (10-12%) increases as the thickness ratio increases from 1 to 2. The effects of pre-straining (in a direction in parallel with the bend line) on the minimum bending radius are found to be minimal.

Tailor-made blanks are sheet metal assemblies that are composed of blanks differing in thickness and/or material. The blanks can be welded or adhesively bonded. Alternatively, a monolithic sheet can be machined to create the required thickness variations. The tailor-made blanks made by the latter method are called machined tailor-made blanks and are the subject of the current chapter.

The presence of two different thicknesses in a blank causes additional difficulties. The areas with different thicknesses show different forming behavior such as different minimum bending radii and springback behavior. The transition from one thickness to the other causes stress concentrations. As a result, the forming limits of tailor-made blanks are different from the forming limits of the parent material.

Relatively limited information is available about the independent effects of thickness difference on the formability of tailor-made blanks. The vast majority of previous studies have been focused on tailor-welded blanks where the effects of thickness difference are mixed with the effects of the welding process. Tailor-welded blanks with thickness ratios ranging from 1 to 2 are studied in these studies [1-8]. In most cases, it is shown that the formability decreases as the thickness ratio increases [9]. Moreover, the previous studies have mostly considered deep drawing and uniaxial stretching conditions and limited information about the effects of the thickness difference on bendability is available. In this chapter, the machined tailor-made blanks will be studied. The effects of thickness difference are isolated from the

welding effects in the case of machined TMBs. Furthermore, it is the bendability (and not drawability) of the machined TMBs that will be studied.
The 2024-T3 alloy, which is commonly used in the aircraft industry, is selected for the study. The tailor-made blanks are produced with thickness ratios, r, ranging from 1 to 2. Production of the tailor-made blanks with relatively large thickness ratio ($1 \ll r \approx 2$) is associated with some difficulties. These difficulties are due to the residual stresses that are created by cold rolling of the sheet and are released during the machining process and give warpage of the specimen. Therefore, the strips used for production of the specimens with larger thickness ratios are pre-strained to relieve the residual stress. The specimens with small thickness ratios are tested in two different conditions: pre-strained and as-received so that the effects of pre-straining on the bending behavior can be studied. The minimum bending radius of the specimens is used as a measure of bendability and is determined by applying the air-bending process. The effects of the thickness ratio on the bending limits are studied. Once the experimental straining limits are determined, a theoretical approach is used to predict the forming limits of the specimens. The experimental forming limits are compared with the theoretically-predicted forming limits.

Table 11.1. The test matrix of the air-bending experiments.

no.	material	pre-strain	t_1 (mm)	t_2 (mm)	r
1	2024-T3	No	2.5	2.5	1.0
2	2024-T3	No	2.5	2.3	1.1
3	2024-T3	No	2.5	2.0	1.3
4	2024-T3	Yes	2.5	2.5	1.0
5	2024-T3	Yes	2.5	2.3	1.1
6	2024-T3	Yes	2.5	2.0	1.3
7	2024-T3	Yes	2.5	1.7	1.5
8	2024-T3	Yes	2.5	1.5	1.7
9	2024-T3	Yes	2.5	1.3	1.9

11.1. Experiments

All the specimens were cut from the same batch of 2024-T3 sheet that was 2.5 mm in thickness. The release of the residual stresses during the machining process resulted in warpage of the specimens and caused significant variation of the thickness of the machined surface particularly for the specimens with large thickness ratios. Therefore, two groups of specimens were produced as specified in Table 11.1. The first group of the specimens are the ones with relatively small thickness ratios ($1 \leq r \leq 1.3$) that were milled from the as-received sheet. The second group of the specimens had thickness ratios between 1 and 1.9 and were 1.2% pre-strained in rolling direction prior to the milling process. The pre-straining proved effective for eliminating the warpage of the specimens with large thickness ratios. There was a time interval of about three months between the prestraining and the testing. The as-received and pre-strained base metals were characterized by tensile testing. The tensile test specimens were produced according to the ASTM E8 standard such that the loading direction was in parallel with the rolling direction of the sheets. Six

samples from the as-received material and eight samples from the pre-strained material were tested by using a Zwick/Roell static test machine at a constant deformation rate of 5 mm/min. The strains were measured using an extensometer.
According to the ASTM standard E290-97a for bend testing of materials, the width of air bending specimens has to be at least 8 times the sheet thickness to ensure plane strain conditions. However, some studies have shown that the minimum bending radius is dependent on the bend width for width-to-thickness ratios less than 16 [10]. In order to ensure that the minimum bending radius is independent from the bend width, large width-to-thickness of 24 was used.

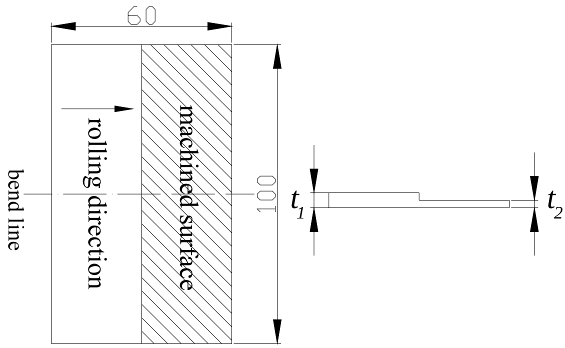

Figure 11.1. The geometry of the air-bending specimens.

The air bending specimens were cut from the sheets in rectangular shapes with a length of 100 mm and width of 60 mm. The bend line was in parallel with the rolling direction. Figure 11.1 presents a schematic drawing of the air-bending specimens. The edges of the specimens were grinded to remove notches and irregularities that could cause crack initiation and premature failure of the specimens during air bending. A press brake with V-type dies and punches with different bending radii were used to bend the specimens at a bend angle of 90°. A die opening of at least 6 times the (largest) sheet thickness was used for the tests [11]. A sheet with a thickness equal to the thickness difference ($t_1 - t_2$) was loosely attached on top of the machined surface to compensate for the thickness difference during the bending experiment. For each series of the specimens, the minimum radius over which the specimen could be safely (without crack) bent was determined with an accuracy of 0.2-0.4 mm.

11.2. Experimental results

The measured values of the yield strength, σ_y, ultimate strength, σ_u, strain at maximum stress, $\varepsilon_{\sigma_{\max}}$, and ultimate strain, $\varepsilon_{\max}$, are presented in Table 11.2. For each property, average (Avg.) and standard deviation (S.D.) of the measured values are listed in this table. The stress-strain curves of two typical samples of the as-received and pre-strained specimens are plotted and compared with each other in Figure 11.2.

The minimum bending radii of series 1 to 3 (see Table 11.1) are plotted vs. the thickness ratio in Figure 11.3a. As one can see in Table 11.1, these are the series for which the base sheet was not pre-strained prior to the machining process. The minimum bending radii of the series 4 to 9 are plotted vs. the thickness ratio in Figure 11.3b. These are the series for which the base sheet was pre-strained prior to the machining process. Linear equations are fitted to the experimental data points presented in Figure 11.3a and Figure 11.3b and the resulting lines are presented in the figures. Whenever the site of crack initiation could be detected, cracks were detected to have started from the thicker side of the specimens and propagated to the thinner side. There were some indications that the crack starts close to the transition line and propagate to the other places within the thicker and thinner side. The trend was clearer for the specimens with larger thickness ratios.

Table 11.2. The summary of the mechanical properties of the as-received and pre-strained specimens.

	as-received		pre-strained	
	Avg.	S.D.	Avg.	S.D.
σ_y (MPa)	363	11	393	1
σ_u (MPa)	494	4	493	2
$\varepsilon_{\sigma_{\max}}$ (%)	15.0	1.3	18.1	0.7
$\varepsilon_{\max}$ (%)	17.2	1.1	19.5	0.5

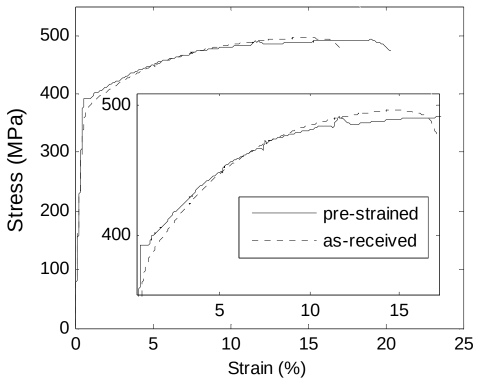

Figure 11.2. The stress-strain curve of two sample specimens in as-received and pre-strained conditions.

11.3. Numerical methods

FEM models of the air bending experiments were made for both monolithic sheets discussed in Chapter 9 (only 2024-T3 series) and the tailor-made blanks discussed in the previous sections of this chapter. Only one-half of the blanks were modeled taking advantage of the symmetry. The bend line was coincident with the symmetry line and symmetry boundary conditions were applied at the bend line. The blank was otherwise free from constraints. The punch and die were assumed rigid. The geometry of the blanks was discretized using three-dimensional continuum elements with three translational degrees-of-freedom and linear hexahedron geometry. The reduced integration scheme with hourglass control was applied. An explicit solver was used to solve the governing elastoplasticity equations. A relatively large number (5-8) of through thickness elements were used so that the bending can be accurately captured. A convergence study was conducted to ensure that the FEM simulation results are independent from the number of through-the-thickness as well as planar elements. The Hollomon's strain hardening law and von Mises yield function were adopted. The parameters of the strain hardening law had been determined during the experimental study (see Chapter 9 and Table 11.2).

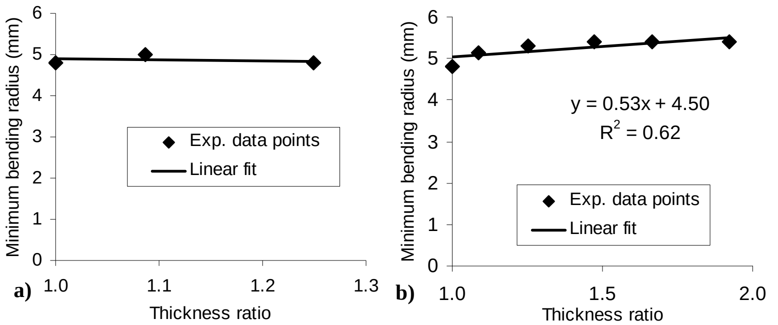

Figure 11.3. The minimum bending radius vs. thickness ratio for the air-bending specimens produced from the as-received (a) and pre-strained (b) sheets.

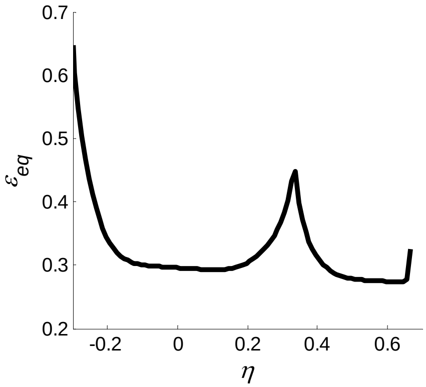

Figure 11.4. The fracture envelope for 2024-T3 as predicted by the Xue-Wierzbicki model and calibrated in Chapter 8.

The numerical modeling was carried out in three stages. First, the air bending of monolithic sheets was simulated using several punch radii to validate the results of the FEM model against analytic theory of pure bending. The calculated strains on the outer (convex) surface of the blank were compared with the strains predicted with the nonlinear bending theory. The second stage was the determination of the minimum bending radius of monolithic sheets. The third stage was determination of the minimum bending radius of tailor-made blanks. A continuum damage plasticity model recently proposed by Xue and Wierzbicki [12-14] was used for the prediction of the failure of the specimens. In Chapter 8, four different approaches for the failure prediction of high strength aluminum alloys were studied. It was concluded that the Xue-Wierzbicki model, despite its relatively low computational cost, is one of the best-performing phenomenological models and can predict the forming limits of high strength aluminum alloys with an accuracy that is comparable with the accuracy of the most sophisticated models, i.e. combination of a Gurson-type model and Marciniak-Kuczynski theory. Therefore, the Xue-Wierzbicki model is used in this chapter.
The effects of both pressure and Lode angle on the fracture envelope are taken into account in the formulation of Xue-Wierzbicki model of damage plasticity. According to the Xue-Wierzbicki model, the fracture occurs once the integral of the modified plastic strain exceeds unity. Therefore, the fracture criterion is given as [12]:

$$\int_0^{\varepsilon_{eq,f}} \frac{d\varepsilon_{eq}}{F(\eta,\xi)} = 1 \tag{1}$$

The plastic strain is scaled by the factor, F, which is a function of two dimensionless invariants: stress triaxiality ($\eta = \sigma_H / \sigma_{eq}$) and deviatoric state parameter, ξ, defined as [12]:

$$\xi = \frac{27J_3}{2{\sigma_{eq}}^3} \tag{2}$$

Dependency on the stress triaxiality and deviatoric stress parameter respectively represent the dependency of the fracture envelope on pressure and Lode angle. For von Mises yield function, isotropic strain hardening, and proportional loading, the fracture criteria can be shown to be explicitly given as an explicit function of the stress triaxiality [12]:

$$\varepsilon_{eq,f}(\eta) = C_1 \mathrm{e}^{-C_2\eta} - (C_1\mathrm{e}^{-C_2\eta} - C_3\mathrm{e}^{-C_4\eta})(1-\xi^{1/n})^n \tag{3}$$

where

$$\xi = \frac{-27}{2}\eta\left(\eta^2 - \frac{1}{3}\right) \tag{4}$$

The parameters C_1 to C_4 are the calibration parameters that need to be determined during a calibration process. In Chapter 8, the Xue-Wierzbicki model for 2024-T3 was calibrated using the experimental data provided by Wierzbicki *et al*. The same calibrated parameters will be used in this study even though the mechanical properties of 2024-T3 and, thus, its calibration parameters can significantly vary from one batch of material to the other. Using these parameters, the fracture locus can be represented in the space of equivalent strain-stress triaxiality (Figure 11.4). For FEM simulations, the damage parameter, D, was defined as:

$$D = \int \frac{d\varepsilon_{eq}}{\varepsilon_{eq,f}(\eta)} \qquad (5)$$

The damage parameter was updated for each time increment according to the following formula:

$$\Delta D \simeq \frac{\Delta\varepsilon_{eq}}{\varepsilon_{eq,f}(\eta)} \qquad (6)$$

The material was assumed to have failed once D reached 1. Several models with different element sizes were made to make sure that the obtained results are independent from the applied mesh. The calculated damage parameter converged with a tolerance of 0.01.

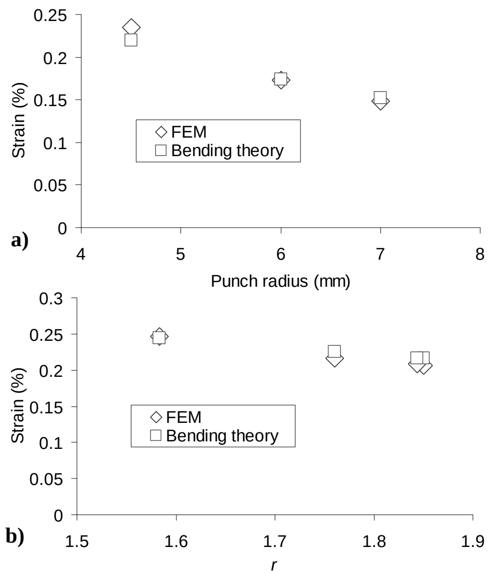

Figure 11.5. Comparison between the maximum strains on the outer surface of bent sheets calculated using FEM and bending theory. Subfigure (a) presents the values for different punch radii but the same sheet thickness of 2.5 mm. Subfigure (b) presents the values for different sheet thicknesses (punch radius = experimentally-determined minimum bending radius).

11.4. Numerical results

Figure 11.5 presents the numerically-calculated values of first principal strain and compares it with the strain values predicted with the nonlinear bending theory [15]. In Figure 11.5a, the strain values are presented for different punch radii but the same sheet thickness (2.5 mm), whereas in Figure 11.5b, the strain values are presented for the experimentally-determined minimum bending radii. Clearly, there is a good agreement between the FEM results and the predictions of the bending theory.

Figure 11.6a presents the minimum bending radii predicted with the FEM simulations and using the Xue-Wierzbicki model and compares the values with the experimentally-determined minimum bending radii. A line is fitted to the numerically-determined values and one can see that the values almost perfectly lay along the line. There is a good agreement between the numerically-obtained values and the experimental minimum bending radii. Figure 11.6b presents the results of numerical simulations for tailor-made blanks.

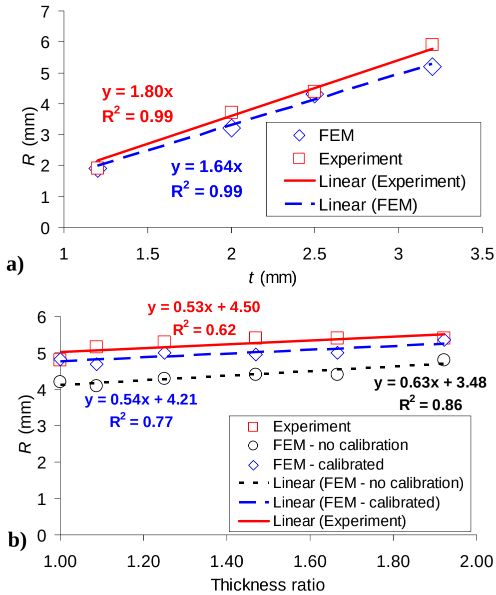

Figure 11.6. Comparison between the minimum bending radii calculated using FEM and the ones determined in the experiments for various monolithic sheets (2024-T3) with different thicknesses (a) and tailor-made blanks with different thickness ratios (b).

Two sets of numerical results are presented in this figure. The first set of results is called non-calibrated results and is obtained using the fracture envelope presented in Figure 11.4. A line is fitted to the data points of the non-calibrated results. The minimum bending radius clearly increases as the thickness ratio increases. One can see that even though the slope of the fitted line of the non-calibrated numerical results, i.e. 0.63, is quite close to that of the experimental data points, i.e. 0.53, the intercept value ($x = 0$) is about 1 mm (4.5-3.48 ≈ 1 mm) different between the two curves. Since the parameters of the Xue-Wierzbicki are taken from the literature and may be somewhat different for the specific batch tested in the experiments, the fracture envelope needs to be tuned such that the fracture envelope reflects the fracture limits of the particular material under study. One normally needs many data points for accurate calibration of the Xue-Wierzbicki model. The data points must present the whole range of stress triaxialities for which the model is to be used. In

Chapter 8, it was shown that using a small number of data points may result in the over-fitting of the model to the particular data points used for calibration. The model would therefore give inaccurate predictions outside the range of the stress triaxialities for which it is calibrated. An easy heuristic calibration method was proposed to tune the fracture envelope such that the numerical results are in agreement with the experimental results. In this method, the ratio of a selected numerical data point to its corresponding experimental data point is used to scale the fracture envelope. The calibration was carried out using a selected data point ($r = 1.7$) and the simulations were repeated using the accordingly-scaled fracture envelope. The results of the calibrated model are presented in Figure 11.6 and a line is fitted to the data points obtained with the calibrated model. It can be seen that both the slope and intercept of the fitted line are very close to those of the line fitted to the experimental values, meaning that the calibration procedure has been quite successful.

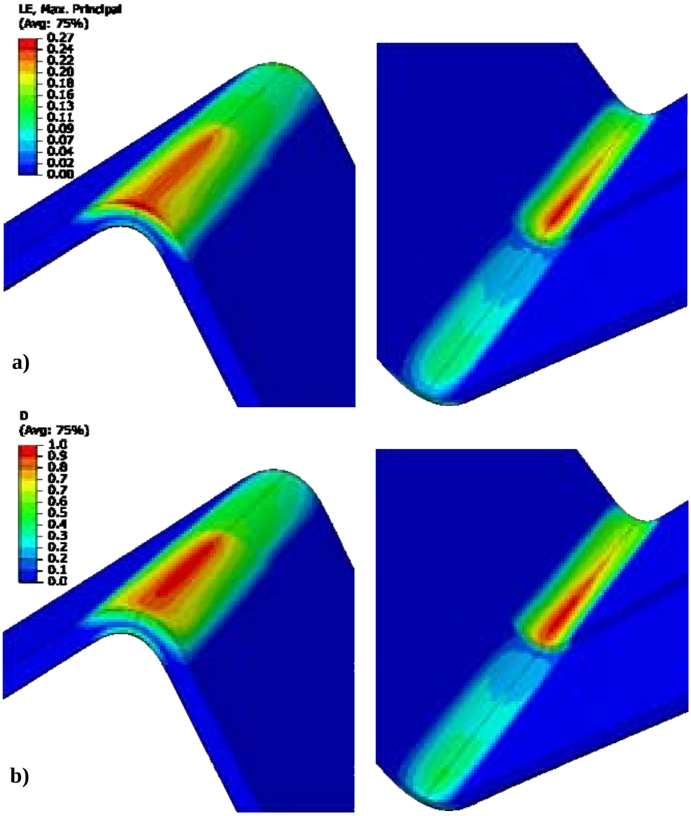

Figure 11.7. Calculated values of the maximum principal strain (a) and damage parameter (b) for a sample tailor-made blank (thickness ratio = 1.7, punch radius = 4.4 mm).

Figure 11.7 presents the distributions of major principal strain (Figure 11.7a) and damage variable (Figure 11.7b) for a sample tailor-made blank ($r = 1.7$, punch radius = 4.4 mm). The values of principal strain and damage parameter are much greater in the thicker side than in the thinner side. There is strain concentration in the inner (convex) surface of the specimen just next to the transition line. Similarly, the damage parameter takes its maximum values in the inner (concave) surface of the specimen in the proximity of the transition line. It is consistent with the observations during the experiments that the crack initiates in the proximity of the transition line and propagates towards the edge of the specimens. Comparison between different specimens with different thickness ratios showed that the maximum damage parameter is calculated to occur in the outer (convex) surface of the specimen for small thickness ratios (1-1.1). For large thickness ratios (1.2-1.9), the maximum damage parameter was calculated to occur in the inner (concave) surface of the specimen close to the transition line.

11.5. Discussions

The differences between the minimum bending radii presented in Figure 11.3a. are within the measurement accuracy and one can conclude that the minimum bending radius of the as-received specimens is independent from the thickness ratio. However, it should be noted that the thickness ratios that can be achieved without pre-straining are relatively small and any possible effect of the thickness difference on bendability is small.

Figure 11.6 shows that both for monolithic sheets and tailor-made blanks, the FEM models can successfully predict the minimum bending radius using the Xue-Wierzbicki model. The fact that the minimum bending radius of tailor-made blanks slightly increases as the thickness ratio increases has to do with the strain concentration near the transition line (see Figure 11.7a). The strain concentration in the proximity of the transition line results in earlier initiation of cracks and, thus, larger minimum bending radii. As already discussed, the FEM models predicted the maximum damage parameters to occur close to the transition line which is in agreement with the experimental observation that crack initiated from the transition line. However, the effects of thickness difference on the bendability are relatively limited as the minimum bending radius increases by a mere 10-12% as the thickness ratio increases from 1 to 1.9. That is partly because the bend and transition lines are perpendicular to each other, thereby minimizing the effects of thickness difference. The thickness ratios that are expected to be used in practice are within the above-mentioned range. Therefore, the bendability of machined TMBs is not much affected by the variation of the thickness, meaning that the safe bending window of machined TMBs is comparable with the safe bending window of the base material.

Comparing Figure 11.3a and Figure 11.3b, one can see that the minimum bending radius of the base metals ($r = 1$) is the same regardless of being tested in the as-received or pre-strained condition. Therefore, the pre-straining does not have any sensible impact on the bendability of the base metals. This is because the pre-straining is performed along the rolling direction and parallel with the bend line. Since the major deformation during the bending is perpendicular to the rolling direction, pre-straining in the direction perpendicular to the rolling direction does not have a significant impact on the bendability of the base metal. Nevertheless, there seems to be a difference between the as-received and pre-strained specimens for thickness ratios more than 1. While the minimum bending radius of the specimens produced from the as-received sheet remains more or less the same as the thickness ratio increases from 1 to 1.3, the minimum bending radius of the specimens produced from the pre-strained sheet slightly (but clearly) increases as the thickness increases from 1 to 1.3. However, the number of the data points is not large enough to warrant a firm conclusion.

Table 11.2 shows that the yield strength of the pre-strained specimens is higher than the as-received specimens. That is due to the strain hardening of the material during the pre-straining process. The ultimate strength is similar between two groups of the base materials. Interestingly, the strain at the maximum stress and ultimate strain of the pre-strained specimens are higher than those of the as-received specimens. Since the pre-straining means that the material is already strained to some extent and the formability of the material is partly exhausted, one would normally expect that the characteristic strains of the pre-strained material should be lower than those of the as-received material. There are two other interesting points. First, the scatter of the tensile properties is much lower for the pre-strained specimens compared with the as-received specimens. Table 11.2 shows that the standard deviation of the tensile properties of the as-received specimens is between 2 and 11 times more than those of the pre-strained specimens. Therefore, the pre-straining seems to have some kind of homogenizing effect on the materials. The second point is that while the stress-strain curve of the as-received material is very smooth, there are some irregularities in the stress-strain curve of the pre-strained specimens (see Figure 11.2). These irregularities were consistently repeated in the eight tested specimens. It is postulated that these three observations are interrelated. The residual stresses left in sheets from rolling process are not homogenously distributed. One explanation for these three observations is that the pre-straining influences the pattern of the residual stress distribution and somehow homogenizes the pattern. A homogenized pattern of the residual stresses means that the areas with higher residual stresses, which effectively act similar to the areas with the smaller thicknesses in the Marciniak-Kuczynski theory [16], are eliminated during the pre-straining. Therefore, any possible localization of the strain is postponed and higher strain values are recorded for the pre-strained specimens. The other explanation is that the observed behavior is due to the interaction between the dislocations and the clusters (early-stage precipitates). The pre-straining influences the pattern of dislocation density distribution and could affect the dynamics of the interactions between the dislocations and clusters. Indeed, previous studies have shown that the large density of dislocations created by pre-straining can change the precipitation sequence of 2024-T3 [17]. This could ultimately result in higher strength values for the pre-strained specimens. A third case is when both scenarios are working at the same time, resulting in increases in both strength and strain limits. Further research is needed to determine whether or not any of these explanations is actually causing the observed effects.

11.6. Conclusions

The bendability of machined aluminum tailor-made blanks was studied in this chapter. Following conclusions can be drawn from the study:

- The Xue-Wierzbicki model can successfully predict the minimum bending radii of both monolithic sheets and machined tailor-made blanks. The predictions are in agreement with the experimentally-determined limits.
- Tailor-made blanks with relatively large thickness ratios are difficult to produce due to the release of the residual stresses during the machining process.
- Pre-straining can be used to eliminate the warpage caused by the release of the residual stresses during the milling process.
- Within the range of tested specimens, the minimum bending radius of the as-received specimens is the same regardless of the thickness ratio.
- The minimum bending radius of the pre-strained specimens increases by 10-12% as the thickness ratio increases from 1 to 1.9. Therefore, one can conclude that the bendability of machined TMBs is similar to that of their corresponding monolithic sheet.
- Pre-straining does not have a significant impact on the bendability of the specimens.
- Pre-straining has some peculiar effects on the mechanical behavior of the specimens that need to be further researched.

11.7. References

[1] S. M. Chan, L. C. Chan, and T. C. Lee, "Tailor-welded blanks of different thickness ratios effects on forming limit diagrams," *Journal of Materials Processing Technology,* vol. 132, pp. 95-101, 2003.

[2] D. Seo, H. Kim, Y. Heo, N. Kim, and H. Y. Kim, "Forming and drawing characteristics of tailor welded sheets in a circular drawbead," *Journal of Materials Processing Technology,* vol. 105, pp. 294-301, 2000.

[3] L. C. Chan, C. H. Cheng, M. Jie, and C. L. Chow, "Damage-based formability analysis for TWBs," *International Journal of Damage Mechanics,* vol. 14, pp. 83-96, 2005.

[4] L. C. Chan, S. M. Chan, C. H. Cheng, and T. C. Lee, "Formability and weld zone analysis of tailor-welded blanks for various thickness ratios," *Journal of Engineering Materials and Technology-Transactions of the ASME,* vol. 127, pp. 179-185, Apr 2005.

[5] L. C. Chan, C. H. Cheng, S. M. Chan, T. C. Lee, and C. L. Chow, "Formability analysis of tailor-welded blanks of different thickness ratios," *Journal of Manufacturing Science and Engineering-Transactions of the ASME,* vol. 127, pp. 743-751, Nov 2005.

[6] H. Kusuda, T. Takasago, and F. Natsumi, "Formability of tailored blanks," *Journal of Materials Processing Technology,* vol. 71, pp. 134-140, Nov 1 1997.

[7] P. A. Friedman and G. T. Kridli, "Microstructural and mechanical investigation of aluminum tailor-welded blanks," *Journal of Materials Engineering and Performance,* vol. 9, pp. 541-551, 2000.

[8] A. A. Zadpoor, J. Sinke, and R. Benedictus, "The mechanical properties and microstructure of friction stir welded tailor-made blanks," *Materials Science and Engineering A,* vol. 494, pp. 281-290, 2008.

[9] A. A. Zadpoor, J. Sinke, and R. Benedictus, "Mechanics of tailor-welded blanks: an overview," *Key Engineering Materials,* vol. 344, pp. 373-382, 2007.

[10] A. I. H. Committee, *ASM Handbook: Volume 18: Mechanical Testing and Evaluation*. Materials Park: ASM International, 2000.

[11] H. Kurtaran, "A novel approach for the prediction of bend allowance in air bending and comparison with other methods," *International Journal of Advanced Manufacturing Technology,* vol. 37, pp. 486-495, 2008.

[12] T. Wierzbicki, Y. B. Bao, Y. W. Lee, and Y. L. Bai, "Calibration and evaluation of seven fracture models," *International Journal of Mechanical Sciences,* vol. 47, pp. 719-743, Apr-May 2005.

[13] L. Xue, "Ductile fracture modeling : theory, experimental investigation and numerical verification," in *Department of Mechanical Engineering*. vol. PhD: MIT, 2007.

[14] L. Xue and T. Wierzbicki, "Ductile fracture initiation and propagation modeling using damage plasticity theory," *Engineering Fracture Mechanics,* vol. 75, pp. 3276-3293, Jul 2008.

[15] C. Wang, G. Kinzel, and T. Altan, "Mathematical modeling of plane-strain bending of sheet and plate," *Journal of Materials Processing Technology,* vol. 39, pp. 279-304, 1993.

[16] Z. Marciniak and K. Kuczynski, "Limit strains in the process of stretch-forming sheet metal," *International Journal of Mechanical Sciences,* vol. 9, pp. 609-620, 1967.

[17] R. Ferragut and A. Somoza, "Positron, age-hardening and precipitation in predeformed 2024 (Al-Cu-Mg) alloy," *Physica Status Solidi (A) Applied Research,* vol. 175, 1999.

Tailor-made blanks for the aircraft industry

12. Conclusions

The research reported in this thesis shed light on the different aspects of TMBs for application in the aircraft industry. The detailed conclusions are given at the end of individual chapters and in the summary. In this final chapter, the main overall conclusions and contribution of the thesis are presented. The obtained results help design engineers in realization of TMBs in the aircraft industry by giving them a priori knowledge of the expected behavior of TMBs and providing them with required modeling and design tools. The main overall conclusions are as follows:

- The failure modes of the different types of TMBs were determined and studied. In general, TMBs fail either in sheet metal (machined and FSW TMBs) or adhesive (some classes of adhesively bonded TMBs). Metal failure is through instability, ductile fracture, or a combination of both. As for the adhesive failure, it may or may not result in delamination depending on the loading conditions.
- The modeling of the different types of TMBs was carried out, the modeling approaches were benchmarked, and appropriate modeling techniques were identified. In particular, it was revealed that:
    - Cohesive interface elements are successful in modeling the failure of the adhesive (Chapter 4).
    - The mechanical properties of the different weld zones of friction stir welded blanks must be implemented in FEM models (Chapter 10).
    - A combination of the Marciniak-Kuczynski theory with Gurson-type modeling of ductile fracture (MK-PMP) is the most sophisticated and accurate model among the four different types of theoretical formability prediction approaches studied in this thesis (Chapter 8). Wilkins and Xue-Wierzbicki are the most accurate phenomenological ductile fracture models. Their accuracy is comparable with the MK-PMP model.
    - Xue-Wierzbicki model can accurately predict the minimum bending radius of monolithic sheets and machined TMBs (Chapter 11).
- The design parameters play an important role in the forming limits of TMBs. In most cases, the forming limits decrease as the thickness ratio increases (Chapters 3, 4, 5, 7, and 11). The combination of materials also plays an important role and can significantly change the mechanical properties (Chapter 7) or failure mode (Chapter 5) of the TMBs.

- The forming limits of TMBs tend to be different in in-plane straining and bending. For example, the in-plane straining limits of adhesively bonded (Chapter 4) and machined TMBs (Chapter 3) significantly decrease as the thickness ratio increases. However, the bendability of machined TMBs only slightly decreases as the thickness ratio increases (Chapter 11).
- The forming limits of TMBs are strongly direction-dependent. Of particular importance is the direction of the major principal strain with respect to the transition line from one thickness/material to the other. The failure criterion and failure mode can be completely different for straining parallel to or perpendicular to the transition line (Chapters 3, 4, and 5).
- In the conventional design of structural parts, the material is selected/known and the task of the designer is to engineer the part and design the manufacturing process. In the case of TMBs, the material itself should be designed such that the cost function of the design is optimized. For example, depending on the direction of the major principal strain with respect to the transition line a tougher or a more ductile adhesive should be used (Chapter 4 and 5). This means more flexibility in design and, at the same time, a more elaborate design optimization task.

12.1. Recommendations for future research

Although several important aspects of TMBs were explored during the course of this project, certain aspects of TMBs remain unexplored. The springback and fatigue behavior of TMBs are probably among the most important ones. In addition, the prediction of the formability of strongly heterogeneous TMBs such as FSW TMBs in complex straining conditions is yet to be studied. Another important topic is residual stress. Residual stresses can influence the formability of TMBs as well as their fatigue properties. Yet another important topic for future research is the optimal design of TMBs. A systematic method for the optimal design of TMBs allows the designers to benefit from the potentials of TMBs to the maximum possible extent. Currently, there is no systematic approach to the design of TMBs neither for the aircraft industry nor for the automotive industry. As the market for TMBs grows in the aircraft industry, even more topics become relevant. Therefore, it is expected that more research is needed in the future to answer these un-answered questions.

Summary

Tailor-Made Blanks (TMBs) are hybrid assemblies made of sheet metals with different materials and/or thicknesses that are joined together prior to forming. Alternatively, a monolithic sheet can be machined to create required thickness variations (machined TMBs). The possibility of having several thicknesses and/or materials in one single structure facilitates optimal material distribution and helps us make ground and air vehicles lighter, more cost-effective, fuel-efficient, and environment-friendly. TMBs technology has been used in the automotive industry for almost two decades mostly in the form of tailor-welded blanks, where steel or aluminum sheets are (laser) welded. The applications of the technology were, however, non-existent in the aircraft industry primarily because the fusion welding processes that are used in the automotive industry are not suitable to the precipitation-hardened high strength aluminum alloys that are used in the aircraft industry. The high welding temperatures of fusion welding techniques is detrimental to the carefully engineered microstructure of those alloys and degrades their mechanical properties. Therefore, alternative joining (production) techniques are needed to produce TMBs in the aircraft industry and take advantage of the possibilities they offer. The problem with the alternative joining (production) techniques is that they (in combination with the new class of material that they are being applied to) create a very little-known application field, where the already available know-how from the automotive industry is not applicable anymore. New research is therefore needed to generate the lacking know-how for application of the TMB concept in the aircraft industry. The objective of this dissertation is to contribute towards generating that missing knowledge.

Three production techniques were selected in harmony with the necessities of the aircraft industry, namely adhesively-bonding, friction stir welding, and machining. Two representative aluminum alloys, namely 2024-T3 and 7075-T6, were chosen for the research. These alloys represent the 2000 and 7000 series aluminum alloys which are extensively used in the aircraft industry.

Aside from the introductory and literature review chapters, the other chapters of this dissertation are organized into two major parts each encompassing several chapters. While the chapters of the first part deal with the mechanical properties and microstructure of TMBs, those of the second part are chiefly dealing with the FEM modeling, formability, and formability prediction of the different types of TMBs.

In the first part, the first chapter is focused on machined TMBs. The second and third chapter deal with adhesively-bonded TMBs, and the topic of the fourth and five chapters is friction stir welded TMBs. In these chapters, two special types of

tensile test specimens were designed, manufactured, and tested to reveal the mechanical properties and uniaxial mechanical behavior of TMBs when in-plane straining is carried out in parallel with or perpendicular to the transition line from one thickness/material to the other. The tensile tests of machined and adhesively bonded TMBs were also simulated using FEM. In the case of friction stir welded TMBs, the microstructural features, chemical composition, global and local mechanical properties, hardness profiles, and fracture mechanism of the TMBs were studied experimentally. The study carried out in the first part of the dissertation resulted in the underlying mechanics of the in-plane straining experiments being known, its failure modes being identified, and the straining limits being determined. Some of the important conclusions of the first part are as follows. First, the straining limits of the different types of TMBs were found to lower as the thickness ratio increases. Second, delamination and adhesive rupture (due to limited ductility of the adhesive) were found to be limiting the in-plane straining capacity of adhesively bonded TMBs when the straining was, respectively, perpendicular to or in parallel with the transition line. FEM models with cohesive interface elements were successful in predicting the delamination load of adhesively bonded TMBs. Third, the microstructure (grain morphology, texture, etc) of friction stir welded TMBs was found to be strongly heterogeneous with mechanical properties varying significantly both through the thickness and perpendicular to the weld seam.

The second part of the thesis consists of four chapters. The first chapter compares four different approaches for formability prediction of high strength aluminum alloys and identifies the best-performing and least computationally-expensive approaches/models. The second chapter studies the effects of thickness on the tensile properties and bendability of the selected alloys and shows that sheet thickness has significant impact on the straining limits of the studied alloys both in in-plane straining and bending. The third chapter studies FEM modeling and failure prediction of friction stir welded TMBs. It concludes that implementation of the mechanical properties of the different zones of the weld significantly improves the capability of the model in predicting strain distribution, springback behavior, and failure strains. The final chapter determines the bending limits of machined TMBs both theoretically and experimentally. It is shown that the minimum bending radius of the machined TMBs increases by a mere 10-12% as the thickness ratio increases from 1 to 1.9. Moreover, the theoretical approach is shown to be able to accurately predict the bending limits of both monolithic sheets and machined TMBs.

The final conclusions of the research carried out in the thesis are presented in the last chapter, where some topics are recommended for further research.

Samenvatting

Tailor-Made Blanks (TMBs) zijn hybride samenstellingen van metaalplaat van verschillende materialen en/of dikte die aan elkaar verbonden worden, voordat ze worden omgevormd. Ook kan, als alternatief, in een monolithische plaat varierende dikten worden aangebracht door frezen (zgn. “machined” TMBs). De mogelijkheid om verschillende dikten en/of materialen in één platine samen te voegen, zorgt voor optimale materiaalverdeling en helpt daarmee voertuigen op de grond en in de lucht lichter, kosteneffectiever, brandstof efficiënter en milieuvriendelijker te maken. De technologie van TMBs wordt al bijna twintig jaar toegepast in de automobiel industrie, voornamelijk in de vorm van Tailor Welded Blanks (TWBs), waarbij staal of aluminium platen (met lasers) aan elkaar worden gelast. De toepassing van de technologie bestond echter nog niet in de vliegtuigindustrie, omdat fusielas processen, zoals toegepast in de automobiel industrie, niet geschikt zijn voor de (hoge sterkte) precipitatie-hardende aluminiumlegeringen van vliegtuigen. De hoge lastemperaturen van deze fusielas processen zijn desastreus voor de zorgvuldig aangebrachte microstructuur in deze legeringen en hun mechanische eigenschappen worden gedegradeerd. Daarom zijn alternatieve verbindings- en productietechnieken nodig voor TMBs voor de luchtvaart en om de mogelijkheden te kunnen uitbuiten.
Het probleem met alternatieve verbindings- en productietechnieken (in combinatie met een nieuwe categorie materialen) is dat zij een weinig bekend terrein van toepassingen vormen, waar de reeds bekende kennis uit de automobiel industrie niet meer bruikbaar is. Nieuw onderzoek is daarom nodig om de ontbrekende kennis voor het toepassen van het TMB concept in de luchtvaart industrie te genereren. Het doel van deze dissertatie is om bij te dragen aan de ontwikkeling van deze ontbrekende kennis.
Drie productiemethoden zijn geselecteerd die zijn afgestemd op de behoeften van de luchtvaartindustrie, namelijk lijmen, wrijvingsroerlassen of “Friction Stir Welding” (FSW) en frezen. Twee representatieve aluminium legeringen, t.w. 2024-T3 en 7075-T6, zijn gekozen voor het onderzoek. Deze legeringen vertegenwoordigen de 2000- en 7000-series, die vaak toegepast worden in de vliegtuigindustrie.
Naast de inleiding en het literatuur overzicht, kunnen de andere hoofdstukken van deze dissertatie ingedeeld worden in twee delen, waarbij elk deel meerdere hoofdstukken bevat. De hoofdstukken van het eerste deel behandelen met name de mechanische eigenschappen en de microstructuur van TMBs, terwijl de hoofdstukken van het tweede deel primair het numerieke modelleren (FEM), de vervormbaarheid en de voorspelling van de vervormbaarheid van de verschillende TMBs beschrijven.

In het eerste deel, is het eerste hoofdstuk gericht op “machined” TMBs. Het tweede en derde hoofdstuk gaan over gelijmde TMBs en het onderwerp van de hoofdstukken vier en vijf zijn FSW TMBs. Voor al deze hoofdstukken werden speciale trekproefstukken ontworpen, gemaakt en getest om de mechanische eigenschappen te bepalen van TMBs als deze in één richting in het vlak, worden belast, waarbij de richting van de grootste rek evenwijdig of loodrecht staat op de grenslijn tussen de ene dikte/materiaalsoort en de andere. De trekproeven voor de gefreesde en gelijmde TMBs werden ook gesimuleerd met FEM. Voor de FSW TMBs zijn de kenmerken van de microstructuur, de chemische samenstelling, de globale en locale mechanische eigenschappen, de hardheidsprofielen en de bezwijkmechanismen experimenteel onderzocht. Het onderzoek, beschreven in het eerste deel van de dissertatie, resulteerde in kennis en inzicht in de onderliggende Mechanica van de vervormingsproeven, in het vaststellen van het faalgedrag en het bepalen van de rekgrenzen. Enkele belangrijke conclusies uit het eerste deel zijn de volgende. In de eerste plaats is gemeten dat de breukrekken van de verschillende soorten TMBs kleiner worden als de dikteverhouding toeneemt. In de tweede plaats dat delaminatie en breuk van de lijm (als gevolg van de beperkte taaiheid van de lijm) de rek mogelijkheden van de gelijmde TMBs in het vlak beperken als de rek plaatsvindt loodrecht respectievelijk evenwijdig aan de grenslijn. FEM modellen met cohesieve grensvlak elementen konden de delaminatie in gelijmde TMBs goed voorspellen. In de derde plaats bleek dat de microstructuur (kristal morfologie, textuur, enz.) van FSW TMBs een sterk heterogeen karakter had waarbij de mechanische eigenschappen sterk varieerden zowel in de dikte als lookrecht op de lasnaad.

Het tweede deel van deze dissertatie bestaat uit vier hoofdstukken. Het eerste hoofdstuk vergelijkt vier verschillende benaderingen om de vervormbaarheid te voorspellen van hoge sterkte aluminiumlegeringen en geeft aan welke methoden/modellen het best presteren en de minste rekentijd vereisen. Het tweede hoofdstuk beschrijft het onderzoek naar de dikte-effecten op de uitkomsten van de trek- en buigproeven van de gekozen legeringen en laat zien dat de plaatdikte een aanzienlijk invloed heeft op de rekgrenzen van de bestudeerde legeringen, zowel voor het rekken in het vlak als voor buigen. Het derde hoofdstuk gaat over het modelleren en voorspellen van het breukgedrag van FSW TMBs. Hieruit volgt dat implementatie van de mechanische eigenschappen van de verschillende zones in de las een aanzienlijke verbetering geeft van de mogelijkheid voor het voorspellen van de rekverdeling, het terugveer gedrag en de breukrekken. In het laatste hoofdstuk worden experimenteel en theoretisch de grenzen voor het buigen van gefreesde TMBs vastgesteld. Hier wordt getoond dat de minimum buigradius van gefreesde TMBs zeer beperkt, met 10-12%, toeneemt als de dikteverhouding toeneemt van 1 tot 1,9. Verder is met de theoretische benadering aangetoond dat het mogelijk is de buiglimieten voor monolithisch als voor gefreesde TMBs nauwkeurig te voorspellen

De eindconclusies van het onderzoek als beschreven in deze dissertatie, worden gegeven in het laatste hoofdstuk waarbij ook enkele onderwerpen worden genoemd voor verder onderzoek.

Curriculum Vitae

Amir Abbas Zad Poor (Zadpoor) was born on the 11th of May 1982 in Qom (Iran). He finished his high school and pre-university education from the National Organization for Development of Exceptional Talents (NODET- Qom, Iran) in 2000 and subsequently started his Bachelor of Science (B.Sc.) study in the Iran University of Science and Technology (Tehran, Iran) majoring in Mechanical Engineering. After finishing his B.Sc. studies in 2004, he joined the Department of Biomedical Engineering at the Amirkabir University of Technology (Tehran, Iran) where he received his Master of Science degree in Biomechanical Engineering in 2006.

Since May 2006, Amir joined the Aerospace Materials Group in the Faculty of Aerospace Engineering at the Delft University of Technology to work on his PhD project on the “tailor-made blanks for the aircraft industry” under the supervision of Prof. dr. ir. Rinze Benedictus and daily supervision of Ir. Jos Sinke. The project was funded by the Netherlands Institute for Metals Research (then Materials Innovation Institute). This thesis covers this PhD study.

List of publications

Journal publications

- Zadpoor, A. A., Sinke, J., Benedictus, R., 2009," Formability prediction of high strength aluminum sheets", International Journal of Plasticity, vol. 25(12), pp. 2269-2297.
- Zadpoor, A. A., Sinke, J., Benedictus, R., 2009, "Bendability of machined aluminum tailor-made blanks", International Journal of Material Forming (proceedings of ESAFORM 2009), In press.
- Zadpoor, A. A., Sinke, J., Benedictus, R., 2009, "Fracture mechanism of aluminium friction stir welded blanks", International Journal of Material Forming (proceedings of ESAFORM 2009), In press.
- Zadpoor, A. A., Sinke, J., Benedictus, R., 2009," The mechanical behavior of adhesively bonded tailor-made blanks", International Journal of Adhesion and Adhesives, vol. 29(5), pp. 558-571.
- Zadpoor, A. A., Sinke, J., Benedictus, R., 2009,"Finite element modeling and failure prediction of friction stir welded blanks", Materials & Design, vol. 30(5), pp. 1423-1434.
    - Among the Top 25 Hottest Articles of the journal (January-March 2009) - Data published by the publisher's website: www.sciencedirect.com.
- Zadpoor, A. A., Sinke, J., Benedictus, R., 2009,"The effects of thickness on the formability of 2000 and 7000 series high strength aluminum alloys", Key Engineering Materials, vol. 410-411, pp. 459-466.
- Zadpoor, A. A., Sinke, J., Benedictus, R., Pieters, R., 2008, "Mechanical properties and microstructure of friction stir welded tailor-made blanks", Materials Science and Engineering A, vol. 494, pp. 281-290.
    - Among the Top 25 Hottest Articles of the journal (July-September 2008) - Data published by the publisher's website: www.sciencedirect.com.
- Zadpoor, A. A., Sinke, J., Benedictus, R., 2008, "Experimental and numerical study of machined aluminum tailor-made blanks", Journal of Materials Processing Technology, vol. 200, pp. 289-300.
- Zadpoor, A. A., Sinke, J., Benedictus, R., 2008, "The effects of friction stir welding on the mechanical properties and microstructure of 7000 series aluminum tailor-welded blanks", International Journal of Material Forming, vol. 1 (S1), pp. S311-S314.

- Zadpoor, A. A., Sinke, J., Benedictus, R., 2008, “Theoretical prediction of failure in forming of friction stir welded blanks", International Journal of Material Forming, vol. 1 (S1), pp. S305-S308.
- Zadpoor, A. A., Sinke, J., Benedictus, R., 2007, “Mechanics of tailor-welded blanks: an overview”, Key Engineering Materials, vol. 344, pp. 373-382.

Submitted / to be submitted journal publications

- Zadpoor, A. A., Sinke, J., Benedictus, R., 2009, "Global and local mechanical properties and microstructure of friction stir welds with dissimilar materials and/or thicknesses", Submitted.
- Zadpoor, A. A., Sinke, J., Benedictus, R., 2009, " Elastoplastic deformation of dissimilar-alloy adhesively-bonded tailor-made blanks”, Submitted.
- Zadpoor, A. A., Campoli, G., Sinke, J., Benedictus, R., 2009, " Fracture in bending- the straining limits of monolithic sheets and machined tailor-made blanks”, Submitted.

Book chapters

- **[Invited]** Zadpoor, A. A., Sinke, J., 2009, “Weld metal ductility and its influence on the formability of tailor-welded blanks”, in *Failure Mechanisms for Advanced Welding Processes*, Edited by Sun, X., Woodhead Publishing Ltd, Cambridge, UK, Final draft submitted, In press.
- **[Invited]** Zadpoor, A. A., Sinke, J., Benedictus, R., 2009, “Tailor-made blanks for the aerospace industry”, in *Tailor Welded Blanks for Advanced Manufacturing*, Edited by Kinsey, B. L. and Wu, X., Woodhead Publishing Ltd, Cambridge, UK, In preparation.
- **[Invited]** Zadpoor, A. A., Sinke, J., Benedictus, R., 2009, “Numerical modeling of TWB forming”, in *Tailor Welded Blanks for Advanced Manufacturing*, Edited by Kinsey, B. L. and Wu, X., Woodhead Publishing Ltd, Cambridge, UK, In preparation.

Conference papers

- Zadpoor, A. A., Sinke, J., Benedictus, R., 2008, “Comparative study of the formability prediction models for high-strength aluminum alloys", Proceedings of the 9th International Conference on Technology of Plasticity (ICTP 2008), Gyengju, South Korea, pp. 1258-1263.
- Zadpoor, A. A., Sinke, J., Benedictus, R., 2008, “Mixed-mode analysis of delamination in adhesively bonded tailor-made blanks", Proceedings of 7th International Conference and Workshop on Numerical Simulation of 3D Sheet Metal Forming Processes (NUMISHEET 2008), Interlaken, Switzerland, pp. 421-426.
- Zadpoor, A. A., Sinke, J., Benedictus, R., 2008, “Optimization of computational procedures for full model strain path dependent analysis of

forming limits", Proceedings of International Deep Drawing Research Group Conference (IDDRG 2008), Olofström, Sweden, pp. 419-428.

- Zadpoor, A. A., Sinke, J., Benedictus, R., 2007, “Springback behavior of friction stir welded tailor-made blanks”, Proceedings of International Deep Drawing Research Group Conference (IDDRG 2007), Gyor, Hungary, pp. 317-324.
- Zadpoor, A. A., Sinke, J., Benedictus, R., 2007, “Prediction of limit strains in limiting dome height formability test”, ESAFORM 2007, Zaragoza, Spain, American Institute of Physics (AIP) Conference Proceedings vol. 907, pp. 258-263.
- Zadpoor, A. A., Sinke, J., Benedictus, R., 2007, “Finite element modeling of transition zone in friction stir welded tailor-made blanks”, NUMIFORM 2007, Porto, Portugal, American Institute of Physics (AIP) Conference Proceedings vol. 908, pp. 1457-1462.

Acknowledgements

More than three years ago, when I started my PhD, I was anything but calm and settled. Having just defended my M.Sc. thesis, I also just got married and moved to the Netherlands all within three weeks. Add to this confusion the fact that I had changed my topic from Biomechanics to Manufacturing. It took us a few months of hard labor to find permanent housing, from then on we gradually felt settled and things started to improve. I felt more and more at home and the playful part of my PhD life started to show up. Having realized that being trusted to do a four-year financed PhD is a one-time opportunity that I should take most advantage of it, I worked long non-stop hours. As hard as it was, I am now comforted when I see my journey in retrospect.

Many people have helped me on this journey. First, I must thank Jos and Rinze not only for their great job of supervising my PhD research, but also for trusting me in the first place. In addition to the high-quality supervision I received, I enjoyed a lot of working freedom thanks to their continuing trust. That helped me develop an independent academic identity, while keeping my connection to the group.

My PhD research was financed by Materials Innovation Institute (formerly Netherlands Institute for Metals Research) whose support is greatly acknowledged. I appreciate the constructive discussions we had in the cluster meetings with other people in the M2i network. Particularly, I would like to thank Ton van den Boogaard and Prof. Han Huétink. They let me benefit from their vision and deep understanding of plasticity through many discussions we had during cluster meetings and metal forming conferences.

I owe a big ‘thank you’ to my other colleagues in the Aerospace Materials group. They helped me in many ways both in work-related and personal matters. Thank you Gemma, Rene, Calvin, Roger, Raph, Gianni, Rik-Jan, Paul, Ligieja, Riccardo, Sharif, Greg, Cory, Milan, and Patricio.

My research was never as successful if it was not for the help of the personnel of the Delft Aerospace Structures and Materials Laboratory (*Vliegtuighal*). We soon became friends and they patiently helped me through all those somewhat troublesome days of experimenting. I would like to thank Berthil Grashof, Frans Oostrum, Kees Paalvast, Michel Badoux, Hans Weerheim, Bob de Vogel, Serge van Meer, and Niels Jalving.

Last but by no means least, I would like to thank the most important people in my life. Mum, thank you for everything you gave me. Thank you for being so demanding and for never being happy enough if I did not do my assignments well enough. Thank you for being the big motivator of whatever achievement I made in my life. Fatemeh, thank you for your never-ending support. Thank you for bearing with me when I worked those long late hours, when everybody else was at home with his/her family. Thank you for letting me work during summer holidays and pretty much any other holiday, when other people vacationed. This whole research was not possible if it was not for your love, understanding, patience, and compassion.